

# Development of a Novel Coastal Retracking Algorithm for SAR Satellite Altimetry

**Florian Schlembach**

Vollständiger Abdruck der von der TUM School of Engineering and Design der Technischen Universität München zur Erlangung eines

**Doktors der Ingenieurwissenschaften (Dr.-Ing.)**

genehmigten Dissertation.

**Vorsitz:**

Prof. Dr. phil. nat. Urs Hugentobler

**Prüfer der Dissertation:**

1. Priv.-Doz. Dr. phil. Marcello Passaro
2. Prof. Dr.-Ing. Florian Seitz
3. Assoc. Prof. Jesús Gómez-Enri, Ph.D.

Die Dissertation wurde am 25.04.2023 bei der Technischen Universität München eingereicht und durch die TUM School of Engineering and Design am 29.09.2023 angenommen.

# Abstract

Satellite altimetry is a spaceborne radar remote sensing technology for the precise observation of the ocean surface and its changes over time. Its measurements allow the determination of geometric and physical parameters such as sea level, significant wave height (SWH) or wind speed in a process called retracking. A global knowledge of the SWH of the oceans is essential for applications such as ocean wave monitoring, industrial shipping route planning, weather forecasting, or wave climate studies.

However, estimation in the coastal zone remains challenging because the received radar echoes are subject to significant interference from strongly reflective targets such as sandbanks, tidal flats, sheltered bays, ships etc. As a result, the estimates are substantially degraded in quality or flagged as invalid.

This work presents the novel coastal retracking algorithm CORAL for synthetic aperture radar (SAR) satellite altimetry to improve the quality of the SWH estimates and increase the number of valid records near the coast. CORAL incorporates an adaptive interference masking scheme to detect and mitigate spurious interfering signals typically caused by strongly reflective targets in the coastal zone. The effectiveness of CORAL is validated using a methodology developed within the European Space Agency Sea State Climate Change Initiative project. With CORAL, the number of valid 20 Hz records in less than 5 km from the coast is increased by more than 25% compared to the best competing coastal retracking algorithm, without degrading the quality of the estimated records. The validation framework used, together with key performance evaluation criteria, was previously developed within the same project to perform a round robin assessment to compare eleven different low resolution mode and eight different SAR mode retracking algorithms to evaluate the best performing algorithm. The importance of the strategy for determining the quality flag provided with the SWH is also highlighted. The findings suggest that the SWH quality flag strategy of the official Level-2 baseline product of the Sentinel-3 mission can be redefined to obtain more robust SWH estimates in the coastal zone.

Furthermore, a case study was conducted to assess whether the SWH estimation from Sentinel-6 Michael Freilich coastal altimetry data can be further improved by using fully focused SAR (FF-SAR) instead of unfocused SAR (UF-SAR) processing. This is motivated by the fact that FF-SAR processing has a theoretical along-track resolution of up to less than half a metre. This suggests that the application of FF-SAR altimetry may provide potential gains over UF-SAR altimetry in resolving and mitigating small-scale interferers in the along-track direction to improve the accuracy and precision of the geophysical estimates. Therefore, a multi-mission FF-SAR processor developed in collaboration with Delft University of Technology and the novel coastal retracking algorithm CORAL are applied to estimate the SWH. A comparison with the high-resolution SWAN-Kuststrook coastal wave model of the Deltares RWsOS North Sea operational forecasting system shows that an FF-SAR-processed dataset yields the highest similarity with the wave model. That is, a correlation of  $\sim 0.8$  at 80% of valid records and a precision gain of up to 29% of FF-SAR vs UF-SAR for 1-3 km from the coast is achieved. The performance gain near the coast has been demonstrated in practice by estimating the decay of SWH from offshore at 30 km to up to 1 km from the coast to be  $26.4\% \pm 3.1\%$ .

# Zusammenfassung

Die Satellitenaltimetrie ist eine weltraumgestützte Radar-Fernerkundungstechnologie zur präzisen Beobachtung der Meeresoberfläche und ihrer zeitlichen Veränderungen. Ihre Messungen ermöglichen die Bestimmung geometrischer und physikalischer Parameter wie Meeresspiegel, signifikante Wellenhöhe (SWH) oder Windgeschwindigkeit durch das sogenannte Retracking-Verfahren. Die globale Kenntnis der SWH der Ozeane ist unerlässlich für Anwendungen wie die Wellenüberwachung, die Planung von Schifffahrtsrouten für die Industrie, die Wettervorhersage oder Studien zum Wellenklima.

In der Küstenzone ist die Schätzung jedoch nach wie vor eine Herausforderung, da die empfangenen Radarechos durch stark reflektierende Objekte wie Sandbänke, Wattflächen, räumlich abgetrennte Buchten, Schiffe usw. erheblich gestört werden. Dies führt dazu, dass sich die Qualität der Schätzungen stark verschlechtert oder sie als ungültig eingestuft werden.

In dieser Arbeit wird ein neuartiger Küstenretracking-Algorithmus CORAL für die Synthetic Aperture Radar (SAR) Satellitenaltimetrie vorgestellt, um die Qualität der SWH-Schätzungen zu verbessern und die Anzahl gültiger Messungen in Küstennähe zu erhöhen. CORAL beinhaltet ein adaptives Störungsmaskierungsverfahren zur Erkennung und Minderung von Störsignalen, die typischerweise von stark reflektierenden Objekten im Küstenbereich ausgehen. Die Wirksamkeit des neuartigen Algorithmus für das Küstenretracking wird anhand einer Methodik validiert, die im Rahmen des Projekts "Sea State Climate Change Initiative" der Europäischen Weltraumorganisation ESA entwickelt wurde. Mit CORAL wird die Anzahl der gültigen 20 Hz Messungen in der küstennahen Zone von weniger als 5 km vor der Küste um mehr als 25% erhöht, verglichen mit dem besten konkurrierenden Küstenretracking-Algorithmus, ohne dass die Qualität der geschätzten Messungen beeinträchtigt wird. Das verwendete Validierungsframework zusammen mit den entscheidenden Kriterien zur Leistungsbewertung wurde zuvor im Rahmen desselben Projekts entwickelt, um eine Round-Robin-Evaluierung durchzuführen, bei dem elf verschiedene Retracking-Algorithmen im Low Resolution Mode und acht verschiedene Retracking-Algorithmen im SAR Mode miteinander verglichen wurden, um den leistungsfähigsten Algorithmus zu ermitteln. Darüber hinaus wird die Bedeutung der Strategie zur Bestimmung der Qualitätskennzeichnung, die zusammen mit dem SWH bereitgestellt wird, hervorgehoben. Die Ergebnisse deuten darauf hin, dass die Strategie für die SWH-Quality Flag des offiziellen Level-2-Baseline-Produkts der Sentinel-3-Mission neu definiert werden kann, um robustere SWH-Schätzungen im Bereich der Küste zu erzielen.

Des Weiteren wurde in einer Fallstudie untersucht, ob die SWH-Schätzung aus Sentinel-6 Michael Freilich Küstenaltimetriedaten durch die Verwendung von voll fokussiertem SAR (FF-SAR) anstelle von unfokussiertem SAR (UF-SAR) weiter verbessert werden kann, da FF-SAR-prozessierte Messungen eine hohe theoretische Auflösung von weniger als einem halben Meter entlang der Bahnspur aufweisen. FF-SAR Altimetrie könnte im Vergleich zur UF-SAR Altimetrie potenzielle Vorteile bei der Auflösung und Entschärfung kleinräumiger Störungen entlang der Bahnspur bieten, um die Genauigkeit und Präzision der geophysikalischen Schätzungen zu verbessern. Daher wurde in Zusammenarbeit mit der Delft University of Technology ein FF-SAR-Multimissionsprozessor entwickelt und der neue CORAL-Algorithmus für das Retracking an der Küste zur Schätzung der SWH eingesetzt. Ein Vergleich mit dem küstennahen, hochauflösenden Wellenmodell SWAN-Kuststrook des operationellen Vorhersagesystems Deltares RWsOS zeigt, dass ein FF-SAR-prozessierter Datensatz die größte Ähnlichkeit mit dem Wellenmodell aufweist. Es wird eine Korrelation von  $\sim 0,8$  bei 80% gültiger Messungen und ein Präzisionsgewinn von bis zu 29% von FF-SAR gegenüber UF-SAR für 1-3 km vor der Küste erreicht. Die praktische Anwendbarkeit wurde durch die Abschätzung des SWH-Abfalls von 30 km bis auf 1 km vor der Küste in der Nordsee auf  $26,4\% \pm 3,1\%$  gezeigt.

# Contents

<b>Abstract</b>	<b>ii</b>
<b>Zusammenfassung</b>	<b>iii</b>
<b>1 Introduction</b>	<b>1</b>
1.1 Motivation . . . . .	1
1.2 Research Questions . . . . .	2
1.3 Thesis Outline . . . . .	4
<b>2 Satellite Altimetry</b>	<b>5</b>
2.1 General Measurement Principle . . . . .	5
2.2 Missions . . . . .	6
2.3 Processing Modes . . . . .	8
2.3.1 Conventional Low Resolution Mode . . . . .	9
2.3.2 Unfocused SAR Altimetry . . . . .	14
2.3.3 Fully Focused SAR Altimetry . . . . .	22
2.3.4 Point Target Responses for SAR Processing Modes . . . . .	27
<b>3 Estimation of Significant Wave Height using Satellite Altimetry</b>	<b>29</b>
3.1 SAMOSA-based Retracking Algorithm . . . . .	29
3.1.1 SAMOSA2 Power Return Echo Model . . . . .	29
3.1.2 Fitting Routine . . . . .	31
3.2 Challenges in Coastal Retracking . . . . .	32
3.3 State-of-the-art Coastal Retracking Algorithms . . . . .	33
<b>4 P-I: Round Robin Assessment of Radar Altimeter Low Resolution Mode and Delay-Doppler Retracking Algorithms for Significant Wave Height</b>	<b>35</b>
<b>5 P-II: Interference-sensitive Coastal SAR Altimetry Retracking Strategy for Measuring Significant Wave Height</b>	<b>37</b>
<b>6 P-III: Benefits of Fully Focused SAR Altimetry to Coastal Wave Height Estimates: A Case Study in the North Sea</b>	<b>39</b>
<b>7 Conclusion and Outlook</b>	<b>42</b>
<b>Bibliography</b>	<b>45</b>
<b>Acronyms</b>	<b>52</b>
<b>Lists of Tables and Figures</b>	<b>53</b>
<b>Acknowledgement</b>	<b>54</b>
<b>A Appendices</b>	<b>55</b>

# 1 Introduction

## 1.1 Motivation

The sea state as an essential climate variable (ECV) combines the local wind-generated sea surface waves and the long-period swell waves that travel thousands of kilometres across the oceans. Both are characterised by their heights, lengths (or periods) and directions. The sea state is an important ECV for parameterising the air-sea flux, quantifying storm intensity and associated climate patterns at large scales, and currents at small scales (Ardhuin et al. 2019).

Knowledge of the sea state is relevant for ocean weather forecasting (Cavaleri et al. 2012), data assimilation for wave models (Hersbach et al. 2020) and the Copernicus Marine Environment Monitoring Service (CMEMS) (Le Traon et al. 2019), the monitoring and model improvement of extreme events (Scharroo et al. 2005; Ablain et al. 2006; Madsen et al. 2015), climate studies (Stopa et al. 2016; Timmermans et al. 2020), scientific studies such as air-sea interactions of surface breaking waves (Melville 1996; Janssen et al. 2013), and other ocean applications such as optimisation of industrial ship routing (Tsou and Cheng 2013; Zacccone et al. 2018).

The sea state in the coastal zone is of particular interest because it has the greatest societal impact near the coast, with approximately 23-37% of the world's population living within 100 km of the coast (Glavovic et al. 2022). Towards the coast, waves dynamically interact with currents and the seabed where nearshore effects such as wave energy transformation (Lippmann et al. 1996; Contardo et al. 2018; Bryan and Power 2020), wave run-up (Dodet et al. 2018), sediment transport (Elfrink and Baldock 2002; Chowdhury and Behera 2017; de Vries et al. 2020) and dissipation effects (Wright 1976; Wang and Kraus 2005; Power 2020; Bryan and Power 2020) occur. Observations of the sea state in the coastal zone are essential for scientific studies related to coastal risks (Ferreira et al. 2009; Sajjad and Chan 2019), coastal protection (Pilarczyk 1990; Charlier et al. 2005), and coastal defense and safety (Silvester and Hsu 1997; Arens et al. 2013; Bouma et al. 2014).

One way to measure wave heights globally is through satellite altimetry, a spaceborne remote sensing technology that has been in operational use for more than three decades to determine sea level, wave height, and wind speed. The continuous, multi-decadal measurement provided by several satellite altimetry missions allows the establishment of a long-term historical record, which is essential for estimating trends to support a scientific quantification of climate change, such as the global mean sea level (GMSL) rise (Cazenave et al. 2014; Cazenave et al. 2018; Legeais et al. 2018) or wave heights and wind speed (Ribal and Young 2019).

The measurement principle of satellite altimetry is based on the measurement of the echoes of transmitted frequency-modulated pulses as a function of the two-way travel time. From the shape of the returned/received and processed pulse echoes and their amplitudes, the three geophysical variables sea surface height (SSH), significant wave height (SWH) and wind speed can be derived in a process called retracking, where a model waveform is fitted to a measured waveform generated from the received pulse echoes. SWH is the statistical description of the wave height and is defined as four times the standard deviation of the sea surface elevation (Holthuijsen 2007).

The measurement of SWH in the coastal zone using satellite altimetry is challenging due to the complex processes that occur near the coast. As a result, coastal SWH observations are often discarded or of poor quality due to coastal interference from highly reflective targets such as sandbanks, tidal flats, sheltered bays, shipping platforms, or calm waters near the coast. This has led to the emergence of the relatively new field of coastal altimetry (Vignudelli et al. 2011). Many works have addressed the challenges of coastal altimetry (Fenoglio-Marc et al. 2010; Vignudelli et al. 2011; Cipollini et al. 2009; Gómez-Enri et al. 2010; Cipollini et al. 2012; Gomez-Enri et al. 2016). Timmermans et al. (2020)

assessed extreme wave heights from satellite altimetry, which agrees well with in-situ data up to 5 km from the coast, but lacks adequate spatio-temporal sampling for closer distances to the coast.

The evolution of satellite altimetry technology from low resolution mode (LRM) to delay-Doppler altimetry (DDA), also known as synthetic aperture radar (SAR) altimetry, unfocused synthetic aperture radar (UF-SAR) altimetry or synthetic aperture radar mode (SARM), has facilitated the use of coastal observations: Conventional LRM altimetry has a circular radar footprint of  $\sim 7$  km, whereas SAR altimetry has an improved along-track resolution of  $\sim 300$  m by exploiting the Doppler shifts of the received echoes (Raney 1998). The relatively novel fully focused synthetic aperture radar (FF-SAR) processing scheme, first demonstrated by Egido and Smith (2017), can be applied to further increase the theoretical along-track resolution to up to  $\sim 0.5$  m.

Tailored retracking algorithms have been developed to account for the coastal interference, such as ALES (Passaro et al. 2014) for the conventional LRM altimetry or SAMOSA+ (Dinardo et al. 2018) for SARM, as described in more detail in Section 3.3.

However, the existing coastal retracking approaches are either designed for LRM altimetry with limited along-track resolution, limiting the minimum distance-to-coast (dist-to-coast), or still show potential in terms of quality and quantity of the SWH estimates near the coast. For instance, the EUMETSAT baseline SARM retracker shows a degraded correlation of less than 0.20 with in-situ buoy data within 20 km of the coast, and a state-of-the-art retracker shows only 16.5% of the remaining valid estimates within 5 km of the coast (Schlembach et al. 2020); see Chapter 4 for further details.

The need to estimate SSH or SWH even closer to the coast is specified in the current draft of the mission requirement documents of the Copernicus Sentinel-3 Next Generation Topography (S3NG-T) team, which defines a requirement to provide SSH and SWH estimates up to 3 km and, as an extended target, up to 0.5 km from the coast (ESA 2022a).

The objective of this PhD project is to develop a novel coastal retracking algorithm to improve the quality and quantity of SWH estimates obtained from SAR satellite altimetry data as close to the coast as possible. To achieve this, a comprehensive analysis of existing SWH estimation strategies for both LRM and SARM altimetry is carried out to identify key performance metrics and evaluate current state-of-the-art retracking algorithms. In addition, the developed retracking algorithm will be combined with the novel FF-SAR altimetry, which may provide additional gains in obtaining SWH estimates even closer to the coast.

## 1.2 Research Questions

In order to meet the objective formulated in the previous section, the following research questions are to be addressed:

### **Q-I: What are the main differences between the various methodologies for wave height estimation by satellite altimetry and what are the challenges?**

Wave heights can be estimated by different methods, depending on the mission, its objectives and the altimeter instrument used. The type of altimeter instrument usually determines the mode of operation of the altimeter and thus the processing methodology, either as a conventional LRM altimeter or as a SARM altimeter, or both simultaneously (if the altimeter configuration allows). The processing methodologies differ in the Level-1b (L1b) and Level-2 (L2) processing (retracking) schemes (see Section 2.3.2) and have a significant impact on the quality and validity of the geophysical records estimated from the altimeter measurements.

This research question aims to evaluate the differences and challenges of the different processing methodologies. Both LRM and SARM missions, as well as several retracking algorithms, will be compared through the evaluation of an adequate selection of meaningful evaluation metrics. In addition, the main challenges in estimating wave heights using satellite altimetry will be identified.

**Q-II: How can the estimation of coastal wave heights be improved compared to the baseline altimetry product and the state-of-the-art processing schemes?**

One of the challenges highlighted by the evaluation of the different processing methodologies in Q-I is the estimation of coastal wave heights. The quality and quantity of wave height estimates decreases when approaching the coastline. However, there are significant differences between the different processing schemes.

The objective of this research question is to investigate how the performance of coastal wave height estimation can be improved compared to the standard European Organisation for the Exploitation of Meteorological Satellites (EUMETSAT) product, hereafter referred to as the EUMETSAT baseline product, and other state-of-the-art processing schemes. Therefore, the goal is to develop a novel processing scheme that improves both the quality and the quantity of the coastal wave height estimates in the coastal zone.

**Q-IIa: What are the gains of applying the FF-SAR instead of the UF-SAR processing scheme for coastal wave height estimation?**

The FF-SAR processing scheme has a theoretical along-track resolution of up to less than half a metre. This suggests that the application of FF-SAR altimetry may offer potential gains over UF-SAR altimetry in the along-track direction to improve the quality of the geophysical estimates.

The aim of this research question is to investigate what gains can be achieved by using the FF-SAR instead of the UF-SAR processing scheme in conjunction with the novel coastal retracking algorithm developed in this PhD project.

**Q-IIb: How close to the coast can wave heights be estimated by combining FF-SAR processing with a coastal retracking algorithm?**

As mentioned in the introduction, the ability to measure SWH in the coastal zone even closer to the coast is in high demand, e.g. for the study of nearshore effects.

The aim of this research question is to investigate how close to the coast it is possible to obtain robust SWH estimates by applying FF-SAR altimetry with the novel coastal retracking algorithm developed in this PhD project.

### 1.3 Thesis Outline

This PhD thesis is written as a cumulative thesis, consisting of the three first-author publications referred to in this thesis as follows:

- P-I** Schlembach, F.; Passaro, M.; Quartly, G. D.; Kurekin, A.; Nencioli, F.; Dodet, G.; Piollé, J.-F.; Arduhin, F.; Bidlot, J.; Schwatke, C.; Seitz, F.; Cipollini, P.; Donlon, C. Round Robin Assessment of Radar Altimeter Low Resolution Mode and Delay-Doppler Retracking Algorithms for Significant Wave Height. *Remote Sensing* 2020, 12 (8), 1254. <https://doi.org/10.3390/rs12081254>.
- P-II** Schlembach, F.; Passaro, M.; Dettmering, D.; Bidlot, J.; Seitz, F. Interference-sensitive Coastal SAR Altimetry Retracking Strategy for Measuring Significant Wave Height. *Remote Sensing of Environment* 2022, 274, 112968. <https://doi.org/10.1016/j.rse.2022.112968>.
- P-III** Schlembach, F.; Ehlers, F.; Kleinherenbrink, M.; Passaro, M.; Dettmering, D.; Seitz, F.; Slobbe, C. Benefits of fully focused SAR altimetry to coastal wave height estimates: A case study in the North Sea. *Remote Sensing of Environment* 289 (2023) 113517. <https://doi.org/10.1016/j.rse.2023.113517>.

and the following co-authored publication:

- CP-I** Ehlers, F.; Schlembach, F.; Kleinherenbrink, M.; Slobbe, C. Validity Assessment of SAMOSA Retracking for Fully-Focused SAR Altimeter Waveforms. *Advances in Space Research* 2022. <https://doi.org/10.1016/j.asr.2022.11.034>.

The above research questions are related to first author and co-authored publications as shown in Figure 1.1. The first-author publications build on each other and are assigned to the correspondingly numbered research questions. The co-authored publication CP-I supports P-III and helps to address the research questions Q-IIIa and Q-IIIb.

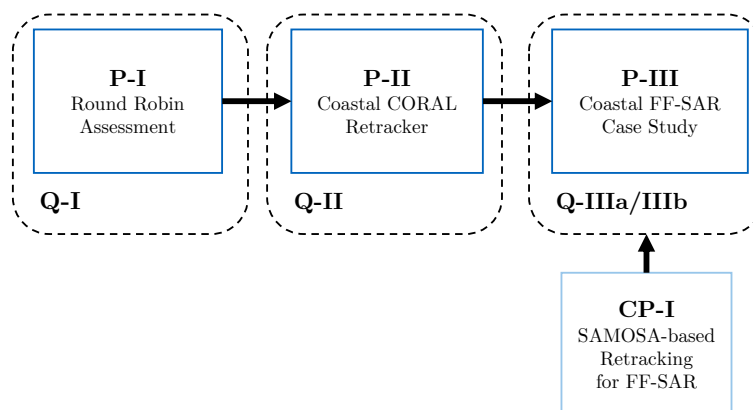


**Figure 1.1** Structure of this PhD project with regard to the three first-author publications P-I-II-III, the co-authored publication CP-I, and the research questions addressed.

This thesis is structured as follows: Chapter 2 introduces satellite altimetry with its different missions, the measurement principle and the different processing modes. Chapter 3 describes how the SWH is extracted in the retracking process, the challenges of coastal retracking, and the state-of-the-art coastal retracking algorithms. Chapter 4, Chapter 5 and Chapter 6 summarise the content of the corresponding first-author publications and place them in the context of this thesis. Chapter 7 concludes this PhD project by answering the research questions from Section 1.2 and giving an outlook on future work.



## 2 Satellite Altimetry

This chapter describes the fundamentals of satellite altimetry and is structured as follows: First, the general measurement principle of satellite altimetry is explained. This is followed by a brief overview of the relevant altimetry missions and the different processing modes, starting with the conventional LRM processing mode. This includes a discussion of the shape and size of the radar footprint on the ground that is illuminated by the transmitted frequency-modulated radar pulses, the pulse compression and deramping principle, and the ocean return waveform model. This serves as a basis for the explanation of the more advanced UF-SAR and FF-SAR processing modes and their implied characteristics.

### 2.1 General Measurement Principle

The measurement principle is based on the measurement of the echoes of frequency-modulated pulses that are transmitted via a nadir-pointing dish antenna to obtain the three geophysical variables SSH, SWH, and (surface) wind speed.

Figure 2.1 shows an orbiting satellite transmitting pulses towards the Earth in relation to the altimetric heights and associated reference surfaces relevant to this thesis. The measurement of the two-way travel time determines the range  $R$  between the altimeter and the instantaneous sea surface, and allows the SSH to be obtained, which together with the satellite altitude  $h_{\text{alt}}$  is usually referenced to a reference ellipsoid (e.g. WGS84) (Chelton et al. 2001). The mean sea level (MSL) is averaged from satellite altimetry data over many years so that it does not contain seasonal, semi-annual, annual or spurious SSH signals (Rosmorduc et al. 2011).

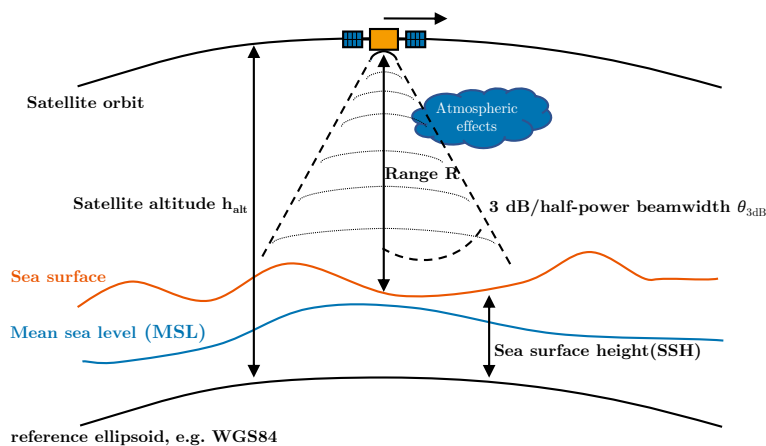


**Figure 2.1** Diagram of the measurement principle of satellite altimetry in relation to the instantaneous sea surface, MSL, and SSH. Image inspired by Piccioni (2021).

To achieve a high accuracy of the range measurement  $R$  to MSL, numerous corrections must be applied such as propagation corrections due to atmospheric refraction (due to the presence of water vapour, dry gases and free electrons), geophysical corrections due to tides and dynamic atmospheric correction, and instrument corrections (Doppler shift, antenna displacement etc.). Furthermore, the sea state bias correction accounts for sea state induced effects combining the electromagnetic and

skewness biases (Chelton et al. 2001, Chapter 3.2). This dependence emphasises the importance of the sea state estimation (SWH) together with the SSH.

The time series of the magnitude-squared (power) values of the received echo return (with its bins called range gates) is referred to as the waveform (Chelton et al. 2001). The basic principle behind the estimation of the SWH from the received waveform is that the reflected echoes are stretched in time as a result of the pulses being reflected at different times from the wave crests and troughs (Chelton et al. 2001, Section 6). That is, a higher SWH causes a greater stretching of the reflected pulses, corresponding to a less steep slope of the waveform leading edge (LE). The SWH is thus related to the slope of the LE of the received power waveform, from which the SWH can be extracted.

The (surface) wind speed is derived from the amplitude of the received waveform.

The three geophysical parameters SSH, SWH, and (surface) wind speed are obtained by a process called retracking, where a model waveform is fitted to the measured waveform generated from the received pulse echoes. The processing of the measured waveform depends on the altimeter type (LRM or SARM) of the altimeter mission and thus on the processing mode. Each processing mode requires a corresponding model waveform to be fitted to perform the extraction of the three geophysical parameters. Further details of the respective missions, the processing modes and the retracking process are given below.

## 2.2 Missions

This section gives a brief overview of the satellite altimetry missions, their objectives, their general mission parameters and altimeter types that are most relevant to this PhD project or to the explanations within this thesis. Figure 2.2 shows the timeline of modern radar altimetry missions from the launch of the first mission in the 1990s, ERS-1, until the end of the Sentinel-6 Michael Freilich (S6-MF) next generation mission.

TOPEX is a joint National Aeronautics and Space Administration (NASA) and National Centre for Space Studies (CNES) satellite altimeter mission launched in August 1992. It was equipped with the first dual-frequency spaceborne radar altimeter system capable of detecting ionospheric delays in the radar path of the signal (Fu et al. 1994). The mission was specifically designed to provide global measurements of the Earth's oceans and their circulation system. To date, it is known for its high accuracy and consistency in obtaining sea level measurements, and is considered as the first reference altimetry mission for ocean altimetry to ensure a continuity of long-term records of global SSH measurements.

The Jason series includes the three satellite altimetry missions Jason-1 (J1), Jason-2 (J2), and Jason-3 (J3), launched in 2001, 2008, and 2016, respectively. Since these are considered as to be follow-on missions to TOPEX, they operated in an identical orbit and follow the same objective of measuring the ocean surface topography. The altimetry reference mission status has been inherited from TOPEX by each of its Jason successors and thereafter by S6-MF.

The CryoSat-2 (CS2) satellite altimeter mission was launched in April 2010 with the primary objective of measuring sea ice thickness and sea ice cover (ESA 2023a), but which is also used for other targets such as the ocean, coastal or inland waters. Its main payload is the SAR interferometric radar altimeter (SIRAL) altimeter instrument, which operates in three different modes, namely the conventional pulse-limited LRM, SARM, and SAR interferometric mode (SARIn), among which are switched according to a specific geographic mask depending on the surface. The CS2 mission is thus the first satellite altimeter to be equipped with a SAR altimeter, which increases the along-track resolution to resolve the variability of the geophysical estimates on finer spatial scales.

Another SAR satellite altimeter mission from European Space Agency (ESA) is Sentinel-3 (S3), launched in 2012 (ESA 2023b). Its main objective is to measure ocean surface topography, as well as ocean and land surface temperature and colour. With the SAR radar altimeter (SRAL) instrument (Le Roy et al. 2009), S3 is the first satellite mission to operate fully in SARM, providing global measurements of the coastal zone, sea ice, ice sheet margins, and inland waters (Donlon et al. 2012).

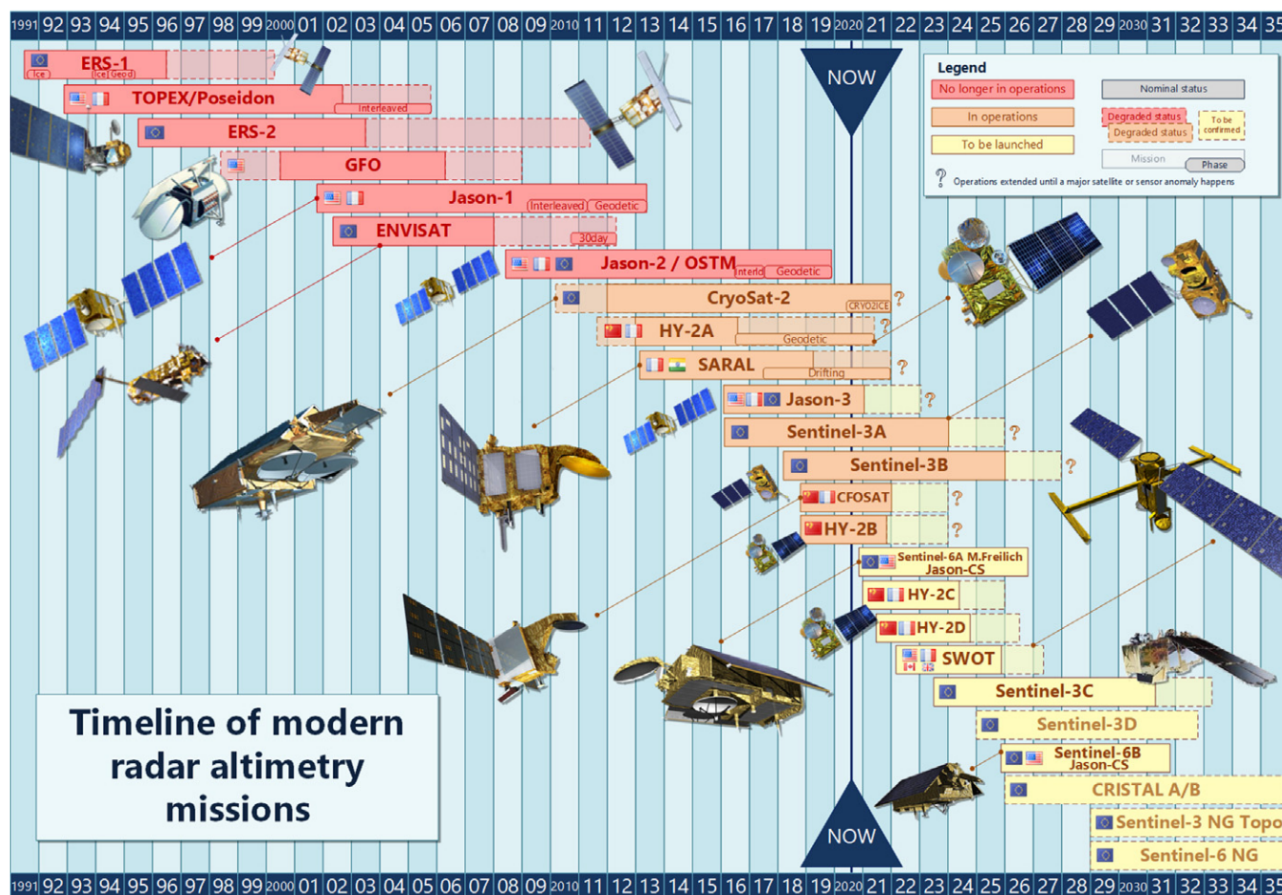


**Figure 2.2** Timeline of modern satellite altimetry missions (status of 2020). Image taken from Abdalla et al. (2021).

Both CS2 in SARM and S3 transmit the pulses in a so-called closed-burst transmission mode, where the transmission of a burst (containing 64 pulses) is followed by a transmission-free reception period (more details are described later in Section 2.3.2). While conventional LRM altimetry requires uncorrelated pulses to be transmitted at a relatively low pulse repetition frequency (PRF) of approximately 2–4 kHz, SAR processing demands highly correlated pulses. For this reason, the CS2 and S3 transmit at a very high PRF of  $\sim 18$  kHz (Raney 1998).

The S6-MF satellite altimetry mission is the most recent ESA altimetry mission, launched in November 2021 (Donlon et al. 2021). It is designed to measure the ocean surface topography as well as inland water targets. It provides continuity in the historical record of sea level measurements, replacing the role of J3 as the new reference altimetry mission. The main payload is the Poseidon-4 nadir-pointing dual-frequency radar altimeter instrument, which operates in an interleaved (or open-burst) mode (Donlon et al. 2021), where pulses are transmitted and received in an interleaved fashion. This allows simultaneous operation as a conventional pulse-limited LRM altimeter and as a SAR altimeter, allowing inter-calibration and seamless continuity with respect to the geophysical variables obtained by the TOPEX and Jason series missions. Moreover, the interleaved mode facilitates the application of the novel FF-SAR processing mode, which further increases the along-track resolution, allowing further improvements in the coastal zone, inland water hydrology (Abdalla et al. 2021) or enhanced capabilities for ocean swell monitoring (Altiparmaki et al. 2022).

General mission parameters of (selected) satellite altimetry missions are summarised in Table 2.1. In general, the more recent altimetry missions are all equipped with a SAR altimeter, which allows measurements with a much higher spatial along-track resolution. Another significant difference between the missions is the orbit configuration, which depends primarily on the main mission objective. For instance, if the mission objective is to obtain a homogeneous measurement of the ocean

**Table 2.1** General mission parameters of (selected) satellite altimetry missions. The most relevant missions to this PhD project are written in bold-faced. The given PRF refers to Ku-band.

Mission	Launch date	Proc. mode	Burst mode	PRF [kHz]	Altitude [km]	Repeat cycle [days]	Inclination [°]
TOPEX	1992	LRM	-	~ 4.2	1336	~10	66
J1	2001	LRM	-	~2	1336	~10	66
J2	2008	LRM	-	~2	1336	~10	66
CS2	2010	LRM/SARM	Closed-burst	~18	717	~369	92
<b>S3</b>	2012	SARM	Closed-burst	~18	814	~10	98.5
<b>J3</b>	2016	LRM	-	~2	1336	~10	66
<b>S6</b>	2020	LRM/SARM	Open-burst	~9	1336	~10	66

surface topography, the inclination is optimised so that the ascending and descending ground tracks are almost perpendicular to each other (as was the case for TOPEX and its succeeding reference missions) for the derivation of geostrophic currents, i.e. steady and horizontal ocean currents where the pressure gradient force is in balance with the Coriolis force. If the focus of the mission is on measurements in the polar zone or on the sea ice and ice sheet measurements, the inclination is chosen so that the satellite reaches such high latitudes, e.g. 92° for CS2 (Abdalla et al. 2021).

## 2.3 Processing Modes

The previous sections introduced the general measurement principle of satellite altimetry and the relevant satellite altimeter missions. This section briefly explains the theoretical background and the main differences between the different processing modes LRM, UF-SAR, and FF-SAR and describes how the averaged waveform is obtained, from which the geophysical estimates SSH, SWH, and wind speed are extracted. Different LRM and UF-SAR retracking algorithms were evaluated together with UF-SAR in the round robin (RR) assessment in P-I, which requires a thorough understanding of the basic principles behind both technologies. The UF-SAR and FF-SAR processing modes were the subject of P-II, P-III, and CP-I.

LRM represents the conventional processing mode that has been used for the majority of altimetry missions to date. Here, the general processing principle of conventional LRM is explained through the elaboration of the footprint size and shape, as well as the pulse compression and deramping technique to maximise the signal-to-noise ratio (SNR). These principles serve as the basis for the explanation of the SARM, which has evolved from the LRM. The SARM can be divided into UF-SAR and the relatively novel FF-SAR processing.

In the following sections, the terms range, delay, and phases are used in the following context: In the conventional LRM, the term range means the distance between the altimeter and nadir, i.e. the closest approach to the sea surface. In SAR processing, the term range is used to express distances between different points in space, e.g. the satellite burst position (the central location when a burst of pulses is transmitted) and a specific surface location. The terms "range direction" or "range dimension" are synonyms for the across-track direction, e.g. when speaking of the radar footprint. Delays correspond to ranges that can be translated between each other via the speed of light and depending on whether a one-way or two-way travel time is meant. A phase defines the shift in time (or position in space) of a waveform. That is, phase alignments or phase corrections represent alignments on a fine scale, which is particularly relevant for FF-SAR processing.

### 2.3.1 Conventional Low Resolution Mode

Moore and Williams (1957), Barrick (1972), and Barrick and Lipa (1985) have shown that, for a rough scattering surface, the average return power can be expressed mathematically by a triple-fold convolution, given by

$$P(t) = \text{FSIR}(t) * \text{PDF}(t) * \text{PTR}(t) \quad (2.1)$$

where  $*$  is the convolution operator, the two-way travel time  $t$  is given as  $t' - (2R_0/c)$ , where  $t'$  is the two-way travel time from the instant of transmission to the reception of the beginning of the LE of the pulse.  $R_0$  is the nadir distance between the satellite and the MSL (assuming a flat sea surface) and  $c$  is the speed of light.

The three terms of the triple-fold convolution in Equation (2.1) are described as follows:

**FSIR**( $t$ ) is the flat-surface impulse response (FSIR) of the averaged backscattered return power from a mean flat surface to an ideal impulse. A general solution for the FSIR was presented in Brown (1977), and a more computationally efficient closed-form solution by Brown (1989).

**PDF**( $t$ ) is the probability density function (PDF) of the sea surface elevations.

**PTR**( $t$ ) is the point target response (PTR) of a single point target (or: single-reflecting facet, single scatterer) within the illuminated scene.

The three terms are described in more detail in the following sections. First, the radar footprint is discussed in terms of its size and shape to form the FSIR. Second, the pulse shape and duration are explained, as well as the basic principle of the pulse compression and deramping techniques, leading to the PDF( $t$ ) and PTR( $t$ ) terms. The combination of the three gives the total mean returned power waveform, which is described at the end of this section.

#### Radar Footprint

The radar footprint represents the area on the ground that interacts with the transmitted pulses. The measurement of the range between the altimeter and the mean surface height is determined by the size of the radar footprint and is therefore one of the most important design considerations for an altimeter system.

First and foremost, the radar footprint must be large enough to average out the effect of waves to determine the MSL (Chelton et al. 1989, Section 2). At the same time, however, the footprint must also be small enough to filter out the effects of oceanic variability at the mesoscale (Chelton et al. 2001).

Another constraint on the upper limit of the footprint size is the fact that a larger beamwidth also collects more spurious reflections, e.g. from land, which is undesirable. Therefore, the smaller the footprint, the closer the altimetric estimates can be obtained to the shoreline. A footprint diameter that satisfies all the constraints has a size of 1–10 km (Chelton et al. 2001).

A straightforward solution to dimensioning the footprint size is to limit the beamwidth of the antenna, called the beam-limited footprint, as shown in Figure 2.3 (a). The beamwidth is defined by the half power/3 dB power of the antenna gain pattern, which is usually assumed to be circularly symmetric and Gaussian (Brown 1977). However, there is a practical problem associated with the beam-limited footprint and the designated footprint size: For instance, a satellite with an altitude of 1000 km and a footprint diameter of 2.5 km gives an antenna beamwidth of  $0.3^\circ$  (Chelton et al. 1989), which corresponds to an antenna diameter of  $\sim 5$  m at 13.6 GHz and is impractical to deploy on a satellite. Moreover, altimeter range measurements performed with such a narrow beamwidth would be very sensitive to antenna pointing errors.

The limitation on the maximum antenna size inherent in a beam-limited footprint can be solved by using a larger beamwidth of  $1-2^\circ$  and transmitting a very short pulse of a few nanoseconds of duration  $T_p$  (Chelton et al. 1989). The diameter of the antenna can thus be reduced to a more feasible

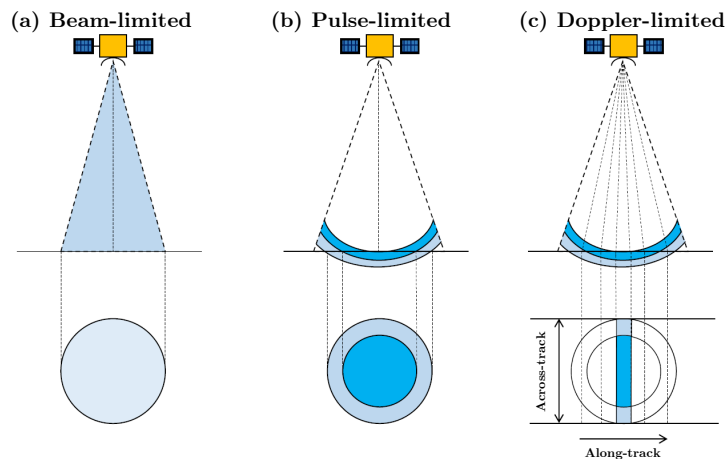


**Figure 2.3** Comparison of (a) beam-limited, (b) pulse-limited and (c) Doppler-limited radar footprints. Image taken from Piccioni (2021).

dimension, e.g. to 1.5 m as for the TOPEX mission. Accordingly, the beam-limited footprint size of TOPEX amounts to 25 km (Chelton et al. 2001) on a flat sea surface, while assuming Ku-band (13.6 GHz), an orbital altitude of  $\sim 1336$  km and a beamwidth of  $1.1^\circ$  (Fu et al. 1994). The size of the footprint is then determined by the length of the pulse duration, as shown by Figure 2.3 (b), and is thus referred to as the pulse-limited footprint.

The size of the pulse-limited footprint can be explained analytically as follows. The evolution of the shape and size of the radar footprint over time  $t$  with respect to the received power  $P(t)$  is shown in Figure 2.4 for an ideal flat sea surface.

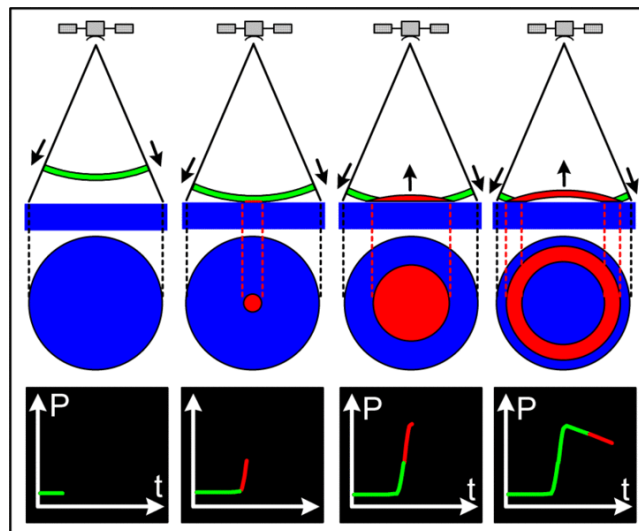


**Figure 2.4** Evolution of the LRM footprint over time  $t$  with respect to the received waveform power  $P(t)$ . Image taken from Aviso+ (2022).

Before the pulse reaches the surface, no power is seen in  $P(t)$ , apart from an instrument-induced thermal noise power (not explicitly shown here). After the LE of the pulse reaches the surface, the power  $P(t)$  increases linearly, corresponding to a linearly growing circle (second and third columns) with the area defined in Chelton et al. (1989, Eq. 1), given by

$$A_{\text{outer}}(\Delta t) = \frac{\pi R_0 c \Delta t}{1 + R_0/R_e} \quad (2.2)$$

where  $\Delta t$  is the relative time with respect to the time when the LE of the reflected pulse reflected from the satellite nadir is received by the altimeter,  $1 + R_0/R_e$  is the correction factor to account for the curvature of the Earth,  $R_0$  is the nadir reference distance between the satellite and the MSL, and  $R_e$  is the radius of the Earth.

The maximum area of the circle  $A_{\max}$  is reached at  $\Delta t = T_p$  (third column of Figure 2.4) when the trailing edge of the pulse is reflected by the surface, and is given by

$$A_{\max} = \frac{\pi R_0 c T_p}{1 + R_0/R_e} = A_{\text{annulus}} \quad (2.3)$$

For  $\Delta t > T_p$  the footprint area becomes an expanding annulus of size  $A_{\text{annulus}} = A_{\max}$  (Chelton et al. 1989, Eq. 4) (rightmost column in Figure 2.4).  $A_{\text{annulus}}$  is no longer dependent on  $\Delta t$  and therefore remains constant on each pulse duration  $T_p$  after the trailing edge is reflected from the nadir of the surface. The LE of the waveform is the most important part, since the derivation of the three retracked parameters strongly depends on it. After the end of the pulse has been reflected by the nadir surface, the shape of the footprint changes into an expanding annulus of constant size  $A_{\text{annulus}}$  for each pulse duration  $T_p$ , as given by Equation (2.4).

If this idealised flat sea surface scenario is extended to a surface with an increased sea state with an  $\text{SWH} \neq 0$ , the maximum footprint area increases and becomes

$$A_{\max, \text{SWH}} = A_{\text{annulus, SWH}} = \frac{\pi R_0 (c T_p + 2 \text{SWH})}{1 + R_0/R_e} \quad (2.4)$$

This is explained by the fact that the maximum off-nadir distance of the footprint is defined by the intersection of the midpoint of the pulse with the wave crests (Chelton et al. 2001, Section 2.4.1). That is, the footprint size increases with increasing SWH, as given by Equation (2.4). For instance, the footprint size of TOPEX at an altitude of 1332 km increases from 2.0 km to 5.5 km or 6.9 km for SWH values of 0.0 m, 3.0 m and 5.0 m, respectively (Chelton et al. 1989, Table 1), which is within the required range for the footprint size described above.

It is important to note that the maximum footprint area  $A_{\max, \text{SWH}}$  depends only on the altitude of the satellite  $R_0$  and the pulse duration  $T_p$ . The altitude is usually set by the orbit configuration. That is, the size of the footprint is determined solely by the effective pulse duration  $T_p$ , which for the majority of altimetry missions is chosen to be 3.125 ns to satisfy the above constraints.

A significant advantage of the pulse-limited footprint to be mentioned is that the altimetric measurement becomes insensitive to antenna mispointing errors, as long as the mispointing angle does not exceed the antenna's half-power beamwidth with respect to nadir (Chelton et al. 2001).

Once the footprint size has been determined, the so-called FSIR can be introduced. The FSIR is defined as the integration of the response of an illuminated area  $A$  with (an assumed constant) backscatter coefficient  $\sigma_0$  to infinitesimally short delta pulses  $\delta(t)$ , given in a general form as

$$\text{FSIR}(t) = \frac{\lambda^2}{(4\pi)^3 L_p} \int_{\text{illuminated area } A} \frac{\delta(t - \frac{2r}{c}) G^2(\mathbf{d}) \sigma_0}{r^4} dA \quad (2.5)$$

where  $\lambda$  is the wavelength,  $L_p$  the propagation loss,  $r$  the range to the elementary scatterer,  $G$  the antenna gain pattern as a function of the ground-projected distance vector  $\mathbf{d}$  to the scattering surface  $dA$  (taking into account any antenna misalignment), and the backscatter coefficient  $\sigma_0$  of the scattering area  $dA$  (Brown 1977; Halimi et al. 2014).

Assuming a circular- and Gaussian antenna gain pattern, no antenna mispointing, a constant backscatter coefficient  $\sigma_0$  over the illuminated area and other approximations (Brown 1977), the general form of Equation (2.5) can be translated into a closed-form solution, defined as

$$\text{FSIR}(t) = P_u \exp\left(-\frac{4ct}{\gamma R_0}\right) \text{U}(t) \quad (2.6)$$

where  $P_u$  is the waveform amplitude given as  $(\lambda^2 G_0^2 c \sigma_0) / [4(4\pi)^2 L_p R_0^3]$  with  $G_0$  being the antenna gain at boresight,  $\gamma = \frac{1}{2 \ln 2} \sin^2 \theta_{3\text{dB}}$  is the antenna beamwidth parameter with  $\theta_{3\text{dB}}$  being the 3 dB/half-power beamwidth, and  $U(t)$  is the Heaviside function (defined as  $U(t) = 1$  for  $t \geq 0$ , otherwise 0) (Brown 1977; Halimi et al. 2014). Accordingly,  $\text{FSIR}(t)$  is a step function that rises to  $P_u$  at  $t = 0$  and slowly decays exponentially as a function of the antenna gain pattern and the satellite altitude. Since  $\text{FSIR}(t)$  is a term of the triple-fold convolution shown in Equation (2.1),  $\text{FSIR}(t)$  has a significant effect on the overall shape of the received power waveform, as shown later in this section.

### Pulse Compression and Deramping

This section briefly explains the principles of pulse compression and deramping to introduce the terms  $\text{PTR}(t)$  and  $\text{PDF}(t)$ , which are part of Equation (2.1).

In a radar system, as in a radar altimeter system, range detection and estimation performance is determined by the SNR, i.e. the higher the better (Richards 2005, Chapter 6). A received signal is superimposed by noise, which has various sources such as spurious reflections of the pulse in the ionosphere and atmosphere (Rosmorduc et al. 2011) and, as a major part, instrument-specific thermal noise originating from electronic components in the radio frequency (RF) signal processing chain of a radar system (Chelton et al. 2001). For simplicity, white noise is usually assumed, being uniformly distributed over the entire frequency range. The SNR of the received, bandwidth-limited pulse is thus determined solely by the signal, which is the total energy of the pulse, calculated as the integration of the power over the pulse duration  $T_p$ .

To satisfy the conflicting requirements of a fixed footprint size and maximising SNR, altimeter radar systems use linear frequency modulation as a pulse compression technique, as is commonly used for range detection in radar systems (Levanon and Mozeson 2004). Here, the transmitted signal is a pulsed harmonic signal of constant amplitude whose frequency is linearly swept from (usually) a higher frequency  $F_{\text{max}}$  to a lower frequency  $F_{\text{min}}$  over a time  $T'_p$ . This signal is called a chirp, characterised by the chirp rate  $\alpha = \frac{F_{\text{max}} - F_{\text{min}}}{T'_p} = \frac{B}{T'_p}$ , where  $B$  is the chirp bandwidth. The targeted very short pulse duration  $T_p = 3.125$  ns is thus expanded to a much longer pulse of length  $T'_p$ , e.g. of length  $102.4 \mu\text{s}$  (Ku-band) for TOPEX (Chelton et al. 1989) or  $32 \mu\text{s}$  for S6-MF (Donlon et al. 2021). When the returned chirp is received, the pulse is compressed so that the same amount of information can be obtained as if a very short pulse of duration  $T'_p$  had been transmitted (Chelton et al. 1989). This allows the SNR to be maximised without any implied cost in terms of range resolution or change in footprint size.

The pulse compression reception technique commonly used in radar altimetry systems is the full-deramp or deramp-on-receive technique, originally developed by Caputi (1971) and introduced by MacArthur (1976) for the SEASAT altimeter. The receiver generates the so-called deramping chirp, which is a delayed replica of the transmitted chirp. After downconversion, the returned chirp is deramped by the multiplication with the deramping chirp shifted in time to a tracking reference point that closely follows the surface to keep the reflected pulse within the receiving window (Chelton et al. 2001). The deramped signal consists of a continuous distribution of frequency components corresponding to the distribution of sea surface elevations  $\text{PDF}(t)$  (Chelton et al. 1989). The  $\text{PDF}(t)$  is usually assumed to be Gaussian (Brown 1977) and can be expressed as a function of the two-way travel time  $t$  by

$$\text{PDF}(t) = \frac{1}{\sqrt{2\pi}\sigma_s} \exp \left\{ -\frac{1}{2} \left( \frac{z}{\sigma_s} \right)^2 \right\} \quad (2.7)$$

where  $\sigma_s$  is the standard deviation of the Gaussian distribution of sea surface elevations  $z$  with respect to the MSL.  $\sigma_s$  is directly related to the SWH as  $\text{SWH} = \sigma_s/4$ .

The last missing term of the triple-fold convolution of Equation (2.1) is  $\text{PTR}(t)$ , which represents the PTR of a single point target (or: single-reflecting facet, single scatterer) within the illuminated



scene. It takes into account the finite length of the transmitted chirp window (Chelton et al. 1989). The  $PTR(t)$  term is given by the power spectral density (PSD) of the transmitted chirp spectral window, which is defined as

$$PTR(t) = \left( \frac{\sin(\pi Bt)}{\pi Bt} \right)^2 = \text{sinc}^2(\pi Bt) \quad (2.8)$$

The convolution of the Gaussian  $PDF(t)$ , which carries the SWH parameter as an essential part of the information, smears the shape of the received waveform as a function of the sea state. This explains the inverse proportionality between the slope's steepness of the LE of the waveform and the SWH, as explained in Section 2.1. The greater the SWH, the greater is the standard deviation  $\sigma_s$  of the  $PDF(t)$  and the greater the smearing of the waveform shape, resulting in a less steep LE slope. This relationship is formulated in the ocean return waveform model as explained in the next section for LRM and in Section 3.1.1 for SARM. Extraction of SWH (as well as SSH and wind speed) is achieved by fitting the model waveform to the received waveform, as described for SARM in Section 3.1.2.

### Ocean Return Waveform Model

With the introduction of all three terms  $FSIR(t)$ ,  $PTR(t)$ ,  $PDF(t)$  of the triple-fold convolution in Equation (2.1), the analytical ocean waveform model, commonly called Brown-Hayne (BH) ocean waveform model, is fully defined. The model was originally described by Brown (1977) and improved by Hayne (1980), who extended the Gaussian SSH distribution by a more realistic third moment to account for the skewed Gaussian shape. The BH model is used in most of the various LRM retracking algorithms as part of the evaluation carried out in P-I.

Figure 2.5 shows a schematic representation of the BH model, which is based on the triple-fold convolution in Equation (2.1). Accordingly, the (subsequent) convolution of the Heaviside-like  $FSIR(t)$  function with the two Gaussian  $PTR(t)$  and  $PDF(t)$  functions smears the shape of the  $FSIR$  in range direction, i.e. in radial off-nadir distance. The centre of the rising LE thus corresponds to the range between the altimeter and the MSL, estimated by determining the time difference from the tracking reference point, called the epoch. The slope of the LE is a function of the standard deviation of the Gaussian term  $PDF(t)$ , from which the SWH is derived according to  $\sigma_s = SWH/4$ . The returned power of the waveform  $P_u$  is translated into the backscatter coefficient  $\sigma_0$ , from which the wind speed can be derived. The trailing edge slope of the waveform is negative and is modulated by the antenna gain pattern and antenna misalignment (see Equation (2.6)) (Amarouche et al. 2004). In addition, a constant thermal noise floor  $T_n$  is additively superimposed and can be seen in the early part of the waveform; it is induced by the electronic components of the altimeter's RF processing chain.

In addition to thermal noise, each of the individual received echoes is strongly affected by what is known as speckle noise, which arises from the randomness of the phases of the echoes reflected from various components of the wave field within the irradiated footprint (Chelton et al. 2001). The individual echoes are thus incoherently averaged to reduce the amount of speckle noise and maximise the amount of information obtained, which requires the echoes to be independent or decorrelated. Berger (1972), Walsh (1982) and Rodriguez and Martin (1994) have therefore investigated the maximum PRF to maximise the amount of information from the transmitted pulses while taking into account the efficient use of satellite power. They found that the maximum PRF depends on the sea state and that the decorrelation length, i.e. the length in along-track distance where independent echoes can be assumed, increases with increasing wave height. For instance, missions such as SEASAT and Geosat used a PRF of 1 kHz, whereas TOPEX used a PRF of about 4 kHz, resulting in more correlated pulses depending on the sea state (Chelton et al. 2001, Section 2.4.2.). Later missions such as the Jason series (J1, J2 and J3) used a PRF of approximately 2 kHz. In a later study, Egido and Smith (2019) have revisited the implications of using a high PRF for the LRM and found a range gate based variability in the statistical properties of the waveform, leading to sea state dependent biases for the SSH and SWH estimates. This is particularly relevant for the S6-MF mission, where both LRM

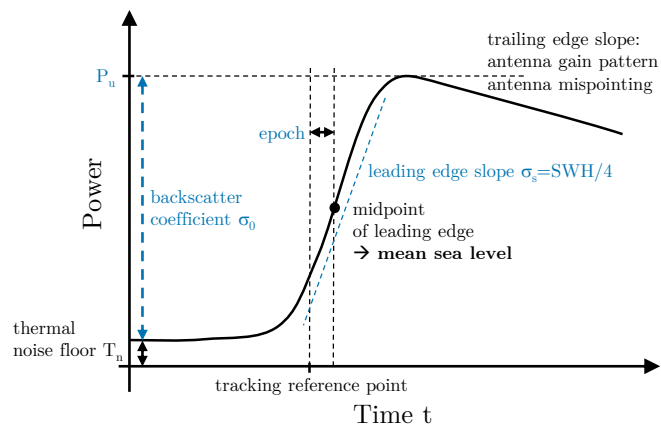


**Figure 2.5** Schematic representation of the theoretical BH waveform model. The extraction of the three free parameters epoch,  $\sigma_s$ , and  $P_u$ , from which the three geophysical estimates SSH, SWH, and wind speed are derived, respectively. Image inspired from Amarouche et al. (2004, Figure 3).

and UF-SAR are operated simultaneously. Indeed, the sea state dependent bias between LRM and UF-SAR for S6-MF-derived data is observed in the case study performed in P-III.

Assuming uncorrelated echoes and the same statistics (e.g. mean power), multiple echoes are averaged over a period of time, called the averaging or integration time, to reduce the amount of speckle noise and form the averaged waveforms (Phalippou and Enjolras 2007). The integration time is usually chosen to be 50 ms, which yields an average of 100 echoes (assuming a PRF of 2 kHz) and results in an averaged waveform with a posting rate of 20 Hz (Chelton et al. 2001).

The formation of the averaged waveforms from the individual received echoes leads to a reduction in the noise of the waveforms. This also applies to the estimation of the three geophysical parameters SSH, SWH and wind speed, which are extracted from the averaged waveform in a process called retracking. The principle of retracking is to find the best fit between the theoretical waveform model and the measured received waveform, usually using a least squares method, by adjusting the three free parameters epoch,  $\sigma_s$  (SWH) and  $P_u$  of the underlying waveform model.

For LRM altimetry and the BH model, the classical retracking algorithms for the parameter estimation are MLE3 and MLE4 (which were part of the retracker assessment in P-I), corresponding to the three- (range, SWH,  $\sigma_0$ ) and four-parameter estimates (with an additional trailing edge slope estimation), respectively. They are based on an unweighted least squares estimate derived from a maximum likelihood estimator (Dumont 1985; Rodriguez and Martin 1994). MLE4 shows notable improvements over MLE3, especially for waveforms that do not conform well with the BH model (Thibaut et al. 2010).

### 2.3.2 Unfocused SAR Altimetry

As an evolution of LRM, SARM, also referred to as SAR altimetry, UF-SAR, or DDA, has been developed with the main objectives of operating more efficiently and effectively, as initially presented in Raney (1998). The first objective targets the more efficient use of the radiated energy used for the estimation of the geophysical parameters, which is achieved by exploiting a much longer signal history along the track than the pulse-limited range of LRM (Raney 1998). The second objective is to improve the spatial selectivity to resolve features of the geophysical estimates at a finer spatial scale.

Both of these objectives are achieved by exploiting the Doppler shift that the pulses exhibit when they are reflected from different scatterers in the along-track direction. The main principle of SAR altimetry is therefore to divide the antenna beam into individual sections in the along-track direction by applying a discrete Fourier transform of all 64 pulses within a single burst, the Doppler filtering, to generate individual Doppler beams, or looks, directed at each along-track surface location. The

looks represent statistically independent realisations, which are then incoherently averaged (after certain range corrections) to produce the multilook or multilooked waveform, resulting in an SNR improvement of approximately 10 dB over conventional LRM altimetry (Phalippou and Enjolras 2007).

An important difference to LRM is the following: LRM integrates the (uncorrelated) received echoes incoherently, whereas UF-SAR coherently processes all 64 received pulses within a burst by performing a discrete Fourier transform to produce the statistically independent looks. The Doppler filtering requires a pulse-to-pulse coherence, which means that the PRF of a SAR altimeter must be higher than for conventional altimeters (Raney 1998). The terminology of coherent processing implies the consideration of the phase of the signal (dealing with the complex-valued waveform), whereas incoherent processing (in this case averaging) corresponds to the processing of the magnitude-squared (power) values of the waveform while ignoring the phase.

The retracking algorithm developed in this PhD project and presented in P-II, uses the processed multilooked waveforms of the EUMETSAT L1b product level to extract the SWH. Although the UF-SAR L1b processing steps described were not required to be implemented, precise knowledge of the L1b processing parameters used is essential to perform the L2 processing (retracking) to derive the geophysical parameters. Furthermore, the explanation of the principle supports the understanding of the FF-SAR processing scheme, which was implemented for the FF-SAR processor used in P-III and CP-I.

### Transmission Modes

Figure 2.6 compares the chronograms of the LRM, SAR closed-burst and SAR open-burst (interleaved) transmission modes. LRM continuously transmits and receives the uncorrelated pulses at a PRF of  $\sim 2$  kHz (sometimes even higher, e.g. for TOPEX:  $\sim 4.5$  kHz), i.e. the reception of the echo is immediately followed by the transmission of the pulse.

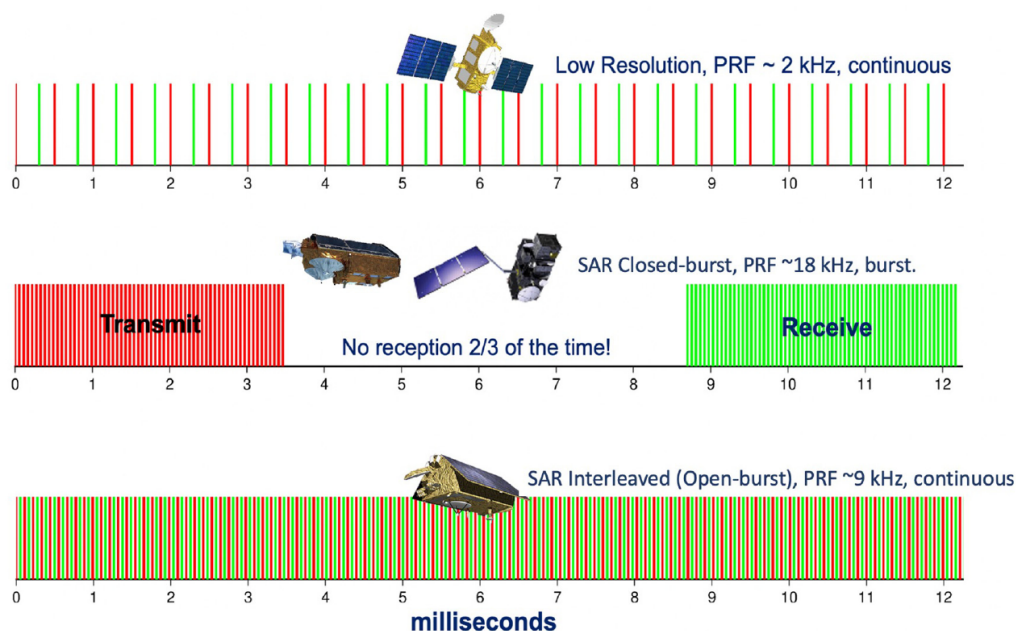


**Figure 2.6** Comparison of the satellite altimeter chronograms for the different transmission modes LRM, SAR closed-burst and SAR open-burst (interleaved). Image taken from Donlon et al. (2021).

The first SAR altimeter missions, CS2 and Sentinel-3A (S3A), use a closed-burst transmission mode in which the pulses are transmitted in bursts with a high PRF of  $\sim 18$  kHz. It is called closed-burst because the transmit period is followed by a transmit-free receive period; leaving about two-thirds of the receive time remains unused.

The burst transmission mode and the PRF have the following constraints (Raney 1998): The burst length can be kept constant and is slightly less than the round trip time from the altimeter to the surface. The burst period must be variable to the extent of  $\sim 5\%$  to accommodate the full span of ranges that may occur in the orbiting altimeter system. The PRF of the SAR altimeter must be small enough not to exceed the pulse period  $1/\text{PRF}$ , but large enough to accommodate the full Doppler bandwidth of the acquired signal within the antenna beamwidth (following the Nyquist theorem). The number of pulses per burst is given by the ratio of the burst length to the pulse period, both kept constant. Based on the above constraints and the choice of the next higher power of two due to the FFT used in the Doppler filtering, the number of pulses per burst is typically chosen to be 64.

To increase the efficient use of the altimeter's transmit/receive time and the number of measurements of each illuminated target, the S6-MF mission firstly deployed the open-burst or interleaved transmission mode. In this mode, the pulses are transmitted at a PRF of  $\sim 9$  kHz to accommodate the echo reception in between the echo transmissions in an interleaved manner (Donlon et al. 2021). The open-burst transmission mode doubles the number of available looks on the same surface location and, more importantly, allows the acquired echoes to be processed simultaneously in both true LRM (as opposed to pseudo LRM discussed in Section 2.3.2) and SARM. The latter is an important requirement for the S6-MF mission to ensure a consistent continuity of geodetic data records with respect to the previous Jason missions and thus to take over the role of J3 as a reference mission. For instance, P-III analysed systematic biases between the EUMETSAT baseline LRM-processed and the UF-SAR- and FF-SAR-processed SWH estimates using the newly developed retracking algorithm.

## Processing Chain

In this section, the altimetry processing chain is briefly explained to familiarise the reader with the common terminology of SAR satellite altimetry products, in particular with regard to the different data levels.

Figure 2.7 shows the processing chain and data levels of the SAR missions S3 and S6-MF. The Level-1a (L1a) data contains the pulses that are preprocessed from the raw L0 data packets (not shown here) that are telemetered from the satellite to the payload data ground segment (PDGS) (ESA 2022c). The L1a data undergoes the L1b processing, which is specific to UF-SAR or FF-SAR processing schemes to form the L1b data, as discussed in Section 2.3. The L1b data contains the received power waveforms, which are then retracked in the L2 processing. The L1b data also contains all the relevant orbital- and instrument-specific parameters and geophysical corrections required for the L2 processing. The retracking process produces the retracking parameters epoch, SWH, and  $P_u$  from which the geophysical estimates SSH, SWH, and wind speed are derived, respectively.

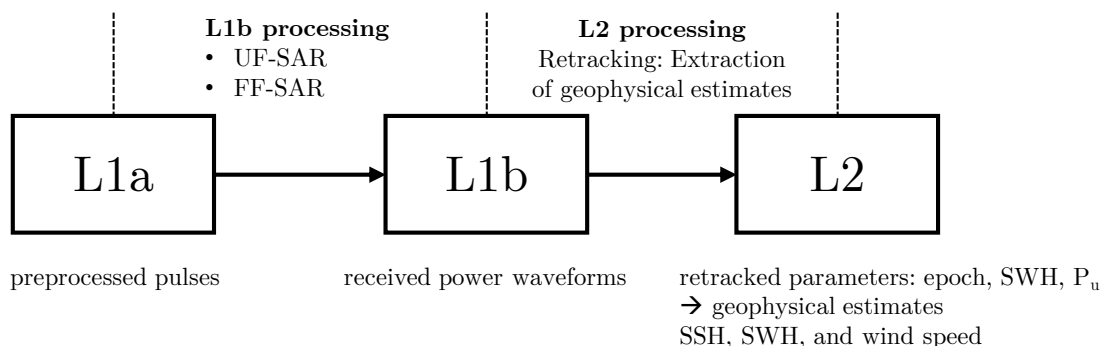


**Figure 2.7** SAR altimetry processing chain and corresponding data levels.

In P-I, the RR assessment of the individual LRM and SARM retracking algorithms performs an evaluation of the retracked SWH estimates and thus takes the L2 products as an input. The developed retracking algorithm presented in P-II processes the L1b data product to extract the geophysical parameters. The case study carried out in P-III starts with the processing of the preprocessed pulses

at the L1a data level to produce the multilooked waveforms at the L1b data level, from which the SWH is extracted at the L2 data level to be compared with a wave model.

For the sake of completeness: Level-3 and Level-4 data levels represent value-added products (not shown here). Level-3 is validated and multi-mission cross-calibrated along-track L2 data. Level-4 is the multi-mission, gridded product derived from Level-3 (Rosmorduc et al. 2011).

## Processing Scheme

In this section, the UF-SAR altimetry processing scheme is elaborated based on the description of the principle given by Dinardo (2020) and the S6-MF L1 product generation specification (PGS) (EUMETSAT 2022b).

The block diagram of the UF-SAR L1b processing scheme is shown in Figure 2.8. The processing scheme starts with the preprocessed pulses in the form of the EUMETSAT baseline L1a product.

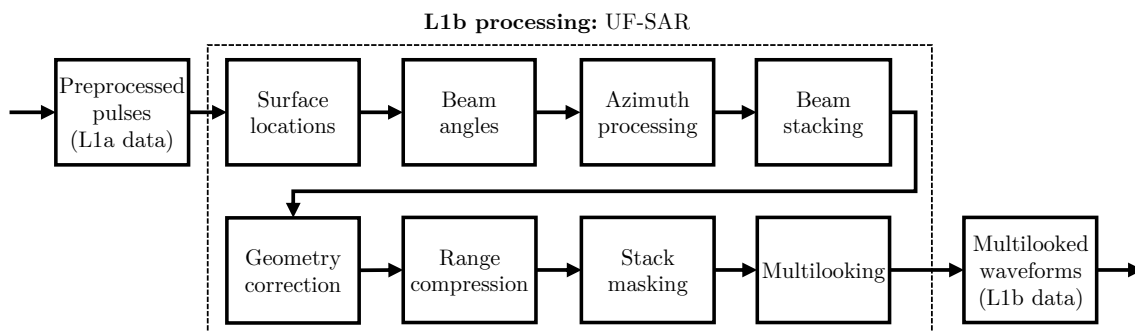


**Figure 2.8** Block diagram of UF-SAR altimetry L1b processing scheme. Image inspired by Dinardo (2020, Fig. 2.27) and EUMETSAT (2022b, Figure 7-8).

The individual Doppler beams (looks) produced by the Doppler filtering as the key principle of SAR altimetry are directed to the designated surface locations. The task of the first processing block of Figure 2.8 is to perform a gridding of the surface locations. The aim is to define the positions of the surface locations and the associated orbit- and surface-related parameters.

The generation of the surface locations is established by an iterative procedure described in detail in EUMETSAT (2022b, Section 7.3.8). The principle is to determine the intersection of the direction of the Doppler beams with the same angular, along-track separation with the ground elevation profile, which is estimated by the onboard tracking. The angular, along-track separation is given by the angular Doppler resolution as a function of satellite velocity, carrier wavelength, and the inverse of the burst duration (EUMETSAT 2022b, Section 7.3.8.4.2).

The task of the next block is to compute the beam angles  $\theta_i$  for each of the surface locations  $i$ , which are defined by the angle between the satellite velocity vector and the vector pointing from the satellite burst position to the previously defined surface location. An example beam angle  $\theta_i$  is shown in Figure 2.9.

Once the beam angles have been calculated, the actual azimuth processing and beam stacking is performed to generate the stack of looks, or Doppler beams, pointing from different burst centre locations to each of the surface locations. In this block, the essential step of SAR processing is represented by beam forming, where the individual Doppler beams are generated by applying an fast Fourier transform (FFT) of size 64 (corresponding to the number of burst pulses) to each of the bursts. The general idea behind this is to exploit the individual Doppler frequency shifts exhibited by each of the surface locations due to the relative velocity between the moving satellite platform and the surface locations. The generated 64 Doppler beams are then spread almost equally across the 3 dB antenna beamwidth, taking into account various uncertainties such as the curvature of the Earth.

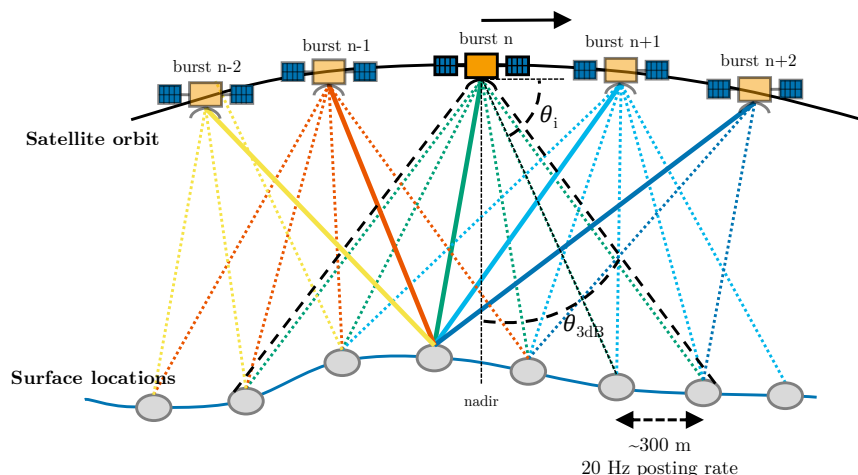


**Figure 2.9** Schematic of the azimuth processing and stacking of individual Doppler beams directed at the elevated gridded surface locations. For clarity, the number of surface locations and Doppler beams are reduced. The nadir direction, the 3 dB beamwidth  $\theta_{3dB}$  and an example beam angle  $\theta_i$  are shown as dashed lines. The solid coloured lines are the Doppler beams forming the stack of looks for a single surface location. Image inspired by Dinardo (2020, Fig. 2.8).

The Doppler beams are now sharpened and have a beam-limited illumination pattern in the along-track direction (Dinardo 2020). Its spatial extent is a function of the satellite velocity, carrier wavelength, and the PRF and has a typical size of  $\sim 300$  m (as is the case for CS2, S3, and S6-MF) (Dinardo 2020, Section 2.1.2.4). The size of the across-track footprint is still enclosed by the dimension of the pulse-limited circle.

Next, beam steering must be performed by applying a pre- and post-FFT phase shift (using the Fourier shift theorem) to direct the beams to the designated surface locations. The phase shift can be divided into a constant phase shift applied to all pulses to steer the central beam to the surface location closest to nadir, and a specific phase shift applied to each pulse individually to align the beams with the designated surface locations.

Beam steering can be performed using either an exact or an approximate method. The latter is much less computationally demanding and is generally applicable to surfaces with low variability, such as the ocean. In this case, the surface locations are assumed to be equally spaced and the phase shift applied to each of the Doppler beams is therefore assumed to be constant. Only the closest beam will then be aligned almost exactly with the surface location closest to nadir (Dinardo 2020). However, this is assumed to be acceptable over low varying surfaces, e.g. the ocean or the coastal zone. The approximate method was thus used for the L1b dataset processed by the coastal retracker presented in P-II. For highly variable surfaces, such as inland scenarios, the exact method is more appropriate, but also more computationally demanding. Here, each of the Doppler beams is steered by an individual angle (Dinardo 2020, Section 2.1.2.4).

Once the individual Doppler beams for each of the bursts have been generated, beam stacking is performed to generate the stack of Doppler beams pointing to each of the surface locations. The solid coloured lines in Figure 2.9 show how the stack is formed by selecting the individual Doppler beams from each of the bursts that point to a single surface location. The individual Doppler beams associated with each surface location represent the independent looks at the same surface location and form the stack matrix with the dimensions of the number of Doppler beams/looks and the number of the received (uncompressed) waveforms of the Doppler-filtered pulses.

In the following, the geometry corrections are applied to the previously generated stack, consisting of the following three corrections (EUMETSAT 2022b, Section 7.3.11.4): The

**Doppler correction** is mainly induced by the vertical component of the satellite's velocity, which causes a shift in the Doppler range that needs to be corrected for.

**Slant range correction** compensates for the differences in radial distance between the satellite burst centres and the surface locations of the individual Doppler beams, as shown by Figure 2.10. After the correction is applied, all the Doppler beams will have the same window delay using the nadir location taken as the reference.

**Window delay misalignment correction** takes into account the differences in the window delay (or tracking reference point as it was previously called) of the different bursts from which the individual Doppler beams are acquired during beam stacking.

Each of the above corrections is translated into phase shifts. These are multiplied by the columns of the stack matrix, corresponding to the Doppler beam dimension, according to the Fourier shift theorem. This results in the geocorrected stack, where all the Doppler beams are aligned in range such that the distance between the returned echoes from the given surface location to the satellite is minimised.

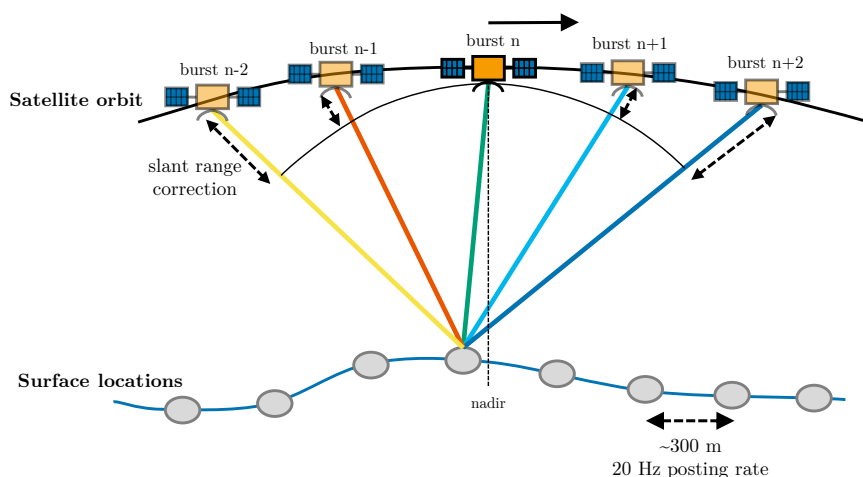


**Figure 2.10** Stacked beams with shown slant range correction. Image inspired by Dinardo (2020, Fig. 2.17)

Range compression is applied to the Doppler beams of the geocorrected stack matrix (or as previously introduced as pulse compression), i.e. an FFT operation is used to convert the (uncompressed) waveforms of length  $N_s$  delay bins into an equivalent number of the so-called range bins, or range gates (EUMETSAT 2022b, Section 7.3.12).

At this point, an optional oversampling of the waveforms can be applied by zero-padding the Doppler beams prior to the FFT application: The Doppler beams of length  $N_s$  are pre- and post-padded with  $((z_p - 1)N_s)/2$  zeros (with  $z_p$  being the zero-padding-factor) before the FFT transform to obtain  $z_p \cdot N_s$  range bins of the range-compressed stack. Zero-padding solves the problem of signal aliasing that occurs when the power bins of the stack are obtained by simply squaring the complex stack bins. This results in an undersampled waveform, which can be problematic for low sea states below 1 m or other targets such as sea ice leads that have a steep LE of the waveform. Smith and Scharroo (2015) therefore suggest using a zero-padding factor of at least 2. The baseline processing chain of previous SARM missions such as CS2 or S3 have not employed a zero-padding ( $z_p = 1$ ), while S6-MF has set a default zero-padding factor of  $z_p = 2$ . In fact, a custom processed S3 dataset was used to evaluate the newly developed coastal retracking algorithm in P-II with a zero-padding factor of  $z_p = 2$  to avoid the aliasing issue for low sea states. The FF-SAR processor used in P-III was also configured with a zero-padding factor of  $z_p = 2$ .

The range-compressed stack matrix is then cleansed of geometry- and processing-related ambiguities and artefacts. EUMETSAT (2022b, Section 7.3.13.1) describes four types of binary masks that can be configured for the S6-MF mission to exclude parts of the stack (i.e. by filling them with blanks):

**Geometry mask** After applying the geometry corrections, the outer Doppler beams were shifted forward to be range-aligned with the nadir beam. The trailing part of the waveform contains no meaningful signal and is simply an artefact of the shifting operation (it contains the thermal noise from the folded early part of each of the waveforms). This type of masking is crucial for the later retracking step, where the theoretical multilooked waveform is created and fitted to the measured multilooked waveform formed from the masked stack.

**Ambiguity mask** The along-track profile of the satellite track is sampled with the PRF, which must be large enough to accommodate the Doppler bandwidth constrained by the altimeter system in terms of the Nyquist theorem. In the case of S6-MF, the PRF is not large enough, so the Nyquist theorem is violated. This causes aliasing of the Doppler spectrum, which is folded back into the outer part of the stack. So the objective of the ambiguity mask is to mask out the folded Doppler ambiguities.

**RMC mask** Masks out the second half of the waveforms due to the data-throughput-optimised range migration correction (RMC) mode used for the S6-MF mission.

**GAP mask** Masks out entire Doppler beams when data gaps have occurred (e.g. due to a non-continuous transmission mode).

Knowledge of the applied masks and their incorporation into the processed multilooked waveform at L1b is essential for the retracking step in L2 processing. For instance, the retracking algorithm developed in P-II and applied in P-III, as well as the L1b processing performed in P-III, require the consideration of the applied masks when generating the model waveform to be fitted to the processed multilooked waveform for parameter estimation. The applied masks are different for each satellite mission and processing baseline setting. For the S6-MF L1a data used in P-III, the geometry, ambiguity, and RMC masks had to be applied in the L1b and the L2 processing.

The Doppler-filtered, geocorrected, range-compressed Doppler beams of the stack represent statistically independent looks at the same surface locations. As with conventional LRM, a single look is heavily affected by speckle and thermal noise.

Speckle noise is multiplicative and results from the reflection of coherently transmitted pulses from an ensemble of illuminated scatterers with random relative phases that are constructively or destructively superimposed (Dinardo 2020, Section 2.1.2.8). The amount of speckle noise is significantly reduced by incoherently averaging the magnitude-squared (power) bins of the Doppler beams, which is called multilooking. The result is multilooked (SAR) waveforms pointing to the designated surface locations, which are much less noisy. During averaging, the outer Doppler beams may be discarded as they do not contribute effectively to the reduction of speckle noise (Gommenginger et al. 2013). For instance, the number of looks for the EUMETSAT S6-MF product with baseline F06 has been reduced from ~448 and to (strictly limited to) 332 to reduce the amount of Doppler ambiguities (EUMETSAT 2022a, Section 3.1.2).

The number of looks used for the multilooking defines the parameter of the total illumination time  $T$ , which is a relevant parameter for the FF-SAR processing chain. Since the UF-SAR processing is emulated by the FF-SAR processing chain with a small modification (as explained at the end of Section 2.3.3), the total illumination time  $T$  has to be adapted accordingly. The above number of looks of 332 of the EUMETSAT baseline thus corresponds to an illumination time of 2.1 s. This setting was particularly relevant for P-III, where the implemented (emulated) UF-SAR processing chain had to mimic the EUMETSAT baseline processing chain as closely as possible.

Once the multilooked waveform has been acquired, the extraction of the three geophysical parameters SSH, SWH, and wind speed is performed by fitting a theoretical power return waveform model in



the retracking processing. Retracking an UF-SAR-processed waveform requires a theoretical power return waveform model adapted for UF-SAR. The theoretical waveform model can also be expressed by the triple-fold convolution defined in Equation (2.1), but with the FSIR( $t$ ) and PDF( $t$ ) extended by the Doppler frequency dimension, given as

$$P(t, f) = \text{FSIR}(t, f) * \text{PDF}(t) * \text{PTR}(t, f) \quad (2.9)$$

The distribution of the surface height elevations PDF( $t$ ) is independent of the Doppler frequency and thus remains the same as in Equation (2.1).

The PTR for LRM was defined by a sinc<sup>2</sup> term as a function of the time delay  $t$ , as given in Equation (2.8). The two-dimensional PTR( $t, f$ ) (2D-PTR) term is now simply given by the multiplication of a sinc<sup>2</sup> as a function of the Doppler frequency  $f$ , given as

$$\text{PTR}(t, f) = \text{sinc}^2(\pi Bt) \text{sinc}^2(\pi \tau_b f) \quad (2.10)$$

where  $\tau_b$  is defined as the burst length (Halimi et al. 2014, Eq. 16).

The extension of Equation (2.9) by the Doppler frequency results in a different waveform shape for UF-SAR-processed waveforms. This is due to the much smaller area integrated for the FSIR as defined in Equation (2.5). Figure 2.3 (b) and (c) show a comparison between the LRM and SARM footprints and the resulting waveforms. Compared to LRM, the SARM footprint is now beam-sharpened in the along-track direction with a size of  $\sim 300$  m due to Doppler filtering and pulse-limited in the across-track direction as for LRM in both dimensions, as shown in Figure 2.11. The sharpening of the beams in the along-track direction results in a much smaller area to be integrated, yielding a much more peaked waveform shape for SARM. The trailing edge of the waveform decays very steeply, whereas that of LRM has a slowly decaying trailing edge. In both cases the steepness is modulated by the antenna gain pattern.

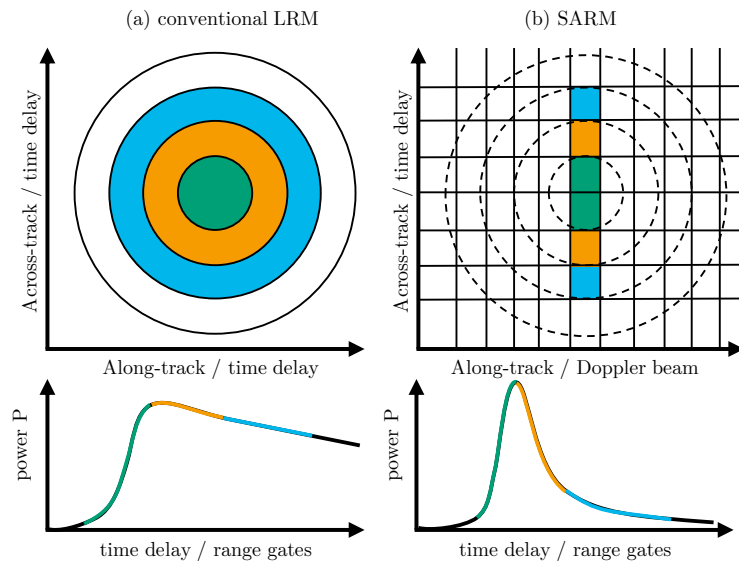


**Figure 2.11** Schematic view of the (a) LRM and (b) SARM footprints and the different shapes of the waveforms shown in the top and bottom panels, respectively. Image inspired by Raney (1998, Fig. 1).

The triple-fold convolution defined in Equation (2.9) can be solved either numerically (Phalippou and Enjolras 2007; Boy and Picot 2013), semi-analytically (Wingham et al. 2004; Halimi et al. 2014), empirically (Garcia et al. 2014), or fully analytically (Ray et al. 2015). The advantage of a fully analytical model is that it is numerically robust, versatile, computationally efficient, and straightforward to implement and use (Dinardo 2020, Section 2.1). The fully analytical SAMOSA model described in Ray et al. (2015) provides a closed-form solution for the SAR power return waveform to derive the three geophysical parameters and is presented in more detail in Section 3.1.1.

### Pseudo Low Resolution Mode

SARM L1a data can be used to generate BH-like waveforms from a SAR altimeter, referred to as the pseudo low resolution mode (PLRM) or reduced SAR (RDSAR) mode (Scharroo 2014). This mode was initially introduced with the CS2 mission to allow a comparison between the altimetric measurements obtained by the LRM and the SARM initially used for CS2. In addition, the continuity and consistency of the estimated geophysical records can be validated as the satellite switches between LRM and SARM. In the first-author paper P-I of this PhD project, the PLRM was used to compare LRM retracking algorithms with those of SARM, while using the same L1a/L1b input data from S3, allowing an objective comparison of their performance.

CS2 operates in closed-burst mode at a very high PRF of  $\sim 18$  kHz, and thus transmits the pulses for only a third of the time. There are therefore far fewer uncorrelated looks available for incoherent averaging of the received pulses as compared to conventional LRM; hence the name pseudo-LRM. The performance of PLRM-processed data is therefore degraded in terms of the precision of the estimates compared to the full LRM mode, which averages a higher number of uncorrelated echoes due to the continuous interleaved samples with a lower PRF (ESA 2019, Section 3.2.1).

For CS2, four bursts of 64 pulses (corresponding to one radar cycle) are used to generate an equivalent PLRM waveform. After several processing steps such as range and phase alignment, amplitude and phase correction, zero-padding, range compression, the echoes are incoherently averaged as in conventional LRM processing (followed by a final low-pass filter correction) (ESA 2019).

Finally, the acquired PLRM waveform can be fitted with the well-known BH waveform model and processed by the MLE3 or MLE4 retracking algorithms. For further details on PLRM processing, the reader is referred to Scharroo (2014) and ESA (2019).

### 2.3.3 Fully Focused SAR Altimetry

FF-SAR altimetry is a novel processing technique developed and first applied to SAR altimeters by Egido and Smith (2017). FF-SAR has a very high theoretical along-track resolution of up to  $\sim 0.5$  m due to a fully focused, coherent processing of a single target over the entire illumination time in which the target is seen by the altimeter. This is also the main difference to UF-SAR altimetry where the pulses are only coherently processed within a single burst. The main requirement for the application of FF-SAR processing is the coherent transmission of the pulses over the entire illumination time, i.e. it can be applied to the current SAR altimetry missions CS2, S3 and S6-MF.

FF-SAR altimetry has great potential in highly heterogeneous scenes such as sea ice (Egido et al. 2020; McMillan et al. 2020; Aublanc et al. 2022), inland waters (Kleinherenbrink et al. 2020; Nielsen et al. 2021), ocean swell monitoring (Altiparmaki et al. 2022), or coastal applications (Amraoui and Moreau 2021). The challenge of coastal altimetry applications is the strong interfering signals from highly reflective targets such as mud or sandbanks, tidal flats, sheltered bays, shipping platforms or calm water surfaces close to the coast (Quartly et al. 2001; Gómez-Enri et al. 2010; Wang and Ichikawa 2017).

Given the very high along-track resolution, FF-SAR potentially allows the resolution, i.e. the spatial separation, of small-scale targets in the along-track direction. In fact, the novel retracking algorithm developed in P-II exploits this, as shown in the case study in P-III, by omitting individual bad SWH records estimated from waveforms strongly affected by coastal interference.

The FF-SAR processor implementation used in this PhD project was originally developed by Kleinherenbrink et al. (2020) for CS2, which uses a back-projection algorithm as presented in Egido and Smith (2017) and described in this section. The extension to S3 and S6-MF was done together in a collaboration with the Delft University of Technology and used for the papers P-III and CP-I. The FF-SAR processing chain is summarised in this section, further details can be found in Kleinherenbrink et al. (2020), Egido and Smith (2017), and CP-I.

The FF-SAR processing chain is shown in Figure 2.12. After calculating the along-track surface locations, the processing is performed on each of them individually, as indicated by the dashed orange boxes.

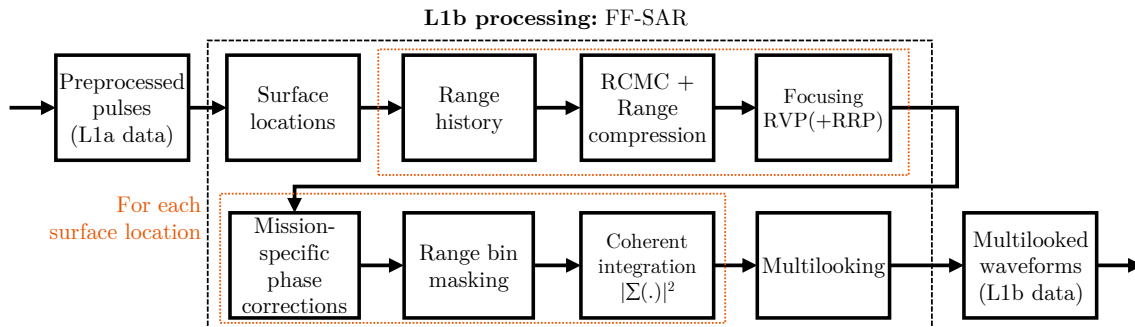


**Figure 2.12** Block diagram of FF-SAR altimetry L1b processing scheme.

The main objective of the FF-SAR processing chain is to perform a range and phase alignment of the pulses resulting from their individual pulse transmission times and locations and instrumental effects (e.g. phase shifts due to tracker range changes, residual carrier phases, inter-burst jumps, etc.). The pulse alignment is performed per surface location before a coherent integration is carried out to form the single look waveform associated with each of the surface location. The perfect pulse alignment and the correct implementation of the FF-SAR processing chain is validated by a so-called flat-phase calibration using transponders, as introduced later in this section.

### Surface Locations

The task of the first block is to define the positions of the surface locations, or focal points, to which the pulses are aligned in range and phase. The gridding of the surface locations is performed based on the separation in along-track distance between the surface locations, which is determined by the along-track resolution  $L_x$  as defined by Egido and Smith (2017, Eq. 27) and given by

$$L_x = \frac{cR_0}{2f_c v_s T} \quad (2.11)$$

where  $v_s$  is the satellite orbital velocity and  $T$  is the coherent integration time. For instance, inserting the nominal parameters of the S6-MF mission with altitude  $R_0 = 1336$  km, carrier frequency  $f_c = 13.575$  GHz, satellite orbital velocity  $v_s = 7200$   $ms^{-1}$  and the selected coherent integration time of  $T = 2.1$  s into Equation (2.11) yields a theoretical along track resolution of 0.98 m.

The difference between the satellite altitude and the tracker (reference) range is used to estimate the elevation of the surface locations with respect to the reference ellipsoid (e.g. WGS84) used at their gridded along-track positions. Assuming a homogeneous surface such as the ocean, the focal points are set on a smooth reference surface obtained by fitting second or fourth polynomial functions to the satellite elevation and tracker range at the burst locations (as usually given in the L1a product) (Egido and Smith 2017; Kleinherenbrink et al. 2020). This ensures that the computed singlelook waveforms at the surface locations are range-aligned and can be used for averaging to form multilooked waveforms.

### Range History

Once the positions of the target surface locations have been determined, the subsequent processing is performed on each of them individually to generate the singlelook waveforms. The computation of each singlelook results in a statistically independent waveform realisation (in terms of speckle noise). The following processing blocks represent the main part of the FF-SAR processing chain, as shown in

the dashed orange boxes in Figure 2.12. The main objective of the FF-SAR processing is to align the delays and phases of the echoes for coherent integration to form the singlelook waveforms associated with each surface location or focal point.

For each surface location, the echoes must first be selected from the L1a data based on the coherent integration time  $T$ , i.e. all pulse echoes  $T/2$  before and after the time of the target surface location. For instance, an integration time of 2.1 s and the S6-MF mission parameters result in a selection of  $\sim 18000$  echoes from  $\sim 290$  bursts.

After selecting the echoes, the pulse radargram matrix  $\mathbf{S}_p$  is formed with the dimensions  $N_p$  times  $N_s$ , where  $N_p$  is the number of selected pulse echoes and  $N_s$  is the number of samples per echo (S6-MF: 256, CS2/S3: 128). The time in the along-track direction is commonly referred to as the slow time  $\eta$  with index  $i$ , the time in the across-track direction as the fast time  $t$  with index  $j$ . The resolution in slow time is given by the PRF of the altimeter, which for S6-MF is  $\sim 9$  kHz and varies along the track to allow for its interleaved transmission and reception. The resolution of the fast time vector  $t_j$  is given by the (uncompressed) pulse length of  $T'_p = 32 \mu\text{s}$  divided by the number of samples per echo  $N_s$ .

The calculated range between the target surface location  $i$  and the  $N_p$  pulse locations is referred to as the range history  $R_i$ .

### Range Cell Migration Correction and Range Compression

The range cell migration correction (RCMC) compensates for the individual delays of the echoes due to the relative motion of the satellite with respect to the surface location. It takes as input the computed range history  $R_i$  from the previous processing block and the tracker ranges  $R_{\text{trk},i}$  associated with echo  $i$ . Kleinherenbrink et al. (2020) divides the RCMC into two separate corrections: The first accounts for the geometric range variation, given as

$$\Phi_{\text{RCMC}} = \exp \left( -2\pi i \alpha \left( 2 \frac{R_i - R_0}{c} - f_{D,i} \right) t_j \right) \quad (2.12)$$

where  $R_0$  is the nadir reference range and  $f_{D,i}$  is the Doppler frequency  $\frac{2f_c v_r}{c}$  where  $v_r$  is the relative velocity of the moving satellite at each of the pulse locations and the surface location and  $f_c$  the carrier frequency (Egido and Smith 2017, Eq. 24).

The second part of RCMC is the variation of the tracker range during the coherent integration time, formulated as

$$\Phi_{\text{trkvar}} = \exp \left( -2\pi i \alpha \left( 2 \frac{R_{\text{trk},0} - R_{\text{trk},i}}{c} t_j \right) \right) \quad (2.13)$$

where  $R_{\text{trk},0}$  and  $R_{\text{trk},i}$  are the tracker ranges for the (interpolated) nadir reference tracker range and echo  $i$ , respectively.

The range-aligned pulse radargram  $\mathbf{S}_{\text{RCMC}}(t, \eta)$  is obtained by the element-wise multiplication of the matrices  $\Phi_{\text{RCMC}}$  and  $\Phi_{\text{trkvar}}$  with the pulse radargram  $\mathbf{S}_p$ , given by

$$\mathbf{S}_{\text{RCMC}}(t, \eta) = \mathbf{S}_p \circ \Phi_{\text{RCMC}} \circ \Phi_{\text{trkvar}} \quad (2.14)$$

where  $\circ$  denotes the Hadamard product operator.

The range alignment is followed by the range compression step, where the range-aligned radargram  $\mathbf{S}_{\text{RCMC}}$  is zero-padded (typically by a factor of two) and a discrete Fourier transform is applied in the fast time dimension  $t$ , as explained in Section 2.3.1. This yields the range-compressed complex pulse radargram  $\mathbf{S}_{\text{rc}}$  with dimensions  $(z_p \cdot N_p)$  times  $N_s$  where  $z_p$  is the integer zero-padding factor.

## Focusing

Focusing is then performed, which includes the correction of residual video phase (RVP) and residual range phase (RRP) to align the pulse echoes in phase. The RVP is a residual phase that is only apparent on altimeters with a deramp-on-receive or full deramp technique to demodulate the chirped echoes, such as CS2 and S3. S6-MF, in contrast, uses a matched filter approach (Donlon et al. 2021) that does not incorporate an RVP for deramping and therefore does not require the RVP correction to be applied.

The RVP and RRP corrections are, according to Kleinherenbrink et al. (2020, Eqs. 3 and 4), given as

$$\Phi_{\text{RVP}} = \exp\left(2\pi i \frac{\alpha}{2} \left(2 \frac{R_i - R_{\text{trk},i}}{c}\right)^2\right) \quad (2.15)$$

and

$$\Phi_{\text{RRP}} = \exp\left(2\pi i f_c \frac{2(R_i - R_{\text{trk},i})}{c}\right) \quad (2.16)$$

Both terms are now multiplied by the range-compressed complex pulse radargram  $\mathbf{S}_{\text{rc}}$  to give the RVP- and RRP-corrected complex radargram  $\mathbf{S}_{\text{p,RVP-RRP}}$ .

## Mission-specific Phase Corrections

To perform a final phase correction, mission-specific phase corrections have to be performed. These relate to inter-burst phase jumps, tracker range phase jumps, and final phase calibrations and are described in detail for the three missions CS2, S3, and S6-MF in CP-I.

The mission-specific phase corrections are expressed mathematically by a simple phasor term  $\exp(-i\phi_{c,i})$ , where  $\phi_{c,i}$  is the phase correction associated with echo  $i$ . The phasor is then multiplied by each column (pulse) of the RVP-RRP-corrected complex radargram  $\mathbf{S}_{\text{p,RVP-RRP}}$  yielding the fully focused range-and-phase-corrected complex radargram  $\mathbf{S}_{\text{ff}}$  with dimensions  $(z_p \cdot N_p)$  times  $N_s$ .

## Transponder Calibration

The in-orbit calibration of altimeters is usually performed using transponder sites. Transponders are active reflectors where the impinging pulses are most transparently amplified and reflected in the same direction with a very high SNR. Any other reflective target in the vicinity of the transponder will thus return a much weaker signal. The transponder is therefore an ideal point target for measuring and calibrating amplitude and phase.

To assess the phase alignment of the pulses and thus validate the correct implementation of the FF-SAR processing chain, the transponder location is used as the surface location (or focal point) and the phase history of the range bin corresponding to the transponder location is computed. After unwrapping (modulo  $2\pi$ ) and detrending (a linear trend corresponds to a small offset between the surface location and the transponder's along track position), the phase history can be analysed. A so-called flat-phase calibration and successful calibration of the FF-SAR processing chain is achieved when the maximum magnitude of the detrended phase history over the integration time is in the range of a few millimetres (expressed in absolute Ku-band wavelength).

The resulting phase history of the fully focused radargram  $\mathbf{S}_{\text{ff}}$  with the surface location pointing towards the transponder is shown in Figure 2.13. The flat-phase calibration is successfully established: It can be seen that the phase is (almost) perfectly aligned over the entire coherent integration time  $T$  with a deviation of less than 0.5 mm, which is a remarkable performance in terms of phase coherence.

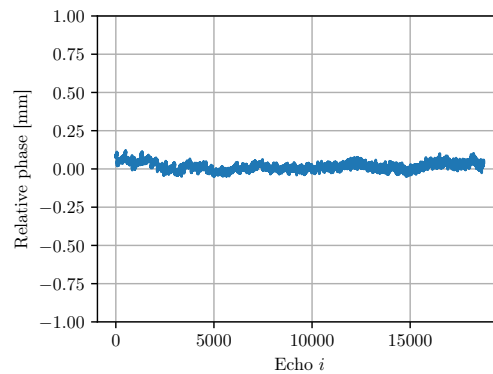


**Figure 2.13** The achieved flat-phase calibration with the fully aligned, detrended phase history for the CDN1 Cal/Val transponder site on Crete, Greece, is shown as a function of the number of pulses within the coherent integration time  $T$  for the S6-MF altimeter (cycle 38, pass 18).

### Range Bin Masking

The fully focused complex radargram  $S_{ff}$  now needs to be cleansed from geometry- and processing-related ambiguities and artefacts, which is referred to as range bin masking and corresponds to the stack masking operation, as applied to the stack of Doppler beams for UF-SAR (see Section 2.3.2). The application of the different types of masks will blank parts of the pulse echoes of  $S_{ff}$ .

The masking is done for the same reasons as for UF-SAR: The geometry mask is applied to account for the geometric shift during the RCMC operation. The trailing part of the shifted echoes contains the cyclically shifted part of the waveform before the LE, and thus no meaningful signal, and is simply an artefact of the shift operation (see Egado and Smith (2017, Fig. 3 (a))). The ambiguity mask removes Doppler ambiguity effects that are caused by spectral folding of the aliased Doppler frequency due to the limited PRF (S6-MF only). The RMC and GAP mask can be optionally applied if required (S6-MF RMC mode is active, data gaps have occurred). For the FF-SAR processing applied in P-III, the geometry, ambiguity, and RMC masks were applied to blank out parts of  $S_{ff}$ .

### Coherent Integration

After the range bin masking, the fully focused echoes can now be coherently combined by integrating  $S_{ff}$  along the slow time dimension  $\eta$ : The  $N_p$  complex values are summed, while including the phase information, and then magnitude-squared to obtain the  $N_s$  range bins of the real-valued singlelook waveform. The singlelook waveform represents an independent waveform realisation associated with the target surface location.

### Multilooking

Singlelook waveforms are strongly affected by speckle noise, which is caused by the many distributed, independent scatterers within the radar footprint. Retracking and extracting of geophysical parameters from the singlelook waveform would thus produce very noisy estimates.

Therefore, multiple singlelooks are averaged to form a multilooked waveform, or multilook, which removes a significant amount of speckle noise. The resulting multilook points to the central singlelook surface location, but contains the signal from the adjacent singlelook surface locations. The number of averaged singlelooks determines the posting rate of the multilooked (L1b) waveform. The more singlelooks are used for averaging, the lower the speckle noise contribution and the more precise the geophysical estimates will be (assuming a homogeneous surface). Thus, averaging  $\sim 300$  singlelook waveforms with a gridded along-track separation of  $\sim 1$  m (setting an integration time of  $T = 2.1$  s) will result in a multilooked waveform every  $\sim 300$  m with a posting rate of approximately 20 Hz.

Although the UF-SAR processing methodology differs slightly from that of FF-SAR, the multi-looking operation is similar in that the aim is to reduce the amount of speckle noise by averaging independent realisations around a target surface location. The difference is that UF-SAR uses independent Doppler beams (with an along-track resolution of  $\sim 300$  m) pointing at the same surface location, whereas FF-SAR uses the adjacent singlelooks with an along-track resolution of  $\sim 1$  m ( $T = 2.1$  s) to perform the averaging.

### Unfocused SAR Emulation

UF-SAR-processed L1b products can be generated as a by-product of the FF-SAR processing chain, allowing to mimic the original UF-SAR discussed in Section 2.3.2 and as presented in Egido and Smith (2017) and Egido et al. (2020). This type of simultaneous generation of both FF-SAR- and UF-SAR-processed waveforms for SWH assessment using the same L1b processing chain was applied for P-III and CP-I. The use of this by-product allowed an objective comparison between the FF-SAR- and UF-SAR-derived SWH data in P-III.

The time for the coherent integration of the (range- and phase-corrected) pulses of each individual burst is reduced from the total illumination time  $T$  to the burst duration, which differs from FF-SAR where all pulses are coherently integrated over  $T$ . The UF-SAR illumination time corresponds to the number of bursts selected to compute each singlelook and the generated looks (Doppler beams) used for multilooking. The range-aligned and phase-corrected Doppler-beam stack is obtained by squaring the magnitude of the coherently integrated bursts, from which the UF-SAR multilooked waveform is then obtained by incoherent summation.

The multilooked UF-SAR waveforms could be collected every  $\sim 1$  m along with each of the FF-SAR singlelooks (Egido et al. 2020). However, since the UF-SAR emulation reduces the theoretical along-track resolution from  $\sim 1$  m to  $\sim 300$  m (assuming a static scenario of scatterers within  $T$  (Egido and Smith 2017)), the multilooked waveforms are selected at locations  $\sim 300$  m apart to obtain independent (uncorrelated) realisations. These are comparable to the multilooked waveforms contained in the EUMETSAT baseline L2 product at 20 Hz posting rate, while assuming matched locations. However, a significant difference is the absence of the spurious range-walk error, as investigated by Guccione (2008) and Scagliola et al. (2021). In terms of SWH estimation, the range-walk error can cause a bias of a few centimetres, which was analysed in CP-I and also observed in P-III. A correction of the range-walk error is on the roadmap of the UF-SAR EUMETSAT baseline processing chain and is planned for baseline F09 and scheduled for Q3 2023 (Scharroo et al. 2022).

Some authors report an increased precision by averaging successive UF-SAR estimates from 40 Hz or 60 Hz posting rates onto 20 Hz (Dinardo et al. 2015; Egido et al. 2020). However, this step was found to introduce a correlation between adjacent 20 Hz records and is therefore not considered a viable option; see P-III (Appendix A). Thus, an apparent gain in precision may be partly due to the effective low-pass filtering of the geophysical estimates and a corresponding loss in resolution, which is undesirable.

### 2.3.4 Point Target Responses for SAR Processing Modes

This section discusses in more detail the differences between the 2D-PTRs inherent in UF-SAR and FF-SAR processing. As mentioned earlier in the previous section, the obvious advantage of FF-SAR over UF-SAR is the high theoretical along-track resolution.

The theoretical 2D-PTR of both FF-SAR and UF-SAR can be derived analytically as in Egido and Smith (2017), but also measured over transponder sites. Since the transponder represents a target with an SNR that is orders of magnitude higher than any other adjacent target, the 2D-PTR of the transponder as a point target can be measured by calculating the singlelook waveforms for the gridded surface locations surrounding the transponder surface location.

This has been done for S6-MF and the Crete transponder site for cycle 38, pass 18. The corresponding 2D-PTRs for UF-SAR and FF-SAR are shown in Figure 2.14 (a) and (b), respectively. Each column

represents a singlelook waveform focused on each gridded surface location. The transponder is thus located at along-track distance  $x = 0$  m: The focused singlelook waveform is represented by the  $\text{sinc}^2$  shape corresponding to Equation (2.8), and is basically the same for both UF-SAR and FF-SAR. The along-track PTR differs from UF-SAR to FF-SAR: In general, it is given by  $\text{sinc}^2\left(\frac{x}{L_x}\right)$ , with  $x$  being the along-track distance (Eqs. 2 and 3 in CP-I). The width of the  $\text{sinc}^2$  is thus scaled by the along-track resolution  $L_x$ , as given in Equation (2.11), showing the inverse proportionality of the along-track resolution and the coherent integration time  $T$ . Substituting  $T = 1/\text{BRF} \approx 1/140$  Hz and  $T = 2.1$  s for UF-SAR and FF-SAR in Equation (2.11), one obtains the along-track resolutions  $L_x$  of  $\sim 300$  m and  $\sim 1$  m, respectively.

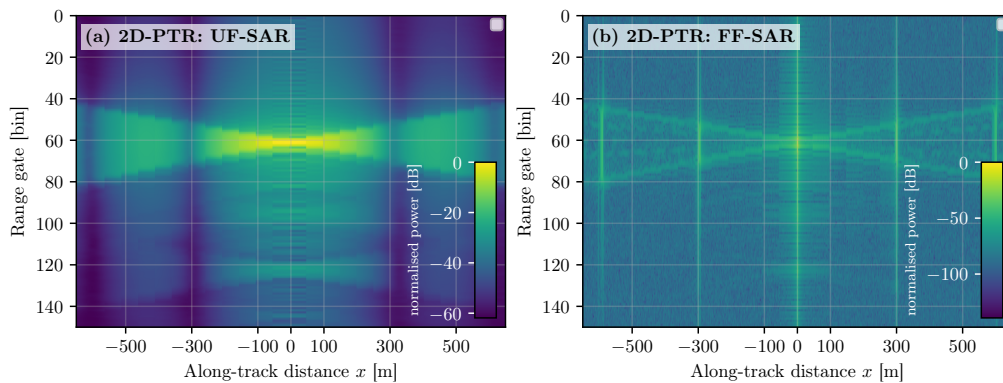


**Figure 2.14** The UF-SAR and FF-SAR 2D-PTRs are shown in (a) and (b) as a function of the along-track distance  $x$  from the transponder position at  $x = 0$  and range gates over the Crete CDN1 transponder of Sentinel-6 (cycle 38, pass 18), respectively.

The peaks seen at along-track distance  $x \approx 300$  m for the FF-SAR 2D-PTR in Figure 2.14 (b) are the so-called grating lobes and result from the transmission of calibration and C-band pulses in each of the radar cycles; see the interleaved chronogram in EUMETSAT (2022b, Section 2.1). These peaks are rather small for S6-MF due to its interleaved transmission mode, accounting for only  $\sim 1\%$  of the total power, but cannot be completely ignored, though. The implications of the grating lobes, and in particular their relevance in coastal scenarios, are further discussed in P-III.

Unlike S6-MF, which uses the interleaved operation mode, CS2 and S3 are more affected by the grating lobes due to the closed-burst operation mode (see Figure 2.6), as shown in CP-I (Fig. 4 Panel F) for Sentinel-3B. This results in stronger and more frequent grating lobes at integer multiples of the along-track distances of  $\sim 90$  m (Egido and Smith 2017; Guccione et al. 2018).

With the high along-track resolution, FF-SAR has the highest potential for inland water targets, which are usually highly specular targets and therefore well resolved. In the ocean, however, the effective along-track resolution is degraded by wave motion effects. In particular, vertical wave motions, cause an additional shift in their Doppler frequency, which in turn leads to a blurring of the signal in the along-track direction (Buchhaupt 2019; Egido and Ray 2019), deteriorating the along-track resolution. At the same time, the signal is smeared in the range direction causing a widening of the waveforms (CP-I). This leads to a sea state dependent overestimation of the SARM-derived SWH with respect to in-situ and conventional LRM-processed altimetry data, as shown in Moreau et al. (2017), Moreau et al. (2018), and Abdalla et al. (2018) for CS2 and in Moreau et al. (2017) and Raynal et al. (2018) for S3. The SWH bias with respect to LRM-derived estimates and a regional wave model is analysed and discussed in more detail in P-III.



## 3 Estimation of Significant Wave Height using Satellite Altimetry

Retracking is part of the L2 processing and represents the process of the extraction of the geophysical estimates SSH, SWH, and wind speed from the multilooked waveform.

Retracking algorithms can be divided into three different categories (Dinardo 2020): Empirical, physical, and statistical retrackers. Empirical retrackers are based on a heuristic approach, in which an empirically-based relationship is established between the waveform and the geophysical quantities. The approach of physical retrackers is to fit the waveform to an idealised mathematical model. In its most accurate form, the model is a numerical solution and mimics the processing chain and physical effects (e.g., the interaction of the pulse with the Earth's surface) as closely as possible. The closed-form analytical (or semi-analytical) solution of a physical retracker meets certain simplifying assumptions, making the computation of the model more robust, versatile, and computationally cheaper. The third category of retrackers uses a statistical approach that exploits statistical information from neighbouring measurements.

Here, as well as in P-II and P-III, the focus is on a physical retracker that is based SAMOSA2 as an open ocean power return echo model for UF-SAR waveforms (Ray et al. 2015). The idea is to fit the measured, multilooked waveform to SAMOSA2 in a least squares sense, e.g. with the Levenberg-Marquardt (Moré 1978) or the trust region reflective (TRR) (Branch et al. 1999) optimisation algorithms.

### 3.1 SAMOSA-based Retracking Algorithm

The ESA-funded project 'Development of SAR Altimetry Mode Studies and Applications over Ocean, Coastal Zones and Inland Water' (SAMOSA) (Gommenginger et al. 2010) was initiated in 2007. The objective was to exploit the high potential of performance improvements provided by SARM over LRM for ocean, coastal, and inland water scenarios and to develop a practical implementation of a new theoretical, physical SAR echo waveform model.

The fully analytical SAMOSA2 power return echo model was later published by Ray et al. (2015) and is to date the standard open ocean waveform model for UF-SAR waveforms used in the baseline processing chains of the CS2, S3, and S6-MF missions. The technical description of the SAMOSA2 model is given in the non-publicly available detailed processing model (DPM) document with version 2.5.2 (2017, pers. comm. Jérôme Benveniste). A publicly available technical description of the SAMOSA2 model is given in the product generation specification document of the S6-MF high-resolution (HR) processing chain (EUMETSAT 2022c, Section 4.5.2). An explanatory description of the different terms of the equations of the SAMOSA2 model can be found in Dinardo (2020).

#### 3.1.1 SAMOSA2 Power Return Echo Model

The modelled, multilooked SAMOSA2 waveform is given by the generation of the theoretical stack formation, which is composed of the individual singlelook waveforms, or Doppler beams, pointing to a particular surface location. The mathematical equations of the SAMOSA2 model are fully documented in EUMETSAT (2022c, Section 4.5.2.3). Here, it is described at a high-level to facilitate the understanding of the model generation.

To generate a multilooked waveform, SAMOSA2 takes instrument-specific and sensor parameters from the L1b product, as well as other configuration-related, parameters as an input. The following

parameters are taken from the L1b product: Latitude, altitude, altitude rate, orbital velocity, mis-pointing angles (pitch and roll), track direction (ascending or descending), PRF, beam stack angles (the angle between the surface location and the burst centre associated with each of the beams), and the tracker reference gate. As the CORAL retracker presented in P-II and used in P-III is based on SAMOSA2, it also takes these values as an input to extract the SWH.

The fully analytical SAMOSA2 model from Ray et al. (2015) makes several approximations, such as the Gaussian approximation of the PTR (Ray et al. 2015). To account for this, a sea state dependent look-up table (LUT) is used for the  $\alpha_p$  value that is part of the model. The  $\alpha_p$  LUT is mission and processing mode dependent. Therefore, dedicated  $\alpha_p$  LUTs had to be used for P-II and P-III, depending on whether the retracking was to be done with S3 or S6-MF and with UF-SAR- or FF-SAR-processed waveforms.

Moreover, for computational efficiency, two other LUTs are tabulated, which are two terms based on scaled Bessel functions that do not depend on instrument-specific or sensor parameters and are therefore the same across different missions (Dinardo 2020).

Figure 3.1 shows exemplary normalised, multilooked, SAMOSA2 waveforms with a varying SWH of 0.25, 0.75, 1.0, 2.0, 5.0, 7.0, 9.0 m,  $P_u = 1.0$  and epoch = -250 ns (setting PRF = 9.2 kHz, BRI = 1/140 Hz, receiving bandwidth  $B_r = 395$  MHz, zero-padding factor  $z_p = 2$ , and assuming fixed L1b parameters of a random measurement). It can be seen that the steepness of the LE is inversely related to the SWH, i.e. a higher SWH corresponds to a less steeper slope of the LE. It is important to note that unlike the ocean return waveform model in LRM, the SWH has a greater effect on the trailing edge of the waveform. As with the LE, a low SWH has a steep trailing edge, whereas a high SWH corresponds to a more slowly decaying trailing edge. The epoch is given by the time difference between the epoch reference gate (located in range bin 256 (0-based) for S6-MF) and the reference point of the SAMOSA2 model, which is at level 0.8422 of the maximum peak amplitude (Dinardo 2020, Eq. 3.23). The epoch reference gate acts as a reference point within the receiving window, to which the onboard tracking unit adjusts the receiving window (on a per multi-burst radar cycle) and thus the tracker range to smoothly follow the surface being sampled. In this way, the LE of the waveform is kept at approximately the same position (gates 80-100 for S6-MF). It is therefore straightforward to calculate the measured range from the altimeter to the MSL using the relationship  $R_{\text{trk}} - \text{epoch} \cdot \frac{c}{2}$ , where  $\text{epoch} \cdot \frac{c}{2}$  corresponds to the one-way travel distance between the tracker reference point (translated from the epoch reference gate) and the MSL.  $P_u$  corresponds to the retracked, peak amplitude of the waveform and can be converted into the ocean backscatter coefficient  $\sigma_0$  according to EUMETSAT (2022c, Section 4.6.2), from which in turn the wind speed can be derived (EUMETSAT 2022c, Section 5.3.4).

The SAMOSA2 model was developed as an open ocean power return echo model for UF-SAR altimetry. However, CP-I showed that the SAMOSA2 model can also be applied to FF-SAR-processed L1b waveforms. It was also shown that the UF-SAR- and FF-SAR-processed L1b waveforms for S3 (and consequently also for CS2) are very similar, so that the SAMOSA2 model can be used for retracking without any modification. For S6-MF, however, the LE of the FF-SAR-processed waveform is inherently steeper than for its UF-SAR-processed counterpart, which is explained by the absence of the major grating lobes of CS2 and S3 due to the closed-burst transmission mode (and the presence of only minor grating lobes), as discussed in CP-I. Accordingly, the zero-Doppler beam of SAMOSA2 resembles much better with the FF-SAR-processed waveform of S6-MF. The retracking of S6-MF FF-SAR-processed waveforms performed in P-III and CP-I therefore used the zero-Doppler beam.

Furthermore, as mentioned earlier, a modified  $\alpha_p$  is used to generate the SAMOSA2 model since its generation depends, among other parameters, on the total illumination time and also on the coherent integration time  $T$  used in the L1b processing, which is inherently different for FF-SAR and UF-SAR. The modified  $\alpha_p$  LUT used in this PhD project and for P-III is the one produced within the ESA L2 GPP project (ESA 2021).

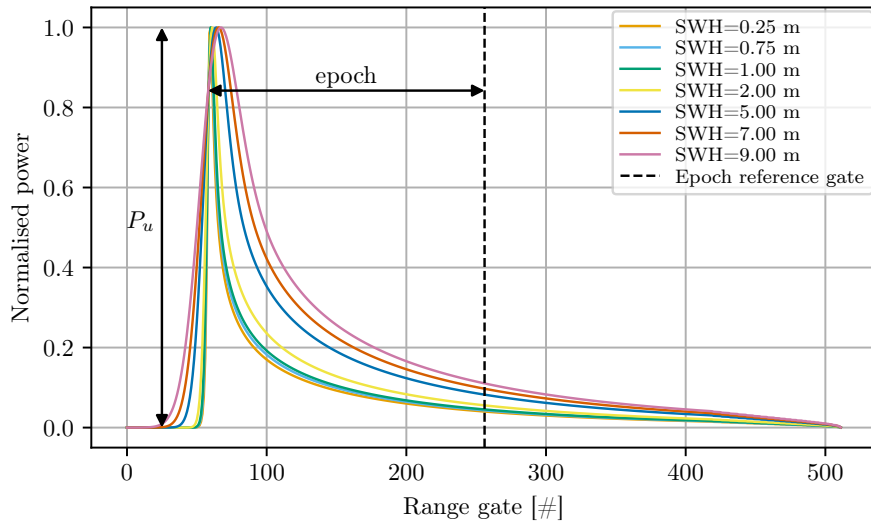


**Figure 3.1** Normalised, modelled, multilooked SAMOSA2 waveform with varying SWH of 0.25, 0.75, 1.0, 2.0, 5.0, 7.0, 9.0 m.

### 3.1.2 Fitting Routine

The extraction of the retracked estimates  $P_u$ , SWH, and epoch is done by fitting the theoretical SAMOSA2 model, which is configured with the corresponding instrument-specific and sensor parameters from the L1b product. The fitting routine is described in detail in the SAMOSA DPM (SAMOSA Detailed Processing Model, 2017, Section 4.2.2, pers. comm. Jérôme Benveniste) and EUMETSAT (2022c, Section 4.5.2.3.4), and is briefly described below. The description assumes the mission-specific parameter configuration of S6-MF.

1. Normalise the received, multilooked waveform by its maximum.
2. Select the range gates of the waveform to be fitted. For instance, S6-MF fits over gates [22, 264] ( $z_p = 2$ , 0-based) due to the RMC mode.
3. Estimate the thermal noise floor by averaging the configured noise gates (in S6-MF: gates [26, 34] ( $z_p = 2$ , 0-based)).
4. Fit the theoretical, multilooked SAMOSA2 waveform to the normalised, received multilooked waveform using a least squares optimisation algorithm (e.g. Levenberg-Marquardt (Moré 1978) or TRR (Branch et al. 1999)):
  - a) Add the estimated thermal noise floor to the theoretical, multilooked waveform.
  - b) Set initial values for the three free parameters, e.g.  $P_u = 1.0$ , SWH = 2.0 m, epoch =  $[-\text{inf}, \text{inf}]$  (S6-MF). The closer the initial values are chosen to the truth, the more likely it is that the solution will converge to the optimal solution.
  - c) Perform an iterative fitting procedure until the maximum number of iterations is reached or the fit tolerance (as configured) is exceeded.
  - d) If the fitting procedure fails for any reason, the quality flag for that measurement is set to false, indicating a bad measurement.
5. The misfit is computed by taking the root mean square (RMS) differences of the fitted range bins between the theoretical, fitted SAMOSA2 model waveform and the received, measured waveform.

6. The quality flag is set to true (bad estimate), if the misfit exceeds an empirical threshold value of 4, otherwise it is set to false (good estimate). This approach is not part of the baseline processing chain, but has been shown to be an effective quality measure, e.g. in Dinardo et al. (2018) and P-I.
7. The free parameters returned after the last iteration step yield the epoch, SWH, and  $P_u$  estimates.

The fitting procedure and the retracking of a multilooked waveform is shown as an example in Figure 3.2 (a). The measured waveform represents a typical open ocean waveform with no coastal interference. It can be seen that the fitted SAMOSA2 model agrees well with the measured waveform. The obtained free parameters give estimates of  $P_u = 1.04$ , SWH=2.19 m, and epoch=-183.14 ns (related to the epoch reference gate 256 (0-based)).

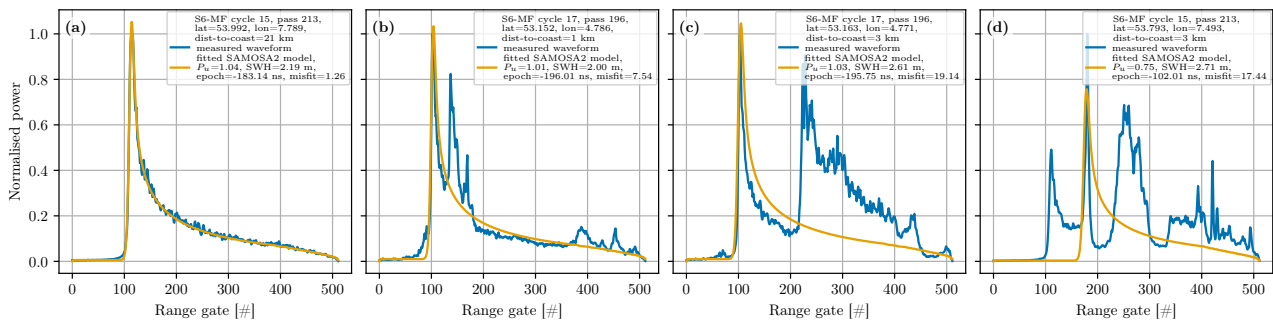


**Figure 3.2** Retracked, multilooked UF-SAR waveforms with the open ocean SAMOSA-based retracker showing typical waveforms from (a) the open ocean and from the coastal zone in (b-d), which are strongly affected by spurious coastal interference. The measured and fitted waveforms are shown in blue and orange, the S6-MF cycle and passes, the location of the measurement, and the dist-to-coast are given in the titles of the legends.

### 3.2 Challenges in Coastal Retracking

Retracking multilooked waveforms in the coastal zone is more challenging because of the spurious signal components that can be present in the returned echoes and negatively affect the estimation of the geophysical estimates. The spurious signal interference in the radar echo returns originate from strongly reflective targets such as mud- or sandbanks, tidal flats, sheltered bays, shipping platforms, or calm waters close to the coast.

Gómez-Enri et al. (2010) have studied altimetric echoes from the Envisat mission over a Mediterranean island, showing spurious interference with a hyperbolic characteristic arising from calm waters in the coastal zone. Here, the position of the strongly reflective targets in the along-track direction in the power echo radargram follows a hyperbolic law, which generally applies to off-nadir targets appearing after the LE of the multilooked waveform. The position of the spurious peaks will therefore depend on the off-nadir position and the elevation. A ship's deck platform located around nadir can cause spurious signals before the LE of the waveform. In the worst case, the spurious signal components of the interfering target will coincide with the LE. In this case, the interfering target will be slightly off-nadir and elevated above the MSL, causing the retracked estimates to be significantly degraded.

Figure 3.2 (b-d) show typical examples of retracking of multilooked waveforms affected by spurious coastal interference. Figure 3.2 (b) and (c) exhibit a peak that arises after the LE of the waveform. In Figure 3.2 (b) the interference has a peak shape located close to the LE and is thus likely to be from a strongly reflective target close to the nadir. The interference shown in Figure 3.2 (c) is more distant from nadir and has a greater spatial dimension as it spans over a greater number of range gates. The difference in the location of the interference within the waveform between Figure 3.2 (b) and (c) is reasonable as their nadirs are located at a dist-to-coast of 1 and 3 km, respectively. In both cases

Figure 3.2 (b) and (c), the retracked estimates are affected by the interference during the least squares fitting routine.

Since the ground truth of the geophysical data is not known, only an approximate statement can be made about the accuracy of the estimates: The SWH is likely to be overestimated because the wider, less peaked waveforms of higher sea states minimise the difference between the received, interfered waveform and the model waveform (compare with Figure 3.1). In other words: The LE of the fitted model waveform is less steep, corresponding to a higher SWH. The SWH overestimation is more significant for Figure 3.2 (c) due to the higher number of strongly affected (interference) gates.

The coastal waveform shown in Figure 3.2 (d) shows strong interference from reflective targets within the footprint and represents a typical multipeak scenario. The LE corresponding to the sea surface is assumed to be the first peak, as the S6-MF onboard tracking unit tries to keep it at approximately the same position within the receiving window at gate  $\sim 100$ . It can be seen that the wrong LE is fitted by the baseline SAMOSA-based retracker, leading to completely incorrect estimates.

The quality flag derived from all three retracked, coastal waveform examples of Figure 3.2 (b-d) indicate bad estimates since their misfit values all exceed the threshold value 4 (as explained in the previous section) regardless of the degree of interference and quality of the estimates.

As a result, coastal observations are often discarded or of poor quality due to coastal interference caused by strongly reflective targets such as sandbanks, tidal flats, sheltered bays, or calm waters close to the coast. For instance, in P-II it was shown that the correlation of SWH data from the operational baseline product of S3 with in-situ data from buoys is to less than 0.20 for closer than 20 km from the coast. Individual retrackers showed a greatly reduced number of valid estimates of less than 20% of the total points within 5 km from the coast. The novel coastal retracking algorithm presented in P-II significantly increases the number of valid records while improving the quality of the SWH estimates.

### 3.3 State-of-the-art Coastal Retracking Algorithms

In P-I, the performance of eight different LRM and seven different SARM retracking algorithms was compared using a quasi-global dataset, including both open ocean and coastal retrackers.

This section describes a subset of the state-of-the-art coastal retracking algorithms for the SWH estimation that address the challenges of the coastal interference (as introduced earlier) and its mitigation for estimating the geophysical estimates during retracking. The publications presenting the individual coastal retracking algorithms are sorted in chronological order of their date of publication.

In Passaro et al. (2014), a coastal LRM retracker was presented that deals with the spurious signal components in the coastal zone through a retracking algorithm called adaptive leading edge sub-waveform (ALES). ALES + was later introduced in Passaro et al. (2018), adapting ALES to also work in sea ice, coastal, and inland water scenarios. For both variants, only a subwaveform is considered to facilitate the least squares fitting of the model to the noisy waveform. The width of the subwaveform, i.e. the number of gates being included after the LE, depends on the sea state that was estimated in a first retracking step. A second retracking step adjusts the width of the subwaveform to obtain the final estimates of the output. ALES + helps to improve both the quality and quantity of the estimates in the coastal zone for LRM altimeters.

A fundamentally different approach has been introduced by the STARv2 retracking algorithm for LRM altimetry, which is a statistical retracker that takes into account multiple adjacent 20 Hz measurements (Roscher et al. 2017). Here, realistic estimates are selected from a point cloud of possible solutions based on the Dijkstra algorithm (Dijkstra 2022), which chooses the shortest path between connected nodes (estimates) associated with edge weights (differences between adjacent estimates).

Peng and Deng (2018) present the Brown Peaky retracker, which has adapted the physical ALES approach and extended its retracking strategy with an adaptive peak detection method for coastal LRM waveforms. The adaptive peak detection identifies waveform gates affected by spurious interference and down-weights them in the weighted least squares (WLS) fitting procedure used. If the detected

peaky return is too wide or the differences between the iterative retracking steps are too large, the Brown Peaky retracker reverts to the ALES approach.

Dinardo et al. (2018) present the SAMOSA+ coastal retracking algorithm for SAR altimetry that includes all waveform gates for retracking. Apart from individual adjustments in the L1b processor, SAMOSA+ has two main extensions to the baseline SAR Altimetry MOde Studies and Applications (SAMOSA)-based retracker (SAMOSA Detailed Processing Model, 2017, pers. comm. Jérôme Benveniste) that are specific to coastal scenarios. First, it accounts for multipeak waveforms and computes a pointwise product to obtain an averaged first-guess (FG) epoch, facilitating the fitting of the correct LE. Second, it allows for very peaky waveforms to be fitted in a second retracking step to refine the epoch estimate. Both L2 extensions of SAMOSA+ are adopted by COastal Retracker for SAR ALtimetry (CORAL), as presented in P-II.

The coastal SAMOSA++ retracker exploits the range integrated power (RIP) function, i.e. the range-integrated Doppler beams of each measurement, to form a backscattering profile that is fed into the SAMOSA2 model, making it applicable to both diffuse and specular surfaces and allowing a seamless transition between the open ocean and the coastal zone (Dinardo et al. 2020).

Another empirical retracker is provided by RiwiSAR-SWH (Gou and Tourian 2021), which estimates the SWH for coastal waveforms from an empirical relationship between the rise time of the LE and the width of the waveform. This approach ignores potential spurious interference within the trailing edge by completely omitting it from the SWH estimation.

The performance of the coastal retracking algorithms is highly dependent on the processing scheme used (LRM or SARM). Studies presenting novel retracking algorithms usually only evaluate the quality of the estimates only (e.g. in Roscher et al. (2017), Peng and Deng (2018), and Dinardo et al. (2018)), namely the accuracy with respect to in-situ buoy data and the precision as intrinsic noise (as done in P-I), which decreases with a smaller dist-to-coast and an increased coastal interference. A crucial metric that is not considered in most evaluations is the quantity, i.e. the number of valid records, as indicated by the binary quality flag provided with the L2 product. In general, however, the number of valid records also decreases significantly with a decreasing dist-to-coast if the aim of the retracker is to maintain a high quality for the estimates. Ideally, a large number of valid records of high quality are retained in the coastal zone, as determined by the strategy of the retracking algorithm.

The first-author publication P-I, as presented in the following section, makes an objective comparison between the different retracking algorithms, evaluating both the quality and the quantity (in the form of outliers) of the SWH estimates.

It should also be emphasised that for multilooked SAR altimetry waveforms, the SWH has a greater effect on the trailing edge of the waveform than for LRM waveforms, as noted in Section 3.1.1 and shown in Figure 3.1. It is therefore plausible to expect that retracking the entire waveform including the trailing edge will lead to more accurate and precise estimates if the trailing edge is not affected by coastal interference. In the case of coastal interference in the trailing edge of the waveform, the novel coastal retracking algorithm presented in P-II takes the approach of adaptively selecting a subwaveform to be fitted, combining and extending the different strategies of the above coastal retracking solutions.

## 4 P-I: Round Robin Assessment of Radar Altimeter Low Resolution Mode and Delay-Doppler Retracking Algorithms for Significant Wave Height

The objective of this first-author publication is to compare the retracked SWH data of different LRM and UF-SAR retracking algorithms for the J3 and S3A missions, respectively.

Between the publication of the paper and the submission of the thesis, P-I has already been cited 25 times, including highly relevant scientific articles (Dodet et al. 2020; Abdalla et al. 2021; Quartly et al. 2021), as no comparable structured and comprehensive analysis of different retracking algorithms has been carried out to date.

All of the novel retracking algorithms investigated showed improvements in most of the metrics evaluated. An important result of this paper is the fact that the EUMETSAT baseline SARM retracker shows a severely degraded correlation of less than 0.20 with in-situ buoy data within 20 km from the coast, and the state-of-the-art LR-RMC retracker shows only 16.5% of remaining valid estimates within 5 km from the coastline. This paper has therefore identified the greatly reduced number of valid records in the coastal zone as one of the shortcomings of the state-of-the-art retracking algorithms, which ultimately led to the design and development of the novel coastal retracking algorithm as the main novelty of this PhD project, as presented in P-II.

Prior to performing the so-called RR assessment, the set of rules was defined for how the evaluation should be performed, what performance metrics should be extracted and what input dataset should be used for the assessment. The execution of an RR is an essential part of the development phase of an ESA Climate Change Initiative (CCI) ECV project. The Sea Surface Temperature CCI (ESA 2011), Soil Moisture CCI (ESA 2012), and Ocean Colour CCI (Brewin et al. 2015) projects are examples of other CCI projects where RRs were carried out.

The RR assessment was open to both internal and external participants and its general procedure is as follows: A data package containing satellite data, and auxiliary data is distributed to all participants. They apply their algorithms to the data and send back their retracked results. The pre-agreed assessment metrics are extracted from the generated datasets and the best performing algorithm is selected.

This RR assessment was carried out as part of the ESA Sea State Climate Change Initiative project, which was launched in June 2018 (ESA 2022b). The main objective is to produce a consistent long-term, quality-controlled sea state dataset combining data from satellite altimeters, SAR imagers, and in-situ data (ESA 2022b). The focus of the project is on the development, improvement and validation of the respective sea state retrieval algorithms for the extraction of SWH from all ESA altimetry missions and TOPEX and of wave spectra from SAR imaging missions such as ERS and Sentinel-1.

**Schlembach, F.; Passaro, M.; Quartly, G. D.; Kurekin, A.; Nencioli, F.; Dodet, G.; Piollé, J.-F.; Ardhuin, F.; Bidlot, J.; Schwatke, C.; Seitz, F.; Cipollini, P.; Donlon, C. Round Robin Assessment of Radar Altimeter Low Resolution Mode and Delay-Doppler Retracking Algorithms for Significant Wave Height.** *Remote Sensing* 2020, 12 (8), 1254. <https://doi.org/10.3390/rs12081254>.

## Abstract

Radar altimeters have been measuring ocean significant wave height for more than three decades, with their data used to record the severity of storms, the mixing of surface waters and the potential threats to offshore structures and low-lying land, and to improve operational wave forecasting. Understanding climate change and long-term planning for enhanced storm and flooding hazards are imposing more stringent requirements on the robustness, precision, and accuracy of the estimates than have hitherto been needed. Taking advantage of novel retracking algorithms, particularly developed for the coastal zone, the present work aims at establishing an objective baseline processing chain for wave height retrieval that can be adapted to all satellite missions. In order to determine the best performing retracking algorithm for both Low Resolution Mode and Delay-Doppler altimetry, an objective assessment is conducted in the framework of the European Space Agency Sea State Climate Change Initiative project. All algorithms process the same Level-1 input dataset covering a time-period of up to two years. As a reference for validation, an ERA5-based hindcast wave model as well as an in-situ buoy dataset from the Copernicus Marine Environment Monitoring Service In Situ Thematic Centre database are used. Five different metrics are evaluated: percentage and types of outliers, level of measurement noise, wave spectral variability, comparison against wave models, and comparison against in-situ data. The metrics are evaluated as a function of the distance to the nearest coast and the sea state. The results of the assessment show that all novel retracking algorithms perform better in the majority of the metrics than the baseline algorithms currently used for operational generation of the products. Nevertheless, the performance of the retrackers strongly differ depending on the coastal proximity and the sea state. Some retrackers show high correlations with the wave models and in-situ data but significantly under- or overestimate large-scale spectral variability. We propose a weighting scheme to select the most suitable retrackers for the Sea State Climate Change Initiative programme.

## Contribution

The contributions of this reported work can be listed as follows: conceptualization, M.P., G.D.Q., F.N., F.Sc.; methodology, F.Sc., M.P., G.D.Q.; software, F.Sc., A.K.; formal analysis, F.Sc., M.P., G.D.Q., A.K.; investigation, F.Sc., G.D.Q., A.K.; resources, F.Sc., J.-F.P., G.D.D., J.B.; writing—original draft preparation, F.Sc.; writing—review and editing, F.Sc., M.P., G.D.Q., A.K., F.N., C.S., P.C., G.D.D., F.A.; visualization, F.Sc., A.K.; supervision, M.P.; project administration, F.A., P.C., C.D., F.S., ESA SeaState\_cci; funding acquisition, F.A., P.C., C.D., F.S., ESA SeaState\_cci. All authors have read and agreed to the published version of the manuscript.

Criteria	Own contribution
Idea and conceptual design	50%
Implementation and realisation	70%
Analysis and discussion	70%
Figure compilation	90%
Manuscript structure and writing	70%
<b>Overall contribution</b>	<b>70%</b>

**Table 4.1** Own contribution to publication P-I



# 5 P-II: Interference-sensitive Coastal SAR Altimetry Retracking Strategy for Measuring Significant Wave Height

A thorough analysis has been carried out in P-I to compare the performance of a variety of novel LRM and SARM retracking algorithms. It is challenging to select the "best" performing algorithms, but the results of the analysis help to identify the shortcomings of each of them.

The results of P-I led to the development of a new coastal retracking algorithm for UF-SAR, namely CORAL, which is presented in this first-author publication P-II. CORAL is based on the SAMOSA2 waveform model, as introduced in Section 3.1.1, and the coastal SAMOSA+ retracking algorithm. The main innovation of CORAL is represented by a selective subwaveform strategy, called the adaptive interference masking (AIM) scheme. AIM tackles coastal interference to improve both the quality and the quantity ("validity") of the estimates.

CORAL detects and mitigates coastal interference within the multilooked waveform in an iterative retracking approach. The detected interference range gates are omitted from the fitting routine, improving the quality of the SWH estimates. The number of valid records is significantly improved by deriving the quality flag from the misfit of the selected range gates between the received and the fitted model waveform.

In P-II, CORAL is applied to L1b waveforms processed from the same S3A L1a dataset used in P-I. The extracted SWH (L2) data has been validated and the effectiveness of CORAL compared to SAMOSA+ as a competing state-of-the-art coastal retracking algorithm has been demonstrated using the assessment methodology derived from P-I.

**Schlembach, F.; Passaro, M.; Dettmering, D.; Bidlot, J.; Seitz, F. Interference-sensitive Coastal SAR Altimetry Retracking Strategy for Measuring Significant Wave Height.** Remote Sensing of Environment 2022, 274, 112968. <https://doi.org/10.1016/j.rse.2022.112968>.

## Abstract

Satellite altimetry is a radar remote sensing technology for the precise observation of the ocean surface and its changes over time. Its measurements allow the determination of geometric and physical parameters such as sea level, significant wave height or wind speed. This work presents a novel coastal retracking algorithm for SAR altimetry to estimate the significant wave height. The concept includes an adaptive interference masking scheme to sense and mitigate spurious interfering signals that typically arise from strongly reflective targets in the coastal zone. The described procedure aims at increasing the number of valid records in the coastal zone. The effectiveness of the novel retracking algorithm is validated using the methodology recently developed in the framework of the European Space Agency Sea State Climate Change Initiative project. Several different metrics were extracted as functions of sea state and distance to the nearest coast: outliers, number of valid records, intrinsic noise, power spectral density, and correlation statistics for the comparison with wave model and in-situ data. Two coastal case study scenarios complement the validation. The results show that with the presented novel retracking algorithm, the number of valid 20 Hz records in the near coastal zone of less than 5 km off the coast is increased by more than 25% compared to the best competing

coastal retracking algorithm with no degradation of quality of the estimated records. We emphasise the importance of the correct choice of the quality flag that is provided together with the significant wave height. Our findings suggest that the strategy for the significant wave height quality flag of the official baseline Level-2 product of the Sentinel-3 mission can be redefined to obtain more robust significant wave height estimates in the coastal zone.

## Contribution

The contributions to this reported work can be listed as follows: conceptualization, F.Sc., M.P.; methodology, F.Sc., M.P.; software, F.Sc.; formal analysis, F.Sc., M.P.; investigation, F.Sc.; resources, F.Sc., J.B.; writing–original draft preparation, F.Sc.; writing–review and editing, F.Sc., M.P., D.D., F.S.; visualisation, F.Sc.; supervision, M.P.; project administration, F.S., ESA SeaState\_cci; funding acquisition, F.S., ESA SeaState\_cci. All authors have read and agreed to the published version of the manuscript.

<b>Criteria</b>	<b>Own contribution</b>
Idea and conceptual design	80%
Implementation and realisation	90%
Analysis and discussion	85%
Figure compilation	100%
Manuscript structure and writing	80%
<b>Overall contribution</b>	<b>87%</b>

**Table 5.1** Own contribution to publication P-II

## 6 P-III: Benefits of Fully Focused SAR Altimetry to Coastal Wave Height Estimates: A Case Study in the North Sea

In this first-author paper, the newly developed CORAL algorithm presented in P-II is applied in a case study scenario to demonstrate its effectiveness in the coastal zone. Furthermore, the differences between FF-SAR and UF-SAR processing in the coastal altimetry data were investigated. The combination of FF-SAR-processed data with a selective subwaveform retracking algorithm such as CORAL has never been shown to estimate SWH in the coastal zone. The idea behind the application of FF-SAR altimetry is that it may provide potential gains over UF-SAR altimetry in resolving and mitigating small-scale interferers in the along-track direction to improve the accuracy and precision of coastal SWH estimates.

The following research objectives are addressed:

1. Is there an improvement between FF-SAR- and UF-SAR-processed SWH estimates obtained from S6-MF data when approaching the coast as close as possible?
2. Are the statistical improvements observed in coastal SWH estimates also beneficial in practice for determining key metrics such as the variation of SWH from offshore to the coast?

To address both objectives, a statistical analysis based on the methodology developed in P-I is performed, which helps to assess the performance of the different processing configurations, which differ in terms of different processing options (FF-SAR or UF-SAR processing, L1b posting rate, retracking algorithm).

In addition to the novelty of combining FF-SAR altimetry with a selective subwaveform retracking approach, P-III makes an important contribution by comparing the FF-SAR-processed datasets with an UF-SAR-processed dataset that has been consistently processed with an identical processing chain to allow an objective comparison. This provides valuable insights for the scientific altimetry community which benefits can be achieved by applying FF-SAR processing in the coastal zone.

The paper was written as part of the joint, international research collaboration with the Delft University of Technology, which started in April 2021. The tasks carried out within the research collaboration included the following:

- Application of the FF-SAR processing for the SWH estimation in the coastal zone.
- Implementation of the FF-SAR processor: Adaptation of the existing SAR processor to process S3/S6-MF data.
- Interpretation of the retrieved SWH data with respect to a novel coastal, regional, high-resolution wave model.
- Comparison with other processing schemes such as UF-SAR and/or LRM.

Another co-authored publication, CP-I, written in collaboration with the Delft University of Technology, discusses the applicability of the SAMOSA2 open ocean model to retrack FF-SAR-processed waveforms:

Ehlers, F.; **Schlembach, F.**; Kleinherenbrink, M.; Slobbe, C. Validity Assessment of SAMOSA Retracking for Fully-Focused SAR Altimeter Waveforms. *Advances in Space Research* 2022. <https://doi.org/10.1016/j.asr.2022.11.034>.

It analytically explains the subtle differences in the UF-SAR- and FF-SAR-specific waveforms between S3 and S6-MF and thus justifies the fitting of the modelled, zero-Doppler SAMOSA2 waveform with the S6-MF FF-SAR-processed waveform. Therefore, CP-I provides valuable new findings into the relatively new research field of FF-SAR altimetry and serves as an enabler for the execution of the coastal case study presented in P-III.

**Schlembach, F.**; Ehlers, F.; Kleinherenbrink, M.; Passaro, M.; Dettmering, D.; Seitz, F.; Slobbe, C. Benefits of fully focused SAR altimetry to coastal wave height estimates: A case study in the North Sea. *Remote Sensing of Environment* 289 (2023) 113517. <https://doi.org/10.1016/j.rse.2023.113517>.

## Abstract

Estimating the three geophysical variables SWH, sea surface height, and wind speed from satellite altimetry continues to be challenging in the coastal zone because the received radar echoes exhibit significant interference from strongly reflective targets such as sandbanks, sheltered bays, ships etc. FF-SAR processing exhibits a theoretical along-track resolution of up to less than half a metre. This suggests that the application of FF-SAR altimetry might give potential gains over UF-SAR altimetry to resolve and mitigate small-scale interferers in the along-track direction to improve the accuracy and precision of the geophysical estimates.

The objective of this study is to assess the applicability of FF-SAR-processed S6-MF coastal altimetry data to obtain SWH estimates as close as possible to the coast.

We have developed a multi-mission FF-SAR processor and applied the coastal retracking algorithm CORAL to estimate SWH. We assess different FF-SAR and UF-SAR processing configurations, as well as the baseline Level-2 product from EUMETSAT, by comparison with the coastal, high-resolution SWAN-Kuststrook wave model from the Deltares RWsOS North Sea operational forecasting system. This includes the evaluation of the correlation, the median offset, and the percentage of cycles with high correlation as a function of distance to the nearest coastline. Moreover, we analyse the number of valid records and the L2 noise of the records. The case study comprises five coastal crossings of S6-MF that are located along the Dutch coast and the German coast along the East Frisian Islands in the North Sea.

We observe that accurate and precise SWH records can be estimated in the nearshore zone within 1-3 km from the coast using satellite SAR altimetry. We find that the FF-SAR-processed dataset with a Level-1b posting rate of 140 Hz shows the greatest similarity with the wave model. We achieve a correlation of  $\sim 0.8$  at 80% of valid records and a gain in precision of up to 29% of FF-SAR vs UF-SAR for 1-3 km from the coast. FF-SAR shows, for all cycles, a high correlation of greater than or equal to 0.8 for 1-3 km from the coast. We estimate the decay of SWH from offshore at 30 km to up to 1 km from the coast to amount to  $26.4\% \pm 3.1\%$ .

## Contribution

The contributions to this reported work can be listed as follows: conceptualisation, F.Sc.; methodology, F.Sc.; software, F.Sc., F.E., M.K., C.S.; formal analysis, F.Sc., F.E.; investigation, F.Sc.; resources, F.Sc., F.E., M.K., C.S.; writing–original draft preparation, F.Sc.; writing–review and editing, F.Sc., F.E., M.K., M.P., D.D., F.S., C.S.; visualisation, F.Sc.; supervision, M.P., M.K., C.S.; project administration, M.P., F.S., ESA Sea State Climate Change Initiative (SeaState\_cci); funding acquisition, M.P., F.S., ESA SeaState\_cci.

<b>Criteria</b>	<b>Own contribution</b>
Idea and conceptual design	85%
Implementation and realisation	70%
Analysis and discussion	75%
Figure compilation	100%
Manuscript structure and writing	80%
<b>Overall contribution</b>	<b>82%</b>

**Table 6.1** Own contribution to publication P-III

## 7 Conclusion and Outlook

The objective of this PhD project is to develop a novel retracking algorithm to improve significant wave height (SWH) estimates in the coastal zone using satellite altimetry. This is the subject of the three first-author publications summarised below.

Prior to the development of the retracking algorithm, a framework for the assessment of existing low resolution mode (LRM) and synthetic aperture radar mode (SARM)/unfocused synthetic aperture radar (UF-SAR) retracking algorithms of the satellite missions Jason-3 (J3) and Sentinel-3 (S3) with relevant performance metrics was defined within the European Space Agency (ESA) Sea State Climate Change Initiative (SeaState\_cci) project and a so-called round robin (RR) assessment was performed, as described and published in P-I. The RR assessment does not only provides a structured and comprehensive comparison of existing retracking algorithms, but also serves as a new reference on how to objectively compare the performance of retrackers with a focus on SWH estimation. This exercise allowed the shortcomings of existing state-of-the-art retracking algorithms to be identified. The quasi-global, objective assessment of various LRM and UF-SAR retracking algorithms showed that the quality of the SWH records, as well as their validity, deteriorates strongly near the coast.

The second first-author paper P-II is dedicated to the development of the novel COastal Retracker for SAR ALtimetry (CORAL). The application of the adaptive interference masking (AIM) scheme of CORAL allows the detection and mitigation of spurious interfering signals typically caused by strongly reflective targets such as sandbanks, sheltered bays, tidal flats, ships etc. located within the radar footprint of the satellite altimeter. With CORAL, the number of valid records is increased by more than 25% compared to the best competing coastal retracking algorithm, while maintaining a high quality of the estimates in terms of accuracy as shown by a comparison with an ERA5-based wave model. The crucial importance of the correct choice of the quality flag was highlighted. The results suggest that the strategy for the SWH quality flag of the official EUMETSAT baseline Level-2 (L2) product of the S3 mission can be redefined to obtain more robust SWH estimates in the coastal zone.

The third first-author paper P-III applies the newly developed CORAL coastal retracking algorithm to a case study region in the North Sea. The case study is the first known published work to assess whether SWH estimation from coastal altimetry data can be improved by using fully focused synthetic aperture radar (FF-SAR) instead of UF-SAR processing in combination with the CORAL coastal retracking algorithm. This assessment was made by comparing the processed SWH estimates with the high-resolution SWAN-Kuststrook coastal wave model of the Deltares RWsOS North Sea operational forecasting system. It was shown that satellite SAR altimetry can estimate accurate and precise SWH records in the nearshore zone within 1-3 km from the coast, achieving a correlation of  $\sim 0.8$  with 80% of valid records. Moreover, FF-SAR shows a gain in precision of up to 29% over UF-SAR for 1-3 km from the coast and a high correlation of greater than or equal to 0.8 for 1-3 km from the coast for all cycles.

In the North Sea case study area, the decay of SWH from 30 km offshore to up to 1 km from the coast was estimated to be  $26.4\% \pm 3.1\%$ . This is in agreement with the values observed in the study by Passaro et al. (2021), which was however limited to averaged 1 Hz estimates not closer than 3 km from the coast and to LRM altimetry.

The following paragraphs provide answers to the research questions posed in Section 1.2 and draw conclusions for each of them:

**Q-I: What are the main differences between the various methodologies for wave height estimation by satellite altimetry and what are the challenges?**

By far the most important difference between the different methodologies is the given altimeter mode: LRM or SARM. LRM has a circular, pulse-limited radar footprint with a size of ~7 km, while UF-SAR yields an along-track footprint size of 300 m.

Besides the altimeter mode, the chosen retracking algorithm (L2 processing) has a significant impact on the actual performance of the retracked SWH estimates. For this reason, an objective evaluation framework in the form of the RR assessment of the ESA SeaState\_cci project was developed in P-I where five different evaluation metrics were assessed: Percentage and type of outliers, level of measurement noise, power spectral density of along-track SWH (or referred to as wave spectral variability in P-I), comparison with wave models and in-situ data. Choosing the "best" algorithm is challenging, as performance varies greatly with coastal proximity and sea state. For instance, the LR-RMC UF-SAR retracking algorithm shows the highest precision in the open ocean, but suffers from a greatly reduced number of valid records of ~16.5% within 5 km of the coastline. The statistical STARv2 retracker, which makes use of adjacent estimates, shows the highest similarity to the wave model in the challenging coastal zone, but its along-track power spectral density does not correspond to a realistic global climate.

In general, two main challenges have been identified by P-I: First, the estimation of extreme sea states, as the correlation is strongly reduced for SWH greater than 10 m. Second, the estimation of SWH in the coastal zone is significantly degraded in terms of quality (both accuracy and precision) and number of valid records (outliers).

**Q-II: How can the estimation of coastal wave heights be improved compared to the baseline altimetry product and the state-of-the-art processing schemes?**

P-I showed that the number of valid records is greatly reduced within the coastal zone of less than 20 km. P-II evaluated the retracked SWH estimates of the EUMETSAT baseline L2 product to be of poor quality, while showing a correlation coefficient of 0.41 with an ERA5-based wave model within 5 km of the coast.

The novel CORAL coastal retracking algorithm, presented in P-II, implements the AIM scheme which detects and mitigates spurious coastal interference. This allows a significant improvement in the quality flag to greatly increase the number of valid records in the coastal zone, while maintaining a high quality of SWH estimates. Within 5 km of the coast, CORAL significantly improves the quality of estimates compared to the EUMETSAT baseline L2 product and increases the number of valid records by up to 25% compared to the competing coastal retracker SAMOSA+.

**Q-IIIa: What are the gains of applying the FF-SAR instead of the UF-SAR processing scheme for coastal wave height estimation?**

The case study carried out in P-III has shown that the quality and quantity of the estimates can be further improved by applying FF-SAR altimetry in conjunction with the CORAL retracker. An objective comparison between UF-SAR and different FF-SAR processing schemes was ensured by consistently processing both schemes using the same processing chain with a small modification as elaborated in Section 2.3.3.

With respect to UF-SAR, FF-SAR SWH estimates were found to exhibit lower noise, resulting in higher correlation with the numerical wave model, and provide a higher number of valid records and highly correlated cycles.

**Q-IIIb: How close to the coast can wave heights be estimated by combining FF-SAR processing with a coastal retracking algorithm?**

The closest distance-to-coast (dist-to-coast) from which robust estimates can be obtained depends on the given satellite track. The performance of the estimates in terms of their quality (accuracy and precision) and the number of valid records thus depends on several factors such as the angle of

approach to the coast and the presence of strongly reflective targets within the irradiated footprint such as sandbanks, tidal flats, sheltered bays or calm waters close to the coast.

Nevertheless, the case study in P-III shows that by combining FF-SAR processing with the coastal CORAL retracker and subsequent removal of residual outliers, one can obtain robust high-frequency SWH estimates up to 1 km from the coast. Furthermore, it was shown that it is possible to extract realistic estimates of SWH decay from 30 km offshore to 1 km from the coast for the case study area investigated in the North Sea.

The developed CORAL coastal retracking algorithm represents a novel technique to improve SWH estimation using SAR satellite altimetry data in the coastal zone. As its successful applicability to EUMETSAT Sentinel-6 Michael Freilich (S6-MF) baseline data has been demonstrated in P-III and compared to the baseline L2 product, the algorithm could readily be applied to the EUMETSAT S6-MF baseline processing chain, e.g. to produce an operational coastal altimetry product, which has been discussed for many years (Vignudelli et al. 2009). It is expected that CORAL can be easily extended to future evolutions of the S6-MF UF-SAR baseline processing chain, such as the numerical retracking planned for the F09 baseline in Q3 2023 (Scharroo et al. 2022). An operational coastal FF-SAR product could also be considered and used in conjunction with CORAL, providing additional benefits over UF-SAR in the coastal zone, as shown in P-III. The applicability to Sentinel-3A (S3A) was demonstrated in P-II and the extension to other satellite missions is possible, subject to the availability of a suitable waveform model to be fitted.

Furthermore, more scientific studies could benefit from the FF-SAR processing chain presented in P-III to further exploit the SWH estimates very close to the coast. For example, these could be related to the study of coastal extreme sea states as presented by Timmermans et al. (2020), which have the highest societal impact and are particularly relevant for applications such as coastal defense and safety.

Although the focus of this PhD project and the CORAL algorithm has been on the estimation of SWH, it is expected that the observed performance gains on coastal SWH data achieved by CORAL will also be apparent for the sea surface height (SSH) estimates that can be estimated from the retracked range parameter. In addition to coastal sea level, the applicability of CORAL could be extended to a variety of different scenarios such as inland waters and sea ice, which would also likely benefit from an increased number of valid records.

As part of future work on CORAL and the FF-SAR processing chain, it is suggested that more advanced interference mitigation techniques tailored to FF-SAR processed altimetry data be developed. Suppression of signals from static interfering targets such as sandbanks (as identified in P-III) that may be coming from a particular direction could bring additional benefits from FF-SAR processing. Further improvement in the quality flagging after multilooking at the higher posting rates may provide additional gains in the robustness of the L2 estimates. It is also proposed that the differences between the FF-SAR- and UF-SAR-processed datasets should be investigated in more detail to identify and characterise small-scale nearshore features such as breaking waves or shoaling effects that FF-SAR altimetry may be able to resolve.



# Bibliography

- Abdalla, Saleh et al. (2018). "Assessment of CryoSat-2 SAR Mode Wind and Wave Data". In: *Advances in Space Research* 62.6, pp. 1421–1433. ISSN: 18791948. DOI: 10.1016/j.asr.2018.01.044.
- Abdalla, Saleh et al. (Mar. 2021). "Altimetry for the Future: Building on 25 Years of Progress". In: *Advances in Space Research*. DOI: 10.1016/j.asr.2021.01.022.
- Ablain, Michaël et al. (2006). "High Resolution Altimetry Reveals New Characteristics of the December 2004 Indian Ocean Tsunami". In: *Geophysical Research Letters* 33.21. ISSN: 1944-8007. DOI: 10.1029/2006GL027533.
- Altiparmaki, Ourania et al. (2022). "SAR Altimetry Data as a New Source for Swell Monitoring". In: *Geophysical Research Letters* n/a.n/a, e2021GL096224. ISSN: 1944-8007. DOI: 10.1029/2021GL096224.
- Amarouche, L. et al. (2004). "Improving the Jason-1 Ground Retracking to Better Account for Attitude Effects". In: *Marine Geodesy* 27.1-2, pp. 171–197. ISSN: 01490419. DOI: 10.1080/01490410490465210.
- Amraoui, S. and Moreau, T. (Nov. 2021). "Benefits of Using Fast Fully Focused SAR Processing over Different Surfaces and Potential Applications". In: *Sentinel-6 Validation Team (S6VT) Meeting #3*.
- Ardhuin, Fabrice et al. (2019). "Observing Sea States". In: *Frontiers in Marine Science* 6. ISSN: 2296-7745. DOI: 10.3389/fmars.2019.00124.
- Arens, Sebastiaan M. et al. (Oct. 2013). "Dynamic Dune Management, Integrating Objectives of Nature Development and Coastal Safety: Examples from the Netherlands". In: *Geomorphology. Coastal Geomorphology and Restoration 44th Binghamton Geomorphology Symposium* 199, pp. 205–213. ISSN: 0169-555X. DOI: 10.1016/j.geomorph.2012.10.034.
- Aublanc, J. et al. (2022). "Assessment of the Sentinel-3 Fully Focused SAR Processing over the Antarctic Ice Sheet". In: *Living Planet Symposium*.
- Aviso+ (Dec. 2022). *Techniques: Altimetry*. <https://www.aviso.altimetry.fr/en/techniques/altimetry.html>.
- Barrick, D. (Sept. 1972). "Remote Sensing of Sea State by Radar". In: *Ocean 72 - IEEE International Conference on Engineering in the Ocean Environment*, pp. 186–192. DOI: 10.1109/OCEANS.1972.1161190.
- Barrick, Donald E. and Lipa, Belinda J. (Jan. 1985). "Chapter 3 Analysis and Interpretation of Altimeter Sea Echo". In: *Advances in Geophysics*. Ed. by Barry Saltzman. Vol. 27. Satellite Oceanic Remote Sensing. Elsevier, pp. 61–100. DOI: 10.1016/S0065-2687(08)60403-3.
- Berger, T. (May 1972). "Satellite Altimetry Using Ocean Backscatter". In: *IEEE Transactions on Antennas and Propagation* 20.3, pp. 295–309. ISSN: 1558-2221. DOI: 10.1109/TAP.1972.1140196.
- Bouma, Tjeerd J. et al. (May 2014). "Identifying Knowledge Gaps Hampering Application of Intertidal Habitats in Coastal Protection: Opportunities & Steps to Take". In: *Coastal Engineering. Coasts@Risks: THESEUS, a New Wave in Coastal Protection* 87, pp. 147–157. ISSN: 0378-3839. DOI: 10.1016/j.coastaleng.2013.11.014.
- Boy, François and Picot, Nicolas (2013). *Algorithm Theoretical Basis Document (ATBD) of the CPP SAR Numerical Retracker for Oceans*. Tech. rep. Technical Report S3A-NT-SRAL-00099-CNES ESA.; <http://www.satoc.eu/projects...>
- Branch, Mary Ann, Coleman, Thomas F., and Li, Yuying (Jan. 1999). "A Subspace, Interior, and Conjugate Gradient Method for Large-Scale Bound-Constrained Minimization Problems". In: *SIAM Journal on Scientific Computing* 21.1, pp. 1–23. ISSN: 1064-8275. DOI: 10.1137/S1064827595289108.
- Brewin, Bob et al. (June 2015). "The Ocean Colour Climate Change Initiative: III. A Round-Robin Comparison on in-Water Bio-Optical Algorithms". In: *Remote Sensing of Environment* 162. DOI: 10.1016/j.rse.2013.09.016.
- Brown, G. (Jan. 1977). "The Average Impulse Response of a Rough Surface and Its Applications". In: *IEEE Journal of Oceanic Engineering* 2.1, pp. 67–74. ISSN: 1558-1691. DOI: 10.1109/JOE.1977.1145328.

- Brown, G.S. (June 1989). "A Useful Approximation for the Flat Surface Impulse Response". In: *IEEE Transactions on Antennas and Propagation* 37.6, pp. 764–767. ISSN: 1558-2221. DOI: 10.1109/8.29363.
- Bryan, Karin R. and Power, Hannah E. (Jan. 2020). "4 - Wave Behaviour Outside the Surf Zone". In: *Sandy Beach Morphodynamics*. Ed. by Derek W. T. Jackson and Andrew D. Short. Elsevier, pp. 61–86. ISBN: 978-0-08-102927-5. DOI: 10.1016/B978-0-08-102927-5.00004-7.
- Buchhaupt, Christopher (Jan. 2019). "Model Improvement for SAR Altimetry". PhD thesis. Darmstadt: Schriftenreihe Fachrichtung Geodäsie der Technischen Universität Darmstadt.
- Caputi, William J. (Mar. 1971). "Stretch: A Time-Transformation Technique". In: *IEEE Transactions on Aerospace and Electronic Systems* AES-7.2, pp. 269–278. ISSN: 1557-9603. DOI: 10.1109/TAES.1971.310366.
- Cavaleri, L., Fox-Kemper, B., and Hemer, M. (Nov. 2012). "Wind Waves in the Coupled Climate System". In: *Bulletin of the American Meteorological Society* 93.11, pp. 1651–1661. DOI: 10.1175/BAMS-D-11-00170.1.
- Cazenave, Anny, Palanisamy, Hindumathi, and Ablain, Michael (Oct. 2018). "Contemporary Sea Level Changes from Satellite Altimetry: What Have We Learned? What Are the New Challenges?" In: *Advances in Space Research* 62.7, pp. 1639–1653. ISSN: 0273-1177. DOI: 10.1016/j.asr.2018.07.017.
- Cazenave, Anny et al. (2014). "The Rate of Sea-Level Rise". In: *Nature Climate Change* 4.5, pp. 358–361. ISSN: 17586798. DOI: 10.1038/nclimate2159.
- Charlier, Roger H., Chaineux, Marie Claire P., and Morcos, Selim (Jan. 2005). "Panorama of the History of Coastal Protection". In: *Journal of Coastal Research* 21.1 (211), pp. 79–111. ISSN: 0749-0208. DOI: 10.2112/03561.1.
- Chelton, Dudley B. et al. (June 1989). "Pulse Compression and Sea Level Tracking in Satellite Altimetry". In: *Journal of Atmospheric and Oceanic Technology* 6.3, pp. 407–438. ISSN: 0739-0572. DOI: 10.1175/1520-0426(1989)006<0407:PCASLT>2.0.CO;2.
- Chelton, Dudley B. et al. (2001). "Chapter 1 Satellite Altimetry". In: *International Geophysics*. Vol. 69. Elsevier, pp. 1–ii. ISBN: 978-0-12-269545-2. DOI: 10.1016/S0074-6142(01)80146-7.
- Chowdhury, Piyali and Behera, Manasa Ranjan (Aug. 2017). "Effect of Long-Term Wave Climate Variability on Longshore Sediment Transport along Regional Coastlines". In: *Progress in Oceanography* 156, pp. 145–153. ISSN: 0079-6611. DOI: 10.1016/j.pocan.2017.06.001.
- Cipollini, Paolo et al. (2009). "The Role of Altimetry in Coastal Observing Systems". In: *Proceedings of OceanObs'09: Sustained Ocean Observations and Information for Society*. DOI: 10.5270/OceanObs09.cw p.16.
- Cipollini, Paolo et al. (2012). "Conquering the Coastal Zone: A New Frontier for Satellite Altimetry". In: *20 Years of Progress in Radar Altimetry* 1, pp. 3–7.
- Contardo, Stephanie et al. (Oct. 2018). "In Situ Observations and Simulations of Coastal Wave Field Transformation by Wave Energy Converters". In: *Coastal Engineering* 140, pp. 175–188. ISSN: 0378-3839. DOI: 10.1016/j.coastaleng.2018.07.008.
- de Vries, Sierd, Wengrove, Meagan, and Bosboom, Judith (Jan. 2020). "9 - Marine Sediment Transport". In: *Sandy Beach Morphodynamics*. Ed. by Derek W. T. Jackson and Andrew D. Short. Elsevier, pp. 187–212. ISBN: 978-0-08-102927-5. DOI: 10.1016/B978-0-08-102927-5.00009-6.
- Dijkstra, E. W. (July 2022). "A Note on Two Problems in Connexion with Graphs". In: *Edsger Wybe Dijkstra: His Life, Work, and Legacy*. 1st ed. Vol. 45. New York, NY, USA: Association for Computing Machinery, pp. 287–290. ISBN: 978-1-4503-9773-5.
- Dinardo, S., Scharroo, R., and Benveniste, J. (2015). "SAR Altimetry at 80 Hz: Open Sea, Coastal Zone, Inland Water". In: *Ocean Surface Topography Science Team Meeting*.
- Dinardo, Salvatore (Jan. 2020). "Techniques and Applications for Satellite SAR Altimetry over Water, Land and Ice". PhD thesis. Darmstadt: Technische Universität.
- Dinardo, Salvatore et al. (Sept. 2018). "Coastal SAR and PLRM Altimetry in German Bight and West Baltic Sea". In: *Advances in Space Research* 62, pp. 1371–1404. ISSN: 0273-1177. DOI: 10.1016/j.asr.2017.12.018.

- Dinardo, Salvatore et al. (June 2020). "A RIP-based SAR Retracker and Its Application in North East Atlantic with Sentinel-3". In: *Advances in Space Research*. ISSN: 0273-1177. DOI: 10.1016/j.asr.2020.06.004.
- Dodet, G. et al. (2018). "Wave Runup Over Steep Rocky Cliffs". In: *Journal of Geophysical Research: Oceans* 123.10, pp. 7185–7205. ISSN: 2169-9291. DOI: 10.1029/2018JC013967.
- Dodet, Guillaume et al. (Sept. 2020). "The Sea State CCI Dataset v1: Towards a Sea State Climate Data Record Based on Satellite Observations". In: *Earth System Science Data* 12.3, pp. 1929–1951. ISSN: 1866-3508. DOI: 10.5194/essd-12-1929-2020.
- Donlon, C. et al. (July 2012). "The Sentinel-3 Mission: Overview and Status". In: *2012 IEEE International Geoscience and Remote Sensing Symposium*, pp. 1711–1714. DOI: 10.1109/IGARSS.2012.6351194.
- Donlon, Craig et al. (June 2021). "The Copernicus Sentinel-6 Mission: Enhanced Continuity of Satellite Sea Level Measurements from Space". In: *Remote Sensing of Environment* 258, p. 112395. ISSN: 0034-4257. DOI: 10.1016/j.rse.2021.112395.
- Dumont, Jean-Paul (1985). "Estimation Optimale Des Paramètres Altimétriques Des Signaux Radar" POSEIDON". PhD thesis.
- Egido, A. and Ray, C. (2019). "On the Effect of Surface Motion in SAR Altimeter Observations of the Open Ocean". In: *Ocean Surface Topography Science Team (OSTST) meeting*.
- Egido, Alejandro, Dinardo, Salvatore, and Ray, Christopher (Mar. 2020). "The Case for Increasing the Posting Rate in Delay/Doppler Altimeters". In: *Advances in Space Research*. ISSN: 0273-1177. DOI: 10.1016/j.asr.2020.03.014.
- Egido, Alejandro and Smith, Walter H. F. (2017). "Fully Focused SAR Altimetry: Theory and Applications". In: *IEEE Transactions on Geoscience and Remote Sensing* 55.1, pp. 392–406. ISSN: 1558-0644. DOI: 10.1109/TGRS.2016.2607122.
- (May 2019). "Pulse-to-Pulse Correlation Effects in High PRF Low-Resolution Mode Altimeters". In: *IEEE Transactions on Geoscience and Remote Sensing* 57.5, pp. 2610–2617. ISSN: 1558-0644. DOI: 10.1109/TGRS.2018.2875622.
- Ehlers, Frithjof et al. (Nov. 2022). "Validity Assessment of SAMOSA Retracking for Fully-Focused SAR Altimeter Waveforms". In: *Advances in Space Research*. ISSN: 0273-1177. DOI: 10.1016/j.asr.2022.11.034.
- Elfrink, Berry and Baldock, Tom (May 2002). "Hydrodynamics and Sediment Transport in the Swash Zone: A Review and Perspectives". In: *Coastal Engineering. Surface and Swash Zone Mechanics* 45.3, pp. 149–167. ISSN: 0378-3839. DOI: 10.1016/S0378-3839(02)00032-7.
- ESA (2011). *Sea Surface Temperature Project: Round Robin (Algorithm Comparison)*. <http://www.esa-sst-cci.org/?q=round%20robin>.
- (2012). *Soil Moisture Project: Round Robin Exercise*. <https://www.esa-soilmoisture-cci.org/node/122>.
- (June 2019). *SCOOP Project: Algorithm Theoretical Basis Document (ATBD), D1.3*. [http://www.satoc.eu/projects/SCOOP/docs/SCOOP\\_D1.3\\_ATBD\\_v17.pdf](http://www.satoc.eu/projects/SCOOP/docs/SCOOP_D1.3_ATBD_v17.pdf).
- (2021). *Sentinel-6 L2 GPP Project (European Space Agency Noordwijk, The Netherlands)*. Tech. rep.
- (June 2022a). *Copernicus Sentinel-3 Next Generation Topography (S3NG-T), Mission Requirements Document (MRD), v0.41, Draft as of 14.06.2022, ESA, Noordwijk, The Netherlands*.
- (2022b). *ESA Sea State CCI Project*. <http://cci.esa.int/seastate>.
- (Dec. 2022c). *Sentinel-3 PDGS: Payload Data Ground Segment*. <https://sentinel.esa.int/web/sentinel/missions/sentinel-3/ground-segment/core-ground-segment/pdgs>.
- (Feb. 2023a). *CryoSat Earth Online*. <https://earth.esa.int/eogateway/missions/cryosat>.
- (Feb. 2023b). *Sentinel-3 - Sentinel Online*. <https://sentinel.esa.int/web/sentinel/missions/sentinel-3>.
- EUMETSAT (2022a). *Sentinel-6 Payload Data Processing (PDP) Processing Baseline F06 - Product Notice*. <https://www.eumetsat.int/media/48237>.
- (2022b). *Sentinel-6/Jason-CS ALT Level 1 Product Generation Specification (L1 ALT PGS), Version v4D*. Tech. rep.

- EUMETSAT (2022c). *Sentinel-6/Jason-CS ALT Level 2 Product Generation Specification (L2 ALT PGS), Version v4D*. Tech. rep.
- Fenoglio-Marc, L. et al. (2010). "Coastal Sea Surface Heights from Improved Altimeter Data in the Mediterranean Sea". In: *International Association of Geodesy Symposia* 135. June 2008, pp. 253–261. ISSN: 09399585. DOI: 10.1007/978-3-642-10634-7\\_33.
- Ferreira, Ó. et al. (2009). "Coastal Storm Risk Assessment in Europe: Examples from 9 Study Sites". In: *Journal of Coastal Research*, pp. 1632–1636. ISSN: 0749-0208. JSTOR: 25738066.
- Fu, Lee-Lueng et al. (1994). "TOPEX/POSEIDON Mission Overview". In: *Journal of Geophysical Research: Oceans* 99.C12, pp. 24369–24381. ISSN: 2156-2202. DOI: 10.1029/94JC01761.
- Garcia, Emmanuel S., Sandwell, David T., and Smith, Walter H.F. (2014). "Retracking Cryosat-2, Envisat and Jason-1 Radar Altimetry Waveforms for Improved Gravity Field Recovery". In: *Geophysical Journal International* 196.3, pp. 1402–1422. ISSN: 0956540X. DOI: 10.1093/gji/ggt469.
- Glavovic, B.C et al. (2022). "Cross-Chapter Paper 2: Cities and Settlements by the Sea. In: *Climate Change 2022: Impacts, Adaptation and Vulnerability. Contribution of Working Group II to the Sixth Assessment Report of the Intergovernmental Panel on Climate Change*". In: *Cambridge University Press, Cambridge, UK and New York, NY, USA*, pp. 2163–2194. DOI: 10.1017/9781009325844.019..
- Gomez-Enri, Jesus et al. (2016). "Coastal Altimetry Products in the Strait of Gibraltar". In: *IEEE Transactions on Geoscience and Remote Sensing* 54.9, pp. 5455–5466. ISSN: 01962892. DOI: 10.1109/TGRS.2016.2565472.
- Gómez-Enri, Jesús et al. (2010). "Modeling Envisat RA-2 Waveforms in the Coastal Zone: Case Study of Calm Water Contamination". In: *IEEE Geoscience and Remote Sensing Letters* 7.3, pp. 474–478. ISSN: 1545598X. DOI: 10.1109/LGRS.2009.2039193.
- Gommenginger, Christine et al. (2010). "Development of SAR Altimetry Mode Studies and Applications over Ocean , Coastal Zones and Inland Water ( SAMOSA ) Detailed Processing Model of the Sentinel-3 SRAL SAR Altimeter Ocean Waveform Retracker National Oceanography Centre , Southampton". In: *Contract* 44.20698.
- Gommenginger, Christine et al. (Nov. 2013). *Review of State of Knowledge for SAR Altimetry over Ocean. Report of the EUMETSAT JASON-CS SAR Mode Error Budget Study*. <https://eprints.soton.ac.uk/366765/>. Monograph.
- Gou, Junyang and Tourian, Mohammad J. (Dec. 2021). "RiwiSAR-SWH: A Data-Driven Method for Estimating Significant Wave Height Using Sentinel-3 SAR Altimetry". In: *Advances in Space Research*. ISSN: 0273-1177. DOI: 10.1016/j.asr.2021.12.019.
- Guccione, Pietro (Sept. 2008). "Beam Sharpening of Delay/Doppler Altimeter Data Through Chirp Zeta Transform". In: *IEEE Transactions on Geoscience and Remote Sensing* 46.9, pp. 2517–2526. ISSN: 1558-0644. DOI: 10.1109/TGRS.2008.918863.
- Guccione, Pietro, Scagliola, Michele, and Giudici, Davide (Dec. 2018). "2D Frequency Domain Fully Focused SAR Processing for High PRF Radar Altimeters". In: *Remote Sensing* 10.12, p. 1943. DOI: 10.3390/rs10121943.
- Halimi, Abderrahim et al. (July 2014). "A Semi-Analytical Model for Delay/Doppler Altimetry and Its Estimation Algorithm". In: *IEEE Transactions on Geoscience and Remote Sensing* vol. 52, pp. 4248–4258. DOI: 10.1109/TGRS.2013.2280595.
- Hayne, G. (Sept. 1980). "Radar Altimeter Mean Return Waveforms from Near-Normal-Incidence Ocean Surface Scattering". In: *IEEE Transactions on Antennas and Propagation* 28.5, pp. 687–692. ISSN: 1558-2221. DOI: 10.1109/TAP.1980.1142398.
- Hersbach, Hans et al. (2020). "The ERA5 Global Reanalysis". In: *Quarterly Journal of the Royal Meteorological Society* 146.730, pp. 1999–2049. ISSN: 1477-870X. DOI: 10.1002/qj.3803.
- Holthuijsen, Leo H. (2007). *Waves in Oceanic and Coastal Waters*. Cambridge: Cambridge University Press. ISBN: 978-0-521-12995-4. DOI: 10.1017/CBO9780511618536.
- Janssen, Peter AEM et al. (2013). *Air-Sea Interaction and Surface Waves*. European Centre for Medium-Range Weather Forecasts Reading, UK.

- Kleinherenbrink, Marcel et al. (Feb. 2020). "The Performance of CryoSat-2 Fully-Focussed SAR for Inland Water-Level Estimation". In: *Remote Sensing of Environment* 237, p. 111589. ISSN: 0034-4257. DOI: 10.1016/j.rse.2019.111589.
- Le Roy, Y. et al. (July 2009). "SRAL, a Radar Altimeter Designed to Measure a Wide Range of Surface Types". In: *2009 IEEE International Geoscience and Remote Sensing Symposium*. Vol. 5, pp. V-445-V-448. DOI: 10.1109/IGARSS.2009.5417636.
- Le Traon, Pierre Yves et al. (2019). "From Observation to Information and Users: The Copernicus Marine Service Perspective". In: *Frontiers in Marine Science* 6. ISSN: 2296-7745.
- Legeais, Jean-François et al. (Feb. 2018). "An Improved and Homogeneous Altimeter Sea Level Record from the ESA Climate Change Initiative". In: *Earth System Science Data* 10.1, pp. 281–301. ISSN: 1866-3508. DOI: 10.5194/essd-10-281-2018.
- Levanon, Nadav and Mozeson, Eli (2004). *Radar Signals*. John Wiley & Sons.
- Lippmann, T. C., Brookins, A. H., and Thornton, E. B. (May 1996). "Wave Energy Transformation on Natural Profiles". In: *Coastal Engineering* 27.1, pp. 1–20. ISSN: 0378-3839. DOI: 10.1016/0378-3839(95)00036-4.
- MacArthur, J. (Sept. 1976). "Design of the SEASAT-A Radar Altimeter". In: *OCEANS '76*, pp. 222–229. DOI: 10.1109/OCEANS.1976.1154217.
- Madsen, Kristine S. et al. (2015). "Blending of Satellite and Tide Gauge Sea Level Observations and Its Assimilation in a Storm Surge Model of the North Sea and Baltic Sea". In: *Journal of Geophysical Research: Oceans* 120.9, pp. 6405–6418. ISSN: 2169-9291. DOI: 10.1002/2015JC011070.
- McMillan, M, Egido, A, and Muir, AS (2020). "First Assessment of Fully Focused SAR Altimetry over Ice Sheets". In: *AGU Fall Meeting Abstracts*. Vol. 2020, C034–07W.
- Melville, W K (1996). "The Role of Surface-Wave Breaking in Air-Sea Interaction". In: *Annual Review of Fluid Mechanics* 28.1, pp. 279–321. DOI: 10.1146/annurev.fl.28.010196.001431.
- Moore, R. K. and Williams, C. S. (Feb. 1957). "Radar Terrain Return at Near-Vertical Incidence". In: *Proceedings of the IRE* 45.2, pp. 228–238. ISSN: 2162-6634. DOI: 10.1109/JRPROC.1957.278394.
- Moré, Jorge J. (1978). "The Levenberg-Marquardt Algorithm: Implementation and Theory". In: *Numerical Analysis*. Ed. by G. A. Watson. Lecture Notes in Mathematics. Berlin, Heidelberg: Springer, pp. 105–116. ISBN: 978-3-540-35972-2. DOI: 10.1007/BFb0067700.
- Moreau, T., Rieu, P., and Aublanc, J. (2017). "Investigation of SWH Bias in SAR Altimetry Mode". In: *Ocean Surface Topography Science Team (OSTST) meeting*.
- Moreau, T. et al. (2018). "Impact of Long Ocean Waves on Wave Height Retrieval from SAR Altimetry Data". In: *Advances in Space Research* 62.6, pp. 1434–1444. ISSN: 18791948. DOI: 10.1016/j.asr.2018.06.004.
- Nielsen, Karina et al. (June 2021). *A New Fully-Focused SAR Altimetry Processor in the ESA G-POD SARvatore Family: Validation and Applications on Inland Waters*. DOI: 10.13140/RG.2.2.28915.40485.
- Passaro, Marcello et al. (2014). "ALES: A Multi-Mission Adaptive Subwaveform Retracker for Coastal and Open Ocean Altimetry". In: *Remote Sensing of Environment* 145, pp. 173–189. ISSN: 00344257. DOI: 10.1016/j.rse.2014.02.008.
- Passaro, Marcello et al. (2018). "ALES+: Adapting a Homogenous Ocean Retracker for Satellite Altimetry to Sea Ice Leads, Coastal and Inland Waters". In: *Remote Sensing of Environment* 211. February, pp. 456–471. ISSN: 00344257. DOI: 10.1016/j.rse.2018.02.074.
- Passaro, Marcello et al. (June 2021). "Global Coastal Attenuation of Wind-Waves Observed with Radar Altimetry". In: *Nature Communications* 12.1, p. 3812. ISSN: 2041-1723. DOI: 10.1038/s41467-021-23982-4.
- Peng, Fukai and Deng, Xiaoli (July 2018). "Validation of Improved Significant Wave Heights from the Brown-Peaky (BP) Retracker along the East Coast of Australia". In: *Remote Sensing* 10.7, p. 1072. DOI: 10.3390/rs10071072.
- Phalippou, L. and Enjolras, V. (July 2007). "Re-Tracking of SAR Altimeter Ocean Power-Waveforms and Related Accuracies of the Retrieved Sea Surface Height, Significant Wave Height and Wind

- Speed". In: *2007 IEEE International Geoscience and Remote Sensing Symposium*, pp. 3533–3536. DOI: 10.1109/IGARSS.2007.4423608.
- Piccioni, Gaia (2021). "Exploit Satellite Altimetry to Improve Coastal Tide Estimation". PhD thesis. Technische Universität München.
- Pilarczyk, Krystian W., ed. (1990). *Coastal Protection: Proceedings of the Short Course on Coastal Protection, Delft University of Technology, 30 June - 1 July 1990*. Rotterdam: Balkema. ISBN: 978-90-6191-127-2.
- Power, Hannah E. (Jan. 2020). "6 - Breaking Waves". In: *Sandy Beach Morphodynamics*. Ed. by Derek W. T. Jackson and Andrew D. Short. Elsevier, pp. 103–130. ISBN: 978-0-08-102927-5. DOI: 10.1016/B978-0-08-102927-5.00006-0.
- Quartly, G. D., Srokosz, M. A., and McMillan, A. C. (Dec. 2001). "Analyzing Altimeter Artifacts: Statistical Properties of Ocean Waveforms". In: *Journal of Atmospheric and Oceanic Technology* 18.12, pp. 2074–2091. ISSN: 0739-0572. DOI: 10.1175/1520-0426(2001)018<2074:AAASPO>2.0.CO;2.
- Quartly, Graham D. et al. (Jan. 2021). "An Overview of Requirements, Procedures and Current Advances in the Calibration/Validation of Radar Altimeters". In: *Remote Sensing* 13.1, p. 125. ISSN: 2072-4292. DOI: 10.3390/rs13010125.
- Raney, R.K. (Sept. 1998). "The Delay/Doppler Radar Altimeter". In: *IEEE Transactions on Geoscience and Remote Sensing* 36.5, pp. 1578–1588. ISSN: 1558-0644. DOI: 10.1109/36.718861.
- Ray, Chris et al. (2015). "SAR Altimeter Backscattered Waveform Model". In: *IEEE Transactions on Geoscience and Remote Sensing* 53.2, pp. 911–919. ISSN: 01962892. DOI: 10.1109/TGRS.2014.2330423.
- Raynal, M., Moreau, T., and Tran, N. (2018). "Assessment of the SARM Processing Sensitivity to Swell". In: *Ocean Surface Topography Science Team (OSTST) meeting*.
- Ribal, Agustinus and Young, Ian R. (May 2019). "33 Years of Globally Calibrated Wave Height and Wind Speed Data Based on Altimeter Observations". In: *Scientific Data* 6.1, p. 77. ISSN: 2052-4463. DOI: 10.1038/s41597-019-0083-9.
- Richards, M.A. (2005). *Fundamentals of Radar Signal Processing*. Professional Engineering. McGraw-Hill Education. ISBN: 978-0-07-177648-6.
- Rodriguez, E. and Martin, J.M. (May 1994). "Correlation Properties of Ocean Altimeter Returns". In: *IEEE Transactions on Geoscience and Remote Sensing* 32.3, pp. 553–561. ISSN: 1558-0644. DOI: 10.1109/36.297974.
- Roscher, Ribana, Uebbing, Bernd, and Kusche, Jürgen (2017). "STAR: Spatio-temporal Altimeter Waveform Retracking Using Sparse Representation and Conditional Random Fields". In: *Remote Sensing of Environment* 201, pp. 148–164. ISSN: 00344257. DOI: 10.1016/j.rse.2017.07.024.
- Rosmorduc, V. et al. (Sept. 2011). *Radar Altimetry Tutorial*.
- Sajjad, Muhammad and Chan, Johnny C. L. (June 2019). "Risk Assessment for the Sustainability of Coastal Communities: A Preliminary Study". In: *Science of The Total Environment* 671, pp. 339–350. ISSN: 0048-9697. DOI: 10.1016/j.scitotenv.2019.03.326.
- Scagliola, Michele et al. (2021). "Evaluating the Impact of Range Walk Compensation in Delay/Doppler Processing over Open Ocean". In: *Advances in Space Research. 25 Years of Progress in Radar Altimetry* 68.2, pp. 937–946. ISSN: 0273-1177. DOI: 10.1016/j.asr.2019.11.032.
- Scharroo, R (2014). "RADS RDSAR Algorithm Theoretical Basis Document, Version 0.3". In: *CP4O ESA Project Report. SatOC*. URL [http://www.satoc.eu/projects/CP4O/docs/tud\\_rdsar\\_atbd.pdf](http://www.satoc.eu/projects/CP4O/docs/tud_rdsar_atbd.pdf).
- Scharroo, R. et al. (2022). "Sentinel-6 Products Status". In: *Ocean Surface Topography Science Team (OSTST) meeting in Venice*. DOI: 10.24400/527896/a03-2022.3671.
- Scharroo, Remko, Smith, Walter H F, and Lillibrige, John L (2005). "The Intensification of Hurricane Katrina Observed by Satellite Altimetry". In: *Eos* 86(40).40, p. 366. DOI: 10.1029/2005EO400004.
- Schlembach, Florian et al. (Jan. 2020). "Round Robin Assessment of Radar Altimeter Low Resolution Mode and Delay-Doppler Retracking Algorithms for Significant Wave Height". In: *Remote Sensing* 12.8. DOI: 10.3390/rs12081254.
- Schlembach, Florian et al. (Mar. 2022). "Interference-Sensitive Coastal SAR Altimetry Retracking Strategy for Measuring Significant Wave Height". In: *Remote Sensing of Environment* 274, p. 112968. ISSN: 0034-4257. DOI: 10.1016/j.rse.2022.112968.

- Schlembach, Florian et al. (May 2023). "Benefits of Fully Focused SAR Altimetry to Coastal Wave Height Estimates: A Case Study in the North Sea". In: *Remote Sensing of Environment* 289, p. 113517. ISSN: 0034-4257. DOI: 10.1016/j.rse.2023.113517.
- Silvester, Richard and Hsu, John RC (1997). *Coastal Stabilization*. Vol. 14. World Scientific Singapore.
- Smith, Walter H.F. and Scharroo, Remko (2015). "Waveform Aliasing in Satellite Radar Altimetry". In: *IEEE Transactions on Geoscience and Remote Sensing* 53.4, pp. 1671–1682. ISSN: 01962892. DOI: 10.1109/TGRS.2014.2331193.
- Stopa, Justin E., Arduin, Fabrice, and Girard-Arduin, Fanny (July 2016). "Wave Climate in the Arctic 1992–2014: Seasonality and Trends". In: *The Cryosphere* 10.4, pp. 1605–1629. ISSN: 1994-0416. DOI: 10.5194/tc-10-1605-2016.
- Thibaut, P. et al. (Aug. 2010). "Relative Performance of the MLE3 and MLE4 Retracking Algorithms on Jason-2 Altimeter Waveforms". In: *Marine Geodesy* 33.sup1, pp. 317–335. ISSN: 0149-0419. DOI: 10.1080/01490419.2010.491033.
- Timmermans, Ben, Shaw, Andrew G. P., and Gommenginger, Christine (Dec. 2020). "Reliability of Extreme Significant Wave Height Estimation from Satellite Altimetry and In Situ Measurements in the Coastal Zone". In: *Journal of Marine Science and Engineering* 8.12, p. 1039. DOI: 10.3390/jmse8121039.
- Tsou, Ming-Cheng and Cheng, Hung-Chih (2013). "An Ant Colony Algorithm for Efficient Ship Routing". In: *Polish Maritime Research* 20.3, pp. 28–38.
- Vignudelli, Stefano et al. (Oct. 2009). "The COASTALT Project: Towards an Operational Use of Satellite Altimetry in the Coastal Zone". In: *OCEANS 2009*, pp. 1–6. DOI: 10.23919/OCEANS.2009.5422467.
- Vignudelli, Stefano et al. (2011). *Coastal Altimetry*. ISBN: 978-3-642-12795-3. DOI: 10.1007/978-3-642-12796-0.
- Walsh, Edward J. (1982). "Pulse-to-Pulse Correlation in Satellite Radar Altimeters". In: *Radio Science* 17.4, pp. 786–800. ISSN: 1944-799X. DOI: 10.1029/RS017i004p00786.
- Wang, Ping and Kraus, Nicholas C. (May 2005). "Beach Profile Equilibrium and Patterns of Wave Decay and Energy Dissipation across the Surf Zone Elucidated in a Large-Scale Laboratory Experiment". In: *Journal of Coastal Research* 2005.213, pp. 522–534. ISSN: 0749-0208, 1551-5036. DOI: 10.2112/03-003.1.
- Wang, Xifeng and Ichikawa, Kaoru (2017). "Coastal Waveform Retracking for Jason-2 Altimeter Data Based on along-Track Echograms around the Tsushima Islands in Japan". In: *Remote Sensing* 9.7. ISSN: 20724292. DOI: 10.3390/rs9070762.
- Wingham, D. J. et al. (Oct. 2004). "The Mean Echo and Echo Cross Product from a Beamforming Interferometric Altimeter and Their Application to Elevation Measurement". In: *IEEE Transactions on Geoscience and Remote Sensing* 42.10, pp. 2305–2323. ISSN: 1558-0644. DOI: 10.1109/TGRS.2004.834352.
- Wright, L. D. (1976). "Nearshore Wave-Power Dissipation and the Coastal Energy Regime of the Sydney-Jervis Bay Region, New South Wales: A Comparison". In: *Marine and Freshwater Research* 27.4, pp. 633–640. ISSN: 1448-6059. DOI: 10.1071/mf9760633.
- Zaccone, Raphael, Figari, Massimo, and Martelli, Michele (2018). "An Optimization Tool for Ship Route Planning in Real Weather Scenarios". In: *The 28th International Ocean and Polar Engineering Conference*. OnePetro.

# Acronyms

**AIM** adaptive interference masking  
**ALES** adaptive leading edge subwaveform

**BH** Brown-Hayne

**CCI** Climate Change Initiative

**CMEMS** Copernicus Marine Environment Monitoring Service

**CNES** National Centre for Space Studies

**CORAL** COastal Retracker for SAR ALtimetry

**CS2** CryoSat-2

**DDA** delay-Doppler altimetry

**dist-to-coast** distance-to-coast

**DPM** detailed processing model

**ECV** essential climate variable

**ESA** European Space Agency

**EUMETSAT** European Organisation for the Exploitation of Meteorological Satellites

**FF-SAR** fully focused synthetic aperture radar

**FFT** fast Fourier transform

**FG** first-guess

**FSIR** flat-surface impulse response

**GMSL** global mean sea level

**HR** high-resolution

**J1** Jason-1

**J2** Jason-2

**J3** Jason-3

**L1a** Level-1a

**L1b** Level-1b

**L2** Level-2

**LE** leading edge

**LRM** low resolution mode

**LUT** look-up table

**MSL** mean sea level

**NASA** National Aeronautics and Space Administration

**PDF** probability density function

**PDGS** payload data ground segment

**PGS** product generation specification

**PLRM** pseudo low resolution mode

**PRF** pulse repetition frequency

**PSD** power spectral density

**PTR** point target response

**RCMC** range cell migration correction

**RDSAR** reduced SAR

**RF** radio frequency

**RIP** range integrated power

**RMC** range migration correction

**RMS** root mean square

**RR** round robin

**RRP** residual range phase

**RVP** residual video phase

**S3** Sentinel-3

**S3A** Sentinel-3A

**S3NG-T** Copernicus Sentinel-3 Next Generation Topography

**S6-MF** Sentinel-6 Michael Freilich

**SAMOS** SAR Altimetry MOde Studies and Applications

**SAR** synthetic aperture radar

**SARM** synthetic aperture radar mode

**SeaState\_cci** Sea State Climate Change Initiative

**SIRAL** SAR interferometric radar altimeter

**SNR** signal-to-noise ratio

**SRAL** SAR radar altimeter

**SSH** sea surface height

**SWH** significant wave height

**TRR** trust region reflective

**UF-SAR** unfocused synthetic aperture radar

**WLS** weighted least squares



## List of Figures

1.1	Structure of this PhD project. . . . .	4
2.1	Diagram of satellite altimetry's measurement principle. . . . .	5
2.2	Timeline of modern satellite altimetry missions. . . . .	7
2.3	Comparison of the different footprints. . . . .	10
2.4	Evolution of LRM footprint over time. . . . .	10
2.5	Theoretical LRM waveform model. . . . .	14
2.6	Comparison of the satellite altimeters chronograms. . . . .	15
2.7	SAR altimetry processing chain and corresponding data levels. . . . .	16
2.8	Block diagram of UF-SAR altimetry L1b processing scheme. . . . .	17
2.9	Azimuth processing and beam stacking. . . . .	18
2.10	Stacked beams with slant range correction. . . . .	19
2.11	Schematic view of the LRM and SARM footprints and the waveforms. . . . .	21
2.12	Block diagram of FF-SAR altimetry L1b processing scheme. . . . .	23
2.13	Flat-phase calibration of S6-MF. . . . .	26
2.14	FF-SAR 2D-PTRs of the Crete transponder overpass. . . . .	28
3.1	Normalised, modelled, multilooked SAMOSA2 waveform. . . . .	31
3.2	Retracked, multilooked UF-SAR waveforms with SAMOSA-based retracker. . . . .	32

## List of Tables

2.1	General mission parameters of (selected) satellite altimetry missions. The most relevant missions to this PhD project are written in bold-faced. The given pulse repetition frequency (PRF) refers to Ku-band. . . . .	8
4.1	Own contribution to publication P-I . . . . .	36
5.1	Own contribution to publication P-II . . . . .	38
6.1	Own contribution to publication P-III . . . . .	41

# Acknowledgement

Completing this PhD project has been an incredible journey that would not have been possible without the help and support of so many wonderful people.

First and foremost, I would like to thank my supervisor and friend, Marcello Passaro, for his invaluable guidance, encouragement, and support throughout the entire research process. His expertise in satellite altimetry, his incredible scientific network, his patience, and his great enthusiasm have been essential in shaping my research project and enhancing my skills as a researcher. Thanks for always having an open ear, engaging in discussions about anything, and sharing your positive energy.

I would also like to thank my second supervisor Florian Seitz for giving me the opportunity to do my PhD at DGFI-TUM and for his scientific advice. Thanks goes also to my colleagues at DGFI-TUM and the many events held at the institute. Thanks a lot for the open and fruitful discussions, the pleasant working atmosphere, and the many beers after the weekly DoRus. A big thank you also goes to Julius Oelsmann for being my office mate, and for the open-minded and always exciting discussions.

I truly enjoyed the research collaboration with the Delft University of Technology, for which I would like to greatly thank Cornelis Slobbe for giving me this opportunity. A big thank you goes to him, Marcel Kleinherenbrink, and Frithjof Ehlers together with Marcello for all the fruitful and stimulating discussions and the honest and always constructive feedback. It was a great pleasure to work with them and the collaboration has paved the way for my PhD. Special thanks go to Frithjof for the excellent collaboration, the nice discussions and the joint coding sessions. It was brilliant to work with you!

I would like to thank my family and especially my partner Dani for their unwavering support and encouragement throughout my PhD journey and my son Levi for cheering me up and always giving me a big smile. Their belief in me and constant encouragement have given me the strength to stay focused and overcome the challenges of the PhD journey.

# A Appendices

## A.1 P-I: Round Robin Assessment of Radar Altimeter Low Resolution Mode and Delay-Doppler Retracking Algorithms for Significant Wave Height

Schlembach, F.; Passaro, M.; Quartly, G.D.; Kurekin, A.; Nencioli, F.; Dodet, G.; Piollé, J.-F.; Arduin, F.; Bidlot, J.; Schwatke, C.; Seitz, F.; Cipollini, P.; Donlon, C. **Round Robin Assessment of Radar Altimeter Low Resolution Mode and Delay-Doppler Retracking Algorithms for Significant Wave Height**. *Remote Sens.* 2020, 12, 1254.

**Journal:** Remote Sensing, volume 12, article 1254

**Date of publication:** 16th of April 2020

**DOI:** 10.3390/rs12081254

**Web link:** <https://doi.org/10.3390/rs12081254>

### Copyright

This work was published in the Remote Sensing Open-Access Journal and is thus an open access article distributed under the Creative Commons Attribution License which permits unrestricted use, distribution, and reproduction in any medium, provided the original work is properly cited.

### Contribution













The contributions of this reported work can be listed as follows: conceptualization, M.P., G.D.Q., F.N., F.S. (Florian Schlembach); methodology, F.S. (Florian Schlembach), M.P., G.D.Q.; software, F.S. (Florian Schlembach), A.K.; formal analysis, F.S. (Florian Schlembach), M.P., G.D.Q., A.K.; investigation, F.S. (Florian Schlembach), G.D.Q., A.K.; resources, F.S. (Florian Schlembach), J.-F.P., G.D.D., J.B.; writing—original draft preparation, F.S. (Florian Schlembach); writing—review and editing, F.S. (Florian Schlembach), M.P., G.D.Q., A.K., F.N., C.S., P.C., G.D.D., F.A.; visualization, F.S. (Florian Schlembach), A.K.; supervision, M.P.; project administration, F.A., P.C., C.D., F.S. (Florian Seitz), ESA SeaState\_cci; funding acquisition, F.A., P.C., C.D., F.S. (Florian Seitz), ESA SeaState\_cci. All authors have read and agreed to the published version of the manuscript.

Criteria	Own contribution
Idea and conceptual design	50%
Implementation and realisation	70%
Analysis and discussion	70%
Figure compilation	90%
Manuscript structure and writing	70%
<b>Overall contribution</b>	70%

Own contribution to publication P-I

Article

# Round Robin Assessment of Radar Altimeter Low Resolution Mode and Delay-Doppler Retracking Algorithms for Significant Wave Height

Florian Schlembach <sup>1,\*</sup>, Marcello Passaro <sup>1</sup>, Graham D. Quartly <sup>2</sup>, Andrey Kurekin <sup>2</sup>,  
Francesco Nencioli <sup>2</sup>, Guillaume Dodet <sup>3</sup>, Jean-François Piollé <sup>3</sup>, Fabrice Ardhuin <sup>3</sup>,  
Jean Bidlot <sup>4</sup>, Christian Schwatke <sup>1</sup>, Florian Seitz <sup>1</sup>, Paolo Cipollini <sup>5</sup>  
and Craig Donlon <sup>6</sup>

<sup>1</sup> Deutsches Geodätisches Forschungsinstitut, Technische Universität München (DGFI-TUM), 80333 Munich, Germany; marcello.passaro@tum.de (M.P.); christian.schwatke@tum.de (C.S.); florian.seitz@tum.de (F.S.)

<sup>2</sup> Plymouth Marine Laboratory (PML), Plymouth PL1 3DH, UK; gqu@pml.ac.uk (G.D.Q.); anku@pml.ac.uk (A.K.); fne@pml.ac.uk (F.N.)

<sup>3</sup> Laboratoire d'Océanographie Physique et Spatiale (LOPS), CNRS, IRD, Ifremer, IUEM, Univ. Brest, 29280 Plouzané, France; guillaume.dodet@ifremer.fr (G.D.); jean.francois.piolle@ifremer.fr (J.-F.P.); fabrice.ardhuin@ifremer.fr (F.A.)

<sup>4</sup> European Centre for Medium-Range Weather Forecasts (ECMWF), Reading RG2 9AX, UK; jean.bidlot@ecmwf.int

<sup>5</sup> Telespazio VEGA UK for ESA Climate Office, ESA-ECSAT, Didcot OX11 0FD, UK; paolo.cipollini@esa.int

<sup>6</sup> European Space Agency, ESA-ESTEC/EOP-SME, 2200 AG Noordwijk, The Netherlands; craig.donlon@esa.int

\* Correspondence: florian.schlembach@tum.de

Received: 16 March 2020; Accepted: 9 April 2020; Published: 16 April 2020



**Abstract:** Radar altimeters have been measuring ocean significant wave height for more than three decades, with their data used to record the severity of storms, the mixing of surface waters and the potential threats to offshore structures and low-lying land, and to improve operational wave forecasting. Understanding climate change and long-term planning for enhanced storm and flooding hazards are imposing more stringent requirements on the robustness, precision, and accuracy of the estimates than have hitherto been needed. Taking advantage of novel retracking algorithms, particularly developed for the coastal zone, the present work aims at establishing an objective baseline processing chain for wave height retrieval that can be adapted to all satellite missions. In order to determine the best performing retracking algorithm for both Low Resolution Mode and Delay-Doppler altimetry, an objective assessment is conducted in the framework of the European Space Agency Sea State Climate Change Initiative project. All algorithms process the same Level-1 input dataset covering a time-period of up to two years. As a reference for validation, an ERA5-based hindcast wave model as well as an in-situ buoy dataset from the Copernicus Marine Environment Monitoring Service In Situ Thematic Centre database are used. Five different metrics are evaluated: percentage and types of outliers, level of measurement noise, wave spectral variability, comparison against wave models, and comparison against in-situ data. The metrics are evaluated as a function of the distance to the nearest coast and the sea state. The results of the assessment show that all novel retracking algorithms perform better in the majority of the metrics than the baseline algorithms currently used for operational generation of the products. Nevertheless, the performance of the retrackers strongly differ depending on the coastal proximity and the sea state. Some retrackers show high correlations with the wave models and in-situ data but significantly under- or overestimate large-scale spectral variability. We propose a weighting scheme to select the most suitable retrackers for the Sea State Climate Change Initiative programme.

**Keywords:** satellite altimetry; LRM; delay-Doppler; altimetry; SAR altimetry; significant wave height; round robin; assessment; comparison; retracking; ESA; climate change initiative

---

## 1. Introduction

Space-borne radar altimetry has been a remote sensing approach for many decades. The satellite altimeter adopts a simple principle, as already been described in 1979 by [1]: it emits a short radio-wave pulse and detects the reflected echo from the Earth's surface. From the round-trip time the pulse takes, the distance between the satellite's instrument and the Earth can be estimated. Initially, satellite altimetry over the ocean was used for measuring the ocean surface topography, but it can exploit other properties of the received echoes for retrieving significant wave height (SWH) and wind speed (WS). The SWH is defined as four times the standard deviation (SD) of the sea surface elevation [2]. Acquiring a global knowledge about the oceans' SWH is essential for applications such as ocean wave monitoring (e.g., for the fishing industry, industrial shipping route planning), weather forecasting, or wave climate studies (e.g., [3]).

Brown and Hayne have developed, in 1977, 1980 an open-ocean altimeter waveform model (in the following referred to as the Brown-Hayne (BH) model), with which the SWH can be inferred from the slope of the leading edge of the received echo [4,5]. The key part of the waveform that responds to changes in SWH is the leading edge. As the unwanted extraneous returns in the coastal zone predominantly affect the trailing edge, a whole class of retracking algorithms has been recently developed that focuses on the "subwaveform", i.e., those waveform bins centred around the leading edge. Altimeters that continuously emit and receive pulses in an alternating manner with a pulse repetition frequency (PRF) of 1920 Hz yield a footprint size of around 7 km and are referred to as pulse-limited, Low Resolution Mode (LRM) altimeters. In contrast, the more recent Delay-Doppler altimetry (DDA) altimeters (synthetic aperture radar (SAR) altimeters and synthetic aperture radar mode (SARM) are equivalent terms) transmit bursts of pulses (64 for the Sentinel-3 (S3) altimeters) and make use of both time delay and Doppler shifts of the echoes, resulting in a much narrower footprint and an increased along-track resolution of about 300 m. The appropriate physical-based waveform model for DDA is the SAMOSA model, which was developed in the framework of the European Space Agency (ESA) SAR Altimetry MOde Studies and Applications (SAMOSA) project [6] and published in [7]. The term SAMOSA is also used to refer to the actual retracking algorithm, as documented in [8].

Retracking is the common process of extraction of the geophysical parameters from the received echo and is performed using an algorithmic approach. The authors of [9] categorised three different main types of retracking algorithms. Empirical retrackers are based on a heuristic approach, in which an empirical-based relationship is established between the waveform and the geophysical quantities. The approach of physical-based retrackers is to fit the waveform to an idealised mathematical model. In its most accurate form, the model is a numerical-based solution and mimics the processing chain and physical effects (e.g., the interaction of the pulse with the Earth's surface) as close as possible. The closed-form analytical (or semi-analytical) solution of a physical-based retracker meets certain simplifying assumptions, which makes the computation of the model more robust, versatile, and computationally less expensive. The third category of retrackers uses a statistical approach, which makes use of statistical information of neighbouring measurements.

The focus of this work is an objective assessment of the performance of different retracking algorithms with regards to the estimation of the SWH in dependence of the distance-to-coast (dist2coast) and the sea state.

When estimating the SWH using satellite altimetry, the following main limitations can be identified:

- The contamination of the spurious signal components in the coastal zone results in a deteriorated quality and reduced quantity of SWH estimations [10]. The interfering signals mostly arise from "mirror"-like surfaces, such as melt ponds on sea-ice, or in sheltered bays, [11–13].

These phenomena are similar to the so-called “sigma0-blooms” in the open-ocean [14] but affect significantly more data in the coastal zone.

- The power spectral density (PSD) estimate of the SWH, which is computed as a function of spatial wavelength and denoted as the wave spectral variability, is characterised by a so-called “spectral hump” that masks the along-track variability below 100 km [14].
- The precision of the estimation of extreme sea states is particularly poor [15].
- Very low sea states cause the leading edge of the returned echo to be very steep, implying that that part is only sampled by one or two waveforms gates. Consequently, the precision is also degraded in low sea states [16].

The assessment is part of the Round Robin (RR) exercise that is conducted in the framework of the Sea State Climate Change Initiative (SeaState\_cci) of ESA [17], launched in June 2018. The main objective of the project is the estimation and the exploitation of consistent climate-quality time-series of SWH across different satellite missions.

For conducting the RR assessment, we determined beforehand the set of rules on how the evaluation was to be performed and what performance metrics were to be extracted. The exercise of a RR constitutes an essential part of the development phase of an ESA Climate Change Initiative (CCI) Essential Climate Variable (ECV) project [18]. It is open to both internal and external participants and its general procedure is as follows. A data package containing satellite data, and auxiliary data is distributed among all involved parties. The participants apply their algorithms to the data and send back their output. The pre-agreed assessment metrics are extracted from the generated datasets and the best performing algorithm is selected. The Sea Surface Temperature Climate Change Initiative (SST\_cci) [19], Soil Moisture Climate Change Initiative (SoilMoisture\_cci) [20], and Ocean Colour Climate Change Initiative (OC\_cci) [21] projects are examples of other projects, in which RRs were performed.

Ardhuin et al. [15] have elaborated on the requirements, the existing measurement technologies, and their limitations and the future of how sea states can be observed. Regarding the estimation of the SWH data from altimetry, most of the studies limit the comparison to only a single retracker against external data, or to a new retracker compared to the existing product. The authors of [10] have validated the Adaptive Leading Edge Subwaveform (ALES) algorithm using LRM altimetry for SWH estimation in the coastal zone. The result was validated against in-situ data by assessing bias, SD, slope of regression line, and number of cycles with correlation larger than 0.9. The authors of [22] and [23] have assessed the SWH and WS estimates that were acquired by the missions SARAL/AltiKa and CryoSat-2 (CS2) using the standard retracking algorithms MLE-4 and SAMOSA, while comparing the measurements against in-situ buoy data and wave models. The ESA SAR Altimetry Coastal and Open Ocean Performance (SCOOP) project [24] has conducted the characterisation and improvement of DDA retracking algorithms. The involved teams have made improvements on the retracker and have assessed the resulting performance in comparison against the baseline algorithms but not against several other retracker. Yang and Zhang [25] have validated the baseline retracker SAMOSA and MLE-4 of Sentinel-3A/3B (S3A/B) datasets against open-ocean buoy data of the U.S. National Data Buoy Center (NDBC) network, whilst Nencioli and Quartly [26] have performed a detailed analysis of the same using both models and buoys around the southwest UK. Fenoglio-Marc et al. [27] have validated the performance of the standard SAMOSA retracker from the CS2 mission in the study area of the German Bight. The authors of [28] and [9] have presented a novel SAMOSA+ and SAMOSA++ retracker, while validating their results with in-situ and wave model data.

To the best knowledge of the authors, there has not been any comparable objective and comprehensive comparison between different retracking algorithms in the literature so far. In this pioneering RR exercise for SWH, we have endeavoured to use multi-year quasi-global datasets. However, to prevent an undue load on the various data producers, they were only required to process a selection of tracks spanning the range of conditions to be assessed (see Table 1). In this work, a compromise had to be found between the need to cover several regions of the world, the amount of data for a statistically-meaningful comparison, and the fact that most of the participating algorithms are

not yet associated to an already available global product. A strict time line was set for the participants in order to process the specific set of data. Further discussion can be found in Section 2.

This work is structured as follows: Section 2 describes the data that were used for the assessment of the algorithms, including the Level-1 (L1) input datasets used for retracking, a brief description of the retracking algorithms and also the wave models and the in-situ data used in the validation. Section 3 describes the methodology of the assessment, explaining how the evaluation metrics are extracted and the design of the software framework that is used for the automatic generation of the results. Section 4 presents and discusses the results. Section 5 discusses some lessons that were learnt during the process and should be applied to future RRs. Section 6 draws conclusions and elaborates on the algorithm selection process of the SeaState\_cci consortium.

## 2. Data

### 2.1. Original Altimeter Data

In order to conduct an objective evaluation of different retracking algorithms, it is crucial that all algorithms process exactly the same data. It was therefore decided that the input for all providers should be the same L1 along-track data from Sentinel-3A (S3A) and Jason-3 (J3).

The selected J3 dataset is the Sensor Geophysical Data Records (SGDR) version D product that was downloaded from Aviso+ [29]. It contains both the radar waveforms and also SWH estimates generated with the baseline algorithms MLE-3 and MLE-4; these default retrackers are also included in the assessment to provide a benchmark. The time period being used was from the 1st of June 2016 to 30th of June 2018 in order to capture a wide range of sea state conditions.

For S3A, we used Level-1A (L1A)/Level-1B with stack data (L1BS) data acquired from the Copernicus Online Data Access (CODA) catalogue of EUMETSAT [30]. The files cover a time period from 26th of March 2017 to the 30th of June 2018. In contrast to the J3 SGDR dataset files, the geophysical data and standard retracking estimates are not contained in the L1BS files but in the Level-2 (L2) products. For S3A, the default retracking algorithms are SAMOSA for the DDA waveforms and MLE-4-PLRM for the Pseudo Low Resolution Mode (PLRM) ones (see the end of this section for a more detailed description of the latter). To enable these two default algorithms to provide benchmarks, we collocated the needed L2 information with the L1BS locations used by all the developers of new products. The SAMOSA-retracked product that is included in the L2 product has the baseline versions 002 and 003. We had to accept two mixed baseline versions because there was a transition within the investigated period of time.

The individual pole-to-pole tracks of the J3 and S3A missions were selected to maximise the number of in-situ collocations that were used for validation of the retracked datasets, as described in Section 2.2. A summary of the input L1 datasets are listed in Table 1.

**Table 1.** Summary of J3 and S3A input L1 datasets to be retracked.

Mission	Jason-3	Sentinel-3A
# of		
Half-orbits/pole-to-pole tracks	16	30
Cycles	73	17
Period of time in months	24	15
NetCDF files (pole-pole tracks and cycles)	1162	512

### 2.2. Validation Data

In-situ data were gathered by ECMWF. Most of the data came from the operational archive from ECMWF, where all data distributed via the Global Telecommunication System (GTS) are kept. Data from moored buoys and fixed platforms were extracted. These data are usually reported hourly (or less frequently). The bulk of the data comes from moored buoys, with the exception of data from

operating platforms in the North and Norwegian Seas and the Gulf of Mexico. The main data providers are the US, via the NDBC and Scripps, Canada, the UK, France, Ireland, Norway, Iceland, Germany, Spain, Brazil, South Korea, and India. This dataset was supplemented by buoy data obtained from the web sites from the UK Centre for Environment, Fisheries and Aquaculture Science (CEFAS) and the Faeroe Islands network. In addition, buoy data from New-Zealand obtained as part of ECMWF wave forecast validation project were also used. A basic quality control was applied to each hourly time series for each location to remove spurious outliers. The number of buoys selected for the in-situ datasets is given in Table 2. Overall nearly 36% more buoys are available for the S3A dataset than for J3 because more different tracks are used. Most of these buoys are located in the open-ocean, as shown in the map in Figure 1.

**Table 2.** Number of the selected total, open-ocean and coastal buoys for the J3 and S3A missions.

# of	Mission	
	Jason-3	Sentinel-3A
Open-ocean	85	124
Coastal zone	40	46
Total	125	170

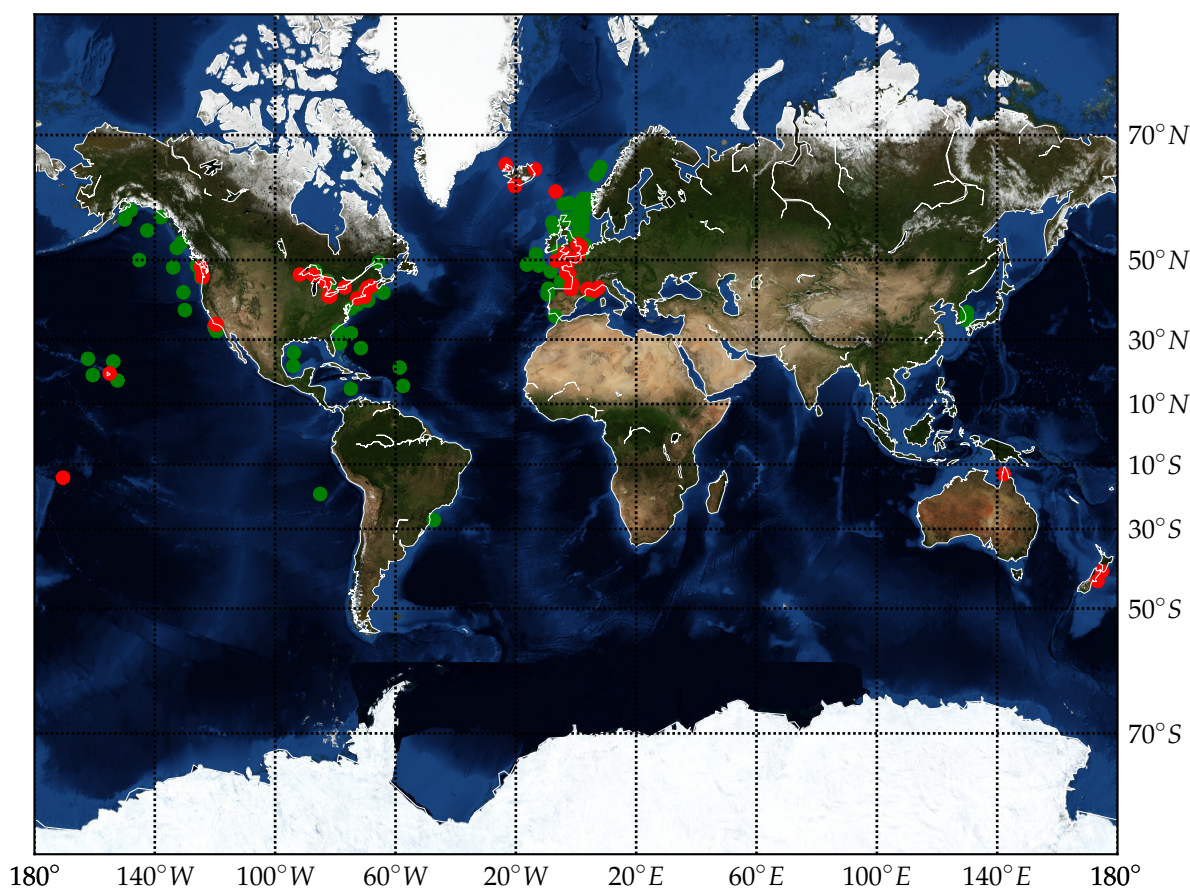


**Figure 1.** A distribution of the buoys used for validation of Delay-Doppler altimetry (DDA) retrackerers. Coastal buoys are shown in red and open-ocean buoys are given in green.

To validate the retracker results, a dataset of collocated remote sensing and in-situ observations was created based on the following constraints, as discussed in [31]: (a) the distance between the along-tracks and the buoys is less than 50 km and (b) the time difference between the along-track points and the buoy record is less than 30 min. If both constraints are satisfied during a pass-over



of the satellite, the 51 measured, 20-Hz SWH points that are located closest to the buoy position are extracted and the median value is computed. The odd number of 51 is chosen for the sake of symmetry. The buoy data is smoothed by applying a 1 h moving average filter.

Besides the in-situ buoy data, a novel wave model from European Centre for Medium-Range Weather Forecasts (ECMWF) is used as a reference for the retracker validation. It is a wave hindcast, which is based on ERA5-forcing and CY46R1 version of the ECMWF wave model (referred to as ERA5-h model in the following). The original ERA5 uses ECMWF's Integrated Forecasting System (IFS) cycle 41r2 and thus benefits from multiple decades of experience in terms of model physics, numerics, and data assimilation [32]. ERA5-h adopts the newer IFS cycle 46r1 and was found to be of even better quality than compared with ERA5 [33]. The crucial difference between both is the fact that no wave data assimilation is performed for ERA5-h as compared with ERA5, for which available space-borne altimetry data is used. ERA5-h is a wave model standalone run that is forced by ERA5 hourly 10 m neutral winds, surface air density, gustiness, and sea-ice cover. It uses different wave physics for wind input and dissipation [34]. It provides hourly estimates for a large number of ECVs. With respect to wave heights and spectra, ERA5-h has an improved resolution of 18 km, 36 directions, and 36 frequencies, as compared to ERA5 with a resolution of 40 km, 24 wave directions, and 30 frequencies.

### 2.3. Overview of Investigated Retracker Datasets

In total, there are 15 new retracked L2 datasets from six research groups (Technical University of Munich (TUM), Plymouth Marine Laboratory (PML), Collecte Localisation Satellites (CLS) in cooperation with the Centre national d'études spatiales (CNES), University of Bonn (UniBonn), isardSAT, University of Newcastle (UON)) incorporated in the assessment. As listed in Table 3, the number of J3 retracking algorithms is 11 (all LRM, including the baseline products MLE-3 and MLE-4) and eight for S3A (including the baseline SAMOSA product, and with three being PLRM datasets).

**Table 3.** Investigated Low Resolution Mode (LRM) and DDA retracking algorithms.

	Retracking Algorithms	Altimeter Mode	Author	Denoised
J3	MLE-3 (reference)	LRM	-	No
	MLE-4 (reference)	LRM	-	No
	WHALES	LRM	TUM	No
	WHALES_adj	LRM	PML/TUM	Yes
	WHALES_realPTR	LRM	PML/TUM	No
	WHALES_realPTR_adj	LRM	PML/TUM	Yes
	Brown-Peaky	LRM	UON	No
	TALES	LRM	UniBonn	No
	Adaptive	LRM	CLS/CNES	No
	Adaptive_HFA	LRM	CLS/CNES	Yes
	STARv2	LRM	UniBonn	Yes (inherently)
<b>Total Number</b>				11
S3A	SAMOSa (reference)	DDA	SAMOSa project [6]	No
	WHALES-SAR	DDA	TUM	No
	DeDop-Waver	DDA	isardSAT	No
	LR-RMC	DDA	CLS/CNES	No
	LR-RMC_HFA	DDA	CLS/CNES	Yes
	MLE-4-PLRM (reference)	PLRM	-	No
	TALES-PLRM	PLRM	UniBonn	No
	STARv2-PLRM	PLRM	UniBonn	Yes (inherently)
<b>Total Number</b>				8

The column "Denoised" in Table 3 indicates whether a denoising technique was applied to the retracked dataset in order to decrease the noise content in the along-track SWH series. This could have been applied either implicitly within the retracking algorithms as for the STARv2 algorithm

(as discussed in Section 2) or explicitly, a-posteriori to the retracked L2 dataset. Examples for explicit techniques are the intra-1-Hz adjustment [35] or high-frequency adjustment (HFA) [36], and an empirical mode decomposition (EMD)-based technique [37].

Rules for the RR also required that the data producer supply a quality flag to indicate whether the proponents rated the individual estimates as good (0) or bad (1).

In the following sections, the retracking algorithms, which participated in the RR, are briefly described. Where a peer-reviewed publication exists, we provide the citation. Otherwise, an extensive description of the algorithms can be found in [38]. While the focus of the paper is on the ensemble of statistics adopted to highlight differences among the retrackers, it is important to highlight the basic characteristics of the algorithms in order to be able to discuss the different performances.

### 2.3.1. LRM Retracking Algorithms

The established algorithm applied on the vast majority of LRM altimetry missions is named MLE-3: this maximum likelihood estimator uses the analytical BH model for retrieving the three parameters range, SWH, and signal amplitude. It was superseded by MLE-4 [39], which also allows for instrument mispointing. MLE-3 and MLE-4 actually implement an unweighted least squares (LS) fit of the analytical model to the observational data, while neglecting the expected statistics of the fading noise contribution. However, a simple weighted scheme exhibits greater along-track variability, with the introduction of correlated errors between range and SWH estimations [40].

The mathematical form, such as the BH model, assumes that the shape of the emitted radar pulse corresponds to a Gaussian and that the reflecting surface is homogeneous within the irradiated footprint, which can be between 2 and 20 km in diameter depending upon conditions [41]. First of all, the true pulse shape does not conform exactly to the ideal, so a facsimile of the emitted pulse is recorded internally, known as the Point Target Response (PTR), which can be used to develop an instrumental correction. Second, the assumption of homogeneity in the footprint often breaks down for winds speeds lower than 3 m/s and in the coastal zone because of reflections from nearby land or “bright target” responses from sheltered bays [12,13]; therefore new algorithms have been advocated to overcome these problems.

Passaro et al. [42] developed the ALES retracker to utilise only waveform bins around the leading edge, with the selection of bins being dependent upon the SWH estimate from an initial pass. Although originally developed to improve estimates of range in the coastal zone, it was also demonstrated to give more robust estimates of SWH in the German Bight [10]. The fitting of the received echo to the idealised BH model is established using the Nelder-Mead optimisation approach, which is a computational efficient algorithm for solving non-linear optimisation problems [43]. The WHALES algorithm is an improved version of ALES, in which the derivation of wave height has been optimised by developing a set of adapting weights in the fitting process, which changes according to a first estimation of the SWH performed based on the leading edge.

The standard WHALES algorithm makes a correction for the true PTR shape using a look-up table (LUT)-based on that used for MLE-4 output. A bespoke correction for WHALES was developed by running a series of simulations using a representation of the true PTR shape and examining the mean bias recorded by the WHALES algorithm assuming a standard Gaussian PTR. At wave heights greater than a few metres, this correction was uniform and similar to that from the MLE-4 LUT; however, at low SWH, especially < 0.8 m, the derived correction varied markedly with the position of the leading edge. With the correction applied as a function of wave height and leading edge position, the algorithm is referred to as WHALES\_realPTR.

The above-described algorithms treat each waveform completely independently. However, as both wave height and range are derived predominantly from the waveform bins within the leading edge, they both exhibit sensitivity to the individual realisations of fading noise in that span of the waveform. In practice, the fading noise-related anomalies between the two are significantly correlated [40], with an error in range of a few centimetres being typically associated with a commensurate error in

SWH of ten times that magnitude, although the coefficient of proportionality does depend upon the particular retracker and altimeter [35]. Thus, if the noise-related error in range can be ascertained, for example, by use of a high-pass filter (HPF), an appropriate adjustment of the SWH can be calculated. Such a correction was available for the WHALES retracker, producing algorithms WHALES\_adj and WHALES\_realPTR\_adj for the two versions of WHALES previously introduced. The use of such adjustments was found to be very effective in making a significant reduction in small scale noise for MLE-4 applied to Jason-2, Jason-3, and AltiKa data [35].

The Brown-Peaky retracker [44] has been developed as a variation of the ALES approach, which defaults to using all waveform bins if no peaky signal is detected. If a peak is detected, the estimation of the geophysical parameters is performed using a weighted least squares (WLS) method. The range bins that are affected by the peak are thus down-weighted and their impact is mitigated. The algorithm developers have already assessed their product around the coasts of Australia [45].

TALES is another ALES-derivative developed by TU Darmstadt [28]. In contrast to the original ALES [46], TALES uses a numerical waveform model called Signal Model Involving Numerical Convolution (SINC) instead of the BH model [47]. Hence, no LUT is required for estimating the SWH. In addition, SINC can be adapted to more complex sea surface representations, such as weakly non-linear wave theory and a real PTR [38,47].

The model that is used for the Adaptive retracker is similar to the BH model. However, in contrast to classical retrackers, such as MLE-4, it does not assume a Gaussian-like PTR, which often also requires a LUT to provide minor corrections. Instead, it follows a numerical solution, where the real PTR is approximated by taking into account altimeter instrumental characterisation data such as the antenna beam pattern or the characteristic of the integrated low-pass filter (LPF). Likewise, it accounts for different surfaces of the sea such that it is able to cope with different degrees of roughness (diffuse or peaky) [38]. There was also a variant of this product, termed Adaptive\_HFA, which included an additional along-track filtered correction term, based on the approach described in [36]. It is important to remark that for both the “adjusted” variants of WHALES and Adaptive, there is no smoothing or filtering of the SWH data but solely of the range of information to provide the corrections.

A significantly different approach to decrease the noise in the optimisation of the SWH estimation is version 2 of the STAR algorithm [48] (STARv2), although the BH model and a subwaveform technique are also employed. The original STAR algorithm has been applied to both LRM and PLRM altimetry data. STAR follows a traditional Maximum Likelihood Estimation (MLE) approach that retracks all detected subwaveforms. This yields a point cloud of values containing sea surface height (SSH), SWH, and  $\sigma^0$ . To determine the final values of SSH, SWH, and  $\sigma^0$ , a shortest path algorithm was used [48]. This is based on the assumption that neighbouring 20-Hz measurements are similar to each other. The STARv2 retracker incorporates an additional weighting factor into the selection of the individual steps from one 20-Hz measurement position to the next, which also reduces the appearance of measurement noise as along-track variability.

### 2.3.2. DDA Retracking Algorithms

Whilst the majority of altimetry missions launched to date have been LRM altimeters, the latest generation exploit the phase coherence of bursts of individual echoes sent at a much higher pulse repetition frequency, in a technique, referred to as DDA or also known as SAR altimetry [49]. By application of SAR-like processing, better localisation can be achieved of the part of the ocean generating the echo, and these echoes can be combined over a wider range of views (“multi-looking”) to help improve the signal-to-noise ratio (SNR). The first instrument to offer DDA mode was CS2 (launched in 2010), and this was followed by S3A/Sentinel-3B (S3B) in 2016 and 2018, respectively.

SAMOSA is the baseline retracking algorithm that is part of the standard L2 product of the EUMETSAT CODA. (Strictly speaking, the term SAMOSA is related to the ESA project [6], in which the waveform model and the retracker were developed [8], but is commonly used to refer to the retracking algorithm on the standard products.) It uses the fully analytical, open-ocean SAMOSA2 waveform

model [7] that is expressed in terms of Scaled Spherical Modified Bessel functions and includes the zero- and first-order terms, as described in [28]. To establish the non-linear fitting of curves, it uses the bounded Levenberg-Marquardt Least-Squares Estimation Method (LEVMAR-LSE) [50] algorithm (as an implementation for the Levenberg-Marquardt non-linear LS optimisation algorithm) to extract the three geophysical parameters range, SWH, and amplitude  $P_{ii}$ .

WHALES-SAR is the DDA counterpart of WHALES. Similarly, WHALES-SAR only considers a subwaveform and thus avoids spurious backscattered signals in the trailing edge of the waveform that mostly arise in the coastal zone and applies a weighted estimation. However, instead of being based on a physical-based retracker, it exploits the estimation of the rising time of the leading edge, which is performed using a simplified BH model with a different trailing edge slope. It, therefore, infers the SWH by means of an empirical relation that is based on a comparison with simulated DDA waveforms [38,51].

The DeDop-Waver retracker provided by isardSAT starts the processing from the L1A data, incorporating several instrumental and DDA-specific corrections. The essential retracking step is performed by following the original SAMOSA model [7] with additional steps, such as noise floor estimation, stack modelling, stack masking, and multi-looking. [52]

The L1A-to-L1BS processing of the Low Resolution with Range Migration Correction (LR-RMC) retracker follows the unfocused SAR altimetry approach from [53] with the difference that bursts of four beams are combined and averaged. Thus, it improves the measurement precision compared to unfocused SAR altimetry over open-ocean [38]. The retracking procedure to convert the L1BS to a L2 dataset is established by a numerical approach. In contrast to a conventional retracker, it uses pre-simulated power echo models that are based on altimeter instrumental characterisation data such as the real antenna pattern and the range impulse response, which were measured pre-launch, and also it takes into account instrumental ageing issues. For fitting the waveform to the model, a WLS estimator that is derived from a MLE is used. [38]

Same as for the Adaptive LRM retracker, as described in Section 2.3.1, a second variant LR-RMC\_HFA is taken into consideration, which includes an additional smoothing step using the HFA algorithm [36].

These algorithms for DDA processing make use of the time delay and Doppler shift information that is contained in the return echo, whereas their forerunners only used the information binned in terms of delay. Although the extra information in the Delay-Doppler (DD) processing has been expected to give improved accuracy, there were concerns for climate studies about whether the derived values would be consistent with those from conventional LRM altimeters. Thus, for S3, there is a parallel processing line that ignores the delay information to produce PLRM waveforms. The shape of these waveforms will match the BH model, but the noise level in the waveforms is higher than for a conventional LRM instrument operating continuously, owing to the lower number of independent returns being averaged. For continuity, the S3A L2 products contain these PLRM waveforms and estimates of range, SWH and  $\sigma^0$  based on them (denoted as MLE-4-PLRM in the following). The providers of TALES and STARv2 also applied their retracking approaches to these waveforms, and these are also evaluated to provide a yardstick, with which to assess whether DDA algorithms provide the anticipated benefits. In the following analysis, we add the suffix '-PLRM' to their names to clearly distinguish their source.

### 3. Methodology

In order to objectively assess the performance of the individual retracking algorithms, the following five different types of analyses were evaluated: outliers, noise, wave spectral variability, and the comparison against a wave model and against in-situ data. All metrics from the analyses are generated as a function of the dist2coast and the sea state. The terms coastal and open-ocean are used for dist2coast values of less than or greater than 20 km, respectively, with the classification of sea states being as in Table 4.

**Table 4.** Definition of sea states.

Sea State	SWH Range
Low	0 m < SWH < 2 m
Average	2 m < SWH < 5 m
High	SWH > 5 m
Very high	SWH > 10 m

### 3.1. Retracking Framework

The complete analysis code is set up as a Python-3-package, retracker validation (retrackval), which is available on request. Its main objective is to make the assessment process as transparent and objective as possible. It is platform-independent, easy-to-setup (with about 10 commands), and the full algorithm validation is reproducible by running a fully-automated script.

When reading the netCDF file of the individual dataset, the SWH data variable undergoes a first quality check. The SWH value is set to not-a-number (NaN), if one of the following conditions are met:

- The SWH value is set to NaN by the retracked dataset provider;
- The quality flag is set to “bad” by the retracked dataset provider;
- The sea-ice flag is set (not used in outlier analysis and not needed in spectral analysis or buoy comparisons);
- All values around 0 m with tolerance of  $1 \times 10^{-4}$  m. This is necessary as some retrackers set the estimated SWH value to zero, when they fail, which may give a misleading perception of the confidence with the along-track noise being 0.0 m.

In order to run the analyses as a function of dist2coast, the corresponding dist2coast value of each measurement at any location is determined from a  $0.01^\circ$  resolution dataset from Pacific Islands Ocean Observing System (PacIOOS) [54], which has an uncertainty of up to 1 km. For some of the analyses, data were averaged from 20 Hz (300 m along-track) to 1 Hz ( $\sim 6$  km), using a median of the 20 values, provided that no more than 3 were NaN. This was useful for the comparison against the wave model (as the resolution of the ERA5-h wave model is 18 km). Also in the noise analysis, the SD was calculated over groups of 20 samples.

When reducing the longitude/latitude-pair vectors, the median of the 20 20-Hz values are taken. Likewise, the median of the 20 SWH values is computed, with the additional constraint that there must exist at least 17 valid values (neither NaN, bad quality flag, nor marked as being sea-ice) of the 20 20-Hz-points. Otherwise, the resulting 1-Hz SWH is set to NaN.

### 3.2. Outlier Analysis

In some situations, the retracking algorithms are not able to retrieve a reasonable estimate for the SWH from the received echo. This might be due to (a) received echoes that contain strong spurious signal components, which predominantly occur in the coastal zone, (b) extremely steep and poorly defined leading edges (likely apparent in very low sea states), or (c) very noisy waveforms that are typical of echoes reflected from within storms, with very high waves and potentially intervening rain [55]. These conditions significantly reduce the number of valid retracked SWH observations. Thus, the coastal zone, very low sea states, and storms represent key situations for major improvement. This makes the outlier analysis a particularly relevant component of the RR assessment. For detecting outliers, the following three criteria are defined:

**invalid** Data missing (already set to NaN) or quality flag set to ‘bad’ (1).

**out\_of\_range** If a value is out of the expected range of  $[-0.25, 25]$  m. (Note noisy estimations may sometimes return sub-zero values.)

**mad\_factor** This criterion compares the value with its 20 closest neighbours (10 before and 10 after). It is implemented using median and median absolute deviation (MAD), which are statistically

robust measures. Data are discarded if they exceed median plus  $3 * 1.4826 * MAD$ , with median and MAD calculated on 20-point sliding windows, and the factor 1.4826 converts the MAD to SD equivalent for a normal distribution [56].

If one of the criteria is applicable, the individual measurement is considered to be an outlier. The evaluated metrics are the total number of outliers and the number of outliers in the coastal zone as a function of the *dist2coast*, considering bands of less than 20, 10, and 5 km from the coast. This analysis is performed on the 20 Hz-data, and the total number of outliers is given by the sum of the individual outlier types excluding potential overlapping indices (one measurement might be marked by multiple types, e.g., *mad\_factor* and *out\_of\_range*).

Furthermore, as an exception of the outlier analysis, there is no sea-ice flag considered, when reading the netCDF files. The sea-ice flag would be considered as another kind of quality flag, marking a measurement as invalid. The outlier analysis should be on estimations of SWH in the ocean and do not take into account points on surfaces, for which such estimation does not exist, such as land and sea-ice covered areas.

### 3.3. Noise Analysis

The intrinsic noise that is implied in the SWH sequence is defined as the standard deviation (SD) of the 20-Hz SWH data within a 1-Hz distance. This procedure is based on the assumption that the SWH measurements that were taken from an irradiated footprint of approximately 7 km (corresponding to a 1-Hz measurement) and is mostly dominated by noise [15,27]. The variations of the 20-Hz sampling points, which amounts to a distance of roughly 300 m is, thus, considered to be noise.

The following metrics are evaluated by the retrackval framework:

- Median of all noise values: as a function of *dist2coast* (open-ocean and coast);
- Median of all noise values: as a function of sea state and *dist2coast* (open-ocean and coast);
- Median noise values vs. SWH ranges with a resolution of 0.25 m.

The reduction of 20-Hz to a 1-Hz dataset containing the noise values is performed as described in Section 3.1. Likewise, the 20-Hz dataset is read and bad data is discarded accordingly, while outliers detected in the previous sections are not.

### 3.4. Wave Spectral Variability

The preceding section described the intrinsic and short term variability affecting the precision of successive measurements. An extension of this analysis is to explore the variability as a function of length scale, i.e., an along-track spectral analysis, as in [35,57].

The interest here is in the perspective of mapping and monitoring applications, where the finest scale information may not be immediately useful, but the interest is in the correct characterisation of the variability at scales of 25–100 km. To assess such variability, we consider successive 1024-point sections of the SWH data (corresponding to ~300 km along-track) and determine Fourier components using the Welch periodogram method. This method applies a Hann window to the data to mitigate the effects of any discontinuity between the values at the end of each section. As the analysis is achieved using fast Fourier transform (FFT), the data must be free from any missing values. To produce sufficient spectra for averaging, we utilise any segment that has less than 5% missing data and fill in the gaps with simple linear interpolation. We also adopt the procedure of calculating the spectra from sections commencing every 512 points along-track (i.e., 50% overlap), as the Hann weighting downplays the contributions from the outer edges of each section [58]. This analysis was deliberately constrained to data that was from the open-ocean (by setting a *dist2coast* > 20 km), free from land, or sea-ice (flag taken from the baseline products), so that the information derived is exclusively about the wave height field of that retracker rather than being affected by other phenomena.

### 3.5. Comparison against Wave Model

In the subsequent analyses, the accuracy and precision of the retracked SWH estimates are to be compared by the ERA5-h wave model described in Section 2, as has been done in [22,23]. The model is a gridded product and features a resolution of 18 km. It is, thus, as acceptable to perform the co-location (using an interpolation) on the 1-Hz SWH data points (corresponding to 7 km).

The process of the comparison analysis is performed as follows:

1. Reducing the datasets from 20-Hz to 1-Hz;
2. Taking the union of the indices of both datasets considering non-NaN values only;
3. (Out-of-range values were already set NaN, thus discarded during the netCDF reading procedure);
4. Performing a linear LS regression on the two coupled series.

As a result, the following metrics are evaluated in this analysis:

- Pearson correlation coefficient;
- Slope of linear fit;
- standard deviation of differences (SDD);
- Median bias of differences;
- 2D-histogram plot.

The SDD and the median bias of differences is computed according to

$$\text{SDD} = \text{std}(|\text{SWH}_{\text{model}} - \text{SWH}_{\text{retracker}}|), \quad (1)$$

and

$$\text{median bias} = \text{median}(\text{SWH}_{\text{model}} - \text{SWH}_{\text{retracker}}) \quad (2)$$

where *std* denotes the SD, and  $|\cdot|$  the absolute magnitude operator.

Figure 2 shows the 2D-histogram plots for the retracked MLE-4 in comparison against the ERA5-h wave model for (a) coastal and (b) open-ocean scenarios, respectively. The 2D-histogram plots are generated by assigning the two coupled datasets to SWH-intervals with a bin size of 0.25 m (taking the SWH value of the wave model as the reference). Hereby, each pair of a coupled SWH estimate corresponds to one point in the 2D-histogram. The number of the coupled estimates is colour-coded on a common logarithm-scale. The dashed line indicates a perfect correlation between the two series (correlation coefficient and slope of value 1.0). The solid red line is the result of the linear regression analysis.

When comparing Figure 2a, open-ocean and b, coastal scenarios, it can be clearly seen from the distribution of the points that there are higher sea states in open-ocean areas, as expected. The MLE-4 retracker significantly overestimates low sea states, in which the values have a large spread in these cases. This is an important remark, when discussing Figure 7 in Section 4, in which high noise values are noticeable for high sea states. There is only a minor difference between the two calculated median bias values  $-0.036$  and  $0.072$  m. However, the difference of the SDDs of  $0.850$  and  $0.308$  is significant, which indicates better precision of MLE-4 for the SWH estimates in open-ocean scenarios.

The aforementioned metrics are generated by the retrackval framework for all included J3 and S3A datasets. Consequently, a large set of figures and statistical numbers are generated. Plots such as the 2D-histogram plots are convenient for a detailed analysis of the comparison against another reference dataset. In order to ease the objective assessment of the individual retracker against a reference dataset, Section 4 will limit the evaluation to the metrics correlation coefficient, SDD and median bias of differences.

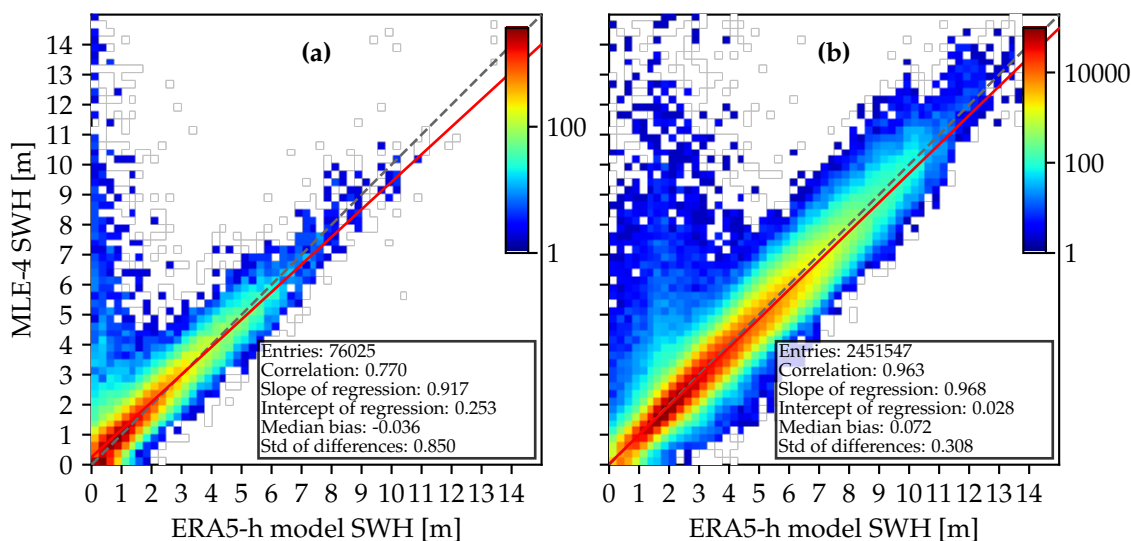


**Figure 2.** A 2D-histogram of MLE-4 against ERA5-h model considering (a) coast only and (b) open-ocean only. An SWH-interval bin size of 0.25 m is used.

### 3.6. Comparison against In-Situ Data

The retracked SWH measurements are compared with the in-situ buoy records to carry out independent evaluation of accuracy and limitation of the retracking algorithms, as has been done in [22,23]. The evaluation results can be affected by the errors and outliers in the retracked data as well as in the buoy measurements. The retracking framework described in Section 3.1 is adapted to reduce the adverse effect of these errors. Accordingly, the SWH measurements are set to NaN values if one of the conditions, described in Section 3.1, are met. The exceptions are the sea-ice flag that is not considered for buoy measurements and a new requirement for retracked points to be off the coast. The last one is implemented by checking the `dist2coast` parameter.

Next, all the 51, non-NaN retracked SWH values collocated with a record in the buoy dataset (see Section 2) are reduced to obtain one retracked SWH value (applying the median). The discrepancy between retracked SWH and buoy measurements is estimated as

$$DS = SWH_{buoy} - SWH_{altimeter}, \quad (3)$$

where  $SWH_{buoy}$  is the in-situ buoy measurement of SWH, and  $SWH_{altimeter}$  the median of the closest 51 SWH values.

The accuracy of SWH values is calculated from the discrepancy values over all buoy records. As some buoys produce inaccurate data, which may affect overall results, an additional procedure is introduced to identify such buoys and exclude them from the analysis. To identify anomalies in the buoy dataset, an error is estimated for each buoy as  $Err_{buoy} = median(|DS_i|)$ , where  $i$  is the buoy's index. If the error  $Err_{buoy}$  exceeds 1 m for buoy  $i$ , this buoy is considered as unreliable and its records are discarded. Given that the majority of the buoys match well with the various altimeter estimates, a median error of this magnitude implies a poorly calibrated buoy or else one that is too far from the altimeter track as to not provide representative ground truth values (see [26]).

The accuracy analysis is carried out on the selected buoys by calculating the Pearson correlation coefficient, the SDD and the median bias of the differences, with these metrics calculated for the different sea state regimes listed in Table 4. The SDD and the median bias are computed using the discrepancies estimated in accordance with Equation (3) and for all reliable buoy records.



#### 4. Results and Discussion

Running the validation with retrackval produces a large set of figures that cannot be presented and discussed individually in this paper. Instead, a small subset of most representative figures will be taken into account in the following sections, in order to provide a comprehensive analysis of the results. The full set of figures can be found in the Supplementary Materials section of this article..

##### 4.1. Outlier Analysis

Figure 3 shows the number of total outliers of J3 vs. S3A in dependence of the dist2coast. For open-ocean scenarios, Brown-Peaky (J3) and WHALES-SAR (S3A) have the least amount of total outliers, accounting for 8.1% and 15.8%. The outliers of all retrackerers stay below 20%, with the exception of STARv2-PLRM, which amounts to 27%. The J3 retrackerers tend to be less prone to outliers, but since the two satellites follow different ground tracks, this hypothesis needs to be considered with care. Among the new retrackerers, J3 datasets contain less outliers. This is likely to be a consequence of a more conservative use of the quality flag, since in the standard products (MLE-3 for J3 and SAMOSA for S3A) the opposite is observed.

When approaching the coast, the number of outliers is significantly increased for both LRM and DDA retrackerers. The number of outliers range from ~28% to ~55% (LRM) and from ~43% to ~60% (DDA) for the best performing retrackerers (approaching coast in the intervals 20, 10, and 5 km), which are Brown-Peaky and TALES for J3 and SAMOSA, WHALES-SAR, and TALES-PLRM for S3A. It appears that the number of outliers quasi-linearly increase with a decreasing dist2coast. The differences of the amount of total outliers can be quite large, for example, when considering areas that are very close to the coast (less than 5 km), SAMOSA is able to produce estimates for almost 50% of the measurements, whereas Adaptive retrieves only 16.5% of valid SWH samples.

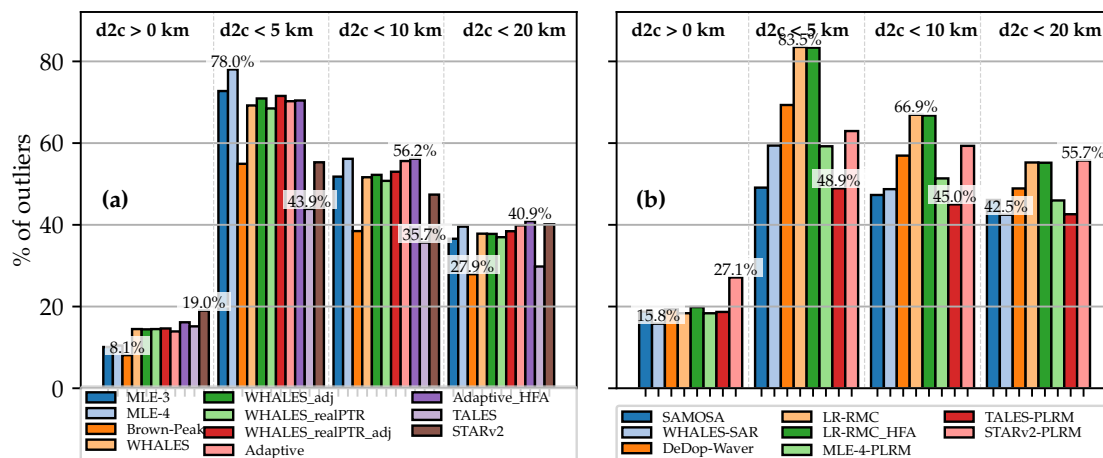


Figure 3. The total number of outliers as a function of dist2coast for (a) J3 and (b) S3A.

Figure 4 depicts the distribution of the outliers types invalid, out\_of\_range, and mad\_factor as a function of dist2coast for the retrackerers Brown-Peaky and TALES. They both follow a subwaveform approach that discards the trailing edge of the waveform, which is mostly contaminated by spurious signals in the coastal zone. One might, thus, expect a similar outlier behaviour, but their number of outliers differ. TALES exhibits a significant amount of about 15–23% of out\_of\_range outliers, whereas Brown-Peaky shows none but instead an increased amount of invalid estimates (21% vs. 11% for dist2coast < 20 km). This underlines the role of quality flag: It is up to the strategy of the individual retracker, whether to decide if an estimate is set to be bad or remained as a potential outlier (out\_of\_range or mad\_factor). Interestingly, in general, the fraction of mad\_factor outliers is increased only slightly by a factor of about two when approaching the coast, whereas the total amount of outliers

increases significantly, meaning that the mad\_factor does only weakly depend upon the dist2coast. In contrast, the estimate is either good or very bad or missing in the coastal zone, yielding the measurement to be an outlier of type invalid or out\_of\_range.

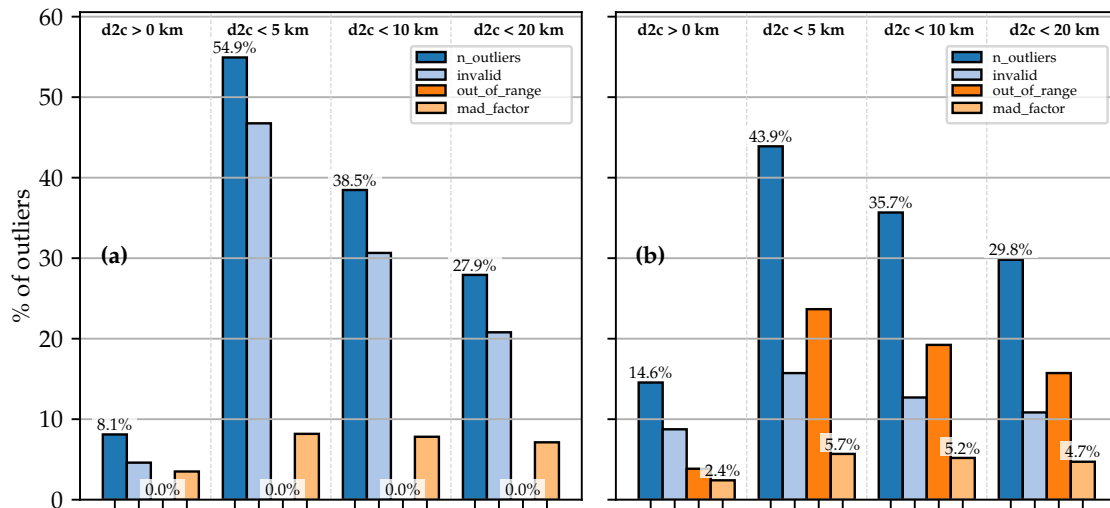


Figure 4. A comparison of outlier types as a function of dist2coast for the retracker (a) Brown-Peaky and (b) TALES.

In Figure 5, the outlier types of the two DDA retracker SAMOSA and WHALES-SAR are shown. Both exhibit a low amount of total outliers, as shown in Figure 3. SAMOSA’s major fraction of outliers mostly accounts for invalid estimates, no out\_of\_range values, and only few mad\_factor-type outliers. This signifies that it is capable of correctly identifying which values might be reliable estimates. The total amount remains relatively constant in the coastal zone with about 48%, even when further decreasing the dist2coast. In comparison, as shown in Figure 5b, WHALES-SAR (which still exhibits one of the best outlier characteristics of the investigated retracker) sets some SWH estimates to out\_of\_range values. This might arise from the fact that only a subwaveform is considered. Likewise, as with SAMOSA, the number of invalid points make up the majority of outliers and the number of mad\_factor samples remain relatively constant between about 3–5%.

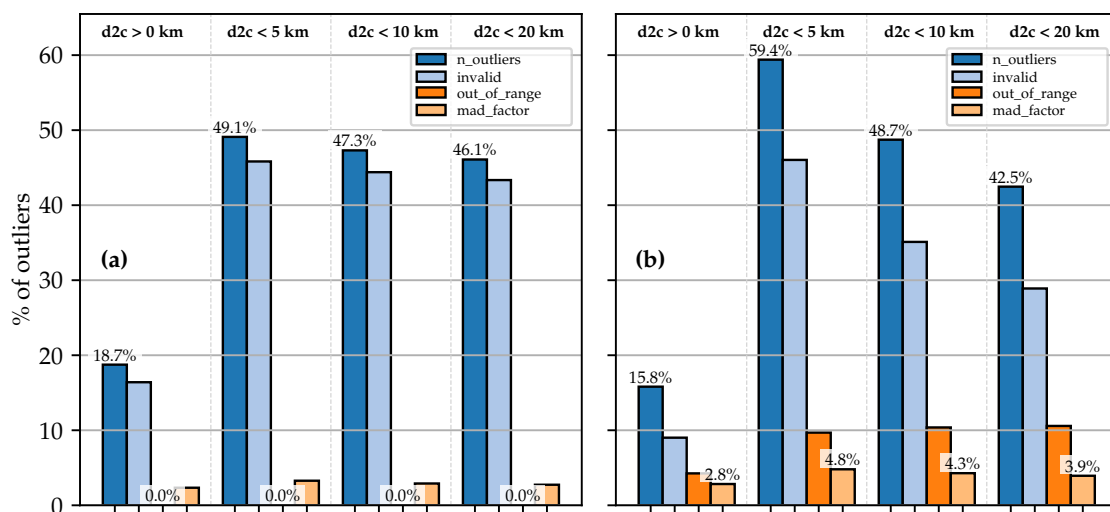


Figure 5. A comparison of outlier types as a function of dist2coast for the retracker (a) SAMOSA and (b) WHALES-SAR.

To conclude the outlier analysis, one can state the following points:

- The number of outliers is significantly increased in the coastal zone and increases further when approaching coast.
- In open-ocean, the number of total outliers amounts to less than 20%.
- Most of the retracker's outlier types are invalid samples, which originate from measurements, the quality flag of which is poorly defined.

#### 4.2. Noise Analysis

In this section, the intrinsic noise of the retracked datasets is evaluated. As described in Section 3.3, the noise is defined as the SD of a 20-Hz measurement of the along-track series.

As already noted in Section 2, an important fact to consider is that some of the investigated retracked datasets already have a denoising technique applied:

- J3: WHALES\_adj, WHALES\_realPTR\_adj, Adaptive\_HFA, and STARv2
- S3A: LR-RMC\_HFA, STARv2-PLRM

These datasets exhibit a reduced noise performance and need to be evaluated separately. It also has to be noted that some of the denoising techniques can be applied independently a-posteriori after the SWH estimates (L2 data) were retrieved so they can be applied to arbitrary retracker. Other retracker, such as the STARv2/STARv2-PLRM algorithm, have an inherent denoising implied.

Figure 6 depicts the median noise values of (a) J3 and (b) S3A in dependence of the area of interest: overall, coast, and open-ocean. For the J3/LRM-retrackers without denoising, Adaptive and WHALES have the least and second least median noise values of about 0.23 m. While also including denoised datasets into consideration, Adaptive\_HFA has the lowest median noise values with about 0.12 m, followed by STARv2 with about 0.18 m. For the S3A algorithms without denoising, DeDop-Waver shows the lowest median noise values with about 0.32 m. Among the denoised algorithms, STARv2-PLRM has the least median noise values with a slight increase for the coastal scenario from 0.17 to 0.25 m. This demonstrates the effectiveness of the used denoising techniques.

When analysing the dependence of the median noise values for open-ocean and coastal scenarios, one can notice a slight increase of noise, which is more or less pronounced on the individual algorithms. For instance, STARv2's value is increased from about 0.18 to about 0.24 m, whereas Adaptive\_HFA's value is increased by just 0.01 m. In conclusion, it can be stated that there is only a minor dependence on the dist2coast.

Figure 7 depicts the noise as a function of SWH and the different sea states, as defined in Table 4. The plots demonstrate the strong dependence of the sea state. The results are in accordance with the ones shown in Figure 6.

For LRM, Adaptive exhibits the best noise performance for all sea states (no denoising applied). With denoising applied, Adaptive\_HFA has the lowest noise level for low and average sea states, whereas STARv2 outperforms Adaptive\_HFA for high and very high conditions.

With respect to S3A and low sea states, the noise levels of WHALES-SAR, DeDop-Waver, LR-RMC\_HFA (denoised), and STARv2 (denoised) are at a similar level. For average, high and very high sea states, STARv2-PLRM shows significantly low noise values. This might be explained by the nature of the STARv2-PLRM algorithm, for which neighbouring SWH estimates are taken into account for reducing abrupt changes in the estimates and thus reducing the SD of the 20-Hz measurements (the same applies to the LRM version of STARv2). Thereafter comes the LR-RMC algorithm as the second best of the S3A retracker at average, high, and very high sea states.

For very low significant wave heights (SWHs) of less than 1 m, one can observe an increased noise level. This is due to the fact that sea states with very low wave heights induce a waveform with a very steep slope of the leading edge, which thus is undersampled. Smith and Scharroo [16] have investigated this issue and suggested a simple zero-padding, with which this effect can be mitigated.

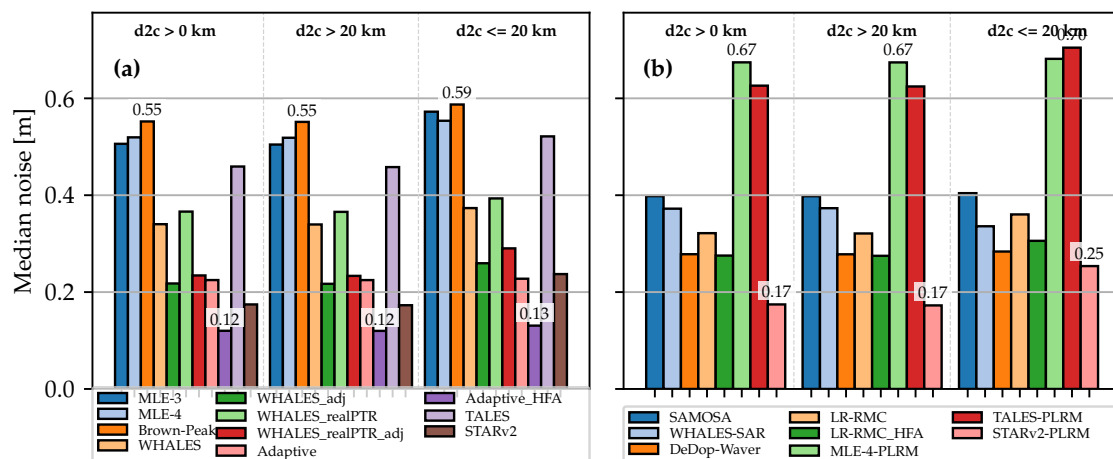


Figure 6. Median noise as a function of dist2coast for (a) J3- and (b) S3A-retracking algorithms.

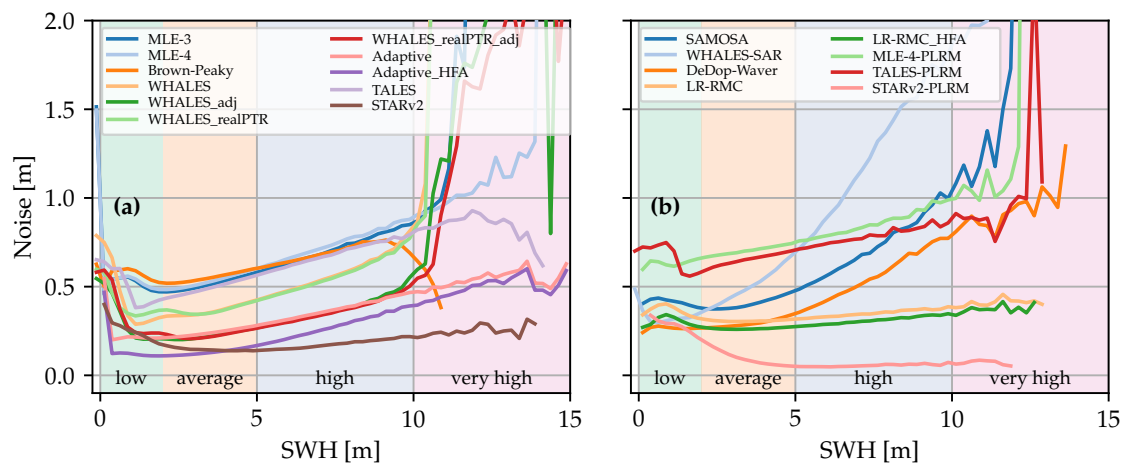


Figure 7. Noise level of the individual retracers as a function of significant wave height (SWH) for (a) J3- and (b) S3A-retracking algorithms with the sea state noted at the bottom.

Comparing the noise level of the standard retracers MLE-4 and SAMOSA (LRM vs. DDA) for low and average sea states, one can conclude that the performance is improved significantly, which is in accordance with the literature [59].

Furthermore, it can be stated that most of the novel retracers show significant improvements across all sea states, as compared with the standard retracers MLE-4 and SAMOSA. This is particularly pronounced for high and very high sea states, for which both retracers show at least twice as much noise level as compared to the novel approaches.

When comparing the absolute noise levels evaluated here with those mentioned in the literature, one can observe that they differ from each other. For instance, [27] has conducted a study in the German Bight and estimated the noise values of 6.7 and 13 cm (for SWH values around 2 m) for DDA and PLRM (considering open-ocean measurements with  $\text{dist2coast} \geq 10$  km), respectively. In [60], noise values were retrieved to be 8.5 cm and 11.09 for DDA and LRM for open-ocean scenarios across all sea states. Ref. [15] has compared the noise for a full cycle of the missions J3, S3B-LRM, and S3B-SARM, and estimated them to be 0.50 cm, 0.47 cm, and 0.38 m for SWH values of around 2 m, respectively. From this, it can be concluded, that the intrinsic noise performance strongly depends upon the region of interest, the sea state, and whether the coastal zone is included or not in the considerations. With the values evaluated in this RR exercise, ranging from 0.12 to 0.70 m, the findings are in accordance to the literature.

To sum up the noise analysis, the following can be stated:

- The intrinsic noise shows only a minor dependence on the dist2coast and strong dependence on the sea state.
- The noise of most of the novel retracking algorithms considered is lower than the baseline.
- DDA retrackers show a better noise performance than their adapted PLRM counterpart.

#### 4.3. Wave Spectral Variability Analysis

##### 4.3.1. Jason-3

Spectra of J3 LRM data were determined for around 62,000 segments (each including 1024 20-Hz measurements), except for TALES for which there were only ~50,000 segments because of the greater occurrence of flagged data for that retracker. The spectra of S3A data were estimated for about 24,000 segments for most of the retrackers. For TALES, only 15,000 segments were available. At long wavelengths, the spectra for all retrackers should predominantly relate to the real geophysical signal, whilst at the smallest wavelengths, it is similar to the measure of sensitivity to fading noise shown in Figure 6. In between these wavelengths, there are a variety of different behaviours.

First, considering the J3 LRM data (Figure 8a), one notes that the de facto reference provided by MLE-4 exhibits a “spectral hump” between 8 and 50 km [14]. Most of the newer algorithms have lower spectra levels than that within this band, whereas the simpler algorithm MLE-3 has higher noise levels for wavelengths of 8 km and upwards. This may indicate that the actual waveform shapes are responding to other factors, for example, slight variations in sea surface skewness [61] or in the angle between the surface perpendicular and the antenna boresight that are better represented by the MLE-4 algorithm. In the absence of any waveform bins being deemed to contain anomalous peaks, the Brown-Peaky algorithm effectively reverts to MLE-4; thus, its mean/median spectrum is similar to that of MLE-4, although it does exhibit extra variability in the 8–25 km band. TALES shows slightly lower noise levels than MLE-4 for all scales below 25 km, but the difference is always less than 10%.

The four flavours of WHALES have almost identical behaviour at large wavelengths, with their associated power levels below 50 km being at least 45% lower than for MLE-4, with those having a correction for covariant errors [35] being significantly lower again for scales under 15 km. Those versions of WHALES incorporating a bespoke PTR correction show slightly greater noise levels than those corrected using an empirical LUT. For the Adaptive algorithm, which already has one of the lowest noise levels, the version with the HFA again reduces the noise level at scales below ~50 km. This latter adjustment is effective over a longer span of scales (i.e., all those below 50 km) than the WHALES version (<15 km) partially because it calculates height anomalies relative to a longer along-track scale.

Finally, the performance of STARv2 is noteworthy, in that it achieves the lowest spectral levels in the 25–100 km range of wavelengths but has produced an unexpected spectral shape. The procedure it uses for fitting a SWH profile through the cloud of solution space certainly amounts to significant filtering, reducing the noise levels; however, the cause of the undulations in the spectrum are not yet understood.

Whilst there are many buoys providing frequency and directional spectra of waves, these give no indication on the spatial variability of wave properties. For spatial scales of the order 10 to 200 km and away from shorelines, the variability of SWH seems to be dominated by the effect of surface current on the waves, with a spectrum of SWH that closely follows the shape of the spectrum of the current kinetic energy [62]. The negative slope of the kinetic energy (KE) spectrum reflects the cascade of energy from large mesoscale features to smaller scales, with a typical slope close to  $k^{-2}$  [63,64]. The influence of wave–current interactions means that different wave spectra may be encountered in regions with pronounced current variability [Villas-Boas et al., in prep.]. The dashed lines indicate slopes in the 50–100 km range of  $k^{-2}$  and  $k^{-3}$ , as aids for comparison as been done in [37].

### 4.3.2. Sentinel-3A

Figure 8b shows the spectra obtained from the S3A data. At the long wavelength end ( $\sim 300$  km), most curves converge to the same value as noted for J3 because, at this scale, the variability in SWH is dominated by the real large-scale signal. Again, TALES has slightly lower power levels than MLE-4 through all scales, with less of a pronounced spectral hump around 10 km, and the STARv2 retracker produces much lower levels but does not have the features manifest in the output of other algorithms. At scales below 100 km, the algorithms based on PLRM data broadly match their equivalents for J3; however, the noise levels are higher because these waveforms correspond to the averaging of  $\sim 36$  independent pulses, whereas for J3 it is 90. The SWH spectra for MLE-4-PLRM and TALES-PLRM at scales below  $\sim 30$  km are roughly twice that of their J3 analogues; for STARv2-PLRM, the factor is only  $\sim 1.4$ , but this may be due to the details of the process used to fit an SWH profile through its solution space.

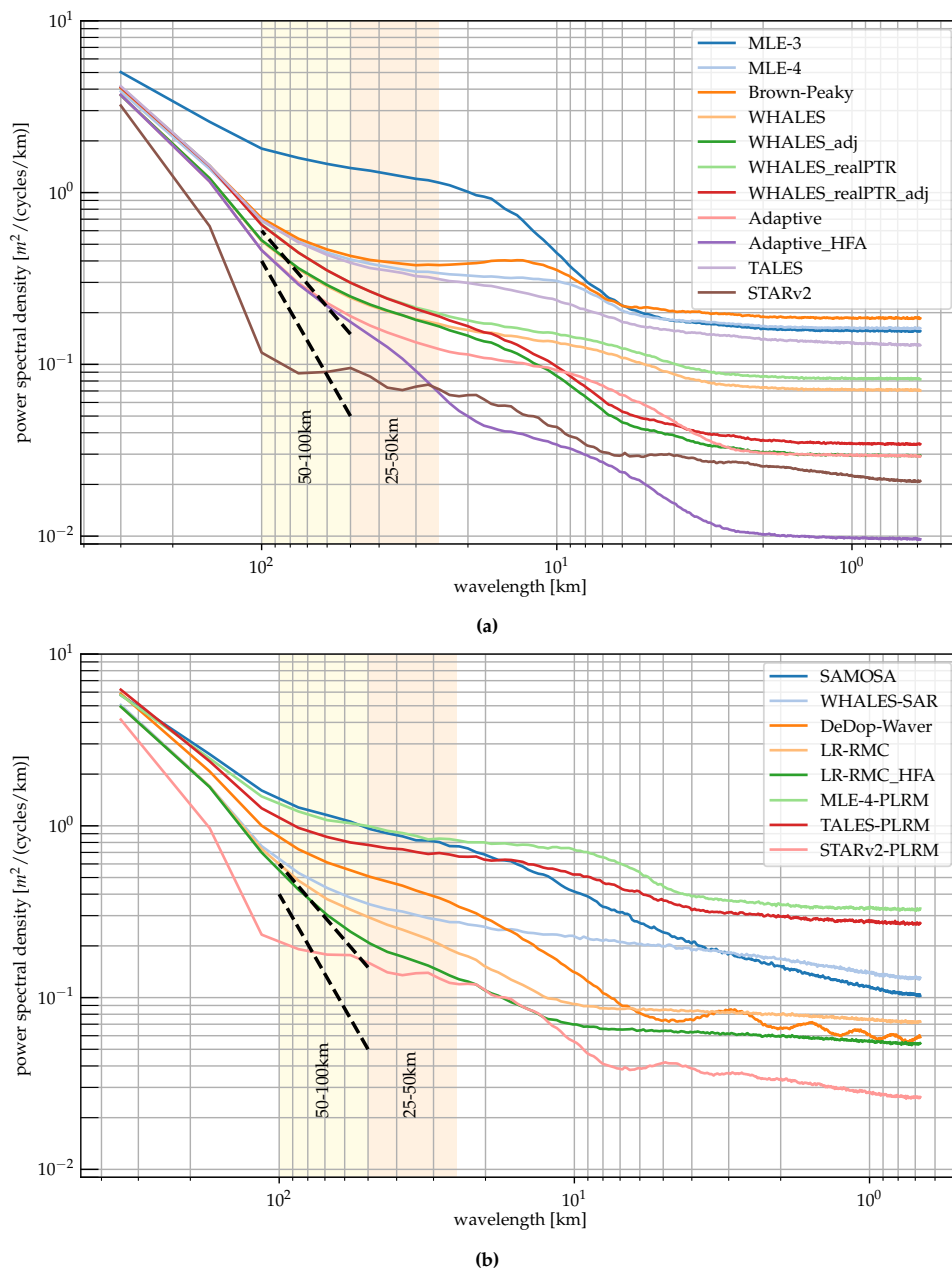


**Figure 8.** Mean spectra of SWH from the various retrackerers, calculated from 1024-point segments using the Welch periodogram method. (a) LRM retrackerers for J3. (b) LRM (applied to PLRM) and DDA retrackerers for S3A. The dashed lines indicate the spectral slope associated with processes giving a  $k^{-2}$  or  $k^{-3}$  spectrum.

Of the retrackers that make use of the DDA waveforms, all the new ones show reduced noise levels compared with SAMOSA. The WHALES-SAR algorithm shows much lower spectral levels than SAMOSA between 4 and 200 km, with SAMOSA only outperforming it at the finest scales. The LR-RMC algorithm has significantly lower noise levels than WHALES or SAMOSA over all scales below  $\sim 50$  km, with the application of the HFA significantly reducing noise levels at wavelengths below 50 km. The DDA retracker DeDop-Waver also has very low noise levels at the shortest scales but shows undulations in the spectrum below 7 km.

The DeDop-Waver dataset was originally calculated on a different set of nominal waveform locations, and then linearly interpolated to the same locations as the other datasets. Simulation work by Chris Ray (pers. comm. 2020) suggests that this is likely to be the cause of the undulations in its spectra. This linear interpolation will also cause the analysis of its noise levels to lead to slightly lower values than would have been the case if that dataset had matched the same locations as the others.

There have been many authors in the last decade who have looked at spectra of sea surface height from altimetry, with the largest wavelengths showing a clear geophysical signal, the smallest wavelengths being totally measurement noise, and with indications of a “spectral hump” [14] in the range of 8 to 50 km. Sandwell and Smith [40] had earlier shown a plateau in the spectrum associated with MLE-3 applied to ERS-1 data, but as their “two-pass” retracking solution involved filtering the initial SWH estimates, it does not yield a meaningful curve for SWH spectra. The most useful prior example is from the seminal work by Dibarboure et al. [14] as they contrast SWH spectra from Jason-2 (J2), CS2 DDA and CS2 PLRM, noting that the much smaller along-track resolution of the DDA led to spectra without the hump observed in other datasets. That paper showed major gains from DDA processing but was based only on sections across a patch of quiescent ocean. Our analysis, averaging spectra throughout the global ocean still shows “power excess” in the 10 to 50 km band, but this may reflect different pertinent geophysical processes in this regime, such as wave-current interactions.

#### 4.4. Comparison against Wave Model

The statistics of the comparison of the 1-Hz retracked data against the ERA5-based hindcast (ERA5-h) wave model, which does not assimilate any satellite altimetry data, are shown in Figure 9 and Figure 10 for J3 and S3A as a function of dist2coast and the sea state on the left and right columns, respectively. As described in Section 3, the three metrics correlation, median bias, and SDD are presented and discussed in this section.

It needs to be emphasised at this point of the analysis that the comparison against the wave model is limited to the resolution of the ERA5-h wave model (which is 18 km). Since the posting rate of the SWH series and the model are reduced to 1-Hz, potential high-frequency variations of the SWH series might, thus, be masked or some retrackers that inherently smoothen the SWH series might benefit from this type of analysis (e.g., STARv2 or the \_HFA variants). In consequence, this means that if a retracking algorithm, such as STARv2, is strongly filtering an SWH series, it might show an excellent correlation against the wave model and a low SDD, which is shown in the following subsections. However, at the same time, the smoothened SWH series lacks a significant amount of energy, as discussed in Section 4.3.

Moreover, a wave model has limitations in the coastal zone, where wave interactions with bathymetry and land-shading effects often require regional nested very high resolution models to improve the simulations. Therefore, this assessment is complementary to the use of a ground-truth such as a large buoy dataset but can still be useful to derive further noise characteristics of the retracking w.r.t. an independent source and erroneous estimates of SWH (although realistic and therefore not detectable by the outlier analysis) near the coast.

#### 4.4.1. Jason-3

Figure 9 depicts the comparison statistics against the ERA5-h model for the retracked Jason-3 (J3) datasets. In the first row, the correlation coefficient is presented as a function of dist2coast and sea state. Apart from MLE-3, all retrackers show a very good correlation with a coefficient of around 0.97 for the overall and open-ocean scenario. However, in the coastal zone, MLE-3, MLE-4, and TALES show a deteriorated performance with a correlation of 0.8–0.85 (0.49 for MLE-3). The rest of the retrackers show a very high correlation of 0.96 in the coastal zone. For average and high sea state the differences are less pronounced with most of the retrackers showing a high correlation of around 0.92. For low sea states, Adaptive, and STARv2 prove the best correlation with values of around 0.87, whereas MLE-3, MLE-4, and TALES show degraded correlations. For very high sea states, all retrackers (apart from Brown-Peaky) show similar degraded correlations of around 0.72.

The median bias in the second row of Figure 9 depicts how much the SWH is different from the model, with lower values indicating a more accurate dataset. In this case, the median bias depends on both the area of interest and the sea state. For coastal scenarios, it can be said that the estimates tend to be overestimated (meaning the retracked value is higher than the model, recall Equation (2)), whereas for open-ocean the retrieval are rather underestimated. With an increasing sea state, the median bias also tends to increase. STARv2 strongly underestimates large wave heights, showing a median bias of 0.51 m. (Figure 7-top [23]) has plotted the monthly bias for MLE-4 (J2 mission), which ranges at around 0.1 m (sign was aligned, since the definition of the bias is vice versa), which is in accordance of the median bias value of around 0.08 m in Figure 9 (centre row, left for dist2coast > 0 km).

The last row of Figure 9 depicts the SDD. All retrackers show comparable SDD values of around 0.20–0.40 m for very high sea states. MLE-3, MLE-4, and (partially) TALES show increased values for low and average sea states and particularly in the coastal zone. In [22], an SDD value of 0.20 m was reported for MLE-4 for the SARAL/AltiKa mission, which is in good agreement with the value of about 0.25 m, when considering an average sea state as shown in Figure 9 (last row, right).

In conclusion, most of the retrackers show similar performances in terms of correlation, median bias, and SDD for coastal, open-ocean scenarios and most of the sea states, when comparing the 1-Hz retracked data with the ERA5-h wave model. WHALES and WHALES\_realPTR is the second best, still showing a high correlation. MLE-3, MLE-4, and TALES exhibit a deteriorated performance, especially in the coastal zone.

#### 4.4.2. Sentinel-3A

The assessed Sentinel-3A (S3A) retrackers show for the overall and open-ocean scenarios a very high correlation against the ERA5-h wave model of around 0.96 (with the exception of SAMOSA: 0.89). This also applies to the coastal zone, where all retrackers exhibit a high correlation of around 0.95, with the exception of MLE-4-PLRM (~0.75), TALES-PLRM (~0.85) and the standard L2 product SAMOSA (0.43). All retrackers (apart of SAMOSA) show a very good correlation of ~0.9 for average and high sea states. With respect to low sea states, LR-RMC/LR-RMC\_HFA have the highest correlation of 0.88, followed by WHALES-SAR, STARv2-PLRM, and DeDop-Waver, which amount to around 0.83. SAMOSA shows the worst correlation across all sea states. None of the algorithms are able to correctly retrieve very high sea states, with an average correlation of about 0.2 (SAMOSA: around 0.0). The inaccurate estimates for very high sea states might be explained by the very few samples that are available in all datasets: Out of the 512 netCDF files (pole-to-pole tracks), there are only around 260 1-Hz SWH estimates apparent (in comparison for the J3 analysis: around 2100). STARv2-PLRM shows an inverse correlation of  $-0.20$  for very high sea states, which again can be attributed to the scales of denoising that are likely to be too wide to correctly observe areas with very high waves. The authors of [23] have reported correlation values of 0.98 and 0.94 for the CS2 NE Atlantic and Pacific Box, with the latter one being placed in the open-ocean. These are in a rough accordance to the evaluated value of 0.90, as shown in Figure 10 (top row, left, dist2coast > 0 km).



The median bias has only a minor dependence of the dist2coast. LR-RMC, LR-RMC\_HFA, MLE-4-PLRM, TALES-PLRM, and STARv2-PLRM show a very small median bias of less than 0.10 m in the coastal zone. SAMOSA exhibits a very large bias in the coastal zone with a value of  $-0.47$  m, which is in accordance to the degraded correlation, as discussed before. The LR-RMC variants incorporate almost no median bias in open-ocean and in all sea states with less than 0.05 m. For very high sea states, most of the retrackerers have a high median bias. This is as expected from the correlation analysis and might be due to the very few samples that are available for such high sea states. The bias that was retrieved for SAMOSA in the NE Atlantic or Pacific Box of CS2 is very low with values of about  $-0.08$  m and  $-0.03$  m (sign swapped by authors, since the definition of the bias is swapped), as shown in (Figure 5 [23]), which is very well in accordance with the bias value of  $-0.06$  m for the average sea state (Figure 10, centre row, right).

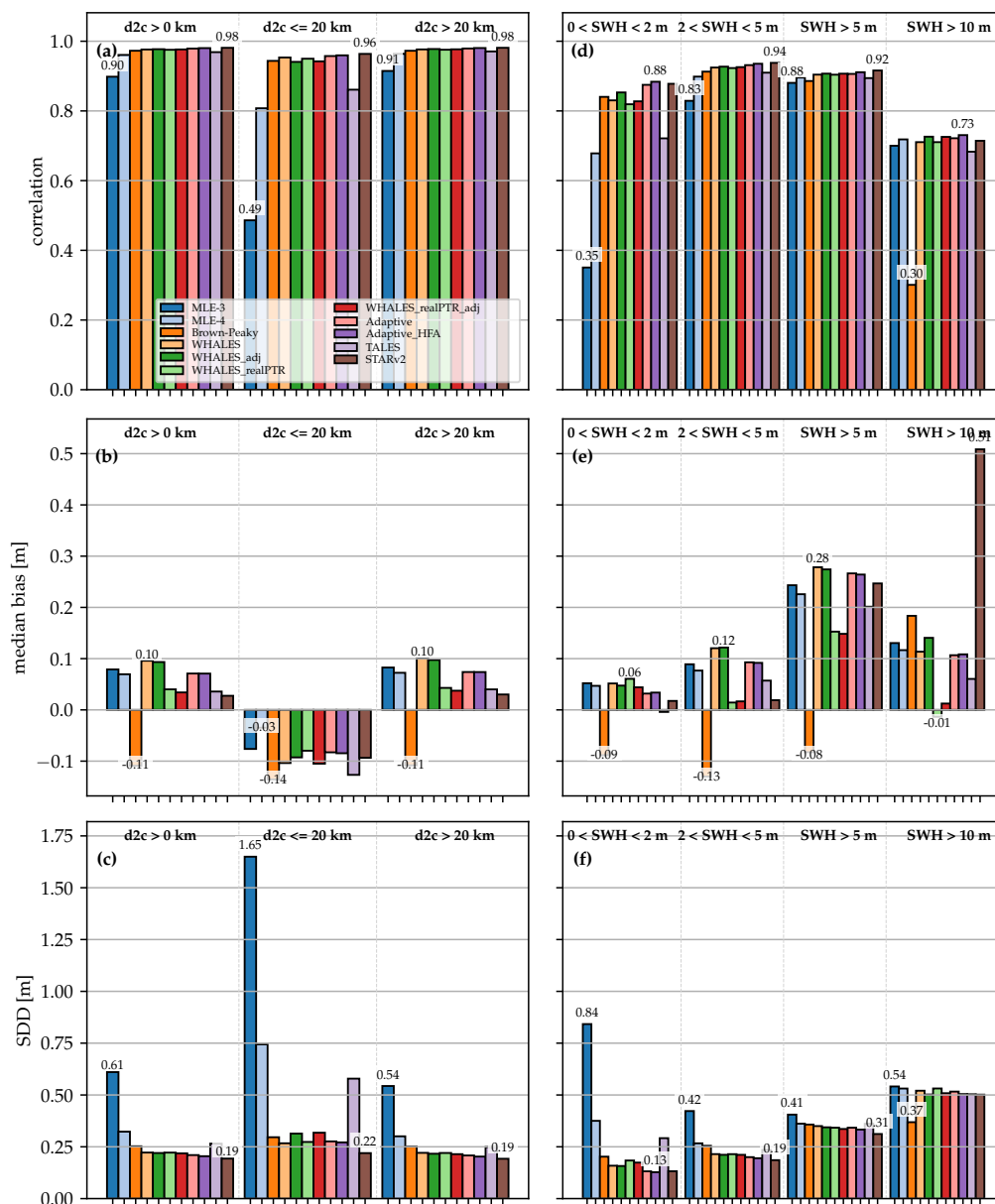


**Figure 9.** Comparison of the (a,d) correlation coefficient, (b,e) median bias, (c,f) SDD against ERA5-h model of the individual J3 retrackerers as a function of dist2coast and of SWH, respectively.

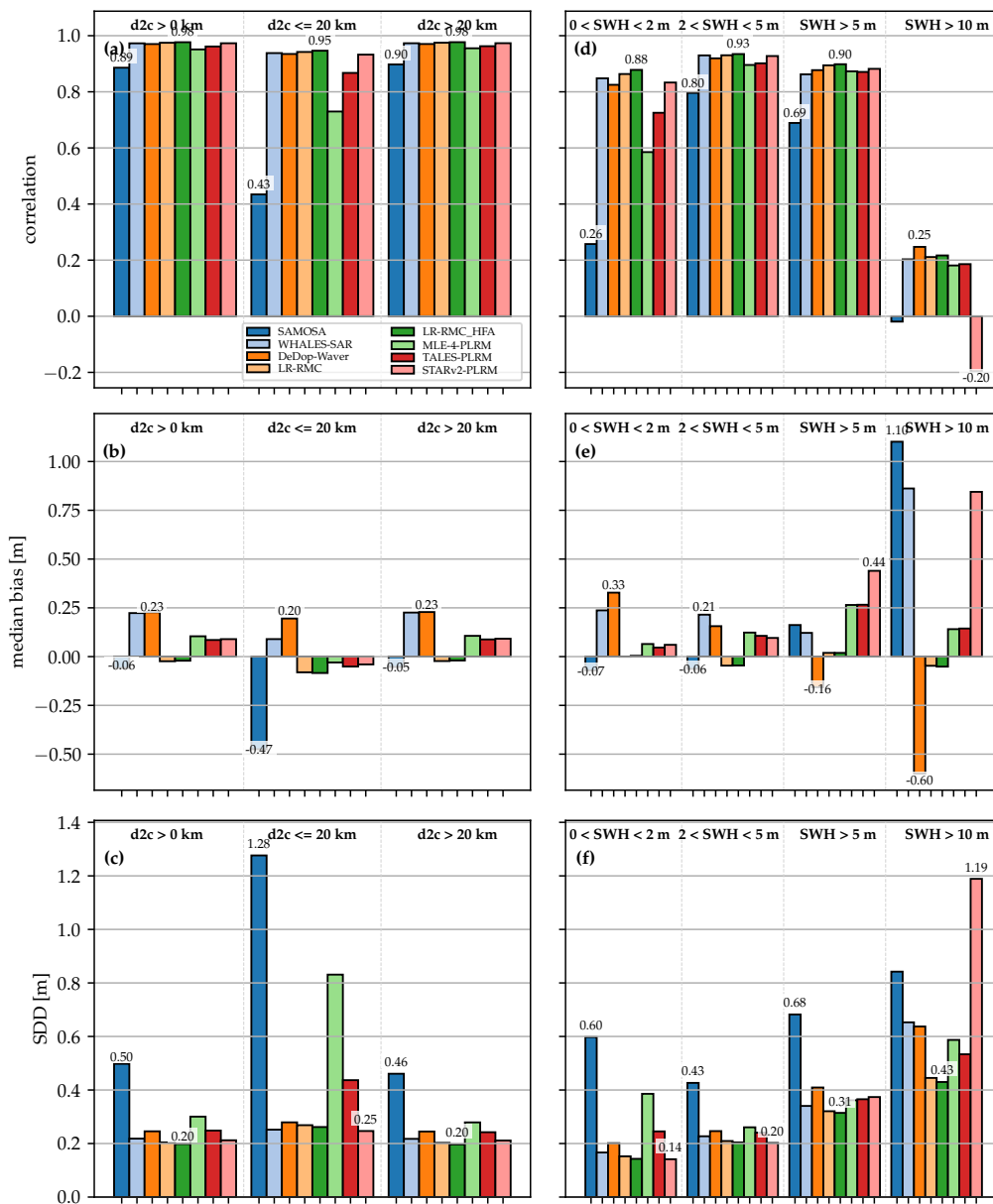


**Figure 10.** Comparison of the (a,d) correlation coefficient, (b,e) median bias, (c,f) SDD against ERA5-h model of the individual S3A retrackerers as a function of dist2coast and of SWH, respectively.

As the majority of the retrackerers (WHALES-SAR, DeDop-Waver, LR-RMC/LR-RMC\_HFA and STARv2-PLRM) shows a good very good correlation in the coastal zone, the SDD also amounts to a very low value of around 0.25 m. All LR-RMC ranks best among the non-denoised algorithms with a strongly deteriorated performance in the coastal zone, showing an SDD value of 0.65 m. Most of the retrackerers show an increasing SDD for the average, high, and very high sea states starting from around 0.30 m. Particularly the PLRM variants (excluding STARv2-PLRM because of its inherent denoising) show increased SDDs both in the coastal zone and for low and very high sea states. This is in agreement with the findings of (Figure 21 [28]), which demonstrates a significantly increased SD for TALEs as compared to an improved SAMOSA-based DDA retracker (SAMOSA+) within the coastal zone. The authors of [23] have assessed SDD values of 0.30 and 0.18 m for the CS2 NE Atlantic Box and Pacific Box. Compared with the value of 0.50 m of SAMOSA as shown in Figure 10 (bottom row, left), the difference is quite significant but might be explained with smoother and less variable conditions in

the tropical Pacific (in the dataset of [23]). Another reason might be the extreme sea states that are included in our investigated datasets, which show a poor correlation as elaborated before.

To sum up the results of the comparison against the ERA5-h analysis, the retracers WHALES-SAR, DeDop-Waver, LR-RMC, and STARv2-PLRM show all a comparable good accuracy and precision. The differences are only minor for both open-ocean and coastal scenarios. LR-RMC shows the smallest median bias values for open-ocean and across all sea states. The differences in terms of correlation and SDD are not significant for the retracers WHALES-SAR, DeDop-Waver, LR-RMC, and STARv2-PLRM. In general, the estimates for very high sea states are very poor for all retracers, very likely due to the scarcity of available records.

An important fact that was not considered in this evaluation is the numbers of valid 1-Hz measurements that is mainly attributed to the supplied quality flag. As described in Section 4.1, the retracers show significant differences in terms of number of outliers. Two of the best performing algorithms LR-RMC and STARv2-PLRM also show the highest number of outliers in the coastal zone with less than 20 km. It becomes obvious here that it is a trade-off between quality and quantity of the measurements.

#### 4.5. Comparison against In-Situ Data

The performance of retracking algorithms is estimated by using buoy datasets described in Section 2. The J3 dataset contains about 7100 records of SWH collocated with altimeter individual tracks and S3A dataset contains about 2500 collocated records. These data are processed and compared with the outputs of different retracking algorithms, as described in Section 3.6. The results of this comparison are summarised in Figure 11 for J3 and Figure 12 for S3. The statistical metrics are estimated as a function of dist2coast for all available data, open-ocean, and coastal zone and also of sea states. It is worth noting here that comparison results are not available for sea state SWH > 10 m, since the in-situ buoy dataset only contains records with smaller waves heights.

To identify unreliable buoy measurements, an error  $Err_{buoy}$  is estimated between each buoy and retracked data (see Section 3.6). In total, 4 out of 125 buoys in J3 dataset and 1 out of 170 buoys in S3A dataset were identified as completely unreliable and discarded from the comparison with altimeter measurements.

##### 4.5.1. Jason-3

The estimates of correlation coefficients for coastal waters, open-ocean, and different sea state conditions, are shown in the top row of Figure 11. Overall, the highest correlation is found for the STARv2 retracking algorithm and the lowest correlation is noted for MLE-3, WHALES\_adj and WHALES\_realPTR\_adj. At the same time, MLE-4, WHALES and WHALES\_realPTR retracers demonstrate a performance similar to that for Adaptive and TALEs retracers. It is seen in the left plot in Figure 11 that, for all retracers, the dist2coast has a significant effect on their performance. For STARv2 retracker, the correlation coefficient reduces from 0.98 in the open-ocean to 0.92 in the coastal zone, and for WHALES\_adj it drops from 0.9 to 0.59. The right top plot in Figure 11 shows how the performance of retracking algorithms is affected by the sea state condition. For all retracers, the best performance is achieved for average sea states, while for low sea states are the most challenging one. For all three sea states in the plot, the best performance is demonstrated by STARv2 retracker and the second best is Brown-Peaky. The worst results are given by MLE-3, WHALES\_adj and WHALES\_realPTR\_adj retracers.

The middle row in Figure 11 shows median bias (i.e., buoy minus altimeter) for different conditions, such as dist2coast and sea states. In these plots, MLE-3 and MLE-4 retracers produce the lowest bias values. Brown-Peaky retracker has the highest bias with the exception of the coastal zone where the highest value belongs to TALEs algorithm. For low sea states, the median bias is negative for all of the tested retracker algorithms; this reflects that for SWH < 1 m, the waveform bins at ~0.47 m separation, are unable to resolve well the slope of the leading edge, and thus all algorithms tend to

give values that are too large. For high sea states (SWH > 5 m), the median bias remains negative only for Brown-Peaky, WHALES\_realPTR and WHALES\_realPTR\_adj retrackerers. Hence, limitations of retracker algorithms become more apparent in calm sea conditions.

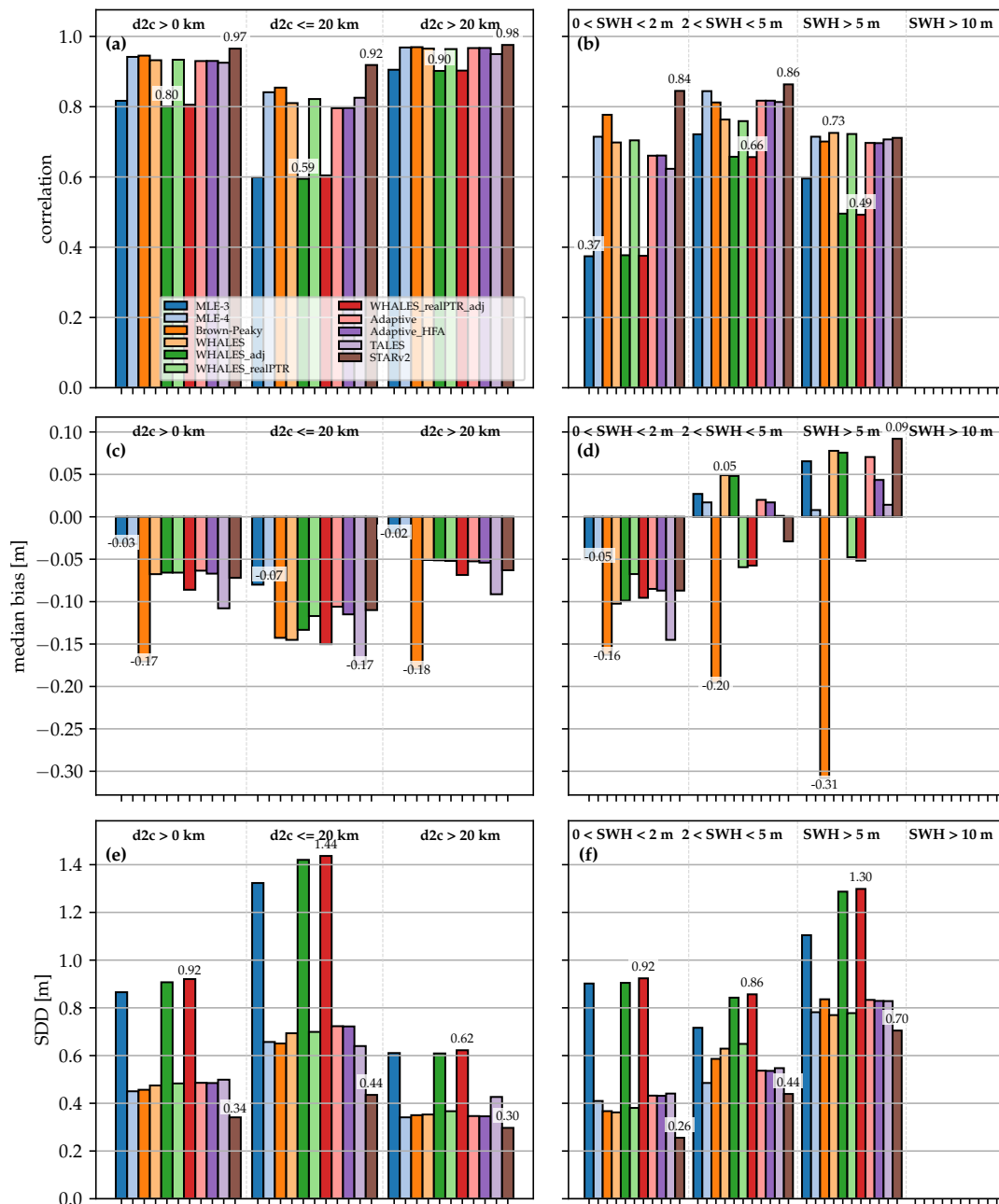


**Figure 11.** Comparison of the (a/b) correlation coefficient, (c/d) median bias, (e/f) SDD against in-situ buoy data of the individual J3 retrackerers as a function of dist2coast and of SWH, respectively.

Overall, the median bias values are much smaller than SDD values shown in the plots in the bottom row of Figure 11. For the open-ocean and coastal zone, the SDD metric behaves similar to the correlation coefficient. The best results are achieved by STARv2 retracker and the worst performance is demonstrated by MLE-3, WHALES-adj and WHALES\_realPTR\_adj. These three algorithms show the worst results for the average sea state conditions and their performance is also poor for the low and high sea states. STARv2 has the lowest values in all three regimes and gives its best performance

in terms of SDD for the low sea states and the worst one for the rough sea. Generally, other retrackerers demonstrate similar behaviour, with increased SDD at higher SWH.

#### 4.5.2. Sentinel-3A

Figure 12 shows the comparison results with buoy data for five DDA retracker algorithms and three PLRM algorithms. The plots of correlation coefficient show the worst performance is achieved by SAMOSA retracker and MLE-4-PLRM is the second worst. All other retrackerers demonstrate similar values of correlation coefficient. In general, the correlation is higher for the open-ocean than for the coastal zone. For the average sea state, it is slightly higher than for the low sea state, but values are significantly decreased for high sea states. However, the plots do not show any obvious advantages of DDA over PLRM retracking algorithms.

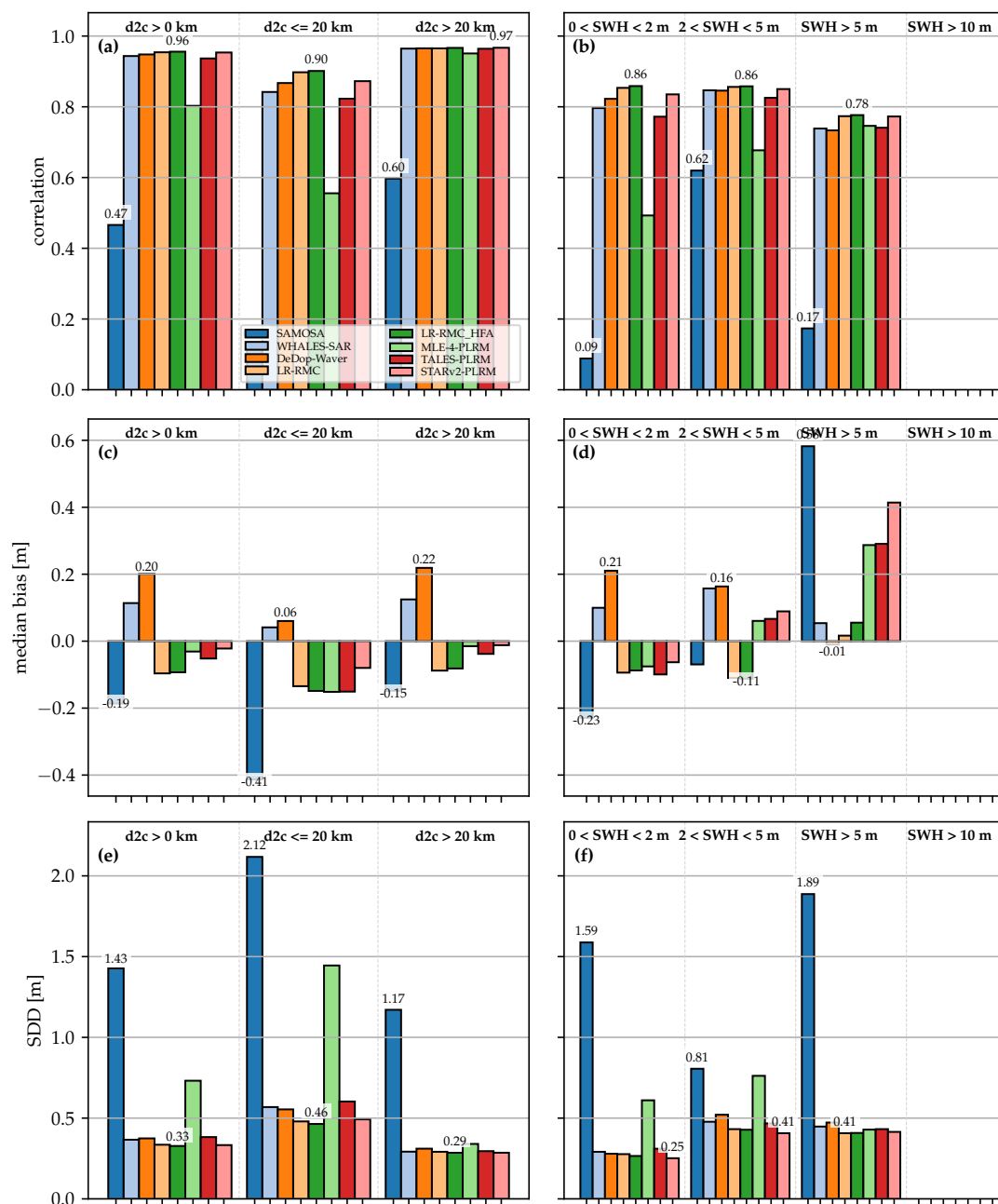


**Figure 12.** Comparison of the (a/b) correlation coefficient, (c/d) median bias, (e/f) SDD against in-situ buoy data of the individual S3A retrackerers as a function of dist2coast and of SWH, respectively.

In contrast to similar plots for J3, the plots of SWH median bias Figure 12 shows a changing sign of offset for different retrackerers. For the coastal zone and for rough sea conditions, the highest and negative bias is estimated for the SAMOSA retracker. The lowest bias is found for the MLE-4-PLRM algorithm in the open-ocean and for the average sea state.

The plots of SDD in Figure 12 confirm the poor performance of SAMOSA retracker in all conditions and sea states, revealed by the correlation coefficient. While MLE-4-PLRM is the second worst retracker in the plots after SAMOSA, it demonstrates relatively good accuracy in the open-ocean and for the high sea state conditions. For all other retrackerers, the SDD values are getting higher in the coastal zone and for average or high sea states. The plots of SDD metric show STARv2 and LR-RMC (and LR-RMC\_HFA) giving the best results but do not reveal any advantages of PLRM over DDA retrackerers or vice versa.

There are dangers in comparing our results with prior studies, as the period of study, the mean wave conditions, and the quality of the buoy dataset may all vary. This is why a full comparative evaluation of algorithms should always be performed applying the algorithms to the same altimeter data and with the same in-situ measurements. Our work showed a typical mismatch, SDD, in the open-ocean of 0.35 m for J3 and 0.30 m for S3, with this value encompassing buoy measurement error, altimeter error, and spatiotemporal variations between the buoy and altimeter locations and times of recording. These SDD values increased to 0.8 and 0.4 m, respectively, when the buoy SWH exceeds 5 m. For typical open-ocean conditions, Yang and Zhang [25] had SDD values of 0.25 m and 0.30 m for S3 DDA and PLRM estimates, respectively, whilst earlier analyses for other altimeters had returned values of 0.25 to 0.30 m [65,66], whereas [67] and [68] had processing systems that credited values of 0.15 to 0.21 m to the same instruments.

Until recently, there have been few attempts to produce estimates for the coastal zone, and the results tend to be very specific for each location, and the editing and selection criteria used. Our results show SDD values of 0.7 m for J3 and 0.5 m for S3 within 20 km of the coast. Wiese et al. [69] achieved errors of 0.5 and 0.4 m, respectively, within 10 km of the coast around the North Sea, whilst Idris [70] showed errors for J2 of 0.2 to 0.4 m within 10–15 km of the Malaysian coast, but the correlation values were low because that is an environment of nearly always low sea states. Thus, our present paper is the first, to our knowledge, to compare multiple algorithms for different altimeters using a consistent approach across a wide network of buoys (albeit that most are located around Europe and the U.S.).

#### 4.6. Selection and Decision Process of ESA SeaState\_cci Consortium

One of the main objectives of the ESA SeaState\_cci project is to produce a consistent climate-quality time-series of SWH estimates across different satellite missions, of which the data was recorded in the past 25 years [71].

For each LRM and DDA, two retracking algorithms are to be selected. PLRM algorithms are not considered at all but used as a direct comparison against the DDA (while practically using the same dataset). Two algorithms are selected for each mode due to practical limits that might arise during the processing porting of the algorithms into a production environment. The selection is based upon criteria described in the SeaState\_cci User Requirement Document [72], i.e., the stability of estimates across different missions, accuracy, and stability of high sea state values, and the accuracy in coastal scenarios. In addition, a survey of SeaState\_cci users was conducted during the project, the outcome of which is that the users of the produced SeaState\_cci dataset have a high interest in long-term SWH data, extreme events, and their impact on the coast [73].

Based on these requirements and in order to objectively evaluate the retracking algorithms, both qualitative and quantitative criteria were formulated. The quantitative are listed in Table 5. Hence, the ranking of the retrackerers is performed based on the the weighting factors, which are chosen such that they suit the requirements of the SeaState\_cci project and its users. Two evaluations are used, a weighted metric scores and a weighted metrics results approach. Both metrics yield the same result, with one exception: WHALES-SAR and DeDop-Waver share the second place among the DDA retracking algorithms, as each of them wins one out of the two scoring schemes.. The qualitative

assessment criterion includes the analysis of the wave spectral variability. It is assumed that below a certain level of the PSD of a SWH series, a certain amount of the signal energy is missing. Hence, two PSD levels  $0.2 \text{ m}^2/(\text{cycles}/\text{km})$  and  $0.05 \text{ m}^2/(\text{cycles}/\text{km})$  were defined for the spectral wavelengths of 100 and 50 km. If the level of a retracked datasets is below these limits, one expects that a significant amount of energy is missing and the retracked SWH does not correspond to a realistic global climate. STARv2 and STARv2-PLRM are the retrackers that break the limits. They are, thus, excluded from the consideration of the ranking.

**Table 5.** Quantitative criteria for ranking the retracking algorithms.

Weighting Factor	Criteria
0.3	Accuracy against wave model for global areas (SDD)
0.3	Accuracy against coastal buoys (SDD)
0.1	Accuracy against wave model for high sea states (SDD)
0.1	Accuracy against wave model for very high sea states (SDD)
0.1	Intrinsic noise (SD)
0.1	Intrinsic noise for the coastal zone (SD)

In conclusion, the retracking algorithms are ranked by taking Table 5 into account, and the retrackers in Table 6 are considered to be the most suited candidates for LRM and DDA altimetry:

**Table 6.** Selection of the SeaState\_cci project management and production team.

Rank	Mode	LRM	DDA
	1.	Adaptive	LR-RMC
2.	WHALES	WHALES-SAR/DeDop-Waver	

## 5. Round Robin Assessment Retrospective

The RR assessment was defined within the SeaState\_cci project. No comparable, objective assessment of different retracking algorithms was conducted before in the field of satellite altimetry. The metrics that were extracted from the datasets were taken, carefully selected, and combined from different sources in the literature. Most of the recent works in this regard limit their assessment to a subset of metrics, or a few or a single retracking algorithm for comparison, or investigate only a regional study area. For these reasons, no pre-defined rules could have been taken for performing such a comprehensive comparison.

The whole framework of the RR exercise was, thus, defined beforehand. During the performance of the RR, a lot of experience was gained, whereby several possible improvements were revealed to the definition of the RR procedure.

The following listing gives a retrospective about the process of this RR assessment:

**EUMETSAT processing baseline was updated.** As announced in [74], a new S3 Processing Baseline (PB) 2.61 (baseline collection (BC) 004) was released by EUMETSAT in January 2020, which reprocesses the data starting from the beginning of the mission. This also affects the L2 products from EUMETSAT, including the retracked SAMOSA dataset. One of the changes is related to the software issue of the SAMOSA retracker that fixes an SWH misestimation for the 20-Hz data. Since the inclusion of the new BC would have yielded an incompatibility with the processed L1 data (baselines 002 and 003), the updated SAMOSA dataset (with the updated BC 004) could not be taken into account for this assessment. However, for future assessments, the updated SAMOSA dataset is to be included, potentially aiming a better performance.

**Selection of in-situ buoy data.** The intention of the design of this RR analysis was to be all-encompassing, making full use of all data available. All the buoys were within 50 km of the

nominal altimeter tracks, and in the open-ocean points this far apart will usually be experiencing the same wave conditions at roughly the same time. This is why Monaldo [31] established that distance as a suitable match-up for altimeter-buoy comparisons in the open-ocean. That criterion has been used by many researchers since, although Ray and Beckley [67] argued that good comparisons could be achieved at up to 70 km. However, the use of such data far from the altimeter track is more questionable when the locations are within 20 km off the coast, as coastal headlands and shoaling bathymetry may affect the propagation and intensity of waves.

Nencioli and Quartly [26] developed a methodology to use model data to help inform the choice of suitable match-ups, showing that some locations 20 km apart could be poorly correlated, whereas other locations much further away but with good exposure would give equivalent measures for validation purposes. In particular, it was noted that a small number of the buoys selected from our validation exercise were in well sheltered locations unrepresentative of those conditions further offshore. However, it had been agreed that all possible data should be used, so there was only minimal discarding of poorly-located buoys.

Similarly, it is noted that some buoys were of a different construction and with potentially different calibrations. All buoys were used in the expectation that errors in the in-situ measurements would affect the assessments of all retracers similarly. Furthermore, the agreed methodology was to use the median of the nearest 51 altimeter records, even if only a few of them were valid. A more meaningful comparison would be to only calculate a mean when a high proportion of the estimates are valid (as an indicator that tracking is working well and that the waveforms are not anomalous). The implications of being more selective in the altimeter and buoy data used will be the subject of a further paper.

## 6. Conclusions

In this work, an objective assessment of several LRM and DDA retracking algorithms has been conducted. Five different types of analyses have been performed for evaluating the performance of the retracking algorithms as a function of *dist2coast* and sea state: outliers, noise, wave spectral variability, comparison against wave model, and in-situ buoy data.

The performance of the retracers strongly depends on both *dist2coast* and sea state, which makes it fairly challenging to select “the” best performing retracking algorithms. Several general conclusions can be drawn from the findings of the analyses. Those are really helpful in identifying the shortcomings of the current state-of-the-art retracking algorithms and are, thus, crucial for potential improvements. The following list summarises our conclusions:

**Significant improvements as compared to standard retracers.** Most of the novel retracking algorithms outperform the standard retracers MLE-4 and SAMOSA for LRM and DDA altimetry in the majority of the metrics. The difference between the standard retracers and the best performing novel retracker is even more pronounced for DDA, particularly when considering the intrinsic noise characteristic or the accuracy in the coastal zone.

**Improvements of the wave spectral variability.** There is notable progress in the solution of the spectral hump problem of the altimeters. It is likely that by a proper choice of the optimisation algorithm and subsequent denoising, the true KE spectrum can be much better represented than in the past. The  $k^{-2}$  slope is typical of ocean surface currents. Why and how it translates into a  $k^{-2}$  SWH spectrum is expected to be caused by wave refraction, but so far, there is only empirical evidence for this.

**Improvement on SWH estimates in the coastal zone.** First, the number of outliers in the coastal zone is significantly high, when compared with the number in open-ocean. For a *dist2coast* of less than 20 km, the number of outliers amounts to almost 40%, for less than 5 km there are only 25% left. When approaching the coast, most of the outliers are invalid points (according to the quality flag set by the retracers). In these cases, the algorithms were not able to retrieve a valid



SWH measurement. There is certainly room for improvements in increasing the number of valid points. The quality of measurements in terms of correlation and SDD is maintained in the coastal zone, which demonstrates the effective usage of the quality flag. However, it becomes obvious that there is a tradeoff between quantity and quality of the measurements..

**Estimation of very high sea states.** Although the data availability is very sparse, the evaluated estimates for very high sea states are inaccurate, when compared against the wave model (no very high state observations were available in the in-situ buoy data). Since the extremes are of very high interest, particularly in the coastal zone, the current performance is considered to be weak.

**Retrackers optimised for high precision.** As shown by the noise analysis, the retracked datasets are characterised by very low noise level across different sea states. This is a very significant improvement, when compared with the standard retrackers MLE-4 and SAMOSA that exhibit a highly increased noise level for high and very high sea states. The efficiency of denoising techniques for reducing the intrinsic noise, such as HFA, the adjustment used for the WHALES variants (\_adj), and inherent denoising schemes (STARv2 retracker) has been demonstrated. However, some of them come with other shortcomings, such as an adverse effect on the accuracy compared with buoys (WHALES\_adj variant).

**Innovative approaches are promising.** The results have shown that the individual retracking algorithms have different strengths and shortcomings. There have been multiple innovative approaches published in the recent past. For instance, Adaptive and LR-RMC follow a numerical approach. Their datasets exhibit a very low noise level but have a decreased number of valid points in the coastal zone. WHALES and WHALES-SAR retrack only a subwaveform focused on the leading edge to estimate the SWH, while showing a very good coastal performance and an increased noise level for higher sea states. STARv2 takes into account neighbouring 20-Hz measurements and assumes that they are similar to each other. The noise is thereby reduced significantly and the accuracy against the coarser resolved ERA5-h wave model is improved. As a result, there is a significant amount of signal energy missing at mesoscale, rendering retracked SWH series to be unrealistic. In conclusion, the results have shown that it is worth looking at innovative approaches for the future retracking algorithm development.

**Supplementary Materials:** The following are available online at <http://www.mdpi.com/2072-4292/12/8/1254/s1>.

**Author Contributions:** The contributions of this reported work can be listed as follows: conceptualization, M.P., G.D.Q., F.N., F.S. (Florian Schlembach); methodology, F.S. (Florian Schlembach), M.P., G.D.Q.; software, F.S. (Florian Schlembach), A.K.; formal analysis, F.S. (Florian Schlembach), M.P., G.D.Q., A.K.; investigation, F.S. (Florian Schlembach), G.D.Q., A.K.; resources, F.S. (Florian Schlembach), J.-F.P., G.D.D., J.B.; writing—original draft preparation, F.S. (Florian Schlembach); writing—review and editing, F.S. (Florian Schlembach), M.P., G.D.Q., A.K., F.N., C.S., P.C., G.D.D., F.A.; visualization, F.S. (Florian Schlembach), A.K.; supervision, M.P.; project administration, F.A., P.C., C.D., F.S. (Florian Seitz), ESA SeaState\_cci; funding acquisition, F.A., P.C., C.D., F.S. (Florian Seitz), ESA SeaState\_cci. All authors have read and agreed to the published version of the manuscript.

**Funding:** This research has been funded by the ESA as part of the SeaState\_cci project of the Climate Change Initiative (CCI). (ESA ESRIN/Contract No. 4000123651/18/I-NB)

**Acknowledgments:** The authors acknowledge the contribution of all the research groups that accepted to provide data and thus improve the significance of this work.

**Conflicts of Interest:** The authors declare no conflict of interest.

## References

1. Gower, J.F.R. The Computation of Ocean Wave Heights from GEOS-3 Satellite Radar Altimeter Data. *Remote Sens. Environ.* **1979**, *8*, 97–114. [[CrossRef](#)]
2. Chelton, D.B.; Ries, J.C.; Haines, B.J.; Fu, L.L.; Callahan, P.S. Chapter 1 Satellite Altimetry. *Int. Geophys.* **2001**, *69*, 1–131. [[CrossRef](#)]
3. Timmermans, B.; Gommenginger, C.; Dodet, G.; Bidlot, J.R. Global wave height trends and variability from new multi-mission satellite altimeter products, reanalyses and wave buoys. *Geophys. Res. Lett.* **2020**, in review.

4. Brown, G.S. The Average Impulse Response of a Rough Surface and Its Applications. *IEEE J. Ocean. Eng.* **1977**, *2*, 67–74. [[CrossRef](#)]
5. Hayne, G. Radar Altimeter Mean Return Waveforms from Near-Normal-Incidence Ocean Surface Scattering. *IEEE Trans. Antennas Propag.* **1980**, *AP-28*, 6. [[CrossRef](#)]
6. ESA. SAMOSA Project: CCN Final Project Report V1.3. Available online: <http://www.satoc.eu/projects/samosa/index.html> (accessed on 13 April 2020).
7. Ray, C.; Martin-Puig, C.; Clarizia, M.P.; Ruffini, G.; Dinardo, S.; Gommenginger, C.; Benveniste, J. SAR Altimeter Backscattered Waveform Model. *IEEE Trans. Geosci. Remote Sens.* **2015**, *53*, 911–919. [[CrossRef](#)]
8. Gommenginger, C. *Development of SAR Altimetry Mode Studies and Applications over Ocean, Coastal Zones and Inland Water (SAMOSA): Detailed Processing Model (DPM) of the Sentinel-3 SRAL SAR Altimeter Ocean Waveform Retracker*, Version 2.5.2. 2017.
9. Dinardo, S. Techniques and Applications for Satellite SAR Altimetry over Water, Land and Ice. Ph.D. Thesis, Technische Universität, Darmstadt, Germany, January 2020.
10. Passaro, M.; Fenoglio-Marc, L.; Cipollini, P. Validation of Significant Wave Height From Improved Satellite Altimetry in the German Bight. *IEEE Trans. Geosci. Remote Sens.* **2015**, *53*, 2146–2156. [[CrossRef](#)]
11. Quartly, G.D.; Srokosz, M.A.; McMillan, A.C. Analyzing Altimeter Artifacts: Statistical Properties of Ocean Waveforms. *J. Atmos. Ocean. Technol.* **2001**, *18*, 2074–2091. [[CrossRef](#)]
12. Gómez-Enri, J.; Vignudelli, S.; Quartly, G.D.; Gommenginger, C.P.; Cipollini, P.; Challenor, P.G.; Benveniste, J. Modeling Envisat RA-2 Waveforms in the Coastal Zone: Case Study of Calm Water Contamination. *IEEE Geosci. Remote Sens. Lett.* **2010**, *7*, 474–478. [[CrossRef](#)]
13. Wang, X.; Ichikawa, K. Coastal Waveform Retracking for Jason-2 Altimeter Data Based on along-Track Echograms around the Tsushima Islands in Japan. *Remote Sens.* **2017**, *9*, 762. [[CrossRef](#)]
14. Dibarboure, G.; Boy, F.; Desjonqueres, J.D.; Labroue, S.; Lasne, Y.; Picot, N.; Poisson, J.C.; Thibaut, P. Investigating Short-Wavelength Correlated Errors on Low-Resolution Mode Altimetry. *J. Atmos. Ocean. Technol.* **2014**, *31*, 1337–1362. [[CrossRef](#)]
15. Ardhuin, F.; Stopa, J.E.; Chapron, B.; Collard, F.; Husson, R.; Jensen, R.E.; Johannessen, J.; Mouche, A.; Passaro, M.; Quartly, G.D.; et al. Observing Sea States. *Front. Mar. Sci.* **2019**, *6*. [[CrossRef](#)]
16. Smith, W.H.; Scharroo, R. Waveform Aliasing in Satellite Radar Altimetry. *IEEE Trans. Geosci. Remote Sens.* **2015**, *53*, 1671–1682. [[CrossRef](#)]
17. ESA. CCI Sea State Project. Available online: <http://cci.esa.int/seastate> (accessed on 13 April 2020).
18. ESA. CCI: What Are the Development Phases for Each CCI Project and Their Associated Documentation? Available online: <http://cci.esa.int/content/what-are-development-phases-each-cci-project-and-their-associated-documentation> (accessed on 13 April 2020).
19. ESA. Sea Surface Temperature Project: Round Robin (Algorithm Comparison). 2011. Available online: <http://www.esa-sst-cci.org/?q=round%20robin> (accessed on 13 April 2020).
20. ESA. Soil Moisture Project: Round Robin Exercise. 2012. Available online: <https://www.esa-soilmoisture-cci.org/node/122> (accessed on 13 April 2020).
21. Brewin, B.; Sathyendranath, S.; Müller, D.; Brockmann, C.; Deschamps, P.Y.; Devred, E.; Doerffer, R.; Fomferra, N.; Franz, B.; Grant, M.; et al. The Ocean Colour Climate Change Initiative: III. A Round-Robin Comparison on in-Water Bio-Optical Algorithms. *Remote Sens. Environ.* **2015**, *162*. [[CrossRef](#)]
22. Abdalla, S. SARAL/AltiKa Wind and Wave Products: Monitoring, Validation and Assimilation. *Mar. Geod.* **2015**, *38*, 365–380. [[CrossRef](#)]
23. Abdalla, S.; Dinardo, S.; Benveniste, J.; Janssen, P.A. Assessment of CryoSat-2 SAR Mode Wind and Wave Data. *Adv. Space Res.* **2018**, *62*, 1421–1433. [[CrossRef](#)]
24. ESA. SCOOP Project. Available online: <http://www.satoc.eu/projects/SCOOP/> (accessed on 13 April 2020).
25. Yang, J.; Zhang, J. Validation of Sentinel-3A/3B Satellite Altimetry Wave Heights with Buoy and Jason-3 Data. *Sensors* **2019**, *19*, 2914. [[CrossRef](#)] [[PubMed](#)]
26. Nencioli, F.; Quartly, G.D. Evaluation of Sentinel-3A Wave Height Observations Near the Coast of Southwest England. *Remote Sens.* **2019**, *11*, 2998. [[CrossRef](#)]
27. Fenoglio-Marc, L.; Dinardo, S.; Scharroo, R.; Roland, A.; Dutour Sikiric, M.; Lucas, B.; Becker, M.; Benveniste, J.; Weiss, R. The German Bight: A Validation of CryoSat-2 Altimeter Data in SAR Mode. *Adv. Space Res.* **2015**, *55*, 2641–2656. [[CrossRef](#)]

28. Dinardo, S.; Fenoglio-Marc, L.; Buchhaupt, C.; Becker, M.; Scharroo, R.; Joana Fernandes, M.; Benveniste, J. Coastal SAR and PLRM Altimetry in German Bight and West Baltic Sea. *Adv. Space Res.* **2018**, *62*, 1371–1404. [[CrossRef](#)]
29. Jason-3: Aviso+. Available online: <https://www.aviso.altimetry.fr/en/missions/current-missions/jason-3.html> (accessed on 13 April 2020).
30. EUMETSAT. Copernicus Online Data Access. Available online: <https://codata.eumetsat.int/> (accessed on 13 April 2020).
31. Monaldo, F. Expected Differences between Buoy and Radar Altimeter Estimates of Wind Speed and Significant Wave Height and Their Implications on Buoy-Altitude Comparisons. *J. Geophys. Res.* **1988**, *93*, 2285–2302. [[CrossRef](#)]
32. Hersbach, H.; De Rosnay, P.; Bell, B.; Schepers, D.; Simmons, A.; Soci, C.; Abdalla, S.; Balmaseda, A.; Balsamo, G.; Bechtold, P.; et al. Operational Global Reanalysis: Progress, Future Directions and Synergies with NWP Including Updates on the ERA5 Production Status. *ERA Rep. Ser. No. 27* **2018**, *27*, 1–63. [[CrossRef](#)]
33. ECMWF. Model Upgrade Improves Ocean Wave Forecasts. Available online: <https://www.ecmwf.int/en/newsletter/159/news/model-upgrade-improves-ocean-wave-forecasts> (accessed on 13 April 2020).
34. ECMWF. Upgrade to Boost Quality of Ocean Wave Forecasts. Available online: <https://www.ecmwf.int/en/about/media-centre/news/2019/upgrade-boost-quality-ocean-wave-forecasts> (accessed on 13 April 2020).
35. Quartly, G.D.; Smith, W.H.F.; Passaro, M. Removing Intra-1-Hz Covariant Error to Improve Altimetric Profiles of  $\sigma^0$  and Sea Surface Height. *IEEE Trans. Geosci. Remote Sens.* **2019**, *57*, 3741–3752. [[CrossRef](#)]
36. Zaron, E.D.; deCarvalho, R. Identification and Reduction of Retracker-Related Noise in Altimeter-Derived Sea Surface Height Measurements. *J. Atmos. Oceanic Technol.* **2016**, *33*, 201–210. [[CrossRef](#)]
37. Quilfen, Y.; Chapron, B. Ocean Surface Wave-Current Signatures From Satellite Altimeter Measurements. *Geophys. Res. Lett.* **2019**, *46*, 253–261. [[CrossRef](#)]
38. ESA. Sea State CCI: Algorithm Theoretical Basis Document v1.1. 2019. Available online: [http://cci.esa.int/sites/default/files/Sea\\_State\\_cci\\_ATBD\\_v1.1-signed\\_0.pdf](http://cci.esa.int/sites/default/files/Sea_State_cci_ATBD_v1.1-signed_0.pdf) (accessed on 13 April 2020).
39. Amarouche, L.; Thibaut, P.; Zanine, O.Z.; Dumont, J.P.; Vincent, P.; Steunou, N. Improving the Jason-1 Ground Retracking to Better Account for Attitude Effects. *Mar. Geod.* **2004**, *27*, 171–197. [[CrossRef](#)]
40. Sandwell, D.T.; Smith, W.H. Retracking ERS-1 Altimeter Waveforms for Optimal Gravity Field Recovery. *Geophys. J. Int.* **2005**, *163*, 79–89. [[CrossRef](#)]
41. Chelton, D.B.; Walsh, E.J.; MacArthur, J.L.; Chelton, D.B.; Walsh, E.J.; MacArthur, J.L. Pulse Compression and Sea Level Tracking in Satellite Altimetry. *J. Atmos. Oceanic Technol.* **1989**, *6*, 407–438. [[CrossRef](#)]
42. Passaro, M.; Cipollini, P.; Vignudelli, S.; Quartly, G.D.; Snaith, H.M. ALES: A Multi-Mission Adaptive Subwaveform Retracker for Coastal and Open Ocean Altimetry. *Remote Sens. Environ.* **2014**, *145*, 173–189. [[CrossRef](#)]
43. Nelder, J.A.; Mead, R. A Simplex Method for Function Minimization. *Comput. J.* **1965**, *7*, 308–313. [[CrossRef](#)]
44. Peng, F.; Deng, X. Validation of Improved Significantwave Heights from the Brown-Peaky (BP) Retracker along the East Coast of Australia. *Remote Sens.* **2018**, *10*, 1072. [[CrossRef](#)]
45. Peng, F.; Deng, X. A New Retracking Technique for Brown Peaky Altimetric Waveforms. *Mar. Geod.* **2018**, *41*, 99–125. [[CrossRef](#)]
46. Passaro, M. Design, Validation and Application of a New Coastal Altimetry Strategy. Ph.D. Thesis, University of Southampton, Southampton, UK, September 2015.
47. Buchhaupt, C.; Fenoglio-Marc, L.; Dinardo, S.; Scharroo, R.; Becker, M. A Fast Convolution Based Waveform Model for Conventional and Unfocused SAR Altimetry. *Adv. Space Res.* **2018**, *62*, 1445–1463. [[CrossRef](#)]
48. Roscher, R.; Uebbing, B.; Kusche, J. STAR: Spatio-Temporal Altimeter Waveform Retracking Using Sparse Representation and Conditional Random Fields. *Remote Sens. Environ.* **2017**, *201*, 148–164. [[CrossRef](#)]
49. Raney, R.K. The Delay/Doppler Radar Altimeter. *IEEE Trans. Geosci. Remote Sens.* **1998**, *36*, 1578–1588. [[CrossRef](#)]
50. Lourakis, M. Levmar: Levenberg-Marquardt Nonlinear Least Squares Algorithms in C/C++ 2004. 2019. Available online: <http://users.ics.forth.gr/~lourakis/levmar/> (accessed on 13 April 2020).
51. Estimating Significant Wave Heights from SAR Waveforms with a Leading Edge Retracker. 2019. Available online: <https://mediatum.ub.tum.de/1487516> (accessed on 13 April 2020).

52. Makhoul, E.; Roca, M.; Ray, C.; Escolà, R.; Garcia-Mondéjar, A. Evaluation of the Precision of Different Delay-Doppler Processor (DDP) Algorithms Using CryoSat-2 Data over Open Ocean. *Adv. Space Res.* **2018**, *62*, 1464–1478. [[CrossRef](#)]

53. Boy, F.; Desjonquères, J.D.; Picot, N.; Moreau, T.; Raynal, M. CryoSat-2 SAR-Mode Over Oceans: Processing Methods, Global Assessment, and Benefits. *IEEE Trans. Geosci. Remote Sens.* **2017**, *55*, 148–158. [[CrossRef](#)]
54. PacIOOS. Distance to Nearest Coastline: 0.01-Degree Grid: Ocean. Available online: [http://www.pacioos.hawaii.edu/metadata/dist2coast\\_1deg\\_ocean.html](http://www.pacioos.hawaii.edu/metadata/dist2coast_1deg_ocean.html) (accessed on 13 April 2020).
55. Guymer, T.H.; Quartly, G.D.; Srokosz, M.A. The Effects of Rain on ERS-1 Radar Altimeter Data. *J. Atmos. Oceanic Technol.* **1995**, *12*, 1229–1247. [[CrossRef](#)]
56. Alvera-Azcárate, A.; Sirjacobs, D.; Barth, A.; Beckers, J.M. Outlier Detection in Satellite Data Using Spatial Coherence. *Remote Sens. Environ.* **2012**, *119*, 84–91. [[CrossRef](#)]
57. Quilfen, Y.; Chapron, B. On Denoising Satellite Altimeter Measurements for High-Resolution Geophysical Signal Analysis. *Adv. Space Res.* **2020**. [[CrossRef](#)]
58. Welch, P. The Use of Fast Fourier Transform for the Estimation of Power Spectra: A Method Based on Time Averaging over Short, Modified Periodograms. *IEEE Trans. Audio Electroacoust.* **1967**, *15*, 70–73. [[CrossRef](#)]
59. Gommenginger, C.; Martin-Puig, C.; Amarouche, L.; Raney, R.K. Review of State of Knowledge for SAR Altimetry over Ocean. Report of the EUMETSAT JASON-CS SAR Mode Error Budget Study. Available online: <https://eprints.soton.ac.uk/366765/> (accessed on 13 April 2020).
60. ESA. Cryosat Plus for Oceans: CP4O. 2015. Available online: [http://lps16.esa.int/posterfiles/paper0519/CP4O\\_FinalReport.pdf](http://lps16.esa.int/posterfiles/paper0519/CP4O_FinalReport.pdf) (accessed on 13 April 2020).
61. Gómez-Enri, J.; Srokosz, M.A.; Gommenginger, C.P.; Challenor, P.G.; Milagro-Pérez, M.P. On the Impact of Mispointing Error and Hamming Filtering on Altimeter Waveform Retracking and Skewness Retrieval. *Mar. Geod.* **2007**, *30*, 217–233. [[CrossRef](#)]
62. Arduin, F.; Gille, S.T.; Menemenlis, D.; Rocha, C.B.; Rasche, N.; Chapron, B.; Gula, J.; Molemaker, J. Small-Scale Open Ocean Currents Have Large Effects on Wind Wave Heights. *J. Geophys. Res. Oceans* **2017**, *122*, 4500–4517. [[CrossRef](#)]
63. Capet, X.; McWilliams, J.C.; Molemaker, M.J.; Shchepetkin, A.F. Mesoscale to Submesoscale Transition in the California Current System. Part III: Energy Balance and Flux. *J. Phys. Oceanogr.* **2008**, *38*, 2256–2269. [[CrossRef](#)]
64. McWilliams, J.C. Submesoscale Currents in the Ocean | Proceedings of the Royal Society A: Mathematical, Physical and Engineering Sciences. 2016. Available online: <https://royalsocietypublishing.org/doi/10.1098/rspa.2016.0117> (accessed on 13 April 2020).
65. Queffelec, P. Long-Term Validation of Wave Height Measurements from Altimeters. *Mar. Geod.* **2004**, *27*, 495–510. Available online: <https://doi.org/10.1080/01490410490883478> (accessed on 13 April 2020). [[CrossRef](#)]
66. Wang, J.; Zhang, J.; Yang, J. The Validation of HY-2 Altimeter Measurements of a Significant Wave Height Based on Buoy Data. *Acta Oceanol. Sin.* **2013**, *32*, 87–90. [[CrossRef](#)]
67. Ray, R.D.; Beckley, B.D. Calibration of Ocean Wave Measurements by the TOPEX, Jason-1, and Jason-2 Satellites. *Mar. Geod.* **2012**, *35*, 238–257. [[CrossRef](#)]
68. Zieger, S.; Vinoth, J.; Young, I.R. Joint Calibration of Multiplatform Altimeter Measurements of Wind Speed and Wave Height over the Past 20 Years. *J. Atmos. Oceanic Technol.* **2009**, *26*, 2549–2564. [[CrossRef](#)]
69. Wiese, A.; Staneva, J.; Schulz-Stellenfleth, J.; Behrens, A.; Fenoglio-Marc, L.; Bidlot, J.R. Synergy of Wind Wave Model Simulations and Satellite Observations during Extreme Events. *Ocean Sci.* **2018**, *14*, 1503–1521. [[CrossRef](#)]
70. Idris, N.H. Wave Energy Resource Assessment with Improved Satellite Altimetry Data over the Malaysian Coastal Sea. *Arabian J. Geosci.* **2019**, *12*. [[CrossRef](#)]
71. Dodet, G.; Piolle, J.F.; Quilfen, Y.; Abdalla, S.; Accensi, M.; Arduin, F.; Ash, E.; Bidlot, J.R.; Gommenginger, C.; Marechal, G.; et al. The Sea State CCI Dataset v1: Towards a Sea State Climate Data Record Based on Satellite Observations. *Earth Syst. Sci. Data Discuss.* **2020**, in review. [[CrossRef](#)]
72. ESA. Sea State CCI: User Requirements Document V1.0. 2019. Available online: [http://cci.esa.int/sites/default/files/Sea\\_State\\_cci\\_URD\\_v1.0-signed.pdf](http://cci.esa.int/sites/default/files/Sea_State_cci_URD_v1.0-signed.pdf) (accessed on 13 April 2020).

73. ESA. Sea State CCI Project: Round Robin: Final Selection and Ranking of Algorithms V1.1. Available online: [http://cci.esa.int/sites/default/files/Sea\\_State\\_cci\\_RR\\_Final\\_Selection\\_v1.1-signed.pdf](http://cci.esa.int/sites/default/files/Sea_State_cci_RR_Final_Selection_v1.1-signed.pdf) (accessed on 13 April 2020).
74. EUMETSAT. Major Evolution of Sentinel-3 Altimetry Products. Available online: [https://www.eumetsat.int/website/home/News/DAT\\_4762430.html](https://www.eumetsat.int/website/home/News/DAT_4762430.html) (accessed on 13 April 2020).

**Sample Availability:** The retrackval framework including the resources that are required for reproducing the results are available upon request.



© 2020 by the authors. Licensee MDPI, Basel, Switzerland. This article is an open access article distributed under the terms and conditions of the Creative Commons Attribution (CC BY) license (<http://creativecommons.org/licenses/by/4.0/>).

## A.2 P-II: Interference-sensitive Coastal SAR Altimetry Retracking Strategy for Measuring Significant Wave Height

Schlembach, F.; Passaro, M.; Dettmering D., Bidlot, J.; Seitz, F. **Interference-sensitive Coastal SAR Altimetry Retracking Strategy for Measuring Significant Wave Height** Remote Sensing of Environment 274 (2022) 112968.

**Journal:** Remote Sensing of Environment, volume 274, article 112968

**Date of publication:** 16th of March 2022

**DOI:** j.rse.2022.112968

**Web link:** <https://doi.org/10.1016/j.rse.2022.112968>

### Copyright

This work was published in the Remote Sensing of Environment journal under the subscription-based publishing model.

### Contribution

The contributions to this reported work can be listed as follows: conceptualization, F.Sc., M.P.; methodology, F.Sc., M.P.; software, F.Sc.; formal analysis, F.Sc., M.P.; investigation, F.Sc.; resources, F.Sc., J.B.; writing–original draft preparation, F.Sc.; writing–review and editing, F.Sc., M.P., D.D., F.S.; visualisation, F.Sc.; supervision, M.P.; project administration, F.S., ESA SeaState\_cci; funding acquisition, F.S., ESA SeaState\_cci. All authors have read and agreed to the published version of the manuscript.

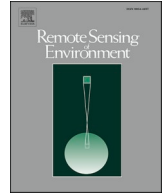
Criteria	Own contribution
Idea and conceptual design	80%
Implementation and realisation	90%
Analysis and discussion	85%
Figure compilation	100%
Manuscript structure and writing	80%
<b>Overall contribution</b>	<b>87%</b>

Own contribution to publication P-II



Contents lists available at ScienceDirect

## Remote Sensing of Environment

journal homepage: [www.elsevier.com/locate/rse](http://www.elsevier.com/locate/rse)

# Interference-sensitive coastal SAR altimetry retracking strategy for measuring significant wave height

Florian Schlembach<sup>a,\*</sup>, Marcello Passaro<sup>a</sup>, Denise Dettmering<sup>a</sup>, Jean Bidlot<sup>b</sup>, Florian Seitz<sup>a</sup>

<sup>a</sup> Deutsches Geodätisches Forschungsinstitut, Technical University of Munich (DGFI-TUM), Arcisstraße 21, Munich 80333, Germany

<sup>b</sup> European Centre for Medium-Range Weather Forecasts (ECMWF), Shinfield Park, Reading RG2 9AX, UK

## ARTICLE INFO

Editor Name: Dr. Menghua Wang

## Keywords:

Satellite altimetry  
SAR altimetry  
Significant wave height  
Retracking  
Algorithm  
SAMOSA  
ESA  
CCI  
Climate change initiative

## ABSTRACT

Satellite altimetry is a radar remote sensing technology for the precise observation of the ocean surface and its changes over time. Its measurements allow the determination of geometric and physical parameters such as sea level, significant wave height or wind speed. This work presents a novel coastal retracking algorithm for SAR altimetry to estimate the significant wave height. The concept includes an adaptive interference masking scheme to sense and mitigate spurious interfering signals that typically arise from strongly reflective targets in the coastal zone. The described procedure aims at increasing the number of valid records in the coastal zone. The effectiveness of the novel retracking algorithm is validated using the methodology recently developed in the framework of the European Space Agency Sea State Climate Change Initiative project. Several different metrics were extracted as functions of sea state and distance to the nearest coast: outliers, number of valid records, intrinsic noise, power spectral density, and correlation statistics for the comparison with wave model and in-situ data. Two coastal case study scenarios complement the validation. The results show that with the presented novel retracking algorithm, the number of valid 20-Hz records in the near coastal zone of less than 5 km off the coast is increased by more than 25% compared to the best competing coastal retracking algorithm with no degradation of quality of the estimated records. We emphasise the importance of the correct choice of the quality flag that is provided together with the significant wave height. Our findings suggest that the strategy for the significant wave height quality flag of the official baseline Level-2 product of the Sentinel-3 mission can be redefined to obtain more robust significant wave height estimates in the coastal zone.

## 1. Introduction

Satellite altimetry is a space-borne remote sensing technology to determine sea level and sea state that has been in use for over three decades. It follows a simple physical principle: the altimeter on-board emits a short radio-wave pulse and measures the round-trip time that the pulse takes from and to the satellite's altimeter instrument after it is reflected from the ocean surface. Since the pulse changes its amplitude and shape as it interacts with the ocean surface, two further parameters can be retrieved, among others: significant wave height (SWH) and wind speed (WS). The SWH is defined as four times the standard deviation of the sea surface elevation (Holthuijsen, 2007). Measuring the ocean's SWH on a global scale is essential for applications such as ocean wave monitoring, the fishing industry, industrial shipping route planning, weather forecasting, or wave climate studies such as Timmermans et al.

(2020).

The conventional technology of satellite altimeters that was first deployed is called pulse-limited low resolution mode (LRM) altimetry. Pulses are transmitted and received on a regular basis with a pulse repetition frequency (PRF) of approximately 2 kHz and eventually processed on the ground to form measurements at a posting rate of 20 Hz, from which the geophysical variables are estimated.

The technology that evolved from LRM is called synthetic aperture radar mode (SARM) altimetry (or Delay-Doppler altimetry (DDA) (Raney, 1998). SARM uses an increased PRF to coherently process groups of radar echoes, which allows the beams to be sharpened in the along-track direction by exploiting the Doppler shift. This enables the generation of multilooked waveforms to increase the signal-to-noise ratio (SNR), which are formed from multiple single-look waveforms that were measured from different satellite positions in orbit. With the

\* Corresponding author.

E-mail addresses: [florian.schlembach@tum.de](mailto:florian.schlembach@tum.de) (F. Schlembach), [marcello.passaro@tum.de](mailto:marcello.passaro@tum.de) (M. Passaro), [denise.dettmering@tum.de](mailto:denise.dettmering@tum.de) (D. Dettmering), [Jean.Bidlot@ecmwf.int](mailto:Jean.Bidlot@ecmwf.int) (J. Bidlot), [florian.seitz@tum.de](mailto:florian.seitz@tum.de) (F. Seitz).

<https://doi.org/10.1016/j.rse.2022.112968>

Received 31 May 2021; Received in revised form 16 February 2022; Accepted 24 February 2022

Available online 16 March 2022

0034-4257/© 2022 Elsevier Inc. All rights reserved.



hypothesis of a flat sea surface, the size of the illuminated area on the ground that contributes to the multilooked waveform is determined by the dimensions of the length of the received waveform in the across-track direction and of the Doppler-limited footprint in the along-track direction, which we refer to as the effective footprint in the following. Following the Pythagorean theorem, the size of the across-track dimension is approximated as

$$R_{ac} = \sqrt{\left(h + c \cdot K \cdot \frac{1}{B_r}\right)^2 - h^2} \approx 14 \text{ km} \quad (1)$$

where an altitude  $h=814$  km, the speed of light  $c=3 \cdot 10^8$  m/s,  $K=128$  range gates of the multilooked waveform, and a receiving bandwidth  $B_r=320$  MHz are assumed for Sentinel-3 (S3). The effective footprint is thus of size  $14 \text{ km} \times 330 \text{ m}$ .

The relationship between the reflected and received power return echoes is formulated in the Brown-Hayne (BH) model by Brown (1977) and Hayne (1980) for LRM and in the SAR Altimetry MOde Studies and Applications (SAMOSA) model (Ray et al., 2015) for SARM altimeters, both being developed for the open ocean. The essential part of the received waveform for the extraction of the aforementioned parameters is the leading edge (LE) of the radar echo. The position of the LE in relation to the absolute position of the receiving window, which is controlled by the on-board instrument, corresponds to the distance of the satellite altimeter's baseplate and the surface on the ground. The WS is related to the peak amplitude of the pulse and the SWH is mostly dominated by the steepness of the LE.

The process of extracting the geophysical variables from the received waveform is called retracking. Retracking algorithms can be subdivided into three main categories: empirical, physical-based and statistical retrackers (Dinardo, 2020). Empirical retrackers, which follow certain heuristics, establish an empirical relationship between the measurement and the geophysical metrics. Physical-based retrackers are based on approximations that model the physical interaction between the electromagnetic pulse and the scattering ocean surface. Statistical retrackers make use of statistical properties of the neighbouring measurements.

According to Dodet et al. (2020), in order to improve the quality of altimetric wave height, novel retracking methods are in particular demand to enhance the 20-Hz estimates' precision, increase the robustness and accuracy in the coastal zone and ice-affected areas, observe the true spatial variability, and improve the estimation for low sea state regimes.

The fitting routines of the retrackers, most of which are based on a least squares cost function, try to find the best fit between the received noisy waveform and the idealised model. Hence, the series of estimates of the geophysical quantities also exhibit uncertainties such as small-scale noise, which is computed as the standard deviation of twenty 20-Hz records and amounts to  $\sim 40$  cm for SWH values of approximately 2 m (Ardhuin et al., 2019; Schlembach et al., 2020). The small-scale noise, whose spatial distance corresponds to  $\sim 7$  km, can be reduced in a post-processing step by several techniques (Zaron and deCarvalho, 2016; Quartly et al., 2019; Quilfen and Chapron, 2019). Speckle noise is present in both open ocean and coastal scenarios. However, the trailing edge of the waveform in the coastal zone is likely to be affected by much stronger spurious signal components, most of which arise from strongly reflective, "mirror"-like surfaces, such as melt ponds on sea-ice, sheltered bays or mud banks (Quartly et al., 2001; Gómez-Enri et al., 2010; Wang and Ichikawa, 2017). As a consequence, the quality of the estimate is degraded because the LS fitting algorithm tries to minimise the sum of the squares of the differences between the model and the received waveform. Besides, the number of estimates decreases as the retrackers may fail to output realistic values. The majority of retrackers deduce the provided quality flag from the goodness of the fit between the fitted model and the received waveform. The larger the spurious signal components are, the larger the misfit of the estimate will be. This effect significantly reduces the number of valid measurements. Schlembach et al. (2020) conducted a very extensive validation of

different retracking algorithms. One assessed metric is the number of outliers, from which most were accounted by records flagged as bad. For instance, the number of outliers amounts to 83.5% for the winning algorithm, Low Resolution with Range Migration Correction (LR-RMC), of the Round Robin assessment in the near coastal zone of distance-to-coast ( $\text{dist-to-coast} < 5$  km). As a result of this assessment, it can be clearly observed that the quality flags used by the retrackers are quite able to identify the valid estimates, since the correlation also remains high in the coastal zone. However, the amount of valid estimates is strongly reduced in most retrackers. It thus becomes obvious that there is a trade-off between the quality and quantity of valid records.

The objective of this work is to present a novel SARM retracking algorithm called COastal Retracker for SAR Altimetry version 1.0 (CORALv1), which specifically targets the estimation of SWH in the presence of strong spurious interference that typically occurs in the coastal zone. The emphasis of the retracking strategy of CORALv1 is placed on the maximisation of the number of valid measurements, while maintaining the quality at the highest standards in both open ocean and coastal zone. CORALv1 takes the processed Level-1B (L1B) data as an input and delivers the retracked variables SWH, epoch, and  $P_u$ , together with the SWH quality flag that indicates the validity of the SWH estimate. The epoch (in time) is the position of the leading edge with respect to the nominal, fixed tracking point, which is defined by the on-board retracker.  $P_u$  corresponds to the maximum amplitude of the received waveform, which can be translated into  $\sigma^0$  or the wind speed. This work, however, focuses on the estimation and evaluation of the SWH only.

It is worthwhile describing other retrackers for LRM and SARM that have dealt with typical issues of the coastal zone. Passaro et al. (2015) presented an LRM retracker that deals with the spurious signal components in the coastal zone by adopting an approach called Adaptive Leading Edge Subwaveform (ALES). Only a portion of the waveform is considered to ease the LS fitting of the model to the noisy waveform. The width of the subwaveform, i.e. the number of gates being included after the LE, depends on the sea state that was estimated in an initial retracking step. A second retracking step adjusts the width of the subwaveform to retrieve the final estimates of the output. ALES helps to improve both the quality and quantity of the estimations in the coastal zone for LRM altimeters. Peng and Deng (2018) has adapted the ALES approach and extended its retracking strategy by an Adaptive Peak Detection (APD) method for coastal LRM waveforms. The APD detects waveform gates that are affected by spurious interference and down-weights them in the WLS fitting procedure that is used. Dinardo et al. (2018) presents the SAMOSA+ (SAM+) coastal retracking algorithm that retracks SARM data starting from Level-1A (L1A). Apart from individual adjustments in the L1B processor, SAM+ has two main extensions to the original SAMOSA-based retracker (SAMOSA Detailed Processing Model, 2017, pers. comm. Jérôme Benveniste) that are dedicated to coastal scenarios. First, it accounts for multippeak waveforms and computes a point-wise product to obtain an averaged first-guess (FG) epoch, which facilitates the fitting of the correct LE. Second, it allows for fitting very peaky waveforms in a second retracking step to refine the epoch estimate and the quality flag. Both Level-2 (L2) extensions of SAM+ are adopted by CORALv1 and are described in detail in Section 3.1. SAMOSA+ processed by GPOD (SAM+-GPOD) as other L2 datasets are external sources and serve as reference for validation and are described in more detail in Appendix A.

This paper is structured as follows: Section 2 describes the L1B dataset used as input for the new CORALv1 retracker to produce the L2 data. It also describes the in-situ and wave model data that is used to validate CORALv1, and the other L2 datasets processed by different retrackers that are used as reference. Section 3 elaborates the retracking strategy with details of the processing steps in CORALv1, though also the methodology of the validation of the retracking results. Section 4 presents and discusses the results. Section 5 draws conclusions and provides an outlook on future work.

## 2. Data

The L1B dataset that was used for retracking and the data that was used to validate the retracked L2 results is taken from the Round Robin assessment presented in Schlembach et al. (2020). The data is available upon request.

### 2.1. Processed level-1B satellite data

In order to ensure the objective assessment of the performance of CORALv1 compared to other retracked L2 datasets (see Section 2.4), it is crucial that all algorithms process exactly the same data. We thus use the same SARM L1A input dataset of the Sentinel-3A (S3A) mission that was used in the Round Robin assessment in Schlembach et al. (2020). It was acquired from the CODA catalogue of the European Organisation for the Exploitation of Meteorological Satellites, which can be downloaded from <https://coda.eumetsat.int/>. The files cover a time period from the 21th of March 2017 to the 26th of July 2018 (16 months), which equals 19 repeat cycles of the satellite. The two mixed baseline versions 002 and 003 had to be accepted as there was a transition within the investigated period of time. In order to have enough data for comparison with the in-situ measurements, 30 pole-to-pole tracks were chosen (see Section 2.2).

As the CORALv1 algorithm starts at the L1B processing stage, the L1B processing (from L1A to L1B) was performed using the S3 SARvatore service of the European Space Agency (ESA) Grid Processing on Demand platform (ESA-GPOD) (version 1.41, L1B processor version 1.37). The set of L1A files were processed with the “coastal zone” profile preset. Hence, a Hamming window is applied in the coastal zone, and a zero padding factor of two (corresponding to an oversampling) and a doubling of the receiving window are used.

### 2.2. In-situ data

In-situ data from buoys and platforms providing wave observations, mostly with an hourly frequency, were collected from the Global Telecommunication System (GTS) distribution of the European Centre for Medium-Range Weather Forecasts (ECMWF).

A basic quality control was applied to each hourly time series for each location to remove spurious outliers. The total number of buoys was 170, including 46 coastal buoys.

Data from buoys and along-track points were compared for validation purposes. The collocation criteria follow Monaldo (1988): measurements are compared for distances smaller than 50 km in space and 30 min in time. If these criteria are satisfied, the buoy value is compared with the median of the closest 51 20-Hz SWH points. (Schlembach et al., 2020).

### 2.3. Wave model

Additionally, altimetry data are compared with the output of a wave hindcast from the ECMWF, called ERA5-h in this work. This is characterised by the ERA5-forcing and the ECMWF wave model version CY46R1 (ECMWF, 2020a, 2020b).

Whereas wave data measured by satellites are assimilated in the standard ERA5 (Hersbach et al., 2020), ERA5-h does not include any assimilation. Moreover, the wave physics for the input and dissipation of Ardhuin et al. (2010) is included in this model run. Notably, the resolution of ERA5-h wave heights compared to ERA5 is improved (14 km instead of 40 km).

### 2.4. External L2 datasets

In order to assess the performance of the novel CORALv1 retracker, four external L2 datasets are used as a reference for validation: SAMOSA-based retracker from EUMETSAT (SAM-EUM), SAMOSA-

based retracker from EUMETSAT with mqe-quality-flag (SAM-EUM-MQE), LR-RMC, and SAM+-GPOD.

The properties of CORALv1 and the external L2 datasets used as a reference for validation are summarised in Table 1. Please refer to Appendix A for further details.

## 3. Methods

We introduce the methodology of the novel retracking algorithm as well as the validation schemes for assessing its robustness and performance in this Section.

### 3.1. CORALv1 retracking algorithm

CORALv1 is a novel coastal retracking algorithm that is based on the SAMOSA2 model (Ray et al., 2015), on the SAMOSA-based retracker as described in the SAMOSA detailed processing model (SAMOSA Detailed Processing Model, 2017, pers. comm. Jérôme Benveniste), and on the coastal SAM+ retracker (Dinardo et al., 2018). The SAMOSA2 model is a fully analytical formulation of the power return echo. It takes into account the instrument-specific and parameters from the L1B product such as orbital parameters (including mispointing angles of the satellite platform). The model makes a Gaussian approximation of the squared point target response (PTR), whose impact is mitigated by the use of a look-up table (LUT) with a sea-state-dependent  $\alpha_p$  value (Dinardo et al., 2018). The mean square slope (MSS) is assumed to be infinite in the normal case, whereas in a special case it is estimated as the third free parameter, replacing the SWH. This will be described in Section 3.1.2. Fig. 1 depicts the flow chart diagram of CORALv1, starting at the L1B processing stage and ending at L2 with the retracked variables SWH, epoch,  $P_{tr}$ , and a misfit value to acquire the quality flag. In the present work, we limit our assessment to the estimation of the SWH.

The detailed explanation of the flow chart is described in the next sections. Here, we provide a brief, descriptive introduction. CORALv1 conducts (at maximum) three SAMOSA-based fitting steps, depending on the dist-to-coast and the peakiness of the received waveform. Steps ① and ② perform a fitting of a theoretical SAMOSA-based model waveform with a novel Adaptive Interference Masking (AIM) scheme, which accounts for parts of the trailing edge that is affected by interference. In step ①, a fixed AIM parameter of  $SWH_{IR}=8$  m is chosen for the generation of an IR waveform to identify strong interference. In case of a dist-to-coast  $< 20$  km, step ② is conducted and the SWH estimate of step ① is taken as the basis for setting  $SWH_{IR}$  to identify also less strong interference. Finally, if the waveform is very peaky, a further modified fitting step ③ is performed to adjust the estimation of the misfit, i.e. the quality flag. In the case of non-peaky waveforms, the misfit is taken from step ① or step ②, respectively.

CORALv1 starts at the L1B processing stage and uses the GPOD L1B product, as described in Section 2.1.

#### 3.1.1. Adaptive interference masking

AIM is a novel technique that deals with coastal interference arising from strongly reflective targets that are located off-nadir. The spurious signals thus occur within the trailing edge of the waveform, i.e. after the waveform's maximum. The objective of AIM is (1) to detect strong, spurious interference in the trailing edge and to mitigate its impact on the least squares fitting procedure and (2) to improve the accuracy of the quality flag to recover SWH estimations from waveforms that are affected by coastal interference.

The methodology of AIM is described as follows: the received waveform vector  $w_r$  of length  $K$  and range gate indices  $k$  (being denoted by  $w_{r,k}$ ) contains the absolute power values. Here  $w_r$  is to be retracked by CORALv1. In the coastal zone,  $w_r$  might be affected by spurious signals, to which we refer to as coastal interference. The interference range gate indices are expressed by  $k_{inf}$ . An exemplary received waveform with weak interference is shown in Fig. 2 (a) as  $w_r$ . In order to

**Table 1**

Properties of CORALv1 and the external L2 datasets used as a reference for validation. The EUMETSAT PB used is 2.68-MARINE with BC 004. GPOD refers to the SARvatore processing service. The variable mqe stands for mean quadratic error and refers to the product variable mqe\_ocean\_20\_ku. Please refer to Appendix A for further details.

L2 dataset	L1B proc.	zero padding	Hamming	PTR	Phys. model	quality flag
SAM-EUM	EUM PB	No	No	Gaussian	SAMOSA2	three-sigma criterion
SAM-EUM-MQE	EUM PB	No	No	Gaussian	SAMOSA2	$\sqrt{100 \cdot \text{mqe}} > 4$
LR-RMC	EUM PB	No	No	Numerical	Numerical	MQE-based
SAM+-GPOD	GPOD	Yes	Yes	Gaussian	SAMOSA2	misfit > 4
CORALv1	GPOD	Yes	Yes	Gaussian	SAMOSA2	misfit <sub>selective</sub> > 4

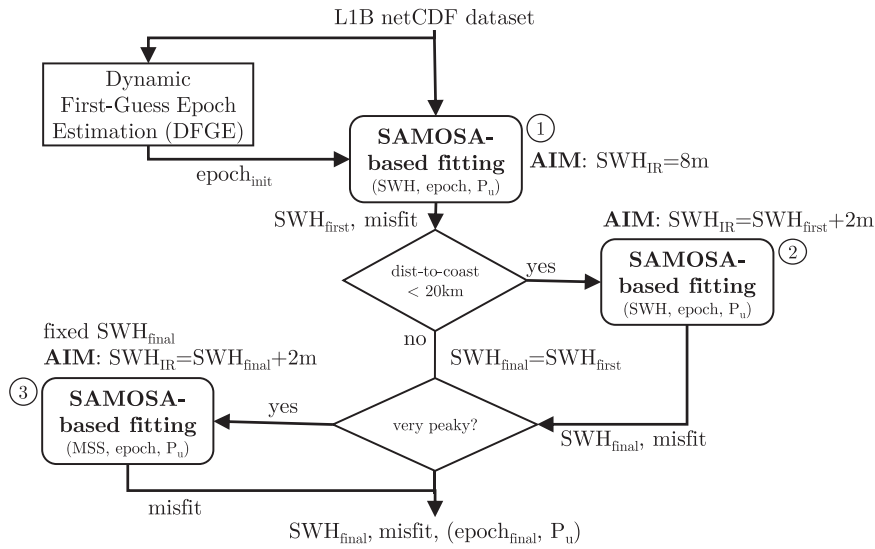


**Fig. 1.** Flow chart diagram for the CORALv1 algorithm.

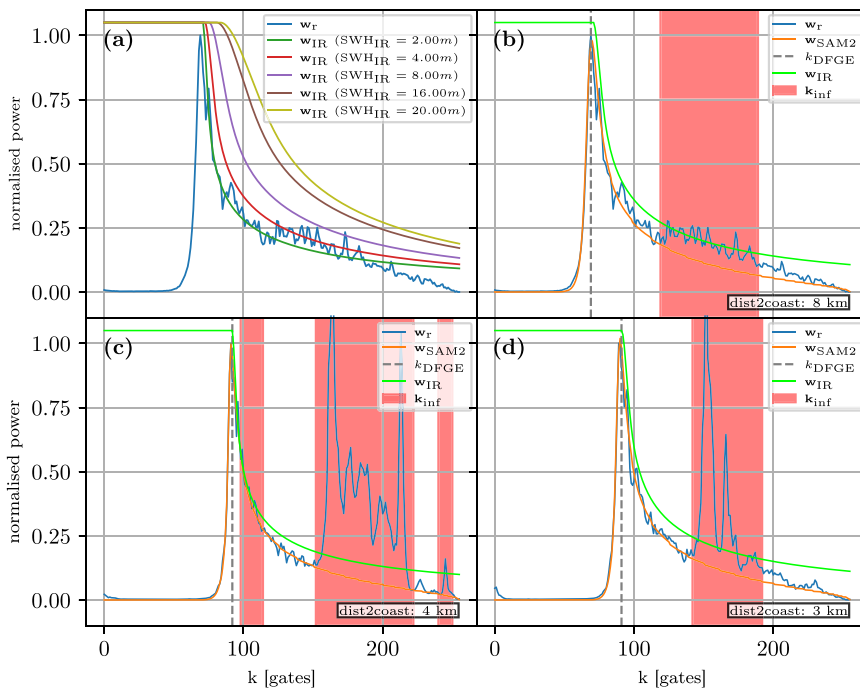


**Fig. 2.** Methodology of AIM. (a) shows an exemplary, weakly perturbed received waveform  $w_r$ , in solid blue and different IR waveforms  $w_{IR}(SWH_{IR})$  with a varying  $SWH_{IR}$  parameter. (b, c, d) show different, received (coastal) waveforms  $w_r$  with spurious interference in the trailing edge and the retracked, fitted model waveforms  $w_{SAM2}$ . The dashed grey lines indicate the estimated FG epochs  $k_{DFGE}$  and the solid lime-coloured lines show the generated, final  $w_{IR}$  waveforms. The detected interference gates  $k_{inf}$  are marked by the red area.  $k_{inf}$  includes gates, whose power values of  $w_r$ , exceed the threshold level of  $w_{IR}$ , and the adjacent  $\pm 10$  gates that were extended, according to Eq. (2) and Eq. (4), respectively. (For interpretation of the references to colour in this figure legend, the reader is referred to the web version of this article.)

detect  $k_{inf}$ , we generate a so-called IR waveform, which is expressed by the vector  $w_{IR}(SWH_{IR})$  of length  $K$ .  $w_{IR}(SWH_{IR})$  is generated with the zero-Doppler, single-look SAMOSA2 model ( $w_{SL-SAM}$ ) with

$SWH = SWH_{IR}$  (Eq. 26 in (SAMOSA Detailed Processing Model, 2017, pers. comm. Jérôme Benveniste)), on account of its low computational complexity and its capability to form a close envelope around the

multilooked waveform  $w_r$  at hand.  $SWH_{IR}$  is omitted in the following for the sake of clarity, while  $w_{IR}$  is used for a threshold-based detection to eventually acquire the interference gates  $k_{inf}$  from  $w_r$ . The generation of  $w_{IR}$  is thus expressed by

$$w_{IR} = \begin{cases} \frac{w_{SL-SAM}}{\max(w_{SL-SAM})} + TN_{emp} & \text{if } k \geq \arg \max_k (w_{SL-SAM}) \\ 1.0 + TN_{emp}, & \text{otherwise} \end{cases} \quad (2)$$

where  $w_{SL-SAM}$  is the zero-Doppler SL-SAM with  $K$  range gates  $k$ , and  $TN_{emp}$  is an empirical thermal noise value, which is set to 0.05.  $w_{IR}$  changes with a varying  $SWH_{IR}$ , as can be seen in Fig. 2 (a). The higher  $SWH_{IR}$  becomes, the less steep the trailing edge gets. This is due to the nature of the SAMOSA model. The interference reference waveform  $w_{IR}$  from Eq. (2) is then used to identify the range gates of  $w_r$ , whose power exceeds the threshold level of  $w_{IR}$ . Those yield the indices of the preliminary interference gates  $k_{pre\_inf}$  and are acquired by

$$k_{pre\_inf} = \text{True}(w_r > w_{IR}) \quad (3)$$

where the  $\text{True}(\cdot)$  operator returns the indices for which the nested boolean array has the value True.

We also assume that gates next to the strong interfering signal peaks are affected by interference, and their values stay below  $w_{IR}$ . In order to include these too, we expand each index element  $m$  of  $k_{pre\_inf}$  by  $\pm 10$  gates to obtain the final set of interference gates

$$k_{inf} = \bigcup_m \{k_{pre\_inf,m} - 10, \dots, k_{pre\_inf,m} + 10 \mid k > k_{DFGE} + 10\} \quad (4)$$

where  $k_{DFGE}$  denotes the range gate  $k$  that serves as an initial value for the iterative estimation procedure and is calculated for each received waveform  $w_r$ , as described in the following sections. A visualisation of the detected interference gates  $k_{inf}$ , as expressed by Eq. (4), is shown in Fig. 2 (b-d). Here, the gates  $k_{inf}$  are marked by the red area. It can be observed that  $k_{inf}$  includes gates, whose power values of the received waveform  $w_r$  exceed the threshold level of  $w_{IR}$ , but also the  $\pm 10$  adjacent gates that were extended, according to Eq. (3) and Eq. (4), respectively.

It can be concluded that the closer  $SWH_{IR}$  is chosen to be to the actual SWH of  $w_r$ , the tighter  $w_{IR}$  is spanned around  $w_r$ . The goal of the retracking strategy of CORALv1, as elaborated in the next section, is to refine  $SWH_{IR}$  in a two-step retracking approach so as to accurately detect all interference gates. Fig. 2 (b), (c), (d) demonstrates how the interference gates  $k_{inf}$  are detected in three exemplary scenarios with perturbed received waveforms  $w_r$ . It can be observed that the methodology works well for scenarios with both weak and strong interference within the trailing edge as all interference gates are correctly detected.

The resulting  $k_{inf}$  indices are used for two purposes: first, these indices discard the gates that are used to calculate the LS between the received waveform  $w_r$  and the ideal model waveform, thus setting the differences in these gates to 0.0. The impact on these gates is thus completely ignored in the fitting process. Second, and this is a very essential step of CORALv1, the misfit, and thus the quality flag of the records, is calculated on the basis of interference-free gates, which gives a significantly improved measure of the goodness of the fit. Similarly, the selective misfit and the quality flag are computed according to Eq. (6) and Eq. (7), excluding  $k_{inf}$ .

### 3.1.2. Retracking strategy

The objective of CORALv1 with AIM is to retain as many measurements as possible in the coastal zone without essentially diminishing the quality: maximising the quantity while maintaining the quality.

The retracking strategy of CORALv1 is composed of a Dynamic First-Guess Epoch (DFGE) processing block (as described in detail in Section 3.1.3) and three individual retracking steps ①, ②, and ③, as depicted in Fig. 1. The DFGE processing block computes the initial FG values for the

epoch variable that serve as initial values for the iterative, least squares fitting of retracking step ① to ease the fitting of the correct LE in case of multipeak waveforms, which typically occur in the coastal zone.

Retracking step ① performs a standard SAMOSA-based fitting using an iterative, least squares fitting scheme with fixed initial values according to the methodology described in Section 3.1.4 and outputs an initial estimate  $SWH_{first}$ . In this step, AIM uses  $SWH_{IR}=8$  m to detect and mask strong spurious signals during the estimation procedure of the geophysical variables. We defend the choice of  $SWH_{IR}=8$  m as it is a good trade-off between tightly enclosing the received waveform  $w_r$  whilst still keeping a large enough margin to it to also accommodate normally-sized speckle-noise, which will not be detected as interference. For interference-free, open ocean waveforms, the final estimate  $SWH_{final}$  is already given by the output  $SWH_{first}$ .

In the case of a coastal waveform with a dist-to-coast  $< 20$  km, retracking step ② is performed to refine the estimates of  $SWH_{first}$  and the misfit. The estimated parameters ( $SWH$ , epoch,  $P_U$ ) of step ① are used as initial values for the iterative fitting and  $SWH_{IR}$  is set to  $SWH_{first} + 2$  m. The value of 2 m is added as another empirical margin to avoid the detection of speckle-noise-affected gates. In this step, the AIM adaptively adjusts  $w_{IR}$  with a more accurate  $SWH_{IR}$  parameter to enhance the interference gates detection; the final estimate of  $SWH_{final}$  and the misfit improve accordingly.

In coastal scenarios, including other scenarios such as sea-ice leads in polar regions, the waveform to be fitted might be very peaky. The pulse peakiness (PP) is defined as  $PP = \frac{\max(w_r)}{\sum_k w_{r,k}}$ . The SAMOSA2 model in retracking steps ① and ② is unable to converge to peaky waveforms; the resulting estimated misfit is thus inaccurate. The last retracking step ③, adopted from the SAM+ retracker, accounts for this and replaces the SWH by the MSS as one of the three free parameters of the fitting procedure, which allows the fitting of peaky waveforms. This step is thus performed only if the received waveform  $w_r$  is very peaky, which is the case if at least one of the following (heuristic) conditions are met, as defined in Dinardo et al. (2020), Eq. 3.36:

$$\begin{aligned} E \cdot PP &< 0.68 \\ E \cdot PP &> 0.78 \\ 100 \cdot PP &> 4 \\ \frac{E}{\text{misfit}} &< 8 \end{aligned} \quad (5)$$

where the entropy is defined as  $E = - \sum_j^K |w_{r,j}|^2 \log_2(|w_{r,j}|^2)$ . The SWH parameter is fixed in this step and set to  $SWH_{final}$  and thus does not lead to any more improvements on the targeted SWH. However, step ③ is crucial for CORALv1 as it allows a more accurate estimate of the misfit value, which in turn gives a more accurate measure for the goodness of the fit, the quality flag (Eq. (6) and Eq. (7)). In case of very peaky waveforms, additional records can be recovered and prevented from being flagged as bad. The misfit value to be calculated is based on the difference between the received and the fitted model waveform, as used by the SAM+GPOD dataset, and is given by

$$\text{misfit} = 100^* \sqrt{\frac{1}{N} \sum_k^K (w_{r,k} - w_{SAM2,k})^2} \quad (6)$$

where  $w_r$ ,  $k$  and  $w_{SAM2,k}$  are the bins of the received and modelled SAMOSA2 waveform with range gate indices  $k$ , respectively (Dinardo et al., 2018, Eq. 31). Unlike SAM+, CORALv1 excludes the interference gates from the misfit calculation, as presented in Section 3.1.1. We thus define this strategy to be a ‘‘selective misfit’’.

As stated in Dinardo et al. (2018), we have defined the quality flag  $q$  as

$$q = \text{misfit} > 4 \quad (7)$$

which is a boolean array with good (False: 0) and bad (True: 1) values.

### 3.1.3. Dynamic first-guess epoch

We adopt the SAM+ approach to assign the initial value of the epoch and refer to it as the Dynamic First-Guess Epoch (DFGE). DFGE is a simple but very effective method to deal with multipeak waveforms and to ease the convergence to the correct LE edge. It takes the point-wise product of a sliding window of  $n_{\text{adj}}$  adjacent waveforms (SAM+:  $n_{\text{adj}}=20$ ) that are located before and after a received waveform  $\mathbf{w}_r$ ,  $i$  and computes its maximum (Dinardo, 2020). It is expressed by

$$k_{\text{DFGE}}[i] = \underset{k}{\text{argmax}} \left( \prod_{j=i-n_{\text{adj}}/2}^{i+n_{\text{adj}}/2} w_{r,j} \right) \quad (8)$$

for all  $N$  normalised, tracker-range-aligned received waveform vectors  $\tilde{\mathbf{w}}_{r,i}$  with the record index  $i=0, \dots, N-1$ , where the  $\underset{k}{\text{argmax}}_k$ -operator denotes the range gate index  $k$  of the waveform, for which the point-wise product has its maximum. Tracker-range-aligned implies a correction that takes into account the on-board tracker-range of the altimeter and aligns all multilooked waveforms in time. We have adopted DFGE for CORALv1 and chosen  $n_{\text{adj}}$  to be equal to 40 so as to take into account more adjacent waveforms in order to get a more robust initial estimate of the FG epoch.

### 3.1.4. Parameter estimation

The standard SAMOSA-based retracker that is used for the SAM-EUM retracker is defined in theory along with its practical implementation in the SAMOSA detailed processing model (SAMOSA Detailed Processing Model, 2017, pers. comm. Jérôme Benveniste), which was developed within the framework of the ESA SAR Altimetry MOde Studies and Application (SAMOSA) project. The detailed processing model document is based on the formulation of the SAMOSA2 model, which is described in detail in Ray et al. (2015). In contrast to the SAMOSA detailed processing model (SAMOSA Detailed Processing Model, 2017, pers. comm. Jérôme Benveniste), we use the PTR Gaussian approximation coefficient value  $\alpha_{\text{p,mean}}=0.5$  as this is allegedly the more correct value (Dinardo, 2020).

We will not describe the details of the SAMOSA2 model as this has been already discussed in the aforementioned references.

In order to fit the SAMOSA2 analytical model, we use the Trust Region Reflective (TRR) algorithm, which constitutes a computationally-efficient method for solving large-scale, bound-constrained minimisation problems (Branch et al., 1999). SWH, epoch, and  $P_u$  are the three free parameters that are optimised to acquire the best fit between the SAMOSA2 model and the received waveform  $\mathbf{w}_r$ . The TRR algorithm finds the solution in an iterative way, which implies the use of initial values and boundaries for each of the free parameters. The closer the initial values are chosen to the truth, the more likely the convergence to the optimal solution becomes. The chosen initial values, the boundaries for the free parameters as well as other optimisation parameters for the

TRR algorithm are set as defined in Table 2. If chosen differently within the retracking strategy, it is noted in the text. Although it is not physical, a negative boundary of  $-0.50$  m for the SWH is set to also accommodate noisy SWH estimations.

Before running the fitting process, the received waveform  $\mathbf{w}_r$  is normalised within waveform samples  $k = k_{\text{DFGE}} - 10, \dots, k_{\text{DFGE}} + 10$ , expressed as

$$\hat{\mathbf{w}}_r = \mathbf{w}_r / \max_{k_{\text{DFGE}}-10, \dots, k_{\text{DFGE}}+10}(\mathbf{w}_r) \quad (9)$$

This accounts for cases, in which very strong interferers are apparent in the trailing edge. Since the initial value of  $P_u$  is set to 1.0, a convergence to a waveform is eased if the normalisation was performed around the correct LE.

## 3.2. Validation

In order to validate the CORALv1, we adopt the methodology of the Round Robin assessment that was developed within the framework of the ESA Sea State Climate Change Initiative (SeaState\_cci) project. Please refer to Schlembach et al. (2020) for full details. In the following, we summarise the methods and mention any changes or additions that we have applied.

Six different types of analyses are performed for the validation: outliers, number of valid records, intrinsic noise, power spectral density, and comparisons with wave model and in-situ data. The statistics number of valid records was added here as compared to Schlembach et al. (2020) to put more emphasis on this statistical measure. The metrics are assessed as functions of sea state and dist-to-coast, as defined in Table 3 and Table 4 respectively. In contrast to Schlembach et al. (2020), we changed the definitions of the lower and upper boundaries slightly and set them consistently to be  $\geq$  and  $<$  respectively. The dist-to-coast grid dataset used is from PacIOOS, which features a resolution of  $0.01^\circ$  (with an uncertainty of  $\sim 1$  km). As the dist-to-coast values are rounded down to integer values, we defend the change from dist-to-coast  $> 0$  to dist-to-coast  $\geq 0$ , which therefore includes more coastal values. In addition to the aforementioned analyses, we perform a short study-case-analysis to highlight the strength of CORALv1 to maximise the number of valid points in the coastal zone.

When reading the retracked datasets (both CORALv1 and those from Section 2.4), we apply the quality flag such that all records flagged as bad are excluded. We only consider ocean records with a dist-to-coast  $\geq 0$  km and disregard the rest. Since CORALv1 does not target scenarios over sea-ice, we discard measurements that were recorded in polar regions, and thus exclude those with a latitude  $> 70^\circ$  and  $< -55^\circ$ . In case of seasonal sea ice within the non-excluded latitudes, we take into account the measured sea\_ice flag from the EUMETSAT L2 product (surf\_type\_class\_20\_ku variable) and exclude these values. Some retracking algorithms initialise the SWH values with 0 m and do not update it in cases where retracking fails. This behaviour yields invalid estimates so that we exclude these values (checking for values of approximately 0 m with tolerance of  $1 \times 10^{-4}$  m).

In Section 3.2.2 and Section 3.2.5, the 20-Hz records are reduced to 1-Hz. The median of each longitude/latitude-pair, SWH, and time vectors is taken from the twenty 20-Hz values to obtain the corresponding 20-Hz record. An additional constraint is imposed to reduce the 20-Hz SWH values: at least 17 valid values (neither not-a-number (NaN), bad quality flag, nor marked as being sea-ice) of the twenty 20-Hz-points

**Table 2**

Optimisation parameters used for TRR algorithm. Ftol, gtol, and xtol are tolerances for terminating the fitting by the change of the cost function, the norm gradients, and the independent variables, respectively.

Optimisation parameter	Value
Init value: SWH	2.0 m
Boundary: SWH	[ - 0.5,20.0] m
Init value: epoch	estimated FG epoch
Boundary: epoch	$\pm 10 k_{\text{DFGE}}$
Init value: $P_u$	1.0
Boundary: $P_u$	[0.2,1.5]
ftol/gtol/xtol	1e-5
Step size	1e-2

**Table 3**

Definition of sea states.

Sea state	SWH range
Low	0 m < SWH < 2 m
Average	2 m < SWH < 5 m
High	SWH > 5 m
Very high	SWH > 10 m

**Table 4**

Definition of zones as a function of dist-to-coast. Dist-to-coast  $\geq 0$  is assumed per default, though not written explicitly.

Zones	Dist-to-coast range
Near coastal zone	dist-to-coast < 5 km
Middle coastal zone	dist-to-coast < 10 km
Far coastal zone / coastal zone	dist-to-coast < 20 km
Open ocean	dist-to-coast $\geq 20$ km

must exist. Otherwise, the resulting 1-Hz SWH is set to NaN (invalid).

### 3.2.1. Outliers

In some cases, retracking algorithms are unable to retrieve a reasonable SWH estimate due to strong interference in the received waveform, which may originate from strongly reflective targets such as mud banks, sheltered bays, shipping platforms etc. The resulting estimate may be detected as erroneous by the retracker itself and thus flagged as bad, depending on the definition of the quality flag. In the other good value cases, the resulting SWH retrievals might be out of the defined range of  $[-0.5, 25.0]$  m or detected via a so-called `mad_factor` criterion (see below). We have therefore evaluated three types of outliers, which are combined into the total number of outliers `n_total`:

**invalid** Missing data (records value set to NaN) or quality flag set to bad (False/1).

**out\_of\_range** If an SWH value is out of the expected range of  $[-0.5, 25]$  m. (Noisy estimations may sometimes return negative value).

**mad\_factor** This criterion takes into account the adjacent 20 records (10 before and 10 after). It is implemented using median and median absolute deviation (MAD), which are statistically robust measures. The value is an outlier if it exceeds the median  $\pm 3 \cdot 1.4826 \cdot \text{MAD}$ , with median and MAD calculated on 20-point sliding windows, and the factor 1.4826 converts the MAD to a STD equivalent for a normal distribution (Alvera-Azcárate et al., 2012).

**n\_outliers** Total number of outliers, i.e. the combination of all three types of outliers. If a record is an outlier of multiple types, it is counted only once with regard to the total amount. As opposed to the residual types of analyses, no sea-ice flag is considered when reading the datasets, as this would correspond to another type of quality flag and mark the records as invalid.

### 3.2.2. Number of valid records

In addition to the assessment in Schlembach et al. (2020), we explicitly evaluate the number of valid 20-Hz and 1-Hz records. Valid records correspond to the complement of the number of invalid outlier types. In other words, valid records represent the number of ocean records that are not located in polar regions (see definition in Section 3.2) and not flagged as bad by the retracker's SWH quality flag. The number of the residual outlier types `out_of_range` and `mad_factor` are not considered in this case, as the objective of this metric is to highlight the number of valid points that the retracker considers to be good. The metric is extracted for both 20-Hz and 1-Hz records. For the valid 1-Hz records, we first perform the 20-to-1-Hz reduction as described in Section 3.2 and then set the number of available relative to the total number of 1-Hz records.

### 3.2.3. Intrinsic noise

Intrinsic noise is defined as the standard deviation of 20-Hz SWH data within a 1-Hz distance. This definition is based on the assumption that the variability at the 20-Hz posting rate (equivalent to an along-track distance of  $\sim 330$  m) is mostly dominated by noise (Ardhuin et al., 2019; Fenoglio-Marc et al., 2015).

In order to compute the STD of the twenty 20-Hz measurements, we impose the constraint that there must be least 17 valid measurements.

In order to compute the standard deviation of the 20-Hz estimates, we perform the 20-to-1-Hz reduction as described in Section 3.2. We

extract the median noise as a function of dist-to-coast and SWH (using a bin size of 0.25 m).

### 3.2.4. Power spectral density

Section 3.2.3 describes the analysis of intrinsic noise and thus the precision of the measurements on a small scale. The power spectral density (PSD) analysis extends this analysis and investigates the along-track spectra of the SWH series on larger scales too, as shown in Quilfen and Chapron (2019) and Boas et al. (2020). For the sake of clarity, and for further details on the explanation and the calculus of the PSD, please refer to the Round Robin assessment article in Schlembach et al. (2020).

### 3.2.5. Comparison with wave model

In order to assess both the accuracy and precision of the estimates, we compare the retracked datasets of CORALv1 and reference retracking algorithms from Section 2.4 with the ERA5-based hindcast (ERA5-h) wave model presented in Section 2.3, as conducted in Schlembach et al. (2020) and Abdalla et al. (2018). The ERA5-h wave model is a gridded product with a resolution of 14 km. The collocation is performed by an interpolation of the gridded product onto the along-track 20-Hz data points of the retracked dataset, before being reduced to 1-Hz. This is considered as reasonable, since the resolution of the 1-Hz dataset is still higher than the ERA5-h wave model at hand ( $\sim 7$  km vs. 14 km).

After the 20-to-1-Hz reduction, we pair the two collocated data series with each other, while only considering valid non-NaN and non-out-of-range values. A linear least squares regression analysis is then performed on the coupled series. We can thus assess the performance with regard to the wave model by analysing the Pearson correlation coefficient, standard deviation of differences (SDD), median bias, and a 2D-histogram plot.

The SDD and the median bias of differences is defined as

$$\text{SDD} = \text{std}(|\text{SWH}_{\text{retracker}} - \text{SWH}_{\text{ERA5-h}}|), \quad (10)$$

and

$$\text{median bias} = \text{median}(\text{SWH}_{\text{retracker}} - \text{SWH}_{\text{ERA5-h}}) \quad (11)$$

where `std` denotes the STD, and `|·|` the absolute magnitude operator.

It has to be noted that the wave model certainly has limitations in the coastal zone due to wave interactions with the local bathymetry or land-shading effects.

### 3.2.6. Comparison with in-situ data

To gain a more independent validation of the retracked results, the assessment of CORALv1 is complemented by the comparison with quality-checked in-situ buoy data, as conducted in Schlembach et al. (2020) (with details on the applied quality control) and Abdalla et al. (2018). We have one buoy measurement for each buoy site for each of the 17 cycles of the altimeter data and collocate it by taking the median of the closest 51 altimeter SWH records, as defined in Section 2.2. A linear regression analysis is conducted from the resulting 17 collocated buoy-altimeter pairs per buoy from which the Pearson correlation coefficient is computed.

The definition for the computation of the SDD and median bias follows the same calculus as for the collocated altimeter-model pairs in Eq. (10) and Eq. (11), respectively.

Another extracted metric is the percentage of cycles for high correlation (PCHC), first developed in Passaro et al. (2015) with the objective of providing a statistic to simultaneously assess the quantity and quality of the data. It calculates the number of cycles that have a high correlation factor of 0.9 in relation to the total number of cycles at hand by iteration. For instance, starting from the computation of the correlation with all altimeter-buoy collocated pairs, the correlation is checked to see if it is above 0.9. If not, the altimeter-buoy pair (corresponding to the altimeter measurement of a specific cycle) with the greatest (absolute)

difference is dropped. This procedure is repeated until the correlation is higher than 0.9. This ultimately results in the percentage of cycles with a correlation coefficient above 0.9. The higher the PCHC is, the better the retracker is able to provide a robust estimate with regard to in-situ data.

All metrics are extracted for buoys that are located in the coastal zone or the open ocean.

### 3.2.7. Coastal case study

We conducted a short case study analysis to emphasise the strength of CORALv1: the maximisation of valid points in the coastal zone. We therefore picked two coastal study case scenarios, for which we compare the SWH series and its corresponding quality flag of CORALv1 with SAM+-GPOD. In addition, we show the corresponding SWH values of the ERA5-h wave model and a collocated buoy measurement. The analysis is complemented by a map, showing the measurements with the corresponding illuminated area on ground.

## 4. Results and discussion

This section assesses the performance of CORALv1 and compares it with the processed datasets of the retracking algorithms SAM-EUM, SAM-EUM-MQE, LR-RMC, and SAM+-GPOD. We place particular emphasis on the comparison with SAM+-GPOD, which is the only coastal retracker being investigated besides CORALv1, unlike the rest, which target open ocean scenarios.

We have simplified the plots for the sake of clarity and readability whenever possible. For fully detailed plots, please refer to the supplementary materials section of this article.

### 4.1. Outliers and number of valid records

Fig. 3 shows the total number of outliers as a function of dist-to-coast. We observe that the number of outliers does not differ as significantly for the open ocean as it does for the coastal zone. In the open ocean, CORALv1 shows the least amount of outliers with 2.53%, whereas SAM-EUM-MQE has the highest value with 6.81%. With regard to the coastal zone, the differences between the different retrackers are much more significant. LR-RMC shows the highest amount of outliers for the near, middle, and far coastal zones after SAM-EUM-MQE. SAM-EUM has the fewest outliers in these cases, followed by CORALv1 and SAM+-GPOD. In the near, middle, and far coastal zones, CORALv1 has 25%, 17% and 12.5% fewer outliers than SAM+-GPOD, respectively.

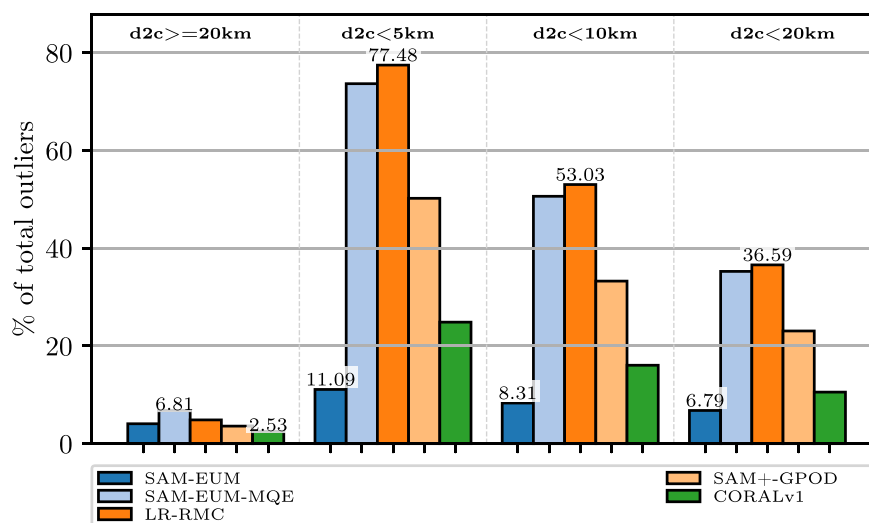


Fig. 3. Total number of outliers for the different retracking algorithms as a function of dist-to-coast, showing open ocean ( $d2c \geq 20$  km), near coastal zone ( $d2c < 5$  km), middle coastal zone ( $d2c < 10$  km), and far coastal zone ( $d2c < 20$  km).  $d2c$  is used here and in the following for dist-to-coast as the shorthand notation.

Fig. 4 shows the distribution of the different types of outliers for CORALv1 and SAM+-GPOD. It can clearly be seen that the total number of outliers is dominated by the invalid outliers, i.e. mostly data flagged as bad. There is a clear dependence on the dist-to-coast. The closer the records are located to the coast, the higher the number of invalid measurements. The types out\_of\_range and mad\_factor are very limited or non-existent and are thus of minor significance.

The numbers of valid 20-Hz and 1-Hz records is shown in Fig. 5. The quantitative numbers correspond to the complement of the invalid outlier type, which is essentially the overall number of records that the retracker assesses as being good estimates. We believe it is important to highlight the number of actual valid measurements, as this is a crucial metric when assessing the quality of the measurements at the same time. SAM-EUM again represents the exception here, as almost no 20-Hz measurements are discarded across all zones (more than 96% of valid records in the near coastal zone). Section 4.4 and Section 4.5 will show that this comes at a high cost in terms of quality. Apart from SAM-EUM, CORALv1 features 25.9%, 17.8%, and 12.9% more valid 20-Hz records compared to the SAM+-GPOD retracker, which has the second highest number of records. The difference of the number of valid 1-Hz records in Fig. 5 (b) is less between the retrackers. Due to the 20-to-1-Hz decrease, the proportional gain of CORALv1 is reduced: since at least 17 valid points out of 20 records are needed, not all 20-Hz-blocks will give a valid 1-Hz record.

CORALv1 features a significantly decreased number of outliers, and thus an increased number of valid records in the coastal zone, particularly when getting closer to the coastline. This increase in additional measurements is achieved by the AIM processing scheme, which enables range gates that are contaminated by reflective targets within the footprint to be masked and the goodness of the model fit, i.e. the quality flag, improved. Section 4.4 and Section 4.5 present and discuss the quality of the recovered retrievals.

### 4.2. Intrinsic noise

Fig. 6 shows the intrinsic noise as a function of SWH for both overall (a) and coastal scenarios (b). For the overall noise performance, we see that LR-RMC clearly outperforms all other retrackers for average and high sea states, with a nearly constant median noise level of  $\sim 0.30$ – $0.33$  m. This is to be expected, since the 20-Hz values of LR-RMC are actually referred to an averaged echo spanning a much larger area (equivalent to four bursts) (Moreau et al., 2021). The SAMOSA-based retrackers, including CORALv1, follow nearly the same noise level curve, which

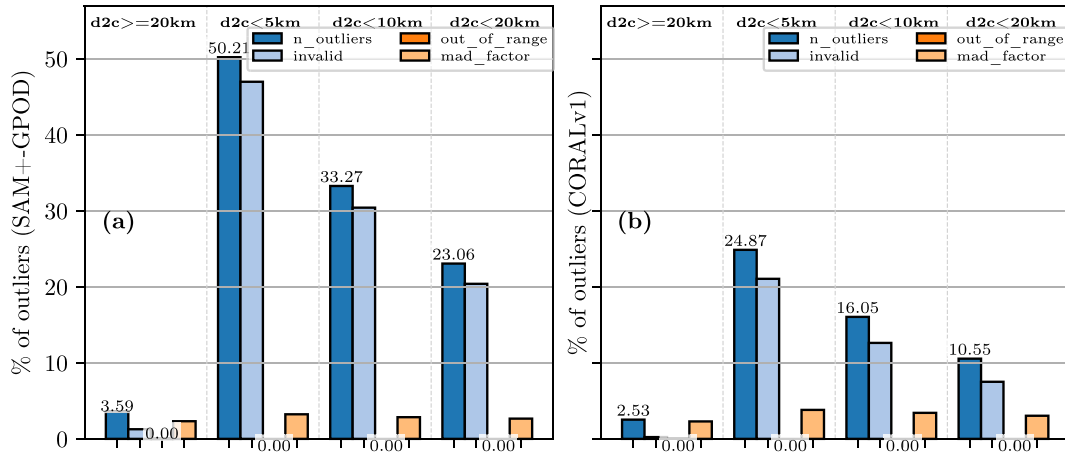


Fig. 4. Distribution of types of outliers for (a) SAM+-GPOD and (b) CORALv1.

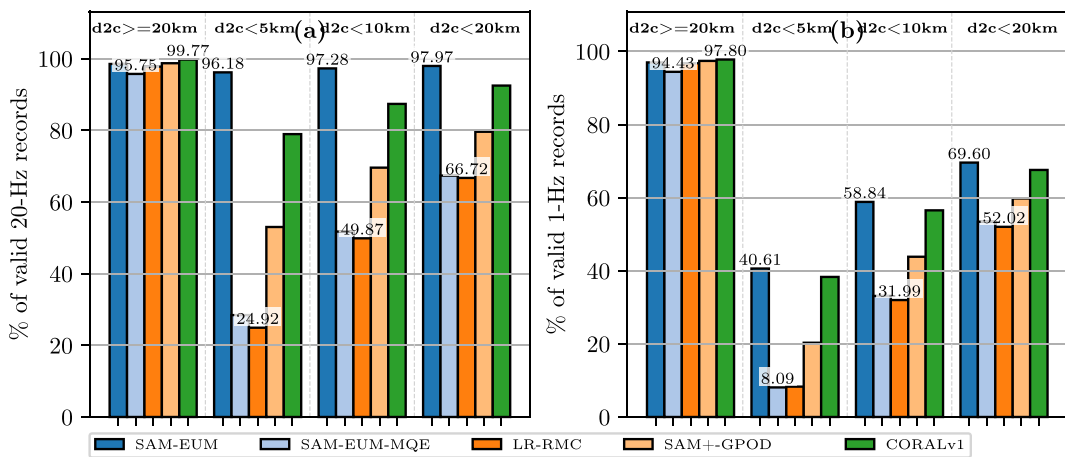


Fig. 5. Number of valid (a) 20-Hz and (b) 1-Hz records for the different retracker.

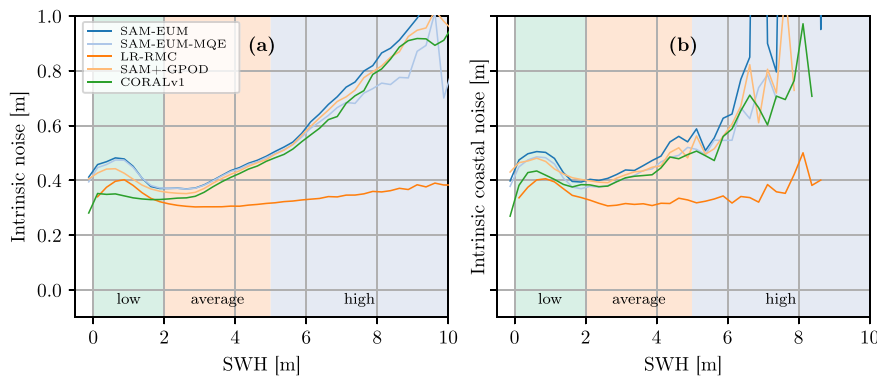


Fig. 6. Intrinsic noise versus SWH for the different retracker: (a) overall scenarios and (b) coastal scenarios.

increases with the SWH. For low sea states, CORALv1 shows the lowest intrinsic noise characteristic with a median noise value of 0.33 m, closely followed by LR-RMC with 0.35 m. The median noise level of the residual retracker ranges between approximately 0.38–0.40 m for low sea states. The intrinsic noise characteristics for the coastal areas does not change significantly, as shown in Fig. 6 (b), although they are less linear because of the reduced number of records. This confirms that the increased number of coastal measurements of CORALv1 does not significantly deteriorate the noise performance, regardless of the SWH. Fig. 7 shows the median noise values as a function of dist-to-coast.

CORALv1 and LR-RMC show only a minor dependence on the proximity to the coastline. LR-RMC's median noise level is increased from 0.32 m to 0.38 m when moving from the open ocean to the near coastal zone, CORALv1's from 0.36 m to 0.52 m, and SAM+-GPOD's from 0.38 m to 0.55 m. The increase in noise of CORALv1 and SAM+-GPOD comes at a cost of the significantly increased number of estimates. SAM-EUM shows a very noticeable increase towards the coast, whereas its quality-flag-improved counterpart SAM-EUM-MQE exhibits only a minor dependence on the dist-to-coast. This shows that the increased values included in SAM-EUM are actually very noisy, thus



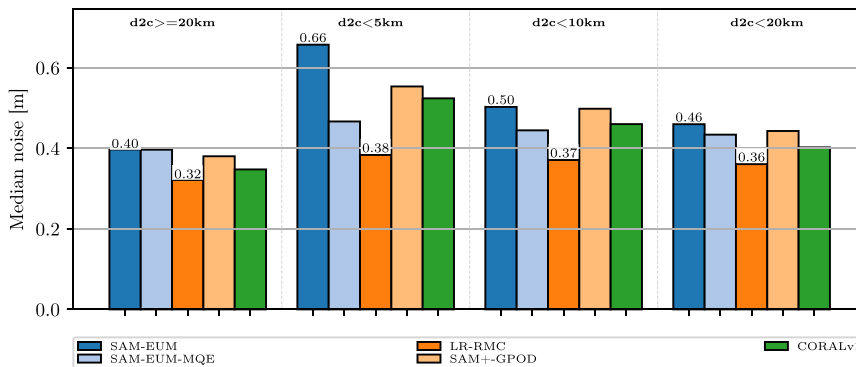


Fig. 7. Median noise for the different retracker as a function of dist-to-coast.

demonstrating the effective use of the newly proposed quality flag of SAM-EUM-MQE.

This analysis has shown the intrinsic noise characteristic of the different retracker. CORALv1 is as good as the rest of the SAMOSA-based retracker for average and high sea states, but not as good as LR-RMC. While this would appear to favour a numerical approach to retracking at open ocean scales, Quilfen and Chapron (2020) demonstrated that post-processing techniques can also be effective in “denoising” the data. CORALv1 outperforms all other SAMOSA-based retracker by ~5–7 cm for low sea states (and is slightly better than LR-RMC). This improvement originates from the oversampling of the multilooked waveform (as described in Section 3.1.4), which targets the strong undersampling of the very steep LE that altimetry waveforms typically exhibit for low sea states (Smith and Scharroo, 2015). For high sea states, the slope of the LE is less steep.

4.3. Power spectral density

Fig. 8 shows the PSD of the along-track SWH of CORALv1 and the residual retracked datasets. The open ocean segments that were taken into account for each of the retracked datasets include both large-scale geophysical signals and noise induced by the altimeter instrument and retracking.

With regard to the very large-scale (greater than 100 km) and the mesoscale range between 100 and 50 km, all retracker show a similar amount of signal content. None of the retracker fall below one of the two defined PSD level boundaries of 0.2 m<sup>2</sup>/(cycles/km) and 0.05 m<sup>2</sup>/

(cycles/km) for 100 km and 50 km, meaning no crucial geophysical signal content is missing. These boundaries were selected by a group of experts in the context of SeaState\_cci as representative values for the PSD content that should be expected at these wavelengths, based on theoretical considerations and model simulations.

In a visual comparison with the non-denoised characteristic from a J2 dataset (Quilfen and Chapron, Fig. 1, right), we can observe a similarity in terms of the shape of the spectral slopes. Dodet et al. (2020) has also investigated long-term 1-Hz along-track spectra of J2 for scales of several hundreds to down to ~50 km and found that the spectral slopes correspond to  $k^{-p}$  with  $p$  ranging between -1.5 to -1.7, which is similar to the results that we found.

One very significant exception is the SAM-EUM retracker, which shows a very pronounced noise level on the mesoscale. The additional samples that SAM-EUM has flagged as good add a significant amount of noise on top of the real large-scale signal. Approaching a small-scale region of the spectra, LR-RMC converges to a nearly constant noise level for scales of up to 10 km. For scales of 25–50 km, SAM+-GPOD shows a slightly increased energy level compared to the counterparts. SAM-EUM-MQE and CORALv1 exhibit nearly the same characteristic in their variability.

From this analysis, we can state that CORALv1 is able to realistically represent global SWH spatial variability, in particular on the 25–100 km scales, where there is a scientific consensus on the expected slope. This is as expected, since only open ocean segments are taken into account here. CORALv1’s extensions are related to the coastal zone only and it reverts to a standard SAMOSA-based retracker in the open ocean.

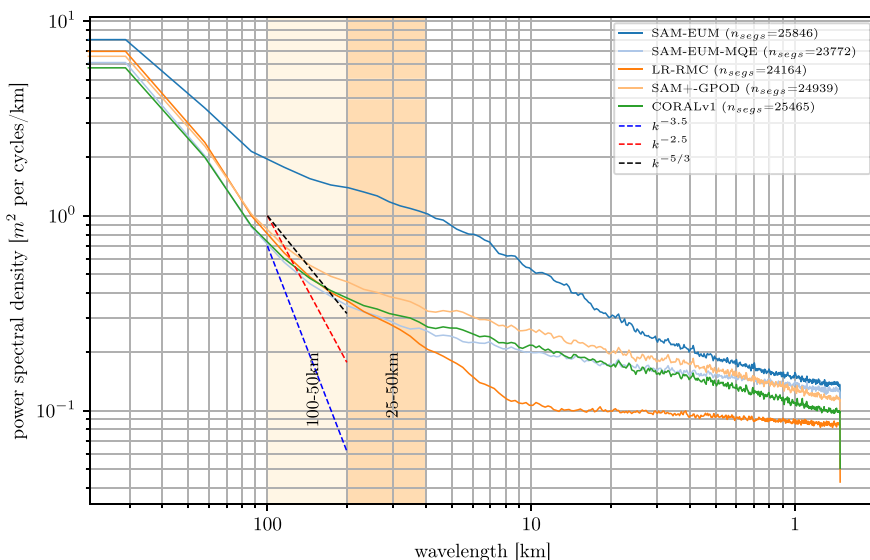


Fig. 8. PSD of the along-track SWH for the different retracker. The spectra are computed over  $n_{segs}$  averaged Fourier-transformed 1024-point segments (including a Hann window) with an overlap of 50%. Each segment is constrained to be located in the open ocean and at least 95% of valid points must be apparent (the residual invalid ones are linearly interpolated). The slopes  $k^{-3}$ ,  $k^{-2.5}$ , and  $k^{-5/3}$  serve as a reference for orientation as described in Quilfen and Chapron (2019) and Bôas et al. (2020).

4.4. Comparison with wave model

In this section, we assess both the accuracy and precision of CORALv1 against the ERA5-h wave model, as described in Section 2.3. We compare the retracked and reduced 1-Hz datasets with the collocated ERA5-h records and perform a linear regression analysis.

Fig. 9 shows the Pearson correlation coefficient, the median bias and the SDD (as per row) of the comparison with the ERA5-h as functions of dist-to-coast (left column) and SWH (right column) for the different retracking algorithms.

The correlation for the open ocean is similarly high for all the investigated retrackers, with a coefficient of greater than or equal to 0.96. For the coastal zone, the correlation is slightly poorer for all retrackers (with LR-RMC slightly ahead of the rest), but still shows high values above 0.82, even in the near coastal zone. The baseline product SAM-EUM is again an exception here, as it exhibits a degraded

correlation in the coastal zone. All of the algorithms estimate low, average, and high sea states very well, showing a good to very good correlation of 0.83 to 0.93 (apart from SAM-EUM for low sea states). With very high sea states, SAM-EUM-MQE has an exceptionally good correlation, but is affected by a strong bias. Abdalla et al. (2018) have reported correlation values of 0.98 and 0.94 for the CryoSat-2 (CS2) NE Atlantic and Pacific Box (open ocean), which is in very good accordance with the values of SAM-EUM. Dinardo et al. (2018) calculated an open ocean correlation value of 0.86 for a monthly mean time series compared to another ECMWF wave model. This is broadly in accordance with the values reported here, though a different region was considered and a different model was used as a reference. Open ocean correlations have been estimated by the multi-mission SeaState\_cci dataset v1 (Dodet et al., 2020) to be 0.89, which correlates well with our results that show very high values of above 0.96.

Fig. 9 (b,e) shows the median bias between the retracked datasets

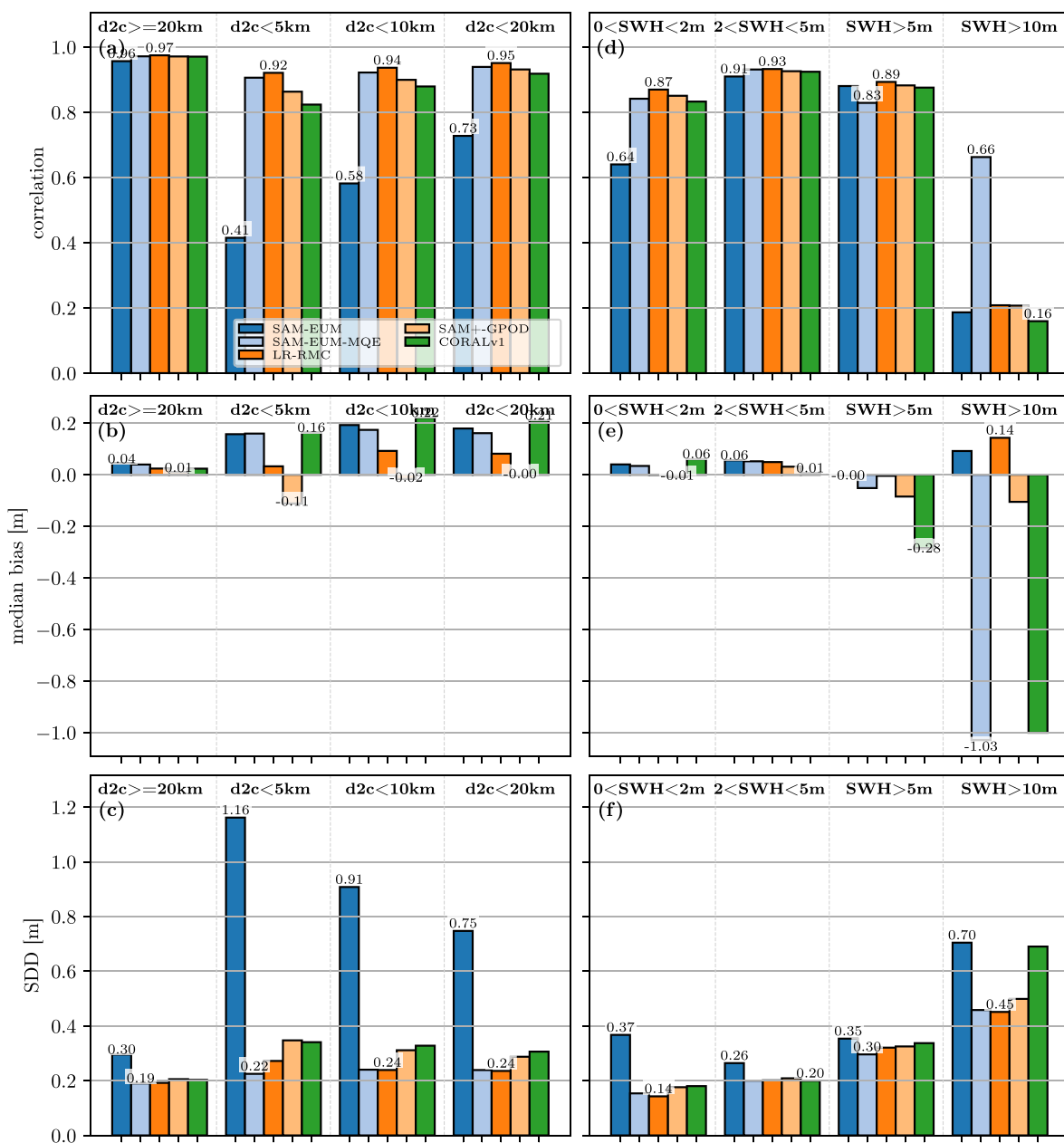


Fig. 9. Comparison with the ERA5-h wave model showing the correlation coefficient, median bias, and SDD as functions of dist-to-coast in (a,b,c) and SWH in (d,e, f), respectively.

and the ERA5-h. All retrackerers show a very small bias of less than 0.04 m for the open ocean. For the middle and far coastal zone, all retrackerers show a slightly increased bias of 0.08–0.18 m, apart from SAM+-GPOD, which features almost none. LR-RMC exhibits a bias close to 0 in the near coastal zone, whereas CORALv1 overestimates by approximately 0.16 m and SAM+-GPOD underestimates by about 0.11 m. For low and average sea states, all retrackerers show a bias of less or equal than 0.06 m. The high and very high sea states are underestimated by CORALv1 by 0.14–0.31 m, but this might be also explained by the scarcity of available records in these very high sea state regimes.

Concerning the median bias found by the comparison with the ERA5-h wave model, we see that the retrackerers overestimate SWH in both the coastal zones and the open ocean. The magnitude of the bias is slightly higher than that for the buoy comparison in the open ocean, but still on a comparable scale. The aforementioned works have estimated bias values of 0.08 m and 0.03 m (Abdalla et al., 2018), 0.07 m (Dinardo, 2020, Table 4.2), and 0.02 m (Dodet et al., 2020), which are in accordance with our values when considering statistical uncertainties.

The residual retrackerers show a low SDD of ~0.19–0.21 m for the open ocean and a slightly increased SDD of ~0.22–0.27 m for the coastal scenarios. The SDDs for CORALv1 and SAM+-GPOD are slightly increased for all zones by ~0.29–0.35 m. The SDD is the lowest for the low SWH regime and increases with sea states ranging from 0.14–0.69 m.

The SDD for SAM+-GPOD that was noted in Dinardo (2020, Table 4.2) is 0.30 m and thus higher than the one we evaluated (0.21 m). This might be due to the quasi-global assessment of altimeter data that we have performed and the assessment of S3A data instead of CS2. The root mean squared error (RMSE) computed in Dodet et al. (2020) is equal to 0.30 m, which is exactly the same value that we have estimated for the SAM-EUM retracker.

Fig. 10 shows the 2D-histogram plots of SAM+-GPOD and CORALv1 for the open ocean in (a,c) and the coastal zone in (b,d). The results of the linear regression analysis compared to the collocated ERA5-h

records can thus be inspected visually. Both retrackerers estimate the SWH very precisely and accurately for both the open ocean and the coastal zone, although both exhibit a few strong overestimations in the low sea state regime (with reference to ERA5-h). The open ocean correlation coefficients and the SDDs are very similar to each other (correlation: 0.971, SDD: 0.206 m vs 0.203 m). In the coastal zone, SAM+-GPOD performs slightly better than CORALv1: SAM+-GPOD-SDD 0.287 m vs. CORALv1-SDD 0.306 m. At the same time, the number of valid (1-Hz) records that CORALv1 retrieves in the coastal zone is significantly higher (by 2332, i.e. roughly 13%) compared to SAM+-GPOD, as already shown in Section 4.1. In the open ocean, the slope of regression is slightly greater or smaller than 1.0 for SAM+-GPOD and CORALv1, respectively, which means that both retrackerers tend to over- and underestimate the SWH as regards ERA5-h. In the coastal zone, SAM+-GPOD and CORALv1 overestimate the SWH as compared to the wave model (except that SAM+-GPOD underestimates low sea states), while showing slope values of 1.149 and 1.072, respectively. This is in accordance with the analysis discussed in Section 4.3.

#### 4.5. Comparison with in-situ data

This section presents and discusses the results of the comparison with in-situ buoy data that is conducted to complement the assessment compared to the ERA5-h wave model.

Fig. 11 shows the Pearson correlation coefficient, the median bias, and the SDD (as per row) of the comparison with the in-situ data, with the separation of open ocean and coastal buoys (left column) and SWH (right column) for the different retracking algorithms.

The differences in the correlation values between the individual retrackerers are marginal for both the open ocean and the coastal zone. SAM-EUM shows coefficient values of 0.94 and 0.86 for the open ocean and coastal zone and is slightly behind the rest of the algorithms, whose coefficient values amount to approximately 0.97 and 0.90, respectively. This is similar for all sea states. Low and average sea states are estimated

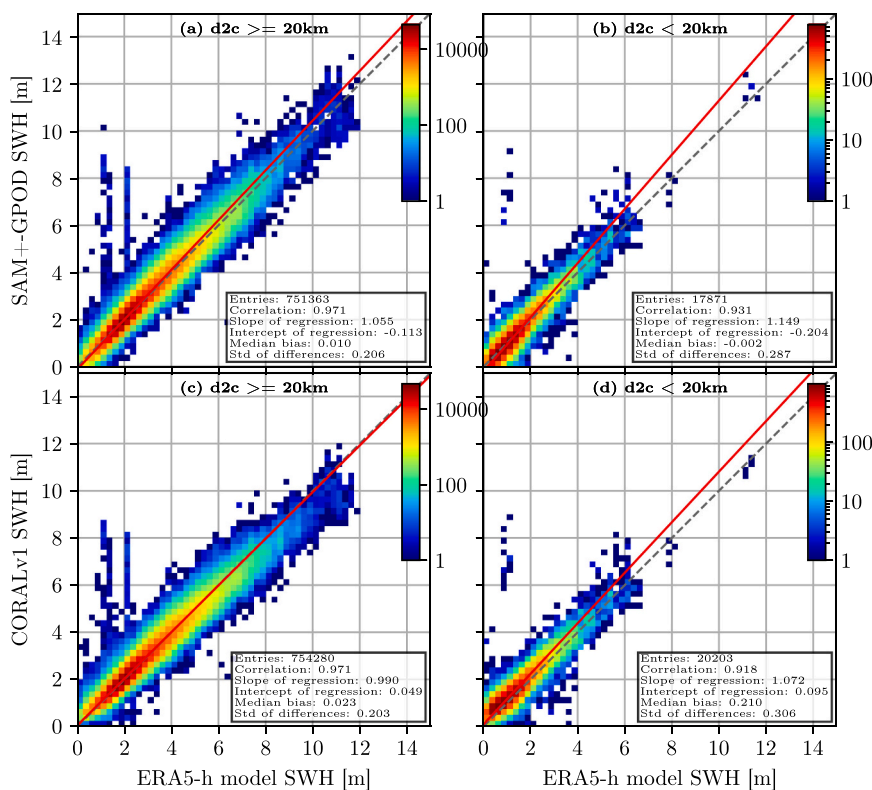


Fig. 10. 2D-histograms that compare SAM+-GPOD (a,b) and CORALv1 retrackerers with the ERA5-h wave model for the open ocean (a,c) and the coastal zone (b,d).

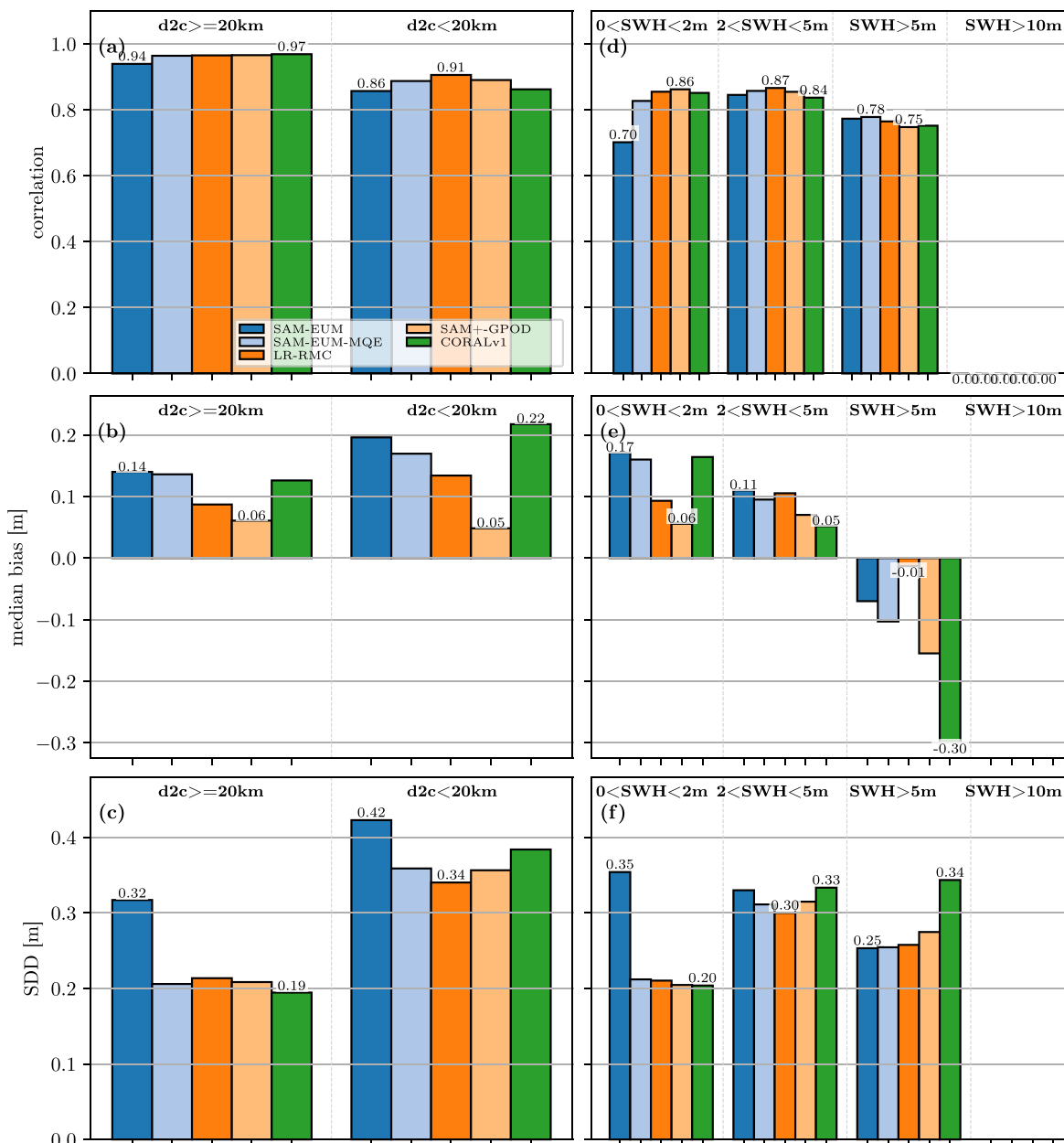


Fig. 11. Comparison with the in-situ data showing the correlation coefficient, median bias, and SDD as functions of dist-to-coast in (a,b,c) and SWH in (d,e,f), respectively.

best with a correlation of  $\sim 0.86$  (except for SAM-EUM with a value of 0.70). There are no collocations available for very high sea states and only 30 for high sea states. In fact, the differences in correlation among the retrackerers for high and very high sea states are rated as non-significant using the framework of [Diedenhofen and Musch \(2015\)](#), which is based on the methodologies described in [Fisher \(1925\)](#) and [Zou \(2007\)](#).

[Dinardo \(2020, Table 4.6, Table 4.5\)](#) has reported correlation values for SAM+-GPOD that range from  $\sim 0.89$ – $0.99$  and slightly lower values  $\sim 0.87$ – $0.95$  for different buoy sites in the open ocean and the coastal zone, respectively, which correlates very well with our findings.

With regard to the median bias, the differences are slightly more pronounced. SAM+-GPOD shows the smallest biases for the open ocean and the coastal zone with values of 0.06 m and 0.05 m. The bias for CORALv1 amounts to 0.13 m in the open ocean and a slightly higher value of 0.22 m in the coastal zone. The SWH retrievals are over-estimated by all retrackerers with respect to low and average sea states.

CORALv1 shows a slightly increased bias for low sea states and the smallest bias of 0.05 m for average sea states. The bias values for high sea states are statistically underrepresented (only 30 collocations) and we consider them to be unreliable.

In [Dinardo \(2020, Table 4.6, Table 4.5\)](#), median biases of 0.2 m and 0.03 m were noted for the open ocean and the coastal zone buoy sites, which are likewise rather smaller than the ones that we have found for SAM+-GPOD (0.06 m and 0.05 m).

The SDD values are shown in [Fig. 11 \(c,f\)](#) and there are no significant differences between the individual retrackerers either, again with the exception of SAM-EUM. For the open ocean and the coastal zone, SDD values of  $\sim 0.20$  m and  $\sim 0.34$  m are found. Low, average, and high sea states, correspond to SDD of  $\sim 0.21$  m,  $\sim 0.31$  m, and  $\sim 0.27$  m, respectively.

The values are broadly in accordance with the ones listed in [Dinardo \(2020, Table 4.6, Table 4.5\)](#), whose medians amount to 0.21 m and 0.39 m for the open ocean and the coastal zone (across all sea states).

Fig. 12 (a) shows the number of altimeter-buoy collocations for the open ocean and the coastal zone, which are paired as described in Section 3.2.6. CORALv1 has the highest number of collocations (471), followed by SAM-EUM (446) and SAM+-GPOD (441). Fig. 12 (b,c) shows the computed PCHC values as functions of dist-to-coast and sea state respectively. The PCHC is computed in the manner defined in Section 3.2.6. No great differences can be observed for the open ocean, as all retracers show a PCHC of at least 93% (lead by CORALv1 with 97%). A significant difference can be seen in the coastal zone, in which CORALv1 shows the highest PCHC of 81%, followed by SAM+-GPOD (76%) and SAM-EUM (75%). This demonstrates the effectiveness of CORALv1 in the coastal zone, meaning that CORALv1 is able to achieve a high correlation with the buoy measurements, while taking into account additional records compared to other retracers. It therefore has the best combined performance in terms of the quality and quantity of retrievals. Likewise, CORALv1 yields the highest PCHCs of 89% and 97% for low and average sea states, respectively. The PCHCs for high sea states are not significant (failing rejection of null hypothesis (Diedenhofen and Musch, 2015)), since their calculated correlations are based on very few measurements (~30).

#### 4.6. Coastal case study

In this coastal case study analysis, we have picked two single satellite overpasses of two coastal areas, for which we compare the retracking results of CORALv1 and SAM+-GPOD, as shown in Fig. 13. The first case study in Fig. 13 (a,b) shows a satellite track that follows a parallel of a nearby coastline (dist-to-coast  $\leq 3$  km) with all footprints being strongly affected by land and an estuary. The quality flag clearly shows that CORALv1 recovers almost all of the 60 measurements (apart from two of them), whereas SAM+-GPOD rejects most of them.

CORALv1 also significantly improves the quality of the estimates, as it shows a very good precision and accuracy compared to both the ERA5-h wave model and the collocated in-situ buoy measurement (with values ~3.5–4 m). In contrast, the rejected records of SAM+-GPOD are correctly flagged as bad because they exhibit a high variability and a poor accuracy compared to the wave model and in-situ buoy data.

The second case study in Fig. 13 (c,d) shows a scenario, in which the satellite track crosses the coastline perpendicularly. Apart from the very last records, no land intrusion is apparent. Both retrackers estimate nearly all records as good, with the very last land-intruded ones being flagged as bad by SAM+-GPOD. SAM+-GPOD shows a negative systematic bias of many tens of centimetres (underestimates) with regard to the estimates of CORALv1. The records of CORALv1 are in good accordance with the wave model and the buoy, estimating an SWH of ~1 m. The buoy estimate is slightly higher, which might be explained by its rather off-shore location, since SWH often decreases closer to the coast, due for example to land sheltering (Passaro et al., 2021). The SWH estimates of SAM+-GPOD are underestimated with respect to the wave

model and buoy measurement. This is in accordance with the finding for the median bias value of -0.11 m for the near coastal zone, as shown in Fig. 9 (b).

The two case studies demonstrate those scenarios in which CORALv1 has its strengths over SAM+-GPOD. A significant number of valid estimates is recovered for cases, in which the effective footprints are affected by land, while showing a very good precision and accuracy compared to the ERA5-h wave model and buoys. In cases where the footprint is not affected by land, the differences between CORALv1 and SAM+-GPOD are minor.

### 5. Conclusion and future work

The retracking algorithm CORALv1 has been presented in this work. It specifically targets the estimation of SWH in the coastal zone. In the open ocean, it reverts to a SAM-based retracker (SAMOSA Detailed Processing Model, 2017, pers. comm. Jérôme Benveniste), and in the polar zone (including the marginal ice zone) to the SAM+ retracker (Dinardo et al., 2018). It adopts two of the extensions of the coastal SAM+ retracker and implements a novel AIM scheme that further improves both the quality and the quantity of SWH estimates in the coastal zone. It could be demonstrated that the quality flag that is usually provided with the retracked outputs plays a crucial role in terms of the quality and quantity of the records. The increase of additional valid 20-Hz records achieved by CORALv1 in the near, middle, and far coastal zone amounts to 22%, 16%, and 12%. There is no downside in this gain in terms of precision, which is assessed by the analyses of intrinsic noise and PSD. The comparison with the ERA5-h wave model and 168 buoys (including 45 coastal buoys) demonstrates that the accuracy is comparable with the other competing retracking algorithms too. Notably, we have validated CORALv1 not only compared to currently available products, but also against the most recent and successful algorithms, which are not yet in operational use. CORALv1 is able to provide an increased number of good quality, valid records for (unfocused) SAR altimetry close to the coastline.

The quality flag plays a crucial role when it comes to assessing the goodness of the measurements within the coastal zone. With the aid of the AIM scheme, CORALv1 is able to drastically fine-tune the quality flag on each individual record and thus recover valuable coastal estimates. The baseline L2 product SAM-EUM of the S3 mission provided by EUMETSAT sets a very loose quality flag, from which many records are retained in the coastal zone, but are of actually a very poor quality. We propose adjusting the quality flag of the baseline SAM-EUM product so that fewer coastal records of a higher quality are maintained. The validation results with the redefined quality flag of SAM-EUM literally looks like a different dataset, which underlines the crucial importance of the quality flag determination strategy.

In this work, we have demonstrated the effectiveness of CORALv1 with the AIM scheme and how the quantity in the coastal zone can be

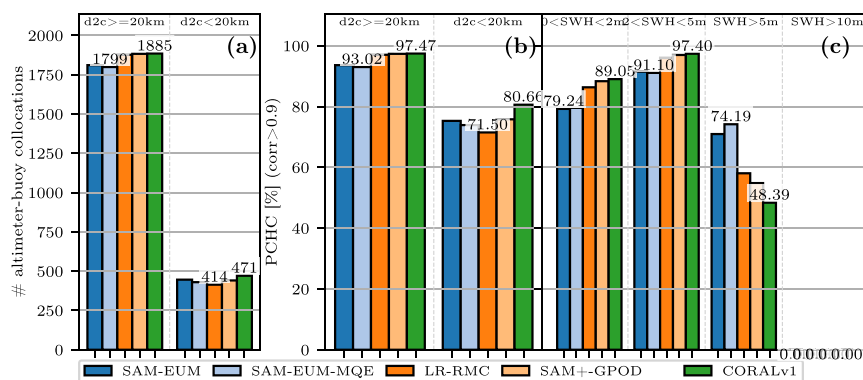
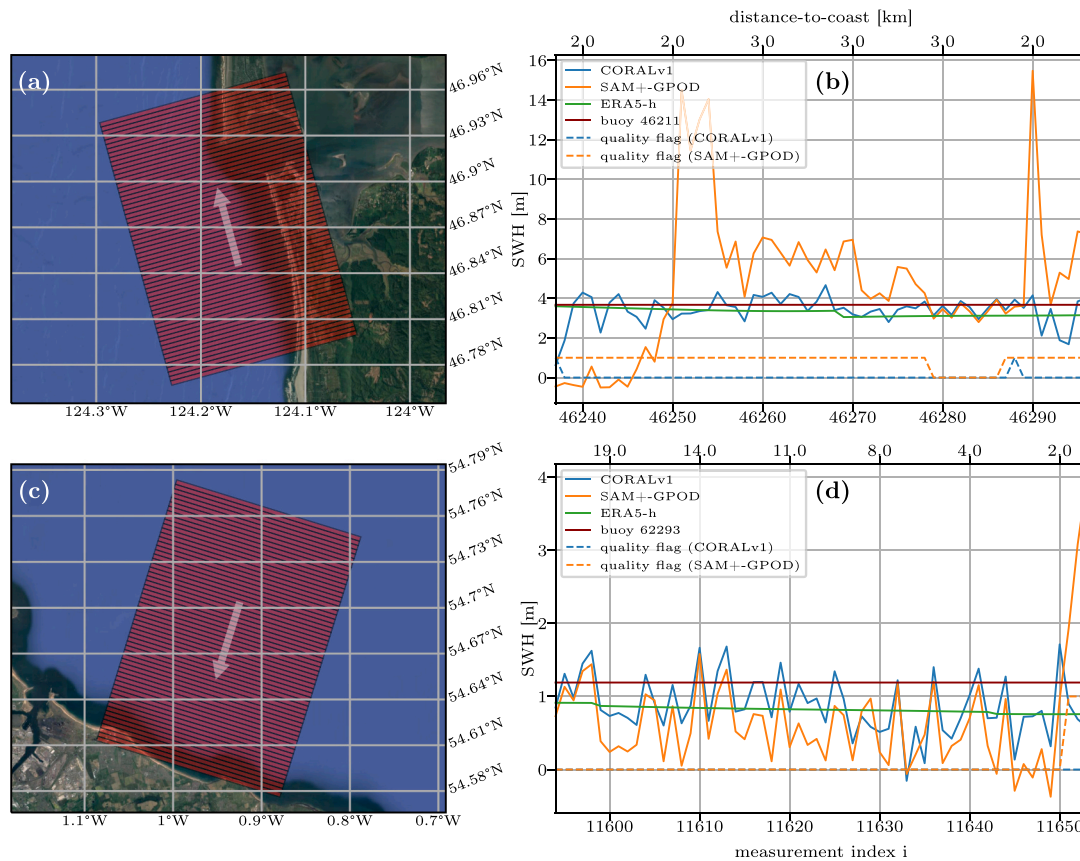


Fig. 12. Number of matching entries in (a), PCHC as functions of (b) dist-to-coast and (c) SWH.



**Fig. 13.** Two coastal case studies showing maps of the effective footprints, size 14 km × 330 m, of each of the sixty 20-Hz along-track measurements (~20 km of along-track distance) on the left panels and the corresponding retracked SWH series and its quality flag estimates of CORALv1 and SAM+-GPOD. The ERA5-h wave model and a collocated buoy are shown in solid green and dark red as external references. The quality flag (0: good, 1: bad) is depicted in dashed blue (CORALv1) and orange (SAM+-GPOD). The two case studies in (a,b) and (c,d) show measurements from the S3A tracks of cycle 30 and of relative orbits 90 and 265 with their centre records located at (46.87° N, 124.17° W) and (54.68° N, 0.94° W), respectively. (For interpretation of the references to colour in this figure legend, the reader is referred to the web version of this article.)

increased significantly. The possibility of greatly increasing the amount of high-rate data in the coastal zone and the reliability of its quality flag, particularly in the last 5 km from the coast, where wave properties rapidly change with the nearshore bottom topography, may allow an observation of wave phenomena such as wave refraction, diffraction, as well as frictional, shoaling, breaking and resonant processes (Dodet et al., 2019). Moreover, we also aim to assess the benefits of CORALv1 in terms of sea level and backscatter determination. This will allow us to study the influence of sea state on sea level (such as through wave setup, see Melet et al. (2018)) and to evaluate the sea state bias affecting range measurements close to the coast (Passaro et al., 2018). Moreover, we are planning to investigate the adaptation of CORALv1 to SAMOSA++ instead of SAM+, which allows CORALv1 to seamlessly converge both diffusive or specular waveform shapes in one step (Dinardo et al., 2020). This thus yields a two-step retracking strategy.

Although the focus of this retracking scheme is the coastal zone, further studies will assess its ability to increase the amount of correct SWH retrievals in other challenging areas such as the Marginal Ice Zone. When illuminated by a nadir radar signal, the latter typically produces waveform shapes that are peaky or affected by interference. However, the application of CORALv1 would first need to exploit a waveform classification method to distinguish open water from sea ice.

We applied CORALv1 to multilooked synthetic aperture radar (SAR) waveforms of the S3A mission. Moreover, the algorithm could also be applied to other SAR altimeter missions such as CS2 or the recently launched Sentinel-6 Michael Freilich (S6-MF). Another future application is the application of CORALv1 on fully-focused synthetic aperture

radar (FF-SAR) L1B waveforms. S6-MF is equipped with the novel Poseidon-4 (P4) altimeter instrument that performs a nearly continuous transmission of Ku-band pulses, thus allowing full use of the FF-SAR technology. FF-SAR has a high potential to allow estimates in coastal scenarios due to its intrinsically high spatial resolution and to get even closer to the coastline. However, it is likely that coastal FF-SAR waveforms, given the across-track pulse-limited footprint size, will also be affected by strong coastal interference and CORALv1 with AIM aims to provide a useful scheme for improving retracking in the coastal zone.

**Credit author statement**

The contributions of this reported work can be listed as follows: conceptualisation, F.Sc., M.P.; methodology, F.Sc., M.P.; software, F.Sc.; formal analysis, F.Sc., M.P.; investigation, F.Sc.; resources, F.Sc., J.B.; writing—original draft preparation, F.Sc.; writing—review and editing, F.Sc., M.P., D.D., F.S.; visualisation, F.Sc.; supervision, M.P.; project administration, F.S., ESA SeaState\_cci; funding acquisition, F.S., ESA SeaState\_cci.

**Declaration of Competing Interest**

The authors declare that they have no known competing financial interests or personal relationships that could have appeared to influence the work reported in this paper.

## Acknowledgement

The authors gratefully acknowledge the ESA Grid Processing on Demand (ESA-GPOD) team for processing the SAM+-GPOD dataset, Salvatore Dinardo for his support in implementing the SAM+ retracking algorithm, Guillaume Dodet and Jean-François Piollé together with the ESA SeaState\_cci team for preparing the processing and validation data, and Collecte Localisation Satellites (CLS) for providing the LR-RMC dataset. Thank you very much to the three anonymous reviewers who helped improve this article. We are also very thankful for the computational and data resources provided by the Leibniz Supercomputing

Centre ([www.lrz.de](http://www.lrz.de)). We further would like to acknowledge the contributions of Python (Van Rossum and Drake, 2009) and the following Python packages that we used: NumPy (Harris et al., 2020), SciPy (Virtanen et al., 2020), pandas (McKinney, 2010), Matplotlib (Hunter, 2007), and Cython (Behnel et al., 2011).

## Funding

This research has been funded by the European Space Agency as part of the Sea State Climate Change Initiative (SeaState\_cci) project (ESA ESRIN/Contract No. 4000123651/18/I-NB).

## Appendix A. External L2 datasets

### A.1. SAM-EUM

The SAMOSA-based retracker from EUMETSAT (SAM-EUM) is the implementation of the standard retracking algorithm used in the ground segment of the Sentinel-3 (S3) processing chain and is part of the official baseline Level-2 (L2) product of EUMETSAT Copernicus Online Data Access. As the L2 product from European Organisation for the Exploitation of Meteorological Satellites has only includes the records over ocean, whereas the processed Level-1B with stack data (L1BS) product also contains records over land, the baseline L2 datasets need to undergo a conversion procedure. This involves the assembly of multiple L2 files according to their time dimension to retain the original L1BS data alignment, which allows for a comparison of the original L2 products with the retracked L1BS data. This work uses the latest L2 dataset with baseline collection (BC) 004 from EUMETSAT. The dataset was processed with SRAL L1 IPF (SR-1) version 06.18, which is part of the S3 Processing Baseline (PB) 2.68-MARINE (EUMETSAT, 2020). BC 004 is the first S3 reprocessing campaign that has reprocessed the data from the beginning of the Sentinel-3A/3B missions, allowing the comparison of a consistently processed, long-term dataset (acquired from Copernicus Online Data Access for reprocessed data, accessible under <https://codarep.eumetsat.int/>). Two different versions of the SAM-EUM L2 dataset are used in this work as a reference for validation: SAM-EUM and SAMOSA-based retracker from EUMETSAT with *mqe-quality-flag* (SAM-EUM-MQE). Both versions are essentially the same dataset, but have with a different quality flag for the significant wave height (SWH) records. The quality flag indicates which of the SWH measurements are to be considered good (0) or bad (1). SAM-EUM uses the original *swh\_ocean\_qual\_20\_ku* variable, which is defined as the 20-Hz measurements used to compute the 1-Hz average (the low-resolution data product also being part of the product). The flag is estimated using a three-sigma criterion. Each 20-Hz record that deviates from the mean of the valid 20-Hz measurements by at least 3 times the STD is flagged as bad. This is repeated until no more values are discarded from the twenty 20-Hz measurements (pers. comm. Bruno Lucas). The second version SAM-EUM-MQE uses a different quality flag that has been extended by the authors of this work and is based on the data variable *mqe\_ocean\_20\_ku*. The *mqe\_ocean\_20\_ku* variable represents the mean quadratic error for each SWH record between the fitted SAMOSA2 waveform model and the received multilooked waveform. As announced in the product notice for PB 2.68-MARINE (EUMETSAT (2020)), the calculus of the *mqe\_ocean\_20\_ku* variable is erroneous and was wrongly squared. After reversing the squaring, we still find that the misfit value is not as to be expected, when comparing it with our own fitting. After empirical estimations, *misfit\_eum* is in a reasonable, expected range, if computed as

$$\text{misfit\_eum} = \sqrt{100 * \sqrt{\text{mqe}}} \quad (\text{A.1})$$

The quality flag  $q$  is thus computed as  $q = \text{misfit\_eum} > 4$ , which yields a boolean array with good (0) and bad (1) values.

SAM-EUM uses the fully analytical, open ocean SAMOSA2 waveform model (Ray et al., 2015) that is expressed in terms of Scaled Spherical Modified Bessel functions and includes the zero- and first-order terms, as described in Dinardo et al. (2018). The bounded Levenberg-Marquardt Least-Squares Estimation Method (Lourakis, 2004) algorithm is used (as an implementation for the Levenberg-Marquardt non-linear least squares optimisation algorithm) to perform a non-linear fitting of the received waveform and the idealised SAMOSA2 model, and, to extract the three fitting variables SWH, epoch, and amplitude  $P_r$ . For a more detailed description of the SAMOSA2 model, please refer to the description of Coastal Retracker for SAR Altimetry version 1.0 (CORALv1) in Section 3.1, which is also based on this model.

### A.2. LR-RMC

The Low Resolution with Range Migration Correction (LR-RMC) algorithm was part of the Round Robin assessment that was performed within the framework of the European Space Agency (ESA) SeaState\_cci project and was chosen to be the most suitable candidate among the evaluated synthetic aperture radar (SAR) retracking algorithms (Schlembach et al., 2020). The L2 dataset is taken from this assessment. The ranking of the retracking algorithms was based on quantitative criteria, whose main focus is the accuracy and precision of the estimations of SWH in global and coastal areas with the emphasis on high and very high sea states. Although LR-RMC is an open ocean retracker, and the comparison with a coastal-dedicated might not be fair when assessing statistical metrics in the coastal zone, it was considered worthy of inclusion it as it serves as a valuable external source to validate the performance. In this work, we use the same LR-RMC dataset that was used for the assessment in Schlembach et al. (2020). The LR-RMC dataset used the same Level-1A (L1A) input data for processing, on which the EUMETSAT Level-1B (L1B)/L2 datasets and thus the CORALv1 L2 dataset is also based.

LR-RMC uses a dedicated L1A-to-L1BS processing scheme in which the four bursts (each with 64 pulses) of a radar cycle are incoherently combined to form a multibeam echo. This enlarges the effective size of the footprint and allows the effect of surface waves and small-scale noise to be averaged out. The impact of swell waves is thus completely removed. (Moreau et al., 2021) L2 processing follows a numerical approach that uses pre-simulated power echo models. These were derived from altimeter characterisation data such as the real antenna pattern and the real range impulse response, which were measured pre-launch. This also takes into account instrumental ageing effects. Fitting of the real waveform to the modelled waveform is done using a WLS estimator that is derived from a Maximum Likelihood Estimation. (ESA, 2019).

### A.3. SAM+-GPOD

SAM+ (SAM+) is a coastal SAR retracking algorithm that was developed by Dinardo et al. (2018) and Dinardo et al. (2020). It is based on the standard SAMOSA-based retracker documented in the SAMOSA detailed processing model (SAMOSA Detailed Processing Model, 2017, pers. comm. Jérôme Benveniste) and extends it by several features that improve the performance in the coastal zone, whereas falls back to the standard SAMOSA-based retracker in the open ocean. Compared to SAM-EUM, it uses a modified L1A-to-L1B processing, in which a zero padding factor of two (corresponding to an oversampling) and a doubling of the receiving window are applied, resulting in a waveform length of 512 range gates (expressed as  $K$  in the following). Additionally, a Hamming window is applied in the along-track direction on burst data, prior to the along-track FFT operation, in the area of the coastal zone (with (dist-to-coast) < 10 km) to reduce the impact of side lobe effects (Dinardo, 2020).

The SAMOSA+ processed by GPOD (SAM+-GPOD) dataset was processed with the “coastal zone” profile preset from the S3 SARvatore service (version 1.41, L1B processor version 1.37, L1B processor version 1.39) of the ESA Grid Processing on Demand platform (ESA-GPOD). The same L1A dataset as described in Section 2.1 was used.

## References

- Abdalla, S., Dinardo, S., Benveniste, J., Janssen, P.A., 2018. Assessment of CryoSat-2 SAR mode wind and wave data. *Adv. Space Res.* 62, 1421–1433. <https://doi.org/10.1016/j.asr.2018.01.044>.
- Alvera-Azcárate, A., Sirjacobs, D., Barth, A., Beckers, J.M., 2012. Outlier detection in satellite data using spatial coherence. *Remote Sens. Environ.* 119, 84–91. <https://doi.org/10.1016/j.rse.2011.12.009>.
- Ardhuin, F., Rogers, E., Babanin, A.V., Filipot, J.F., Magne, R., Roland, A., van der Westhuysen, A., Queffelec, P., Lefevre, J.M., Aouf, L., Collard, F., 2010. Semiempirical Dissipation Source Functions for Ocean Waves. Part I: Definition, Calibration, and Validation. *J. Phys. Oceanogr.* 40, 1917–1941. <https://doi.org/10.1175/2010JPO4324.1>.
- Ardhuin, F., Stopa, J.E., Chapron, B., Collard, F., Husson, R., Jensen, R.E., Johannessen, J., Mouche, A., Passaro, M., Quartly, G.D., Swail, V., Young, I., 2019. Observing Sea States. *Front. Mar. Sci.* 6 <https://doi.org/10.3389/fmars.2019.00124>.
- Behnel, S., Bradshaw, R., Citro, C., Dalcin, L., Seljebotn, D.S., Smith, K., 2011. Cython: The Best of Both Worlds. *Comput. Sci. Eng.* 13, 31–39. <https://doi.org/10.1109/MCSE.2010.118>.
- Bóas, A.B.V., Cornuelle, B.D., Mazloff, M.R., Gille, S.T., Ardhuin, F., 2020. Wave-current interactions at meso- and submesoscales: insights from idealized numerical simulations. *J. Phys. Oceanogr.* 50, 3483–3500. <https://doi.org/10.1175/JPO-D-20-0151.1>.
- Branch, M.A., Coleman, T.F., Li, Y., 1999. A Subspace, Interior, and Conjugate Gradient Method for Large-Scale Bound-Constrained Minimization Problems. *SIAM J. Sci. Comput.* 21, 1–23. <https://doi.org/10.1137/S1064827595289108>.
- Brown, G., 1977. The average impulse response of a rough surface and its applications. *IEEE J. Ocean. Eng.* 2, 67–74. <https://doi.org/10.1109/JOE.1977.1145328>.
- Diedenhofen, B., Musch, J., 2015. Cocor: A Comprehensive Solution for the Statistical Comparison of Correlations. *PLoS One* 10, e0121945. <https://doi.org/10.1371/journal.pone.0121945>.
- Dinardo, S., 2020. Techniques and Applications for Satellite SAR Altimetry over Water, Land and Ice. Ph.D. thesis. Technische Universität, Darmstadt.
- Dinardo, S., Fenoglio-Marc, L., Buchhaupt, C., Becker, M., Scharroo, R., Joana Fernandes, M., Benveniste, J., 2018. Coastal SAR and PLRM altimetry in German Bight and West Baltic Sea. *Adv. Space Res.* 62, 1371–1404. <https://doi.org/10.1016/j.asr.2017.12.018>.
- Dinardo, S., Fenoglio-Marc, L., Becker, M., Scharroo, R., Fernandes, M.J., Staneva, J., Grayek, S., Benveniste, J., 2020. A RIP-based SAR retracker and its application in North East Atlantic with Sentinel-3. *Adv. Space Res.* <https://doi.org/10.1016/j.asr.2020.06.004>.
- Dotet, G., Melet, A., Ardhuin, F., Bertin, X., Idier, D., Almar, R., 2019. The Contribution of Wind-Generated Waves to Coastal Sea-Level Changes. *Surv. Geophys.* 40, 1563–1601. <https://doi.org/10.1007/s10712-019-09557-5>.
- Dotet, G., Piolle, J.F., Quilfen, Y., Abdalla, S., Accensi, M., Ardhuin, F., Ash, E., Bidlot, J. R., Gommenginger, C., Marechal, G., Passaro, M., Quartly, G., Stopa, J., Timmermans, B., Young, I., Cipollini, P., Donlon, C., 2020. The Sea State CCI dataset v1: towards a sea state climate data record based on satellite observations. *Earth Syst. Sci. Data* 12, 1929–1951. <https://doi.org/10.5194/essd-12-1929-2020>.
- ECMWF, 2020a. CY46R1 wave hindcast based on ERA5 forcing 2010–2018. <https://doi.org/10.21957/x26j-bk23>.
- ECMWF, 2020b. Official IFS Documentation CY47R1. In chap. PART VII: ECMWF wave model. <https://doi.org/10.21957/31drbyag>.
- ESA, 2019. Sea State CCI: Algorithm Theoretical Basis Document v1.1. [http://cci.esa.int/sites/default/files/Sea\\_State\\_cci\\_ATBD\\_v1.1-signed\\_0.pdf](http://cci.esa.int/sites/default/files/Sea_State_cci_ATBD_v1.1-signed_0.pdf).
- ESA-GPOD. GPOD - grid processing on demand. <https://gpod.eo.esa.int/>.
- EUMETSAT, 2020. Copernicus Sentinel-3 Product Notice –STM L2 Marine.
- Fenoglio-Marc, L., Dinardo, S., Scharroo, R., Roland, A., Doutour Sikiric, M., Lucas, B., Becker, M., Benveniste, J., Weiss, R., 2015. The German Bight: a validation of CryoSat-2 altimeter data in SAR mode. *Adv. Space Res.* 55, 2641–2656. <https://doi.org/10.1016/j.asr.2015.02.014>.
- Fisher, R., 1925. *Statistical Methods for Research Workers*, 11th Ed. Rev. Statistical Methods for Research Workers, 11th Ed. Rev. Edinburgh, Oliver and Boyd.
- Gómez-Enri, J., Vignudelli, S., Quartly, G.D., Gommenginger, C.P., Cipollini, P., Challenor, P.G., Benveniste, J., 2010. Modeling Envisat RA-2 waveforms in the coastal zone: case study of calm water contamination. *IEEE Geosci. Remote Sens. Lett.* 7, 474–478. <https://doi.org/10.1109/LGRS.2009.2039193>.
- Gommenginger, C., Martin-Puig, C., Srokosz, M., Caparrini, M., Dinardo, S., Lucas, B., Restano, M., Ambrózio, A., Benveniste, J., 2017. Detailed Processing Model of the Sentinel-3 SRAL SAR altimeter ocean waveform retracker, Version 2.5.2, 31 October 2017, Under ESA-ESRIN Contract No. 20698/07/1-LG (SAMOSA), Restricted access as defined in the Contract, pers. comm. Jérôme Benveniste (Jerome.Benveniste@esa.int).
- Harris, C.R., Millman, K.J., van der Walt, S.J., Gommers, R., Virtanen, P., Cournapeau, D., Wieser, E., Taylor, J., Berg, S., Smith, N.J., Kern, R., Picus, M., Hoyer, S., van Kerkwijk, M.H., Brett, M., Haldane, A., Fernández del Río, J., Wiebe, M., Peterson, P., Gérard-Marchant, P., Sheppard, K., Reddy, T., Weckesser, W., Abbasi, H., Gohlke, C., Oliphant, T.E., 2020. Array programming with NumPy. *Nature* 585, 357–362. <https://doi.org/10.1038/s41586-020-2649-2>.
- Hayne, G., 1980. Radar altimeter mean return waveforms from near-normal incidence ocean surface scattering. *IEEE Trans. Antennas Propag.* 28, 687–692. <https://doi.org/10.1109/TAP.1980.1142398>.
- Hersbach, H., Bell, B., Berrisford, P., Hirahara, S., Horányi, A., Muñoz-Sabater, J., Nicolas, J., Peubey, C., Radu, R., Schepers, D., Simmons, A., Soci, C., Abdalla, S., Abellan, X., Balsamo, G., Bechtold, P., Biavati, G., Bidlot, J., Bonavita, M., Chiara, G. D., Dahlgren, P., Dee, D., Diamantakis, M., Dragani, R., Flemming, J., Forbes, R., Fuentes, M., Geer, A., Haimberger, L., Healy, S., Hogan, R.J., Hólm, E., Janisková, M., Keeley, S., Laloyaux, P., Lopez, P., Lupu, C., Radnoti, G., de Rosnay, P., Rozum, I., Vamborg, F., Villaume, S., Thépaut, J.N., 2020. The ERA5 global reanalysis. *Q. J. R. Meteorol. Soc.* 146, 1999–2049. <https://doi.org/10.1002/qj.3803>.
- Holthuis, L.H., 2007. Waves in Oceanic and Coastal Waters. Cambridge University Press, Cambridge. <https://doi.org/10.1017/CBO9780511618536>.
- Hunter, J.D., 2007. Matplotlib: a 2D graphics environment. *Comput. Sci. Eng.* 9, 90–95. <https://doi.org/10.1109/MCSE.2007.55>.
- Lourakis, M., 2004. Levenberg-Marquardt nonlinear least squares algorithms in C/C++.
- McKinney, W., 2010. Data structures for statistical computing in python. Proceedings of the 9th Python in Science Conference, 56–61. doi:10.25080/Majora-92bf1922-00a.
- Melet, A., Meyssignac, B., Almar, R., Le Cozannet, G., 2018. Under-estimated wave contribution to coastal sea-level rise. *Nat. Clim. Chang.* 8, 234–239. <https://doi.org/10.1038/s41558-018-0088-y>.
- Monaldo, F., 1988. Expected differences between buoy and radar altimeter estimates of wind speed and significant wave height and their implications on buoy-altimeter comparisons. *J. Geophys. Res.* 93, 2285–2302. <https://doi.org/10.1029/JC093iC03p02285>.
- Moreau, T., Cadier, E., Boy, F., Aublanc, J., Rieu, P., Raynal, M., Labroue, S., Thibaut, P., Dibarboure, G., Picot, N., Phalippou, L., Demeestere, F., Borde, F., Mavrocordatos, C., 2021. High-performance altimeter Doppler processing for measuring sea level height under varying sea state conditions. *Adv. Space Res.* <https://doi.org/10.1016/j.asr.2020.12.038>.
- PacIOOS. Distance to Nearest Coastline: 0.01-Degree Grid: Ocean. [http://www.pacioos.hawaii.edu/metadata/dist2coast\\_1deg\\_ocean.html](http://www.pacioos.hawaii.edu/metadata/dist2coast_1deg_ocean.html).
- Passaro, M., Fenoglio-Marc, L., Cipollini, P., 2015. Validation of Significant Wave Height From Improved Satellite Altimetry in the German Bight. *IEEE Trans. Geosci. Remote Sens.* 53, 2146–2156. <https://doi.org/10.1109/TGRS.2014.2356331>.
- Passaro, M., Nadzir, Z.A., Quartly, G.D., 2018. Improving the precision of sea level data from satellite altimetry with high-frequency and regional sea state bias corrections. *Remote Sens. Environ.* 218, 245–254. <https://doi.org/10.1016/j.rse.2018.09.007>.
- Passaro, M., Hemer, M.A., Quartly, G.D., Schwatke, C., Dettmering, D., Seitz, F., 2021. Global coastal attenuation of wind-waves observed with radar altimetry. *Nat. Commun.* 12, 3812. <https://doi.org/10.1038/s41467-021-23982-4>.
- Peng, F., Deng, X., 2018. A New Retracking Technique for Brown Peaky Altimetric Waveforms. *Mar. Geod.* 41, 99–125. <https://doi.org/10.1080/01490419.2017.1381656>.
- Quartly, G.D., Srokosz, M.A., McMillan, A.C., 2001. Analyzing Altimeter Artifacts: Statistical Properties of Ocean Waveforms. *J. Atmos. Ocean. Technol.* 18, 2074–2091. [https://doi.org/10.1175/1520-0426\(2001\)018<2074:AAASPO>2.0.CO;2](https://doi.org/10.1175/1520-0426(2001)018<2074:AAASPO>2.0.CO;2).
- Quartly, G.D., Smith, W.H.F., Passaro, M., 2019. Removing Intra-1-Hz Covariant Error to Improve Altimetric Profiles of  $\{\sigma_0\}$  and Sea Surface Height. *IEEE Trans. Geosci. Remote Sens.* 57, 3741–3752. <https://doi.org/10.1109/TGRS.2018.2886998>.



- Quilfen, Y., Chapron, B., 2019. Ocean surface wave-current signatures from satellite altimeter measurements. *Geophys. Res. Lett.* 46, 253–261. <https://doi.org/10.1029/2018GL081029>.
- Quilfen, Y., Chapron, B., 2020. On denoising satellite altimeter measurements for high-resolution geophysical signal analysis. *Adv. Space Res.* <https://doi.org/10.1016/j.asr.2020.01.005>.
- Raney, R., 1998. The delay/Doppler radar altimeter. *IEEE Trans. Geosci. Remote Sens.* 36, 1578–1588. <https://doi.org/10.1109/36.718861>.
- Ray, C., Martin-Puig, C., Clarizia, M.P., Ruffini, G., Dinardo, S., Gommenginger, C., Benveniste, J., 2015. SAR altimeter backscattered waveform model. *IEEE Trans. Geosci. Remote Sens.* 53, 911–919. <https://doi.org/10.1109/TGRS.2014.2330423>.
- Schlembach, F., Passaro, M., Quartly, G.D., Kurekin, A., Nencioli, F., Dodet, G., Piollé, J. F., Ardhuin, F., Bidlot, J., Schwatke, C., Seitz, F., Cipollini, P., Donlon, C., 2020. Round robin assessment of radar altimeter low resolution mode and delay-doppler retracking algorithms for significant wave height. *Remote Sens.* 12, 1254. <https://doi.org/10.3390/rs12081254>.
- Smith, W.H., Scharroo, R., 2015. Waveform aliasing in satellite radar altimetry. *IEEE Trans. Geosci. Remote Sens.* 53, 1671–1682. <https://doi.org/10.1109/TGRS.2014.2331193>.
- Timmermans, B., Shaw, A.G.P., Gommenginger, C., 2020. Reliability of Extreme Significant Wave Height Estimation from Satellite Altimetry and In Situ Measurements in the Coastal Zone. *J. Marine Sci. Eng.* 8, 1039. <https://doi.org/10.3390/jmse8121039>.
- Van Rossum, G., Drake, F.L., 2009. Python 3 Reference Manual. CreateSpace, Scotts Valley, CA.
- Virtanen, P., Gommers, R., Oliphant, T.E., Haberland, M., Reddy, T., Cournapeau, D., Burovski, E., Peterson, P., Weckesser, W., Bright, J., van der Walt, S. J., Brett, M., Wilson, J., Millman, K.J., Mayorov, N., Nelson, A.R.J., Jones, E., Kern, R., Larson, E., Carey, C.J., Polat, I., Feng, Y., Moore, E.W., VanderPlas, J., Laxalde, D., Perktold, J., Cimrman, R., Henriksen, I., Quintero, E.A., Harris, C.R., Archibald, A.M., Ribeiro, A.H., Pedregosa, F., van Mulbregt, P., SciPy 1.0 Contributors, 2020. SciPy 1.0: Fundamental algorithms for scientific computing in python. *Nat. Methods* 17, 261–272. <https://doi.org/10.1038/s41592-019-0686-2>.
- Virtanen, Pauli, et al., Ralf Gommers, Travis E. Oliphant, Matt Haberland, Tyler Reddy, David Cournapeau, Evgeni Burovski, 2020. SciPy 1.0: Fundamental Algorithms for Scientific Computing in Python. *Nature Methods* 17, 261–272. <https://doi.org/10.1038/s41592-019-0686-2>.
- Wang, X., Ichikawa, K., 2017. Coastal waveform retracking for Jason-2 altimeter data based on along-track Echograms around the Tsushima Islands in Japan. *Remote Sens.* 9 <https://doi.org/10.3390/rs9070762>.
- Zaron, E.D., deCarvalho, R., 2016. Identification and Reduction of Retracker-Related Noise in Altimeter-Derived Sea Surface Height Measurements. *J. Atmos. Ocean. Technol.* 33, 201–210. <https://doi.org/10.1175/JTECH-D-15-0164.1>.
- Zou, G.Y., 2007. Toward using confidence intervals to compare correlations. *Psychol. Methods* 12, 399–413. <https://doi.org/10.1037/1082-989X.12.4.399>.
- CLS: Collecte Localisation Satellites  
CORALv1: COastal Retracker for SAR ALtimetry version 1.0  
CS2: CryoSat-2  
DDA: Delay-Doppler altimetry  
DFGE: Dynamic First-Guess Epoch  
dist-to-coast: distance-to-coast  
ECMWF: European Centre for Medium-Range Weather Forecasts  
ERA5-h: ERA5-based hindcast  
ESA: European Space Agency  
EUMETSAT: European Organisation for the Exploitation of Meteorological Satellites  
FF-SAR: fully-focused synthetic aperture radar  
FG: first-guess  
GPOD: Grid Processing on Demand  
GTS: Global Telecommunication System  
IR: interference reference  
J2: Jason-2  
L1A: Level-1A  
L1B: Level-1B  
L1BS:: Level-1B with stack data  
L2: Level-2  
LE: leading edge  
LR-RMC: Low Resolution with Range Migration Correction  
LRM: low resolution mode  
LUT: look-up table  
MAD: median absolute deviation  
MSS: mean square slope  
NaN: not-a-number  
P4: Poseidon-4  
PB: Processing Baseline  
PCHC: percentage of cycles for high correlation  
PP: pulse peakiness  
PRF: pulse repetition frequency  
PSD: power spectral density  
PTR:: point target response  
RMSE: root mean squared error  
S3: Sentinel-3  
S3A: Sentinel-3A  
S6-MF: Sentinel-6 Michael Freilich  
SAM+: SAMOSA+  
SAM+-GPOD: SAMOSA+ processed by GPOD  
SAM-EUM: SAMOSA-based retracker from EUMETSAT  
SAM-EUM-MQE: SAMOSA-based retracker from EUMETSAT with mqe-quality-flag  
SAMOSA: SAR Altimetry MOde Studies and Applications  
SAR: synthetic aperture radar  
SARM: synthetic aperture radar mode  
SDD: standard deviation of differences  
SeaState\_cci: Sea State Climate Change Initiative  
SL-SAM: single-look SAMOSA2 model  
SNR: signal-to-noise ratio  
SWH: significant wave height  
TRR: Trust Region Reflective  
WS: wind speed

## Acronyms

AIM:: Adaptive Interference Masking  
ALES:: Adaptive Leading Edge Subwaveform  
APD:: Adaptive Peak Detection  
BC: baseline collection  
BH: Brown-Hayne

### A.3 P-III: Benefits of Fully Focused SAR Altimetry to Coastal Wave Height Estimates: A Case Study in the North Sea

Schlembach, F.; Ehlers, F.; Kleinherenbrink, M.; Passaro, M.; Dettmering, D.; Seitz, F.; Slobbe, D.C. **Benefits of fully focused SAR altimetry to coastal wave height estimates: A case study in the North Sea** *Remote Sensing of Environment* 289 (2023) 113517.

**Journal:** *Remote Sensing of Environment*, volume 289, article 113517

**Date of publication:** 1st of May 2023

**DOI:** 10.1016/j.rse.2023.113517

**Web link:** <https://doi.org/10.1016/j.rse.2023.113517>

#### Copyright

This work was published in the *Remote Sensing of Environment* journal under the subscription-based publishing model.

#### Contribution

The contributions to this reported work can be listed as follows: conceptualisation, F.Sc.; methodology, F.Sc.; software, F.Sc., F.E., M.K., C.S.; formal analysis, F.Sc., F.E.; investigation, F.Sc.; resources, F.Sc., F.E., M.K., C.S.; writing–original draft preparation, F.Sc.; writing–review and editing, F.Sc., F.E., M.K., M.P., D.D., F.S., C.S.; visualisation, F.Sc.; supervision, M.P., M.K., C.S.; project administration, M.P., F.S., ESA SeaState\_cci; funding acquisition, M.P., F.S., ESA SeaState\_cci. All authors read, reviewed, and accepted the final manuscript.

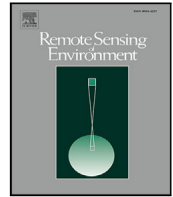
Criteria	Own contribution
Idea and conceptual design	85%
Implementation and realisation	70%
Analysis and discussion	75%
Figure compilation	100%
Manuscript structure and writing	80%
<b>Overall contribution</b>	<b>82%</b>

Own contribution to publication P-III



Contents lists available at ScienceDirect

## Remote Sensing of Environment

journal homepage: [www.elsevier.com/locate/rse](http://www.elsevier.com/locate/rse)

## Benefits of fully focused SAR altimetry to coastal wave height estimates: A case study in the North Sea

Florian Schlembach<sup>a,\*</sup>, Frithjof Ehlers<sup>b</sup>, Marcel Kleinherenbrink<sup>b</sup>, Marcello Passaro<sup>a</sup>, Denise Dettmering<sup>a</sup>, Florian Seitz<sup>a</sup>, Cornelis Slobbe<sup>b</sup><sup>a</sup> Deutsches Geodätisches Forschungsinstitut, Technical University of Munich (DGFI-TUM), Arcisstraße 21, Munich, 80333, Germany<sup>b</sup> Geoscience and Remote Sensing, Delft University of Technology, Stevinweg 1, Delft, 2628 CN, The Netherlands

## ARTICLE INFO

Edited by Menghua Wang

## Keywords:

Satellite altimetry  
SAR altimetry  
FF-SAR  
Fully focused SAR  
UF-SAR  
Unfocused SAR  
Sentinel-6 Michael Freilich  
Significant wave height  
Retracking  
Coastal retracking  
Coastal zone  
Algorithm  
SAMOSA  
CORAL  
Case study  
North sea  
SWH decay  
Coastal SWH variation

## ABSTRACT

Estimating the three geophysical variables significant wave height (SWH), sea surface height, and wind speed from satellite altimetry continues to be challenging in the coastal zone because the received radar echoes exhibit significant interference from strongly reflective targets such as sandbanks, sheltered bays, ships etc. Fully focused SAR (FF-SAR) processing exhibits a theoretical along-track resolution of up to less than half a metre. This suggests that the application of FF-SAR altimetry might give potential gains over unfocused SAR (UF-SAR) altimetry to resolve and mitigate small-scale interferers in the along-track direction to improve the accuracy and precision of the geophysical estimates.

The objective of this study is to assess the applicability of FF-SAR-processed Sentinel-6 Michael Freilich (S6-MF) coastal altimetry data to obtain SWH estimates as close as possible to the coast.

We have developed a multi-mission FF-SAR processor and applied the coastal retracking algorithm CORALv2 to estimate SWH. We assess different FF-SAR and UF-SAR processing configurations, as well as the baseline Level-2 product from EUMETSAT, by comparison with the coastal, high-resolution SWAN-Kuststrook wave model from the Deltares RWsOS North Sea operational forecasting system. This includes the evaluation of the correlation, the median offset, and the percentage of cycles with high correlation as a function of distance to the nearest coastline. Moreover, we analyse the number of valid records and the L2 noise of the records. The case study comprises five coastal crossings of S6-MF that are located along the Dutch coast and the German coast along the East Frisian Islands in the North Sea.

We observe that accurate and precise SWH records can be estimated in the nearshore zone within 1–3 km from the coast using satellite SAR altimetry. We find that the FF-SAR-processed dataset with a Level-1b posting rate of 140 Hz shows the greatest similarity with the wave model. We achieve a correlation of ~0.8 at 80% of valid records and a gain in precision of up to 29% of FF-SAR vs UF-SAR for 1–3 km from the coast. FF-SAR shows, for all cycles, a high correlation of greater than or equal to 0.8 for 1–3 km from the coast. We estimate the decay of SWH from offshore at 30 km to up to 1 km from the coast to amount to  $26.4\% \pm 3.1\%$ .

## 1. Introduction

The knowledge of wave heights in the open ocean is relevant for ocean weather forecasting (Cavaleri et al., 2012), climate studies (Timmermans et al., 2020; Stopa et al., 2016), scientific studies such as for the air–sea interactions of surface-breaking waves (Melville, 1996), as well as for applications such as industrial shipping route planning. Furthermore, wave heights in the coastal zone are of particular interest as about 23%–37% of the world's population lives within 100 km of the shoreline (Glavovic et al., 2022). This is especially true for coastal risk assessment studies (Ferreira et al., 2009; Sajjad and Chan,

2019), coastal protection (Pilarczyk, 1990; Charlier et al., 2005), and coastal safety (Arens et al., 2013). Moreover, there are high demands to measure wave heights even closer to the coast, e.g. for studying nearshore effects such as wave energy transformation (Lippmann et al., 1996; Contardo et al., 2018), sediment transport (Elfrink and Baldock, 2002; Chowdhury and Behera, 2017; de Vries et al., 2020), dissipation effects (Wright, 1976; Wang and Kraus, 2005; Bryan and Power, 2020).

One way to measure wave heights globally is with satellite radar altimetry, which has been in use for over three decades to obtain

\* Corresponding author.

E-mail addresses: [florian.schlembach@tum.de](mailto:florian.schlembach@tum.de) (F. Schlembach), [f.ehlers@tudelft.nl](mailto:f.ehlers@tudelft.nl) (F. Ehlers), [m.kleinherenbrink@tudelft.nl](mailto:m.kleinherenbrink@tudelft.nl) (M. Kleinherenbrink), [marcello.passaro@tum.de](mailto:marcello.passaro@tum.de) (M. Passaro), [denise.dettmering@tum.de](mailto:denise.dettmering@tum.de) (D. Dettmering), [florian.seitz@tum.de](mailto:florian.seitz@tum.de) (F. Seitz), [d.c.slobbe@tudelft.nl](mailto:d.c.slobbe@tudelft.nl) (C. Slobbe).<https://doi.org/10.1016/j.rse.2023.113517>

Received 27 November 2022; Received in revised form 26 January 2023; Accepted 21 February 2023

Available online 6 March 2023

0034-4257/© 2023 Elsevier Inc. All rights reserved.

estimates of sea level and sea state. The measurement principle of satellite radar altimetry is based on measuring the echoes of a transmitted frequency-modulated pulse as a function of two-way travel time. From the shape of the returned/received and processed pulse echoes and their amplitudes, the three geophysical variables sea surface height (SSH), significant wave height (SWH), and wind speed can be derived in a process called retracking, in which a model is fit to the received pulse echoes. The SWH is defined as four times the standard deviation of the sea surface elevation (Holthuijsen, 2007). The most recent operational satellite altimetry processing is called unfocused synthetic aperture radar (UF-SAR)/Delay-Doppler (DD) processing (Raney, 1998), which is applied to the satellite altimetry missions CryoSat-2 (CS2), Sentinel-3 (S3), and Sentinel-6 Michael Freilich (S6-MF).

Measuring wave heights in the coastal zone using satellite altimetry is challenging due to complex processes occurring near the coast, which triggered the emergence of the relatively new research field of coastal altimetry (Vignudelli et al., 2011). Numerous works have addressed the challenges of coastal altimetry (Fenoglio-Marc et al., 2010; Vignudelli et al., 2011; Cipollini et al., 2009, 2012; Gomez-Enri et al., 2016). Timmermans et al. (2020) assessed extreme wave heights from satellite altimetry, which agree well with in-situ data for up to 5 km from the coast but lack proper spatio-temporal sampling for closer distances to the coast. Coastal SWH observations from satellite altimetry are often discarded or are of bad quality due to coastal interference that originates from strongly reflective targets such as sandbanks, sheltered bays, or calm waters close to the shoreline. Schlembach et al. (2022) showed that the correlation of SWH data of the operational baseline product of S3 with in-situ data from buoys amounts to less than 0.20 for closer than 20 km from the coast. Tailored retracking algorithms have been developed to account for the coastal interference, such as ALES (Passaro et al., 2015), Brown-Peaky (Peng and Deng, 2018) for the conventional low resolution mode (LRM) altimetry, and SAMOSA+ (Dinardo et al., 2018), SAMOSA++ (Dinardo et al., 2020), ALES + SAR (Passaro et al., 2021), RiwiSAR-SWH (Gou and Tourian, 2021), CORS (Garcia et al., 2022), or CORALv1 (Schlembach et al., 2022) for UF-SAR altimetry. The enhanced coastal processing algorithms allow the derivation of relevant wave-related statistics in the coastal zone, e.g. as done by Passaro et al. (2021). They investigated the global attenuation of SWH from offshore at 30 km to >3 km off the coast and found the wave heights are globally, on average, 22% smaller than offshore while using the conventional LRM altimetry with a lower posting rate of 1 Hz (and the ALES retracker (Passaro et al., 2015)). The estimation of SWH in the coastal zone with a distance-to-coast (dist-to-coast) of <5 km remains challenging, as the quality of the estimates deteriorates (Schlembach et al., 2022). Nevertheless, the need to approach the coastline even closer is specified by the current draft of the mission requirement documents of the Copernicus Sentinel-3 Next Generation Topography (S3NG-T) team, which has defined the requirement to give SSH and SWH estimates up to 3 km and, as an enhanced target, up to 0.5 km off the coastline (European Space Agency and Noordwijk, The Netherlands, 2022).

As an evolution of UF-SAR altimetry, fully focused synthetic aperture radar (FF-SAR) altimetry constitutes a novel processing technique initially applied to altimetry data by Egido and Smith (2017). It exploits the fully coherent processing of the received radar pulse echoes during the whole target illumination time, by which a theoretical along-track resolution of less than a meter can be achieved for coherent targets. With FF-SAR processing, we expect to acquire SWH estimates that are less affected by strongly reflective targets in the coastal zone due to its inherently high along-track resolution.

The S6-MF mission offers great potential to apply FF-SAR processing due to its open-burst, interleaved operation mode, i.e. the pulses are continuously transmitted and received in a manner that the reception of the pulses occurs in between the phases of transmission (Donlon et al., 2021). That is, only minor spurious grating lobes (or: target replicas) are expected in the along-track direction at multiples of ~300 m (Ehlers

et al., 2022), as compared to the CS2 or S3 missions that exhibit more frequent and stronger grating lobes at ~90 m (Egido and Smith, 2017; Guccione et al., 2018) due to the lacunar sampling/closed-burst operation mode.

This work is a case study to assess the capability of FF-SAR-processed S6-MF coastal altimetry data to obtain SWH estimates as close as possible to the coastline.

In order to achieve this, we formulate the following research objectives:

1. We aim to assess whether the SWH estimation from coastal altimetry data can be further improved by using FF-SAR instead of UF-SAR processing.
2. Furthermore, we want to evaluate whether the statistical improvements observed in the coastal SWH estimates are also beneficial in practice for determining key metrics that are relevant for fields such as coastal protection.

To address both, we aim to perform a(n)

- Comparison of the FF-SAR- and UF-SAR-processed altimetry data with a high-resolution wave model data as a function of dist-to-coast
- Evaluation of the number of valid records and the precision of the altimetry data as a function of dist-to-coast
- Identification and quantification of dissimilarities between the altimetry data and high-resolution wave model data
- Exploitation of nearshore SWH records by the estimation of the change in SWH from offshore towards to the coast

To the best knowledge of the authors, no previous study is known that has performed such an in-depth assessment of FF-SAR-processed wave data estimated by a satellite altimeter.

This paper is structured as follows: Section 2 describes the altimetry and wave model data used. Section 3 explains the processing chain of the altimetry data, the methods to compare the altimetry datasets with the wave model and the estimation of the number of valid records and precision of the altimetry estimates, as well as the metric of the coastal SWH variation. Section 4 presents and discusses the results of the study. Section 5 draws a conclusion and gives an outlook for future work.

## 2. Data

### 2.1. Altimetry

We use S6-MF Level-1a (L1a) and Level-2 (L2) data baseline version F06 in the Non Time Critical (NTC) timeliness. The data was downloaded using the PO.DAAC interface from the NASA Jet Propulsion Laboratory (NASA JPL, 2020). We process the L1a data to acquire two FF-SAR- and one UF-SAR-processed datasets. The processing chain and the settings of the datasets will be described in detail in Section 3.1. In addition, we take the Payload Data Acquisition and Processing High Resolution (PDAP-HR) dataset from the baseline L2 products, which corresponds to the baseline UF-SAR/HR processing chain as described in the S6-MF L2 product generation specification document (EUMETSAT, 2022b). The PDAP-HR dataset is retracked with the open ocean SAMOSA-based retracker (EUMETSAT, 2022b, Section 4.5.2), which is not optimised for the coastal zone. We, though, include it as a reference to highlight the improvements to the SWH estimates by our processing configurations. The provided `swh_ocean_qual` flag is used to exclude bad estimates. The residual estimates represent the number of valid records, which are part of our statistical analysis. For the discussion of the offset with respect to the wave model, we also include the Payload Data Acquisition and Processing Low Resolution (PDAP-LR) product from the baseline L2 product, which is processed according to the LR processing chain (EUMETSAT, 2022b, Section 4.5.1).

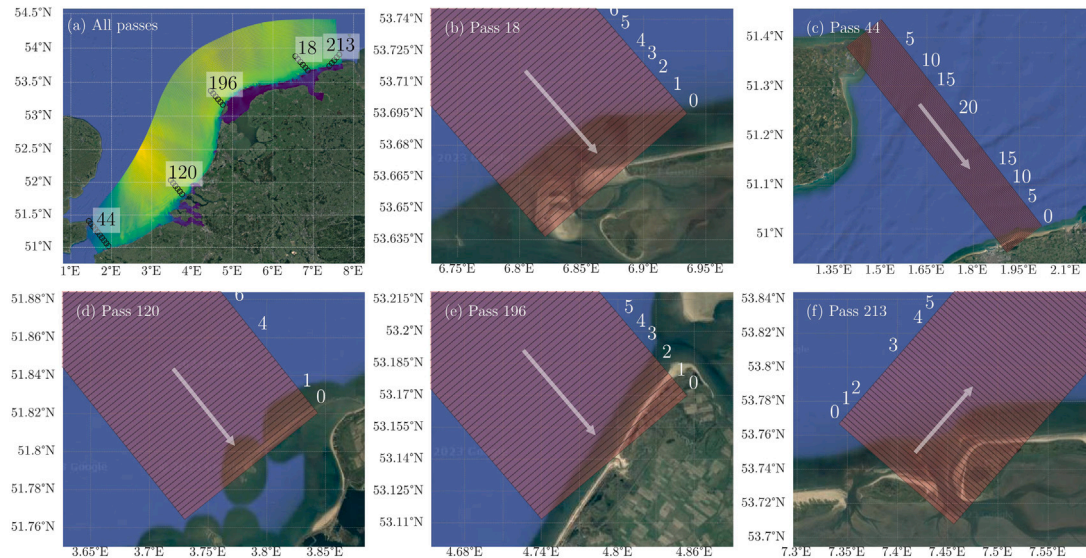


**Fig. 1.** The model domain of the SWAN-Kuststrook wave model with its curvilinear grid is shown in (a). Panels b, c, d, e and f display the S6-MF passes 44, 120, 196, 18, and 213, respectively. The white numbers next to each pass indicate the dist-to-coast values, and the white arrows show the flight direction of the satellite. The estimated effective footprints have a size of  $300 \times 10000$  m (along-track times across-track) and comprise the area on the ground that is estimated to have a major impact on the leading edge (LE) of the multilooked waveform, i.e. on the estimates of the geophysical variables.

We use all available S6-MF data of the year 2021 included in the wave model domain (see next section), which corresponds to cycles 5 to 42 and the five passes 18, 44, 120, 196, and 213. All passes apart from 213 are descending, and, in total, 161 overpasses are available. Measurements from up to 31 km from the coast are included. The rationale behind not encompassing a much larger area from the coast is to limit the computational effort that is inherently large to FF-SAR processing that uses the back-projection algorithm. The dist-to-coast range was thus chosen to be large enough to accommodate the computation of the coastal SWH variation with respect to the offshore SWH around 30 km. We define the outermost contact of the satellite's nadir locations with land as the coastline to avoid the tidal flats of the Wadden Sea. A map of the collocated data is shown in Fig. 1 (a). Fig. 1 (b–f) shows the zoomed-in views of the five individual coastal crossings.

Below is a description of the five S6-MF passes analysed in this study.

**Pass 18** goes over the western tip of the Wadden island Juist, Germany. The first two kilometres off the coast are covered by sandbanks, which deteriorates the accuracy and the validity of the records due to the strongly reflective characteristic of sandbanks.

**Pass 44** crosses over the English Channel, where the satellite passes the UK shoreline with a minimum distance of  $\sim 2$  km and goes south to the French north coast close to Calais and thus comprises two coastal areas. The pass is located on the southwestern edge of the wave model domain. The angle of approach to the coast in the south amounts to approximately  $60^\circ$  ( $90^\circ$  would mean a perpendicular crossing).

**Pass 120** is a coastal crossing located south of Rotterdam. The pass almost perpendicularly crosses a large sandbank called Aardappelenbult. The dist-to-coast is manually set to 0.0 km at the outer edge of the sandbank. This segment of the pass is quite a special coastal crossing, as no land intrusion is apparent for the very last radar footprints.

**Pass 196** is the coastal crossing of the Dutch Wadden island Texel. The angle of approach to the coastline is slightly tilted ( $\sim 108^\circ$ ) such that the footprints of the first 1–2 km off the coast are affected by land intrusion.

**Pass 213** crosses the East Frisian Wadden island Baltrum, Germany. Its effective radar footprints are affected by many strongly reflective targets such as sandbanks, inland waters, and land/human infrastructure.

## 2.2. SWAN-Kuststrook wave model

To assess the potential of FF-SAR-processed S6-MF coastal altimetry data in the SWH estimation, we compared it with model-derived data. We are aware that wave model data cannot be considered the truth. However, it represents a practical way to evaluate the variability of SWH on a fine scale, such as spatial variations towards the coast, whereas buoys, which are mostly not located at the coast, can only provide pointwise measurements with limited resolution in space and time. We use the SWAN-Kuststrook wave model, which is part of the Deltares RWsOS North Sea operational forecasting system. Simulating WAVes Nearshore (SWAN) is a third-generation wave model that simulates random, short-crested wind-waves in coastal regions (Booij et al., 1999) and is developed at the Delft University of Technology. It represents wave evolutions due to wind, white-capping, shoaling, bottom friction, current and depth-induced refraction, diffraction, depth-induced breaking and quadruplet/triad wave-wave-interactions (Day and Dietrich, 2022). The output of the SWAN-Kuststrook wave model is generated by the SWAN software version 41.20A.2, which includes a new set of wave physics (ST6) for the parametrisation of wind input and wind speed scaling, swell dissipation, white-capping, and others (Rogers et al., 2012). The model domain with a snapshot of SWH data is shown in Fig. 1 (a) and encompasses the Dutch North Sea, the Dutch Wadden Sea, the Eastern and Western Scheldt, and the German North Sea along the East Frisian Islands. It is a nested model; the boundary conditions are taken from the regional ECMWF-WAM model that has a  $0.1^\circ$  geographical resolution (Janssen, 2011). The water level and current fields come from runs of the hydrodynamic model WAQUA-ZUNO (Gautier and Caires, 2015) and the wind fields from the High Resolution Limited Area Model (HIRLAM) (Undén et al., 2002). The bathymetry data is computed from EMODnet (EMODnet Bathymetry Consortium, 2018) and Baseline-NL (National Georegister of the Netherlands, 2021) datasets for the deeper parts and near the coast, respectively. The model grid is curvilinear and comprises  $991 \times 310$  points. The grid spacing in the longitudinal and latitudinal directions ranges from 50–1400 m

**Table 1**

L2 datasets used in this study. FFSAR-60 and FFSAR-140 are averaged after the retracking to form L2 estimates at a posting rate of 20 Hz, as described in Section 3.1.2. The PDAP-HR and PDAP-LR datasets are taken from the EUMETSAT baseline L2 product.

Name	L1b: proc. type	L1b: posting rate [Hz]	L2: retracker
FFSAR-60	FF-SAR	60	CORALv2
FFSAR-140	FF-SAR	140	CORALv2
UFSAR-20	UF-SAR	20	CORALv2
PDAP-HR	UF-SAR	20	SAMOSA-based
PDAP-LR	LRM	20	MLE4

and 35–2600 m, respectively, with the closest grid points being located near the coast to resolve small-scale dynamics. An assessment of the performance of the SWAN-Kuststrook wave model was conducted with in-situ observations data from 50 different locations. The performance was compared to the previously operational SWAN-ZUNO model within a hindcast-based analysis of four extreme events, which yields a relative bias of  $-1\%$  (SWAN-ZUNO:  $-12\%$ ) and a scatter index of 23% (SWAN-ZUNO: 22%) for the SWH. The extreme event analysis also comprises phases with low sea states, from which we conclude that the model shows a comparably good performance also for these sea state regimes.

We compare the altimetry- and model-derived data at the locations from the EUMETSAT baseline L2 high-resolution product. The wave model data is mapped to the baseline L2 locations using a bilinear interpolation.

### 3. Methods

In this section, we first describe the processing methodology of the altimetry data starting from the L1a product and ending with the SWH estimates (L2 product). Secondly, we describe the statistical analysis to assess the performance of all L2 datasets. Thirdly, we explain the evaluation of the coastal SWH variation of the L2 datasets towards the coastline.

#### 3.1. Processing of altimetry data

Here, we describe the details of the Level-1b (L1b) processing, starting from the received pulses and ending in the multilooked power return echo waveforms, from which the three geophysical variables SWH, SSH, and wind speed are estimated in the L2 processing stage, as described in Section 3.1.2. Table 1 lists and summarises the key properties of all datasets used in this study.

##### 3.1.1. Level-1b processing

We process the received pulse echoes from the L1a products to acquire the return power waveforms at the L1b data level. This is established using a multi-mission FF-SAR processor implementation originally developed for CS2 by Kleinherenbrink et al. (2020), which applies a back-projection algorithm as presented in Egido and Smith (2017). The extension to the S3 and S6-MF missions is described in detail in Ehlers et al. (2022). The FF-SAR processing includes the range cell migration correction (RCMC), the residual video phase (RVP) correction, and the compensation for additional phase jumps and other mission-specific settings (Ehlers et al., 2022). Here, we describe only specific FF-SAR processing parameters that are used for this study and are summarised in Table 2.

The FF-SAR processor obtains a statistically independent, singlelook waveform every  $\sim 1$  m in the along-track direction while setting a coherent integration time  $T = 2.1$  s. The specific setting of  $T = 2.1$  s has been evaluated to be the most sensitive within the ESA L2 GPP project (European Space Agency and Noordwijk, The Netherlands, 2021). The singlelook waveforms are averaged in a process called multilooking, in which non-overlapping singlelook waveforms are averaged to form multilooked waveforms in distances that correspond to the

**Table 2**

L1b processing parameters used for the FFSAR-60, FFSAR-140, and UFSAR-20 datasets.

Parameter	Value
Illumination time $T$	2.1 s (FF-SAR)/2.4 s (UF-SAR)
Zero-padding-factor	2
Number of range gates $N_r$	512
L1b posting rate	FF-SAR: 60/140 Hz, UF-SAR: 20 Hz
Window applied	None

targeted 60 Hz and 140 Hz L1b posting rates. Both 60 and 140 Hz are odd-numbered multiples of 20 Hz (three and seven) so that the centre of the averaged 60 Hz and 140 Hz measurements can be georeferenced to the 20 Hz records of the baseline L2 product.

The UF-SAR-processed L1b products are a by-product of the same FF-SAR processor, which allows us to mimic the original DD/SAR processing chain Dinardo et al. (2018). The time for the coherent integration of the (range- and phase-corrected) pulses of each individual burst is reduced from the illumination time  $T$  to the burst duration, which is different from FF-SAR, where all pulses over  $T$  are coherently integrated. This reduces the theoretical along-track resolution from  $\sim 1$  m to  $\sim 300$  m, assuming a static scenario of scatterers within  $T$  (Egido and Smith, 2017). The chosen illumination time of  $T = 2.4$  s corresponds to the number of looks (or Doppler beams) of 322 to be in line with the baseline PDAP product (EUMETSAT, 2022a). The Doppler-beam stack is acquired by taking the absolute square of the integrated bursts, from which the UF-SAR-multilooked waveform (as part of the PDAP-HR L1b product) is obtained through summation over all bursts. We can thus collect (correlated) UF-SAR-multilooked waveforms every  $\sim 1$  m along with each of the FF-SAR-singlelooks (Egido et al., 2020). After picking the multilooked waveforms at locations that are nearest to the ones of the EUMETSAT baseline L2 product, we acquire the UFSAR-20 dataset, which closely matches the baseline PDAP-HR product (after the averaging as explained in the next paragraph), but excluding the spurious range-walk error, as investigated by Guccione (2008) and Scagliola et al. (2021). Some authors report an increased precision by averaging consecutive UF-SAR from 40 Hz or 60 Hz posting rates onto 20 Hz (Dinardo et al., 2015; Egido et al., 2020). However, we find that this step introduces a correlation between neighbouring 20 Hz records and is thus not considered as viable option; see Appendix A. Hence, an apparent gain in precision might, in part, be caused by the effective low-pass filtering of the geophysical estimates and a corresponding loss in resolution, which is not desired.

##### 3.1.2. Level-2 processing

The FF-SAR- and UF-SAR-processed L1b multilooked power waveforms are retracked with the COastal Retracker for SAR Altimetry version 2.0 (CORALv2) algorithm to extract the SWH data, as presented in its first version, v1, in Schlembach et al. (2022) (details on differences below). As commonly done for the retracking algorithms, CORALv2 performs a least-squares fitting of the theoretical waveform, the SAMOSA2 model, with the received, multilooked waveforms and extracts the ocean parameters SWH, SSH, and wind speed. The SAMOSA2 model is an analytical formulation of the power return echoes. It takes into account instrument-specific (e.g. pulse repetition frequency, carrier frequency, transmission and reception bandwidths) and orbital parameters such as the altitude, altitude rate, and velocity. In its analytical form, it makes several approximations, such as the Gaussian approximation of the point target response (PTR) (Ray et al., 2015). In order to account for these, a sea-state-dependent look-up table (LUT) is used for the  $\alpha_p$  value that is part of the analytical SAMOSA2 model. The approximations depend, amongst others, on the illumination time  $T$  and also the coherent integration time used in the L1b processing. Hence, we use the  $\alpha_p$  LUT from the PDAP baseline (EUMETSAT, 2022a) for the UF-SAR waveforms, whose illumination time is chosen to be 2.4 s (corresponding to 322 looks) and the coherent

integration time to be the burst repetition interval (BRI) (as for the PDAP-HR product). For FF-SAR, an  $\alpha_p$  LUT is generated considering an illumination time of  $T = 2.1$  s and assuming an unambiguous PTR, i.e. no grating lobes (or azimuth-ambiguities) of the PTR are taken into account (pers. comm. Salvatore Dinardo). This tailored  $\alpha_p$  LUT is then used to fit the SAMOSA zero-Doppler beam against the waveform, as initially presented in [Egido and Smith \(2017\)](#).

CORALv2 is based on SAMOSA+ ([Dinardo et al., 2018](#)) and adds further extensions to mitigate interference that arises from strongly reflective targets in the across-track direction, as is typical in the coastal zone. Furthermore, a better quality flag allows for an over 25% increase in valid estimates closer than 5 km from the coast compared to SAMOSA+ ([Schlembach et al., 2022](#)). CORALv2 has had the following modifications made to it with respect to its first published version, v1: The adaptive interference mitigation scheme is adjusted such that interference that arises in front of the leading edge (LE) is also sensed and masked out for the least-squares fitting process. Moreover, the spurious interference gates are excluded from the computation of the misfit between the fitted, idealised and received waveform, from which the quality flag is deduced. Another modification is the consideration of the range migration correction (RMC) mode that has been activated on-board from S6-MF cycle 33 to accommodate the data volume to be transferred to the ground, which truncates the first ten and roughly the second half of each multilooked waveform (thus reducing the data rate by a factor of two) ([Donlon et al., 2021](#)). In these cases, only the range gates ranging from 11 to 132 (0-based) are fitted against the SAMOSA2 model ([EUMETSAT, 2022b](#)).

We retrack the different datasets from [Table 1](#) (apart from PDAP-HR and PDAP-LR) with CORALv2. The FFSAR-60 and FFSAR-140 are retracked in their corresponding posting rates of 60 Hz and 140 Hz, respectively. For the sake of comparability of the different datasets and the concurrent exploitation of potential gains, we reduce the FFSAR-60 and FFSAR-140 datasets to 20 Hz by taking the mean of all estimates around the location of the centre estimate, which coincides with the baseline L2 location, as defined during the multilooking process described in [Section 3.1.1](#). In the reduction process, we discard the higher posting rate estimates of 60 Hz and 140 Hz that exhibit a bad quality flag to exploit the high FF-SAR resolution.

Despite the application of the adaptive mitigation scheme of the CORALv2 retracker that tackles the interference in the across-track/range direction at its best, outliers cannot be completely avoided, irrespective of the type of L1b processing. Hence, after retracking and reducing the data, we filter out outliers by applying the scaled median absolute deviation (MAD) factor criterion ([Alvera-Azcárate et al., 2012](#); [Schlembach et al., 2020](#); [Passaro et al., 2021](#)). An estimate is seen as an outlier if its value exceeds the range of  $\text{median}_{20} \pm 3 \cdot 1.4826 \cdot \text{MAD}$ , where  $\text{median}_{20}$  and MAD are calculated on the adjacent 20 records, and the factor 1.4826 converts the MAD to a standard deviation equivalent for normally distributed data. In total, 743/18489 (4.0%), 716/18489 (3.9%), and 638/18489 (3.5%) SWH estimates are removed from the FFSAR-60, FFSAR-140 and UFSAR-20 datasets, respectively. The slightly higher amount of detected outliers for FFSAR-140/60 vs UFSAR-20 is expected, as FF-SAR is capable of resolving strongly reflective targets at a much finer scale, leading to isolation and detection of more outliers. In contrast, UF-SAR smears the spurious signal over multiple SWH waveforms, impeding the detection. The obtained numbers are in line with the amount of the scaled MAD criterion-detected outliers found in the Round Robin retracker comparison in [Schlembach et al. \(2020\)](#) for the baseline SAMOSA-based retracker (3%–5%) in the coastal zone with a dist-to-coast of less than 20 km.

### 3.2. Statistical analysis

We divide the statistical analysis into two parts: First, we compare the L2 datasets with the SWAN-Kuststrook wave model and assess Pearson's correlation coefficient, the median offset, and the percentage of

cycles for high correlation (PCHC). The correlation is a statistical measure of the linear relationship between two collocated datasets ranging from  $-1$  to  $1$ . A concurrent increase/decrease in both thus yields a positive correlation. The median offset is defined as  $\text{median}(\text{SWH}_{L2} - \text{SWH}_{\text{model}})$  and is chosen to determine the accuracy of the dataset with respect to the wave model. The PCHC is a statistical metric to assess the quality of the records on a per-cycle-basis, which was developed for the collocation of altimetry data with in-situ data by [Passaro et al. \(2015\)](#). It evaluates the number of cycles that show a high correlation with another collocated reference (here, we use the SWAN-Kuststrook wave model) and puts it into relation to the total number of cycles. [Schlembach et al. \(2022\)](#) assessed a correlation coefficient of 0.82 for a dist-to-coast of less than 5 km for CORALv1 vs a global ERA5-based wave model. We thus consider a correlation of  $\geq 0.8$  as high. The procedure for the computation of the PCHC is established iteratively: First, the correlation between all altimeter-model record pairs is computed. If it is below 0.8, the cycle with the largest absolute, accumulated difference between the collocated altimeter-model pairs is discarded. This procedure is repeated until the correlation of all remaining altimeter-model pairs is greater than or equal to 0.8. The PCHC is thus given as the ratio between the number of remaining cycles and the total number of cycles and amounts to 100% in the optimal and 0% in the worst case.

The second part of the statistical analysis evaluates the number of valid records and the L2 noise. The number of valid records is based on the quality flag, which indicates whether an estimate is good or bad and is provided as a product of the retracking algorithms by each of the L2 datasets. For the CORALv2-retracked L2 datasets FFSAR-140/60 and UFSAR-20, the quality flag is set as follows: First, the misfit is computed by the root mean squared differences between the bins of the received waveform and the idealised, fitted waveform while excluding the bins that are affected by coastal interference. If the misfit exceeds an empirical threshold value of 4, the quality flag is set bad, otherwise true. For further details, refer to [Schlembach et al. \(2022\)](#). The L2 noise is defined as the root-mean-square difference between consecutive 20 Hz measurements, written as

$$n_{L2} = \sqrt{\frac{\sum_{i=1}^{N-1} (\text{SWH}_{i+1} - \text{SWH}_i)^2}{N-1}} \quad (1)$$

where  $N$  is the number of records considered for the computation of the L2 noise.

The statistical quantities are computed as a function of dist-to-coast bands, which are chosen as follows:  $0 \leq \text{dist-to-coast} < 1$  km,  $1 \leq \text{dist-to-coast} < 3$  km,  $3 \leq \text{dist-to-coast} < 5$  km, and  $5 \leq \text{dist-to-coast} < 10$  km (short-hand-noted as 0–1, 1–3, 3–5, 5–10 km).

### 3.3. Coastal SWH variation

We define the change in SWH from offshore towards the coast as the coastal SWH variation. To estimate the coastal and offshore wave heights, we take the median SWH of the two coastal 1–3 km and 5–7 km and the offshore 29–31 km dist-to-coast bands, respectively. The choice of the coastal 5–7 km band and the offshore 29–31 km bands are based on the work of [Passaro et al. \(2021\)](#), where the first valid, 1 Hz SWH estimate is selected for the calculus of the coastal SWH variation after discarding the records for the first three kilometres.

The coastal SWH variation ratios  $A_{2-30}$  and  $A_{6-30}$  are given by

$$A_{2-30} = \left(1 - \frac{\text{median}(\text{SWH}_{1-3})}{\text{median}(\text{SWH}_{29-31})}\right) \cdot 100 \quad (2)$$

and

$$A_{6-30} = \left(1 - \frac{\text{median}(\text{SWH}_{5-7})}{\text{median}(\text{SWH}_{29-31})}\right) \cdot 100 \quad (3)$$

where  $\text{SWH}_{1-3}$ ,  $\text{SWH}_{5-7}$ , and  $\text{SWH}_{29-31}$  are the SWH estimates in the 1–3 km, 5–7 km, and 29–31 km dist-to-coast bands, respectively.

We perform the coastal SWH variation analysis for passes 18, 120, and 196 only, as passes 44 and 213 do not include (collocated) data at a dist-to-coast of around 30 km.

## 4. Results and discussion

### 4.1. Statistical analysis

In this section, we present the results of the statistical analysis, which are summarised in Fig. 2. The column panels of Fig. 2 correspond to the statistic metrics: correlation, number of valid records, median offset, PCHC, and L2 noise. The row panels correspond to the statistical quantities in total and for each of the individual passes.

We first compare the altimetry datasets with the SWAN-Kuststrook wave model and assess the correlation, the median offset, and the PCHC. Secondly, we evaluate the intrinsic quantities of the number of valid records and the L2 noise.

#### 4.1.1. Comparison with the SWAN-Kuststrook wave model

**Correlation.** From Fig. 2 (a), we observe the highest correlation  $>0.8$  between the FF-SAR altimetry and wave model for up to 1 km from the coast, which indicates an increased consistency between both datasets and suggests an improvement since both datasets are independent. FF-SAR shows slightly greater similarities to the wave model than UF-SAR (1–3 km band: FFSAR-140: 0.82, UFSAR-20: 0.66). While showing a high similarity, the altimetry data might exhibit an offset with respect to the wave model. The assessment of the median offset is evaluated after the analysis of the correlation.

However, for closer than 1 km from the coast, these improvements inevitably depend on the altimeter measurement geometry and are hence more or less pronounced depending on the individual satellite track. Passes 120 and 196 show the least amount of land intrusion in the last few footprints closest to the coastline and thus show the highest correlation with the SWAN-Kuststrook wave model. Moreover, it is noticeable that both FFSAR-140/60 datasets show a better correlation than UFSAR-20 for pass 120. This might be due to the spurious interference that arises from strongly reflective targets in the along-track direction, which FF-SAR might be better capable of resolving due to its inherently high along-track resolution of  $\sim 1$  m. This phenomenon will be presented and further discussed in Section 4.2.2.

In general, pass 44 shows deteriorated correlations between all altimetry datasets and the wave model compared to the residual passes. This indicates inaccuracies in the wave model, for which pass 44 lies at the left-most edge of the model domain where modelled data is strongly affected by the boundary conditions from the coarse-grained ECMWF-WAM model.

**Median offset.** With the analysis of the median offset, we address how accurately the altimetry datasets estimate SWH with respect to the SWAN-Kuststrook wave model as a function of the dist-to-coast bands. In the optimal case, no offset should be present. If this is not the case, then a constant offset for different values of dist-to-coast between both is desirable since other metrics can also be compared, e.g. the analysis of the coastal SWH variation, as presented in Section 4.3. A discussion of systematic offsets between the altimetry datasets and the wave model with respect to the open ocean segments of the study (dist-to-coast  $\geq 20$  km) and different sea states is given in Section 4.2.

From Fig. 2 (c), we observe that all altimetry datasets exhibit higher SWH than SWAN-Kuststrook. The FF-SAR-processed datasets exhibit, across all passes, a median offset of  $\sim 32$  cm for up to 3 km from the coast and  $\sim 27$  cm for closer than 3 km from the coast. UFSAR-20 shows a similar offset behaviour towards the coast but  $\sim 13$ – $14$  cm lower in magnitude. The offsets for dist-to-coast closer than 1 km from the coast are relatively constant for FF-SAR, whereas there are greater variations for UF-SAR. That is, with respect to the wave model, FF-SAR is capable of estimating SWH more accurately for closer than 1 km from the coast than UF-SAR and as accurate for up to 3 km from the coast.

The difference in offsets between FF-SAR and UF-SAR is as expected and due to the fitting of the FF-SAR-processed waveforms against the SAMOSA2 zero-Doppler beam that was generated with a so-called

unambiguous PTR approximation (European Space Agency and Noordwijk, The Netherlands, 2021). The used  $\alpha_p$  LUT was thus generated under the assumption of an ideal PTR without considering any grating lobes (Ehlers et al., 2022), which might cause parts of the additional offset. Another part of the offset might be caused by the fitting of the SAMOSA2 zero-Doppler beam itself and the stronger dependence of FF-SAR on vertical wave velocities (Buchhaupt et al., 2021). If the sea surface were static, then the SAMOSA2 zero-Doppler beam waveform would be an appropriate model function (Ehlers et al., 2022). With increasing vertical velocities, the scatterers' signal is moved in the along-track direction and smeared in range such that the waveforms are widened, which causes an overestimation of SWH.

**Percentage of cycles with high correlation.** The PCHC represents the ratio of the cycles that show a high correlation of greater than or equal to 0.8 and the total number of cycles, as described in Section 3.2. In Fig. 2 (d), the PCHC across all passes is shown. The PCHC is related to the correlation shown in the left panels of Fig. 2, which is evaluated over all collocated altimeter-wave model records, whereas the PCHC considers the correlations of the collocations cycle-wise. That is, if the correlation values of a dist-to-coast band are close to 0.8, the PCHC value will also be high, as some cycles might exceed a correlation value of 0.8, while others do not. If all cycles exceed a correlation of at least 0.8, the PCHC value will be 100%.

We observe that up to 3 km from the coast, all CORALv2-retracked datasets show that all cycles are highly correlated, i.e. with correlations of  $\geq 0.8$  (apart from pass 44, from which we assume that the wave model is inaccurate). Approaching the coast yields a decrease in correlation, which corresponds to a decrease in the PCHC. FF-SAR shows, across all passes, higher PCHC values in the 1–3 km dist-to-coast band than UFSAR-20 (100% vs 76%), which is due to pass 213 whose footprints are highly affected by strongly reflective targets such as sandbanks. The PCHCs of the 0–1 km dist-to-coast band vary strongly between the individual passes, which is caused by the varying correlations of each pass. For passes 18 and 44, UF-SAR shows higher PCHCs, which might be due to the scarcity of available records in this dist-to-coast band. In the residual passes, the FF-SAR variants show the highest PCHC scores and, thus, the highest degree of similarity with the SWAN-Kuststrook wave model.

#### 4.1.2. Number of valid records and precision

The number of valid records and the precision, defined as L2 noise, of the altimetry data are analysed, as described in Section 3.2. Both metrics do not require any external data and serve as complementary metrics for the statistical analysis vs the SWAN-Kuststrook wave model. Both measures have a substantial impact on the uncertainty of the estimates. A higher number of valid records yields more independent measurements to reduce the overall uncertainty and allows us to resolve features, such as spatial gradients in SWH when approaching the coastline, at smaller scales. Lower L2 noise values are a direct measure of the variability of the along-track estimates and likewise correspond to a lower uncertainty for each of the estimates.

**Number of valid records.** For up to 3 km from the coast, 95%–100% are seen as good estimates for all CORALv2-retracked products across all passes. For a dist-to-coast closer than 3 km, FF-SAR exhibits more valid estimates than UF-SAR (1–3 km band: FFSAR-140: 79%, UFSAR-20: 49%). That is, FF-SAR better resolves spatial gradients in SWH and exhibits lower uncertainties, which is shown in the coastal SWH variations, as presented in Section 4.3.

The dependency on individual passes can also be seen in the number of valid records. They are coupled with the correlation of the passes, i.e. passes that show a deteriorated correlation likewise exhibit a decreased number of valid records in the corresponding dist-to-coast bands (e.g. pass 18, 0–1 km; pass 44, 1–3 km; pass 213, 1–3 km).

The number of valid records strongly depends on the passes and thus on the angle of approach of the satellite towards the coastline.



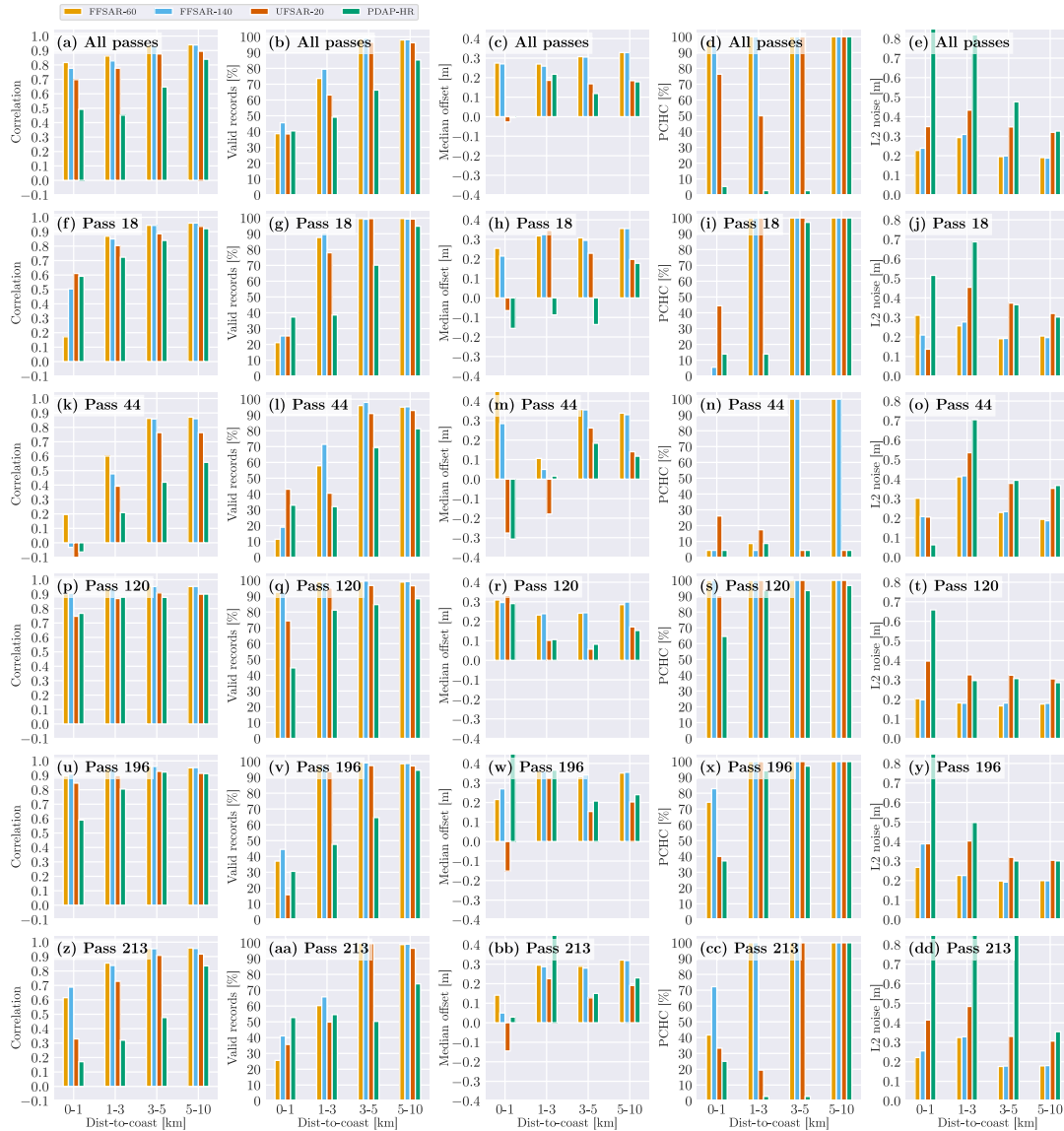


**Fig. 2.** Statistical analysis of the SWH estimates for the FFSAR-60, FFSAR-140, UFSAR-20, and PDAP-HR datasets for all and each of the individual passes. The column panels show the Pearson correlation coefficients, the number of valid records, the median offset, PCHC and L2 noise in the dist-to-coast bands 0–1, 1–3, 3–5, and 5–10 km, respectively. The row panels of the plots correspond to all passes, pass 18, 44, 120, 196, and 213, respectively.

The more the footprints in front of the coastline are affected by land intrusion, the fewer records are indicated as good estimates, and at the same time, show a deteriorated correlation with the wave model. For instance, this can be observed for pass 120, whose footprints are least affected by land (see Fig. 1 (d)) and which shows the highest number of valid records with the highest correlation. In contrast, pass 213, whose footprints are strongly affected by sandbanks and land (see Fig. 1 (f)), shows reduced numbers of estimates (FFSAR-140: 41%–66%) and decreased correlations (FFSAR-140: 0.69/0.84 for the 0–1/1–3 bands).

**L2 noise.** The rightmost column panels of Fig. 2 show the estimated L2 noise of the datasets, as described in Section 3.2. Moreover, Fig. 3 shows, in addition, the furthest offshore dist-to-coast band of 10–30 km and the gain in precision from FFSAR-140 to UFSAR-20 (difference of L2 noise values).

The gain in precision between FF-SAR and UF-SAR is remarkable. Between FFSAR-140 and UFSAR-20, it amounts to 11–15 cm throughout the dist-to-coast bands, corresponding to a relative gain of 29%–43%. The differences between the two FF-SAR variants are

not significant. When approaching the coastline from offshore to the coastline, the L2 noise gradually increases from ~20 cm at 10–30 km to ~30 cm at 1–3 km from the coast, which is attributed to individual estimates that are affected by coastal interference.

With respect to the individual passes, we find that the L2 noise level slightly varies: Pass 120, with the least intrusion of land, shows no significant increase in noise up to the coastline. Other passes that are more affected by land and strongly reflective targets, such as 196 and 213, show an increased noise level for a dist-to-coast of less than 3 km.

The noise level estimates that we find here are in line with the ones that were estimated for the UF-SAR retracking algorithms and S3 in Schlembach et al. (2020). Although they were estimated for a very large dataset and on the basis of the standard deviation of twenty 20 Hz measurements along a 1 Hz along-track distance, they likewise range for average sea states from 30–35 cm and >40 cm for the open ocean and the coastal zone, respectively.

In the rest of this work, we proceed with the analysis of the FFSAR-140 and UFSAR-20 datasets for the sake of simplicity.

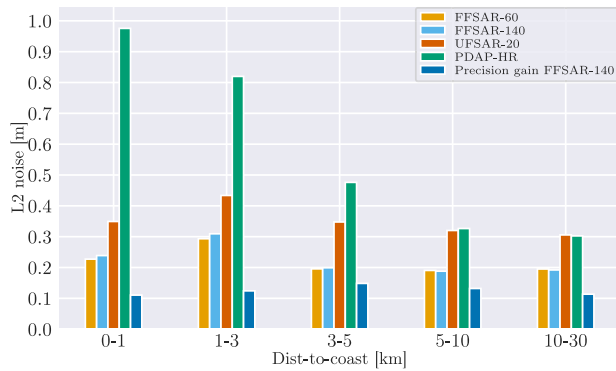


**Fig. 3.** L2 noise for the different dist-to-coast bands, as shown in Fig. 2 (e), but ranging from offshore at 10–30 km down to 0–1 km. In addition, the gain in precision of FFSAR-140 over UFSAR-20 is shown computed as the difference of the L2 noise values of FFSAR-140 and UFSAR-20.

#### 4.2. Dissimilarities between altimetry and the SWAN-Kuststrook wave model

In this section, we investigate the dissimilarities between the altimetry datasets and the SWAN-Kuststrook wave model. We first analyse systematic offsets between both and then look at a specific case where we observe an increase in SWH in the last 1–2 km from the coast.

##### 4.2.1. Systematic offsets

In the statistical analysis in Section 4.1.1, we find offsets between the altimetry data and the SWAN-Kuststrook wave model that are mostly positive, i.e. the altimetry datasets systematically overestimate SWH with respect to the wave model. As described in Section 2.2, the validation of the SWAN-Kuststrook wave model was performed in a hindcast-based analysis of four extreme events against over 50 in-situ sites, which showed only a small relative bias of  $-1\%$ .

The sea-state-dependent overestimation of SAR-derived SWH with respect to in-situ and conventional LRM-processed altimetry data has been shown by Moreau et al. (2017, 2018), and Abdalla et al. (2018) for CS2 and in Moreau et al. (2017) and Raynal et al. (2018) for S3. Since then, it has been shown that the effect is less apparent for longer-period (swell) waves and mainly comes from wave motions (Amarouche et al., 2019; Egido and Smith, 2019; Buchhaupt, 2019). According to the S6-MF mission performance working group, the bias between the PDAP-HR and the PDAP-LR products of the EUMETSAT baseline F06 are linked to vertical wave velocities, which shows  $\sim 10$  cm higher SWH for  $\text{SWH} = 1$  m, and  $\sim 20$  cm higher SWH for  $\text{SWH} = 2$  m (EUMETSAT, 2022a; Martin-Puig et al., 2022). In Section 4.1.1, an additional offset between FF-SAR and UF-SAR found to amount to 13–14 cm. Parts of this mismatch are believed to be linked to different sensitivity of FF-SAR and UF-SAR to vertical wave motion (Buchhaupt et al., 2021). To account for the effect of vertical wave motions and the induced SWH bias, a LUT was proposed by Egido et al. (2022) that applies a sea-state-dependent SWH correction, which is planned to become operational for S6-MF baseline F09 in Q3 2023 (Scharroo et al., 2022). More recently, Buchhaupt et al. (2022) found that the HR-LR inconsistencies also originate from horizontal surface velocities that are caused by current, wind-induced movement, and swells and propose a 2D retracking scheme, which is capable of estimating both vertical wave-particle and along-track surface velocities along with the other three geophysical estimates. Based on simulations shown in Buchhaupt et al. (2022, Slide 27), the SWH bias due to horizontal surface velocities amounts to up to 4.5 cm, depending on the wind speed.

The effect of vertical wave velocities are similarly represented in our analysis: The offsets of the altimetry datasets, including the PDAP-LR product to SWAN-Kuststrook, are shown as a function of SWAN-Kuststrook SWH in Fig. 4 (a), which exhibit a dependency on the sea state. SWAN-Kuststrook underestimates the SWH with respect to the PDAP-LR product by about 5–10 cm in the range of SWH values, which is relatively constant for an SWH of up to 2 m (in between most of the SWAN-Kuststrook estimates range). The magnitude of the offset between the PDAP-HR and PDAP-LR datasets is within the range that is shown in EUMETSAT (2022a, Figure 3). The stronger variations of SWH offsets of larger than 2 m likely arise due to the fewer estimates in this sea state region, which yields a poorer statistical representation.

Fig. 4 (b) shows the probability density function (PDF) of the SWAN-Kuststrook SWH in the offshore part of the considered area (dist-to-coast  $\geq 20$  km), showing a median SWH of 1.08 m (5% percentile: 0.40 m, 95% percentile: 2.52 m). Fig. 4 (c) compares the PDFs of the offshore SWH values of FFSAR-140 and UFSAR-20 including the corresponding median SWH value. The offset between the medians of FFSAR-140/UFSAR-20 and SWAN-Kuststrook is in line with the results of Fig. 4 (a) (1.47 m/1.37 m vs 1.08 m), as well as the relative difference between FFSAR-140 and UFSAR-20 ( $\sim 10$  cm). Few values of  $\sim 1.5\%$  of the UFSAR-20 are located in the smallest bin, potentially caused by suboptimal estimations determined by the lower SWH boundary during the iterative fitting of the retracking procedure. FFSAR-140 is unaffected by this due to the positive offset regarding UFSAR-20. Fig. 4 (d) depicts the median offset of the 5–10 km, 10–20 km, and 20–30 km dist-to-coast bands. The median offsets of the 20–30 km band amount to 42 cm and agree with the ones that can be seen from the differences between SWAN-Kuststrook and the individual datasets in Fig. 4 (a), considering a median SWH of  $\sim 1.0$ . The quality of the PDAP-LR estimates is too poor to analyse the nearshore offsets closer than 10 km from the coast.

##### 4.2.2. Increase in significant wave height estimates

We find that a significant number of the individual overpasses show increasing SWH estimates in the last 1–2 km from the coast, as depicted exemplarily in Fig. 5 (b) for the overpass of cycle 40 and pass 120. The increase is apparent for both the FFSAR-140 and UFSAR-20 datasets, while it is more significant for UFSAR-20 in both the intensity (SWH increase from below 0.5 m to almost 1.5 m) and the dist-to-coast ( $\sim 2$  km). For FFSAR-140, the increase in SWH is up to  $\sim 0.9$  m, and it stretches to  $\sim 1.5$  km off the coast. The reason for the increase is explained by an extraordinarily strong reflective target, which is the straight sandbank at the defined coastline of pass 120 and the absence of any other land intrusions within the footprint, as shown in Fig. 5 (a). This is visualised by the multilooked echo power radargram in Fig. 5 (c) and (d) for FF-SAR and UF-SAR (with a posting rate of 140 Hz), respectively. The grating lobes of the S6-MF along-track PTR (Ehlers et al., 2022, Figure 6, Panel F), which are induced by the strong signal components of the sandbank interferer, can be well identified at distances of multiples of  $\sim 300$  m off the coastline. The bow-tie-like pattern can also be recognised as the power is increasingly smeared over more range gates for waveforms that are further away from the sandbank. The power of the closely located grating lobes is concentrated more in the LE of the waveforms at range gates around bin  $\sim 100$ . This strongly deteriorates the SWH estimates in the first 1–2 km off the coast.

To determine how many overpasses are affected by an increase in SWH in the last three kilometres from the coast, we apply the following empirical constraint:

$$\max(\text{SWH}_{0-3}) > \max(\text{SWH}_{3-5} + n_{1,2}) \quad (4)$$

where  $\text{SWH}_{0-3/3-5}$  are the estimated SWH records for the 0–3/3–5 km dist-to-coast bands and  $n_{1,2}$  the estimated L2 noise, being set to 0.2 m and 0.3 m for FF-SAR and UF-SAR and 0 for SWAN-Kuststrook, respectively.

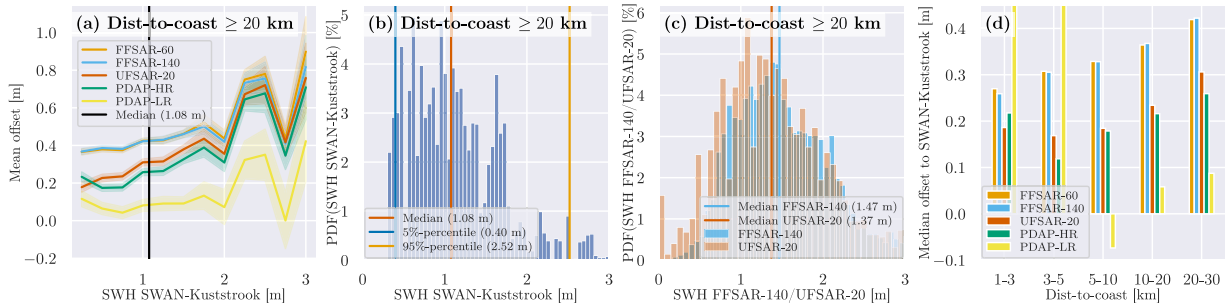


**Fig. 4.** The offset in the open ocean (with dist-to-coast  $\geq 20$  km) of the processed L2 datasets against the PDAP-LR dataset is shown in (a) as a function of the SWH from SWAN-Kuststrook, with the median offshore SWH of 1.03 m from (b). The uncertainty of the mean of each of the bins is given based on the 95% confidence interval. In (b), the PDF of the SWAN-Kuststrook SWH values is displayed with the median and the 5%- and the 95%-percentile as vertical lines. (c) compares the PDFs of the offshore SWH values of FFSAR-140 and UFSAR-20 including the corresponding median SWH value. (d) shows the evolution of the offsets of the individual datasets vs the SWAN-Kuststrook wave model from offshore at 30 km up to 1 km from the coast.

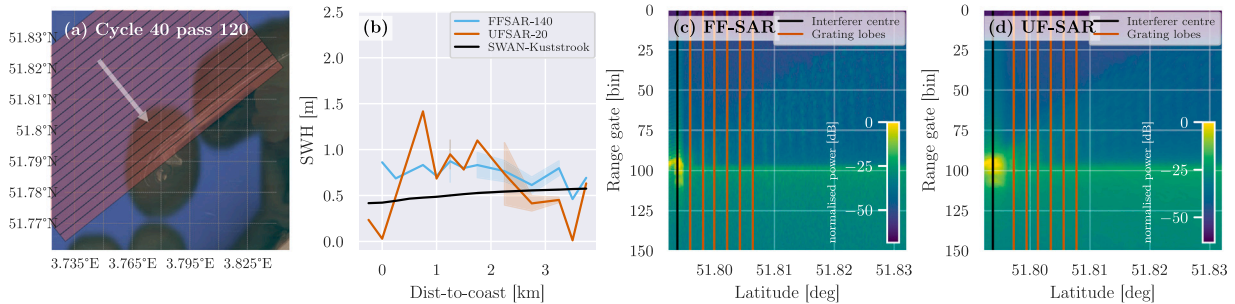


**Fig. 5.** (a) shows a satellite image with the effective radar footprints (corresponding to a posting rate of 20 Hz) and the strongly reflective, straight sandbank, which is crossed perpendicularly by the satellite track. The resulting retracked SWH estimates of the FFSAR-140 and UFSAR-60 datasets and SWAN-Kuststrook are shown in (b) as a function of dist-to-coast for the overpass of cycle 40, pass 120 (the shaded area of the panel indicates the 95% confidence interval of dist-to-coast bins with multiple values). The multilooked echo power radargrams (after the L1b processing) are shown in (c) for FF-SAR and (d) UF-SAR (both with a posting rate of 140 Hz). The centre of the strongly reflective sandbank interferer and the induced grating lobes are shown at distances of multiples of  $\sim 300$  m from the coast as vertical lines.

We apply Eq. (4) to the 138 overpasses (excluding pass 44) for the FFSAR-140 and UFSAR-20 datasets and compute the (sample) mean probability of occurrence of an SWH increase for each of the individual passes, which is shown in Fig. 6. FFSAR-140 tends to be less affected by the SWH increase. However, the margin of error, corresponding to a 95% confidence interval, is quite large, with up to 17.5%, and hence no safe conclusion can be drawn for passes 18, 196, and 213. Pass 120, though, represents an exception, as FFSAR-140 shows a strongly reduced mean probability for an SWH increase of  $9.7\% \pm 10.4\%$ , as compared to UF-SAR with  $52.8\% \pm 17.2\%$ . The SWAN-Kuststrook wave model shows an increase of (only) up to 8 cm for one overpass of passes 18 and 120, none for pass 196, and in  $19.4\% \pm 6.2\%$  of the overpasses for pass 213.

A check for an increasing SWH in SWAN-Kuststrook ( $\max(\text{SWH}_{0-3}) > \max(\text{SWH}_{3-5})$ ) reveals an increase of up to 8 cm for 10 out of the 138 cycles ( $6.5\% \pm 4.1\%$ ), whereas pass 213 is affected most (8), and passes 18 and 120 only once.

### 4.3. Coastal SWH variation

The computed mean coastal SWH variations  $\Delta_{6-30}$  and  $\Delta_{2-30}$  of the FFSAR-140 and UFSAR-20 datasets for the passes 18, 120, and 196 are shown in Fig. 7 (a) and (b), respectively. We exclude overpasses, where SWAN-Kuststrook exhibits low sea states of less than 0.5 m around 30 km from the coast. We justify this since the poor resolution of the leading edge for very low sea states negatively affects the capability of altimeters to estimate SWH in these cases (Smith and Scharroo, 2015). Moreover, the uncertainties (precision) of the two coastal and offshore SWH values propagate through to the ratio of both values (Ku et al., 1966). If both are small, the uncertainty of the ratio becomes very large. These overpasses would yield unrealistic estimates for the coastal SWH

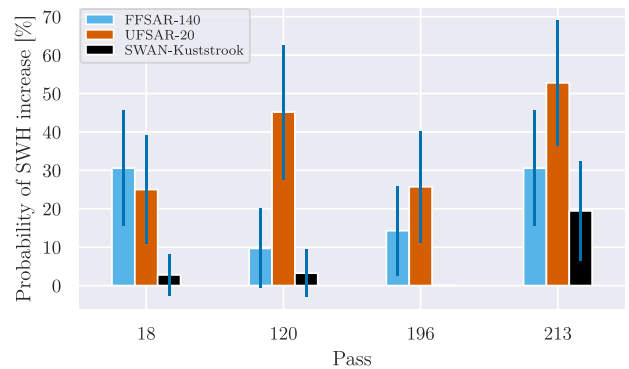


**Fig. 6.** Mean probabilities of occurrence for an SWH increase from 3–5 km to 0–3 km from the coast by applying Eq. (4). The error bars indicate a 95% confidence interval.

variation. In total, 15/105 low-sea-state overpasses are excluded from this analysis.

All coastal SWH variations are positive, i.e. the SWH decays towards the coastline. We observe that both FF-SAR and UF-SAR estimate the decays with respect to the 5–7 km band with no significant differences. In the 5–7 km band, both FFSAR-140 and UFSAR-20 datasets are close to the decays that are estimated by SWAN-Kuststrook (FFSAR-140:  $17.4\% \pm 2.5\%$ , SWAN-Kuststrook:  $15.9\% \pm 2.2\%$ ).

However, there are more significant differences between FF-SAR and UF-SAR for the 1–3 km band: UFSAR-20 strongly underestimates the mean decay for pass 18 and also shows a large standard errors that imply a large uncertainty of the estimated variations. FFSAR-140 is, in

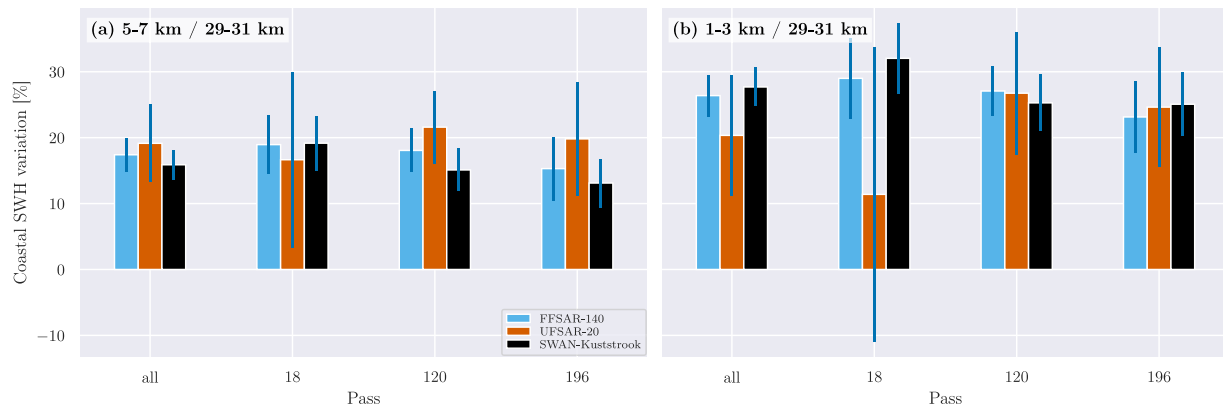


Fig. 7. Mean coastal SWH variations between the SWH between the 29–31 km dist-to-coast band and the 5–7 km or the 1–3 km dist-to-coast bands in (a) and (b), respectively, for the datasets FFSAR-140 and UFSAR-20. The error bars correspond to the 95% confidence interval.

contrast, very close to the decays of the wave model and shows a decay of  $26.4\% \pm 3.1\%$ .

We argue that the difference between FF-SAR and UF-SAR is explained by the differences in their 2D-PTRs. For UF-SAR, it is a sinc<sup>2</sup> with a 3-dB width of  $\sim 300$  m, which causes the reflected power of a single point scatterer to be smeared in this distance in both the along- and across-track direction in a bow-tie-like pattern (Ehlers et al., 2022, Figure 3, Panel B). The 2D-PTR of FF-SAR is instead much peakier, with a width of  $\sim 1$  m in the along-track direction, i.e. the main reflected power is integrated over a much smaller distance in the along-track direction at the actual location of the point scatterer (the minor grating lobes yield only  $\sim 1\%$  of the total, reflected power) (Ehlers et al., 2022, Figure 6, Panel F). Thus, we argue that FF-SAR is better able to resolve (static) small-scale interferers and estimate SWH more accurately for a dist-to-coast of less than 3 km, despite the presence of interfering targets in the across-track direction that are also smeared along-track for UF-SAR.

Passaro et al. (2021) found that the global mean coastal SWH variation at  $>3$  km from the coastline, corresponding to our 5–7 km dist-to-coast band, is 22% with respect to the offshore SWH at 30 km. However, strong variations have been assessed for 14 different regions of the global coastal ocean (Reguero et al., 2015), which show a mean value of  $17.2\% \pm 3.4\%$ . For the Northern and Western Europe region, a decay of 22.41% was evaluated, with an average offshore sea state of SWH = 2.23 m and most of the areas being exposed to an open ocean with a higher ratio of swells of higher wavelengths. That is, considering a lower median SWH value of 1.03 m (from Fig. 4) and the exposure of the milder North Sea, the overall variation we have estimated with the FFSAR-140 dataset is for the 5–7 km dist-to-coast band within an expected range of  $17.4\% \pm 2.5\%$ .

## 5. Conclusion and future work

In this work, we have conducted an extensive coastal case study to assess the applicability of FF-SAR-processed S6-MF coastal altimetry data to obtain SWH estimates as close as possible to the coast. No comparable study has been performed in the past yet. The data included 161 overpasses from five passes, covering the Dutch coast and the German coast along the East Frisian Islands in the North Sea, and 38 cycles, corresponding to the year 2021. Two FF-SAR-processing configurations with the 60/140 Hz L1b posting rates and one UF-SAR processing configuration, UFSAR-20, with a 20 Hz L1b posting rate were used to process L1a data from EUMETSAT to acquire SWH estimates after the retracking process with the coastal retracking algorithm CORALv2. Once the 60/140 Hz FF-SAR datasets have been retracked, they are reduced to form 20 Hz estimates by averaging the estimates for which the quality flag indicates a good estimate. This allows the high along-track resolution of FF-SAR to be exploited.

The processed altimetry datasets, and the baseline PDAP-HR product from EUMETSAT, were compared with the coastal, high-resolution SWAN-Kuststrook wave model from the operational RWsOS operational forecasting system to assess the performance of the altimetry datasets. We observe that accurate and precise SWH records can be estimated in the nearshore zone within 1–3 km from the coast using satellite SAR altimetry. This confirms the finding of recent studies that SAR altimetry can obtain coastal estimates at much higher quality of records when compared to LRM altimetry (Dinardo et al., 2018; Schlembach et al., 2020; Dinardo et al., 2020; Gou and Tourian, 2021) and moreover demonstrates the ability to measure SWH even closer than 3 km from the coastline.

The FFSAR-140 dataset exhibits the highest similarity to the model, showing a correlation coefficient of  $\sim 0.8$  at 45% of valid records for the 0–1 km band and 80% of valid records for the 1–3 km band. All passes, except pass 44, where the model might give inaccurate estimates, show PCHC scores of 100% from 1 km off the coast, i.e. for all cycles, a correlation coefficient of greater than or equal to 0.8 is estimated. We notice a dependence of the performance metrics on the individual passes, which are deteriorated for those where the radar footprints are highly affected by strongly reflective targets such as sandbanks and human-made infrastructure (e.g. pass 213). Such scenarios remain challenging despite the application of FF-SAR altimetry and represent a limitation for satellite altimetry in the nearshore zone. The baseline PDAP-HR product shows strongly deteriorated correlations and a smaller number of valid records for a dist-to-coast of less than 10 km, e.g. a correlation of  $\sim 0.45$  at  $\sim 50\%$  of valid records for the 1–3 km band for all passes. We have observed that the correlation and number of valid records can be further improved if the L1b posting rate is increased for the FF-SAR-variants from 60 to 140 Hz without any sacrifice in precision. We noticed offsets between the FF-SAR- and UF-SAR-processed datasets, which might to a certain fraction be caused by vertical wave velocities that have a different influence for FF-SAR processing (Buchhaupt et al., 2021). With increasing vertical velocities, the scatterers' signal is moved in the along-track direction and smeared in range such that the waveforms are widened, which causes an overestimation of SWH (Ehlers et al., 2022).

The FF-SAR datasets show an L2 noise of  $\sim 20$  cm in the open ocean segments and  $\sim 31$  cm for closer than 3 km from the coast, whereas UFSAR-20 exhibits L2 noise levels of  $\sim 31$  cm and  $\sim 43$  cm, respectively. That is, FF-SAR achieves a gain in precision of  $\sim 37\%$  and up to  $\sim 29\%$  in the open ocean and closer than 3 km off the coast. The PDAP-HR product shows similar L2 noise values as UFSAR-20 for more than 5 km from the coast, and increasingly higher values towards the coast of more than 82% for closer than 3 km off the coast, respectively.

We have also identified dissimilarities between estimates of the altimetry datasets and the SWAN-Kuststrook, which are mainly a consequence of known issues related to SAR altimetry parameter estimation;

see references in Section 4.2. Accordingly, we observed that all FF-SAR- and UF-SAR-processed datasets exhibit a positive offset with respect to the wave model with a median offset of 34 cm (5%-percentile: 17 cm; 95%-percentile: 66 cm). Major parts of the offset are known and are likely caused by the influence of vertical wave velocities that are specific to SAR altimetry processing (FF-SAR more than UF-SAR) (Buchhaupt et al., 2021). This has been shown by including the PDAP-LR from the baseline L2 product in the offset analysis. A much smaller offset of less than 10 cm was observed between the PDAP-LR dataset and the SWAN-Kuststrook wave model for low and average sea states of up to 2.0 m in SWH. The median offset to the model gradually decreases from ~42 cm for 20–30 km from the coast to ~26 cm for less than 1 km off the coast (for FFSAR-140).

In order to exploit the nearshore SWH estimates of the altimetry dataset, we have investigated the coastal SWH variations, which quantify the change in SWH from offshore at 30 km to the two coastal dist-to-coast bands 5–7 km and 1–3 km. With the FFSAR-140 dataset, we observed a mean decay in SWH of  $17.4\% \pm 2.5\%$  and  $26.4\% \pm 3.1\%$  with respect to the 5–7 km and the 1–3 km dist-to-coast bands for the three S6-MF passes 18, 120, and 196. The decays for the 5–7 km band are within the expected range of the ones globally and regionally found in Passaro et al. (2021). We thus demonstrated that the FFSAR-140 processing-configuration is also capable of giving accurate estimates for the coastal SWH variation in regard to the 1–3 km band.

To summarise the results of the individual objectives of this study, we can draw the following conclusions, which have not been shown by any previous work:

**FF-SAR vs UF-SAR** FF-SAR SWH estimates were found to exhibit lower noise, resulting in increased correlation with the numerical wave model, and provide a higher number of valid records and highly correlated cycles, as compared to the UF-SAR estimates.

**High-quality SWH estimates from 1 km from the coast** This case study demonstrates that one can acquire robust high-frequency SWH estimates up to 1 km off the coast by the combination of FF-SAR altimetry, the coastal CORALv2 retracker, and the subsequent removal of residual outliers.

**Estimation of nearshore, coastal SWH variations** With the aforementioned FF-SAR-configuration, we are able to give accurate estimates with respect to a numerical wave model for the coastal SWH variation of up to 1 km from the coast. The approach angle of the satellite track, as well as the existence of strongly reflective targets such as sandbanks, tidal flats, calm waters or human-made infrastructure being located nearshore, are still dominating factors that influence the quality of the SWH estimates, regardless of FF-SAR-processing.

FFSAR-140 represents the processing configuration with the best performance but, at the same time, exhibits the highest amount of computational complexity. However, it must also be noted that the used FF-SAR back-projection processing methodology is not the most efficient one. Guccione et al. (2018) have proposed the omega-kappa FF-SAR processing methodology, which strongly reduces the computational efforts with negligible costs in performance.

In this work, we found that FF-SAR processing combined with a coastal retracker gives additional gains for distances of up to 1 km from the coast in terms of accuracy, precision, and availability of the SWH records. The quality of the nearshore SWH estimates varies depending on the characteristics of the individual crossing of the shoreline, and thus on the existence of strongly reflective targets within the radar footprints. As part of future work, we thus suggest the development of more advanced interference mitigation techniques, tailored to FF-SAR-processed altimetry data. The suppressing of signals from static interfering targets might give an additional gain for FF-SAR processing.

The improvement of the quality flagging after multilooking at the higher posting rates provides additional gains in the robustness of the L2 estimates. We also suggest studying the difference between the FF-SAR- and UF-SAR-processed datasets in more detail to be able to characterise small-scale features such as breaking waves or shoaling effects that FF-SAR might be able to resolve.

#### CRediT authorship contribution statement

**Florian Schlembach:** Conceptualization, Methodology, Software, Formal analysis, Investigation, Resources, Writing – original draft, Writing – review & editing, Visualisation. **Frithjof Ehlers:** Software, Formal analysis, Resources, Writing – review & editing. **Marcel Kleinherenbrink:** Software, Resources, Writing – review & editing, Supervision. **Marcello Passaro:** Writing – review & editing, Supervision, Project administration, Funding acquisition. **Denise Dettmering:** Writing – review & editing. **Florian Seitz:** Writing – review & editing, Project administration, Funding acquisition. **Cornelis Slobbe:** Software, Resources, Writing – review & editing, Supervision.

#### Declaration of competing interest

The authors declare that they have no known competing financial interests or personal relationships that could have appeared to influence the work reported in this paper.

#### Data availability

Data will be made available on request.

#### Acknowledgements

The authors gratefully acknowledge Deltares for the provision of the operational SWAN-Kuststrook wave model. We would like to thank the three anonymous reviewers who helped to improve this article. Further, we would like to acknowledge the contributions of Python (Van Rossum and Drake, 2009) and the following Python packages that we used: NumPy (Harris et al., 2020), SciPy (Virtanen et al., 2020), pandas (McKinney, 2010), Matplotlib (Hunter, 2007), Cython (Behnel et al., 2011), and seaborn (Waskom, 2021).

All authors read and approved the final version of the manuscript.

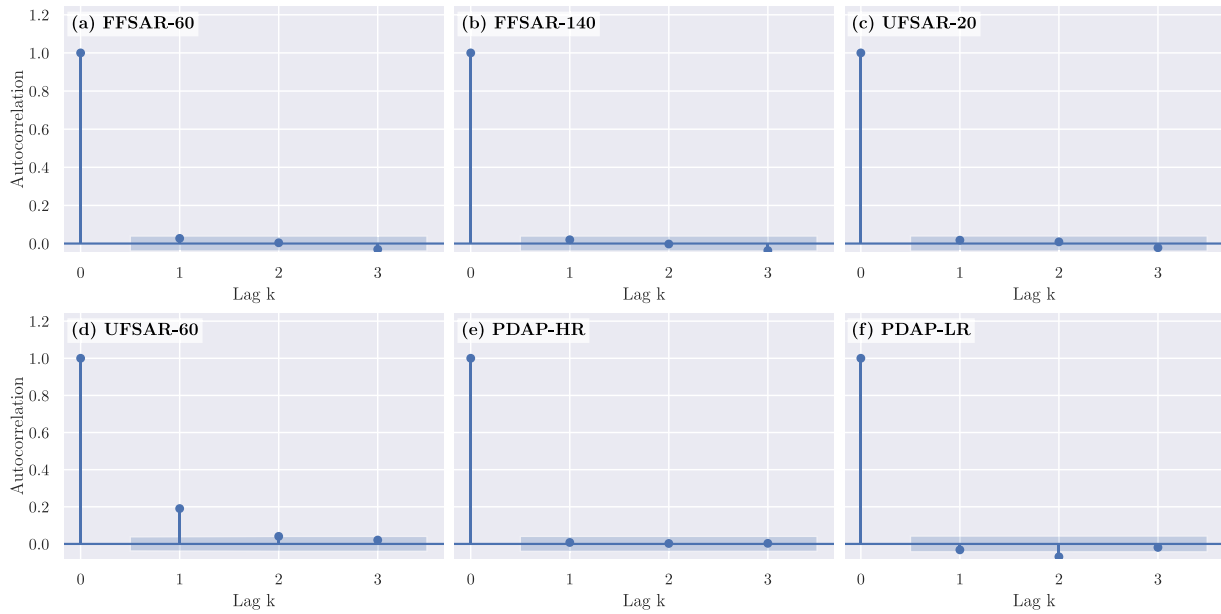
#### Funding

This research has been funded by the European Space Agency as part of the Sea State Climate Change Initiative (SeaState\_cci) project: ESA ESRIN/Contract No. 4000123651/18/I-NB. The FF-SAR SAMOSA LUT generation was funded under ESA contract 4000118128/16/NL/AI.

#### Appendix A. Autocorrelation analysis

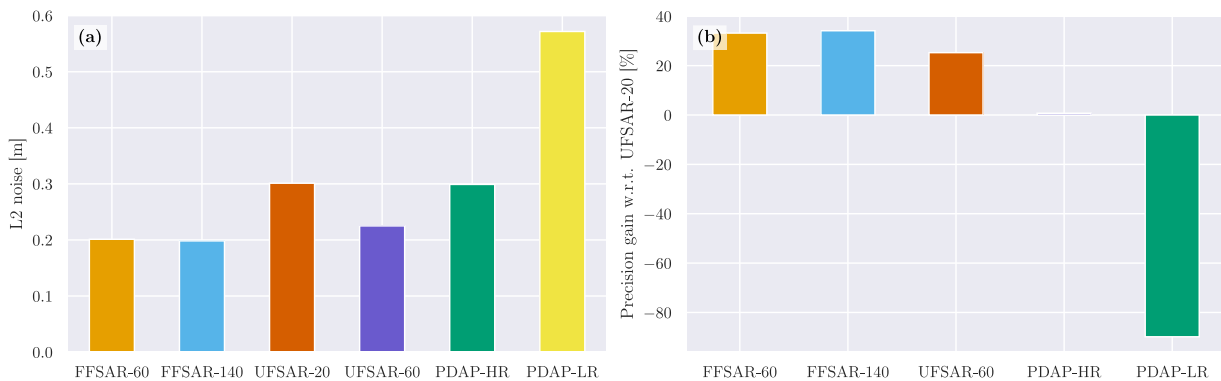
Dinardo et al. (2015) and Egido et al. (2020) suggest increasing posting rates to more than 20 Hz as commonly used by the EUMETSAT baseline products. In this work, the authors assume that the decorrelation length of the radar echoes is much smaller in the along-track direction than the inherent unfocused synthetic aperture radar (UF-SAR) along-track resolution of ~300 m. Hence, depending on the sea state, a precision gain of 20%–30% can be achieved for the geophysical estimates if the posting rates are increased to 40 or 60 Hz and then averaged to form 20 Hz estimates.

We have analysed the autocorrelation function (ACF) of different processing options by considering open ocean segments with a distance-to-coast (dist-to-coast) between 20 km and 30 km. We exclude those that show a larger standard deviation than 20 cm, 30 cm, and 50 cm for fully focused synthetic aperture radar (FF-SAR)-, UF-SAR- and



1

Fig. A.8. Autocorrelation of the datasets FFSAR-60, FFSAR-140, UFSAR-20, UFSAR-60, PDAP-HR, and PDAP-LR in a-f, respectively. The light blue area for  $k \neq 0$  indicates the standard error of white noise, which is approximated as  $\sigma_n = \sqrt{N^{-1}}$ , with  $N$  being the number of estimates.



1

Fig. A.9. The L2 noise of the datasets FFSAR-60, FFSAR-140, UFSAR-20, UFSAR-60, PDAP-HR, and PDAP-LR is shown in (a). The gain in precision is shown relative to UFSAR-20 in (b).

low resolution mode (LRM)-processed datasets, respectively. We have added the two datasets, UFSAR-20 and Payload Data Acquisition and Processing Low Resolution (PDAP-LR), to assess their autocorrelations. The datasets with posting rates of more than 20 Hz are arithmetically averaged to yield the targeted 20 Hz posting rate. The ACFs of the first three lags for the different datasets are shown in Fig. A.8. Apart from UFSAR-60, all datasets exhibit no correlation between their adjacent records, as the ACF stays within the confidence interval of the standard error of white noise (Brockwell and Davis, 1987). UFSAR-60 shows a correlation of  $\sim 0.2$  for lag  $k = 1$ . The resulting L2 noise, or precision, and the gain in precision over UFSAR-20 are shown in Fig. A.9 (a) and (b), respectively. No correlation is observed for the FF-SAR-processed datasets, not even for FFSAR-60 and FFSAR-140. UFSAR-20 shows a gain in precision of 25.3% over PDAP-HR. This is noticeable and in line with the numbers being reported by Egido et al. (2020), who estimated precision gains of 22% and 25% for posting rates of 40 Hz and 60 Hz. Nevertheless, we find that the increased precision of the geophysical estimates is, per se, not an actual gain but comes together with an added correlation between the reduced 20 Hz estimates. The

subsampling of the 20 Hz estimates thus acts as a smoothing or low-pass filter, which smears the effective signal over the subsequent estimate. Consequently, we decided not to include any UF-SAR datasets with posting rates of larger than 20 Hz in this study to allow for a fair comparison of the individual analysed datasets.

Appendix B. Supplementary data

Supplementary material related to this article can be found online at <https://doi.org/10.1016/j.rse.2023.113517>.

References

Abdalla, S., Dinardo, S., Benveniste, J., Janssen, P.A., 2018. Assessment of CryoSat-2 SAR mode wind and wave data. *Adv. Space Res.* 62 (6), 1421–1433. <http://dx.doi.org/10.1016/j.asr.2018.01.044>.  
 Alvera-Azcárate, A., Sirjacobs, D., Barth, A., Beckers, J.-M., 2012. Outlier detection in satellite data using spatial coherence. *Remote Sens. Environ.* 119, 84–91. <http://dx.doi.org/10.1016/j.rse.2011.12.009>.

- Amarouche, L., Tran, N., Herrera, D., 2019. Impact of the ocean waves motion on the delay/Doppler altimeters measurements. In: Ocean Surface Topography Science Team (OSTST) Meeting.
- Arens, S.M., Mulder, J.P.M., Slings, Q.L., Geelen, L.H.W.T., Damsma, P., 2013. Dynamic dune management, integrating objectives of nature development and coastal safety: Examples from the Netherlands. *Geomorphology* 199, 205–213. <http://dx.doi.org/10.1016/j.geomorph.2012.10.034>.
- Behnel, S., Bradshaw, R., Citro, C., Dalcin, L., Seljebotn, D.S., Smith, K., 2011. Cython: The best of both worlds. *Comput. Sci. Eng.* 13 (2), 31–39. <http://dx.doi.org/10.1109/MCSE.2010.118>.
- Booij, N., Ris, R.C., Holthuijsen, L.H., 1999. A third-generation wave model for coastal regions: 1. Model description and validation. *J. Geophys. Res.: Oceans* 104 (C4), 7649–7666. <http://dx.doi.org/10.1029/98JC02622>.
- Brockwell, P.J., Davis, R.A., 1987. Time Series: Theory and Methods. In: Springer Series in Statistics, Springer, New York, NY, <http://dx.doi.org/10.1007/978-1-4899-0004-3>.
- Bryan, K.R., Power, H.E., 2020. 4 - Wave behaviour outside the surf zone. In: Jackson, D.W.T., Short, A.D. (Eds.), *Sandy Beach Morphodynamics*. Elsevier, pp. 61–86. <http://dx.doi.org/10.1016/B978-0-08-102927-5.00004-7>.
- Buchhaupt, C., 2019. Model Improvement for SAR Altimetry (Ph.D. thesis). Schriftenreihe Fachrichtung Geodäsie der Technischen Universität Darmstadt, Darmstadt.
- Buchhaupt, C., Egado, A., Smith, W., Vandemark, D., Fenoglio-Marc, L., Leuliette, E., 2022. 2D SAR altimetry retracking – lessons learned. In: Ocean Surface Topography Science Team (OSTST) Meeting in Venice.
- Buchhaupt, C., Fenoglio, L., Becker, M., Kusche, J., 2021. Impact of vertical water particle motion on focused SAR altimetry. 25 Years of Progress in Radar Altimetry, *Adv. Space Res. 25 Years of Progress in Radar Altimetry*, 68 (2), 853–874. <http://dx.doi.org/10.1016/j.asr.2020.07.015>.
- Cavaleri, L., Fox-Kemper, B., Hemer, M., 2012. Wind waves in the coupled climate system. *Bull. Am. Meteorol. Soc.* 93 (11), 1651–1661. <http://dx.doi.org/10.1175/BAMS-D-11-00170.1>.
- Charlier, R.H., Chaineux, M.C.P., Morcos, S., 2005. Panorama of the history of coastal protection. *J. Coast. Res.* 21 (1 (211)), 79–111. <http://dx.doi.org/10.2112/03561.1>.
- Chowdhury, P., Behera, M.R., 2017. Effect of long-term wave climate variability on longshore sediment transport along Regional Coastlines. *Prog. Oceanogr.* 156, 145–153. <http://dx.doi.org/10.1016/j.pocean.2017.06.001>.
- Cipollini, P., Benveniste, J., Bouffard, J., Emery, W., Gommenginger, C., Griffin, D., Høyer, J., Madsen, K., Mercier, F., Miller, L., et al., 2009. The role of altimetry in coastal observing systems. *Proceedings of OceanObs'09: Sustained Ocean Observations and Information for Society* <http://dx.doi.org/10.5270/OceanObs09.cwp.16>.
- Cipollini, P., Benveniste, J., Miller, L., Picot, N., Scharroo, R., Strub, T., 2012. Conquering the coastal zone: A new frontier for satellite altimetry. In: *20 Years of Progress in Radar Altimetry*, No. 1, pp. 3–7.
- Contardo, S., Hoeke, R., Hemer, M., Symonds, G., McInnes, K., O'Grady, J., 2018. In situ observations and simulations of coastal wave field transformation by wave energy converters. *Coast. Eng.* 140, 175–188. <http://dx.doi.org/10.1016/j.coastaleng.2018.07.008>.
- Day, C., Dietrich, J., 2022. Improved wave predictions with ST6 Physics and ADCIRC+SWAN. *Shore Beach* 59–61. <http://dx.doi.org/10.34237/1009016>.
- de Vries, S., Wengrove, M., Bosboom, J., 2020. A RIP-based SAR sediment transport. In: Jackson, D.W.T., Short, A.D. (Eds.), *Sandy Beach Morphodynamics*. Elsevier, pp. 187–212. <http://dx.doi.org/10.1016/B978-0-08-102927-5.00009-6>.
- Dinardo, S., Fenoglio-Marc, L., Becker, M., Scharroo, R., Fernandes, M.J., Staneva, J., Grayek, S., Benveniste, J., 2020. A RIP-based SAR retracker and its application in North East Atlantic with Sentinel-3. *Adv. Space Res.* <http://dx.doi.org/10.1016/j.asr.2020.06.004>.
- Dinardo, S., Fenoglio-Marc, L., Buchhaupt, C., Becker, M., Scharroo, R., Joana Fernandes, M., Benveniste, J., 2018. Coastal SAR and PLRM altimetry in German Bight and West Baltic Sea. *Adv. Space Res.* 62, 1371–1404. <http://dx.doi.org/10.1016/j.asr.2017.12.018>.
- Dinardo, S., Scharroo, R., Benveniste, J., 2015. SAR altimetry at 80 Hz: Open Sea, coastal zone, Inland Water. In: Ocean Surface Topography Science Team Meeting.
- Donlon, C.J., Cullen, R., Giulicchi, L., Vuilleumier, P., Francis, C.R., Kuschnerus, M., Simpson, W., Bouridah, A., Caleno, M., Bertoni, R., Ranaño, J., Pourier, E., Hyslop, A., Mulcahy, J., Knockaert, R., Hunter, C., Webb, A., Fornari, M., Vaze, P., Brown, S., Willis, J., Desai, S., Desjonqueres, J.-D., Scharroo, R., Martin-Puig, C., Leuliette, E., Egado, A., Smith, W.H.F., Bonnefond, P., Le Gac, S., Picot, N., Tavernier, G., 2021. The Copernicus Sentinel-6 mission: Enhanced continuity of satellite sea level measurements from space. *Remote Sens. Environ.* 258, 112395. <http://dx.doi.org/10.1016/j.rse.2021.112395>.
- Egado, A., Buchhaupt, C., Boy, F., Maraldi, C., Emeline, C., Salvatore, D., Leuliette, E., Moreau, T., 2022. A significant wave height correction to account for vertical wave motion effects in SAR altimeter measurements. In: Ocean Surface Topography Science Team (OSTST) Meeting in Venice.
- Egado, A., Dinardo, S., Ray, C., 2020. The case for increasing the posting rate in delay/Doppler altimeters. *Adv. Space Res.* <http://dx.doi.org/10.1016/j.asr.2020.03.014>.
- Egado, A., Smith, W.H.F., 2017. Fully focused SAR altimetry: Theory and applications. *IEEE Trans. Geosci. Remote Sens.* 55 (1), 392–406. <http://dx.doi.org/10.1109/TGRS.2016.2607122>.
- Egado, A., Smith, W.H.F., 2019. Pulse-to-pulse correlation effects in high PRF low-resolution mode altimeters. *IEEE Trans. Geosci. Remote Sens.* 57 (5), 2610–2617. <http://dx.doi.org/10.1109/TGRS.2018.2875622>.
- Ehlers, F., Schlembach, F., Kleinherenbrink, M., Slobbe, C., 2022. Validity assessment of SAMOSA retracking for fully-focused SAR altimeter waveforms. *Adv. Space Res.* <http://dx.doi.org/10.1016/j.asr.2022.11.034>.
- Elfrink, B., Baldock, T., 2002. Hydrodynamics and sediment transport in the swash zone: A review and perspectives. *Coast. Eng.* 45 (3), 149–167. [http://dx.doi.org/10.1016/S0378-3839\(02\)00032-7](http://dx.doi.org/10.1016/S0378-3839(02)00032-7).
- EMODnet Bathymetry Consortium, 2018. EMODnet Digital Bathymetry (DTM 2018). <http://dx.doi.org/10.12770/18ff0d48-b203-4a65-94a9-5fd8b0ec35f6>.
- EUMETSAT, 2022a. Sentinel-6 payload data processing (PDP) processing baseline F06 - product notice. <https://www.eumetsat.int/media/48237>.
- EUMETSAT, 2022b. Sentinel-6/Jason-CS ALT level 2 product generation specification (L2 ALT PGS), version v4D.
- European Space Agency, Noordwijk, The Netherlands, 2021. Sentinel-6 L2 GPP project.
- European Space Agency, Noordwijk, The Netherlands, 2022. Copernicus sentinel-3 next generation topography (S3NG-T), mission requirements document (MRD), v0.41, draft as of 14.06.2022.
- Fenoglio-Marc, L., Fehlau, M., Ferri, L., Becker, M., Gao, Y., Vignudelli, S., 2010. Coastal sea surface heights from improved altimeter data in the Mediterranean Sea. In: International Association of Geodesy Symposia, Vol. 135, No. June 2008. pp. 253–261. [http://dx.doi.org/10.1007/978-3-642-10634-7\\_33](http://dx.doi.org/10.1007/978-3-642-10634-7_33).
- Ferreira, Ó., Ciavola, P., Armaroli, C., Balouin, Y., Benavente, J., Río, L.D., Deserti, M., Esteves, L., Furmanczyk, K., Haerens, P., Matias, A., Perini, L., Taborda, R., Terefenko, P., Trifonova, E., Trouw, K., Valchev, N., Van Dongeren, A., Van Koningsveld, M., Williams, J., 2009. Coastal storm risk assessment in Europe: Examples from 9 study sites. *J. Coast. Res.* 1632–1636.
- García, P., Granados, A., Guerra, M., Roca, M., Lucas, B., Féménias, P., 2022. The COR5 processor outcomes. Improving the Coastal Ocean SSH & SWH series from the Copernicus altimetry constellation. In: Ocean Surface Topography Science Team (OSTST) Meeting in Venice.
- Gautier, C., Caires, S., 2015. Operational wave forecasts in the Southern North Sea. In: *36th IAHR World Congress*, Vol. 1.
- Glavovic, B., Dawson, R., Chow, W., Garschagen, M., Haasnoot, M., Singh, M., Thomas, A., 2022. Cross-chapter paper 2: Cities and settlements by the sea. In: *Climate Change 2022: Impacts, Adaptation and Vulnerability*, Contribution of Working Group II to the Sixth Assessment Report of the Intergovernmental Panel on Climate Change. Cambridge University Press, Cambridge, UK and New York, NY, USA, pp. 2163–2194. <http://dx.doi.org/10.1017/9781009325844.019>.
- Gomez-Enri, J., Cipollini, P., Passaro, M., Vignudelli, S., Tejedor, B., Coca, J., 2016. Coastal altimetry products in the Strait of Gibraltar. *IEEE Trans. Geosci. Remote Sens.* 54 (9), 5455–5466. <http://dx.doi.org/10.1109/TGRS.2016.2565472>.
- Gou, J., Tourian, M.J., 2021. RiwiSAR-SWH: A data-driven method for estimating significant wave height using Sentinel-3 SAR altimetry. *Adv. Space Res.* <http://dx.doi.org/10.1016/j.asr.2021.12.019>.
- Guccione, P., 2008. Beam sharpening of delay/Doppler altimeter data through chirp zeta transform. *IEEE Trans. Geosci. Remote Sens.* 46 (9), 2517–2526. <http://dx.doi.org/10.1109/TGRS.2008.918863>.
- Guccione, P., Scagliola, M., Giudici, D., 2018. 2D frequency domain fully focused SAR processing for high PRF radar altimeters. *Remote Sens.* 10 (12), 1943. <http://dx.doi.org/10.3390/rs10121943>.
- Harris, C.R., Millman, K.J., van der Walt, S.J., Gommers, R., Virtanen, P., Cournapeau, D., Wieser, E., Taylor, J., Berg, S., Smith, N.J., Kern, R., Picus, M., Hoyer, S., van Kerkwijk, M.H., Brett, M., Haldane, A., Fernández del Río, J., Wiebe, M., Peterson, P., Gérard-Marchant, P., Sheppard, K., Reddy, T., Weckesser, W., Abbasi, H., Gohlke, C., Oliphant, T.E., 2020. Array programming with NumPy. *Nature* 585, 357–362. <http://dx.doi.org/10.1038/s41586-020-2649-2>.
- Holthuijsen, L.H., 2007. Waves in Oceanic and Coastal Waters. Cambridge University Press, Cambridge, <http://dx.doi.org/10.1017/CBO9780511618536>.
- Hunter, J.D., 2007. Matplotlib: A 2D graphics environment. *Comput. Sci. Eng.* 9 (3), 90–95. <http://dx.doi.org/10.1109/MCSE.2007.55>.
- Janssen, P., 2011. IFS documentation – Cy37r2 operational implementation 18 May 2011 PART VII: ECMWF WAVE MODEL. ECMWF.
- Kleinherenbrink, M., Naeije, M., Slobbe, C., Egado, A., Smith, W., 2020. The performance of CryoSat-2 fully-focussed SAR for inland water-level estimation. *Remote Sensing of Environment* 237, 111589. <http://dx.doi.org/10.1016/j.rse.2019.111589>.
- Ku, H.H., et al., 1966. Notes on the use of propagation of error formulas. *J. Res. Natl. Bur. Stand.* 70 (4), 263–273. <http://dx.doi.org/10.6028/jres.070c.025>.
- Lippmann, T.C., Brookins, A.H., Thornton, E.B., 1996. Wave energy transformation on natural profiles. *Coast. Eng.* 27 (1), 1–20. [http://dx.doi.org/10.1016/0378-3839\(95\)00036-4](http://dx.doi.org/10.1016/0378-3839(95)00036-4).
- Martin-Puig, C., Cullen, R., Desjonqueres, J.D., Leuliette, E., Maraldi, C., Meloni, M., 2022. Cal/Val activities performed by the MPWG. In: Ocean Surface Topography Science Team (OSTST) Meeting in Venice.

- McKinney, W., 2010. Data structures for statistical computing in Python. In: Proceedings of the 9th Python in Science Conference. pp. 56–61. <http://dx.doi.org/10.25080/Majora-92bf1922-00a>.
- Melville, W.K., 1996. The role of surface-wave breaking in air-sea interaction. *Annu. Rev. Fluid Mech.* 28 (1), 279–321. <http://dx.doi.org/10.1146/annurev.fl.28.010196.001431>.
- Moreau, T., Rieu, P., Aublanc, J., 2017. Investigation of SWH bias in SAR altimetry mode. In: *Ocean Surface Topography Science Team (OSTST) Meeting*.
- Moreau, T., Tran, N., Aublanc, J., Tison, C., Le Gac, S., Boy, F., 2018. Impact of long ocean waves on wave height retrieval from SAR altimetry data. *Adv. Space Res.* 62 (6), 1434–1444. <http://dx.doi.org/10.1016/j.asr.2018.06.004>.
- NASA JPL, 2020. Sentinel-6A Michael Freilich Jason-CS (sentinel-6A) | PO.DAAC / JPL / NASA. Physical Oceanography Distributed Active Archive Center (PO.DAAC), <https://podaac.jpl.nasa.gov/Sentinel-6>.
- National Georegister of the Netherlands, 2021. Bathymetrie Nederlande – Binnenwaterstraßenkontur - Data Europa EU. <https://data.europa.eu/data/datasets/adn73c4a-ef03-4785-b7f6-942e86b385f7v?locale=de>.
- Passaro, M., Fenoglio-Marc, L., Cipollini, P., 2015. Validation of Significant Wave Height From Improved Satellite Altimetry in the German Bight. *IEEE Transactions on Geoscience and Remote Sensing* 53 (4), 2146–2156. <http://dx.doi.org/10.1109/TGRS.2014.2356331>.
- Passaro, M., Hemer, M.A., Quartly, G.D., Schwatke, C., Dettmering, D., Seitz, F., 2021. Global Coastal attenuation of wind-waves observed with radar altimetry. *Nature Commun.* 12 (1), 3812. <http://dx.doi.org/10.1038/s41467-021-23982-4>.
- Peng, F., Deng, X., 2018. A new retracking technique for brown peaky altimetric waveforms. *Mar. Geod.* 41 (2), 99–125. <http://dx.doi.org/10.1080/01490419.2017.1381656>.
- Pilarczyk, K.W. (Ed.), 1990. Coastal protection. In: *Coastal Protection: Proceedings of the Short Course on Coastal Protection*. Delft University of Technology, 30 June - 1 July 1990, Balkema, Rotterdam.
- Raney, R., 1998. The delay/Doppler radar altimeter. *IEEE Trans. Geosci. Remote Sens.* 36 (5), 1578–1588. <http://dx.doi.org/10.1109/36.718861>.
- Ray, C., Martin-Puig, C., Clarizia, M.P., Ruffini, G., Dinardo, S., Gommenginger, C., Benveniste, J., 2015. SAR altimeter backscattered waveform model. *IEEE Trans. Geosci. Remote Sens.* 53 (2), 911–919. <http://dx.doi.org/10.1109/TGRS.2014.2330423>.
- Raynal, M., Moreau, T., Tran, N., 2018. Assessment of the SARM processing sensitivity to swell. In: *Ocean Surface Topography Science Team (OSTST) Meeting*.
- Reguero, B.G., Losada, I.J., Méndez, F.J., 2015. A global wave power resource and its seasonal, interannual and long-term variability. *Appl. Energy* 148, 366–380. <http://dx.doi.org/10.1016/j.apenergy.2015.03.114>.
- Rogers, W.E., Babanin, A.V., Wang, D.W., 2012. Observation-consistent input and whitecapping dissipation in a model for wind-generated surface waves: Description and simple calculations. *J. Atmos. Ocean. Technol.* 29 (9), 1329–1346. <http://dx.doi.org/10.1175/JTECH-D-11-00092.1>.
- Sajjad, M., Chan, J.C.L., 2019. Risk assessment for the sustainability of coastal communities: A preliminary study. *Sci. Total Environ.* 671, 339–350. <http://dx.doi.org/10.1016/j.scitotenv.2019.03.326>.
- Scagliola, M., Recchia, L., Maestri, L., Giudici, D., 2021. Evaluating the impact of range walk compensation in delay/Doppler processing over Open Ocean. 25 Years of Progress in Radar Altimetry, *Adv. Space Res.* 25 Years of Progress in Radar Altimetry, 68 (2), 937–946. <http://dx.doi.org/10.1016/j.asr.2019.11.032>.
- Scharroo, R., Martin-Puig, C., Meloni, M., Nogueira Loddó, C., Grant, M., Lucas, B., 2022. Sentinel-6 products status. In: *Ocean Surface Topography Science Team (OSTST) Meeting in Venice*.
- Schlembach, F., Passaro, M., Dettmering, D., Bidlot, J., Seitz, F., 2022. Interference-sensitive coastal SAR altimetry retracking strategy for measuring significant wave height. *Remote Sensing of Environment* 274, 112968. <http://dx.doi.org/10.1016/j.rse.2022.112968>.
- Schlembach, F., Passaro, M., Quartly, G.D., Kurekin, A., Nencioli, F., Dodet, G., Piollé, J.-F., Arduin, F., Bidlot, J., Schwatke, C., Seitz, F., Cipollini, P., Donlon, C., 2020. Round robin assessment of radar altimeter low resolution mode and delay-Doppler retracking algorithms for significant wave height. *Remote Sens.* 12 (8), 1254. <http://dx.doi.org/10.3390/rs12081254>.
- Smith, W.H., Scharroo, R., 2015. Waveform aliasing in satellite radar altimetry. *IEEE Trans. Geosci. Remote Sens.* 53 (4), 1671–1682. <http://dx.doi.org/10.1109/TGRS.2014.2331193>.
- Stopa, J.E., Arduin, F., Girard-Arduin, F., 2016. Wave climate in the Arctic 1992–2014: Seasonality and trends. *Cryosphere* 10 (4), 1605–1629. <http://dx.doi.org/10.5194/tc-10-1605-2016>.
- Timmermans, B., Shaw, A.G.P., Gommenginger, C., 2020. Reliability of extreme significant wave height estimation from satellite altimetry and in situ measurements in the coastal zone. *J. Mar. Sci. Eng.* 8 (12), 1039. <http://dx.doi.org/10.3390/jmse8121039>.
- Undén, P., Rontu, L., Jarvinen, H., Lynch, P., Calvo Sánchez, F.J., Cats, G., Cuxart, J., Eerola, K., Fortelius, C., García-Moya, J.A., Jones, C., Lenderink, G., McDonald, A., McGrath, R., Navasqués, B., Woetman-Nielsen, N., Odegaard, V., Rodríguez Camino, E., Rummukainen, M., Room, R., Sattler, K., Hansen Sass, B., Savijärvi, H., Wichers Schreur, B., Sigg, R., Han, T., Tijn, A., 2002. HIRLAM-5 Scientific Documentation. Swedish Meteorological and Hydrological Institute.
- Van Rossum, G., Drake, F.L., 2009. Python 3 Reference Manual. CreateSpace, Scotts Valley, CA.
- Vignudelli, S., Kostianoy, A.G., Cipollini, P., Benveniste, J., 2011. Coastal altimetry. <http://dx.doi.org/10.1007/978-3-642-12796-0>.
- Virtanen, P., Gommers, R., Oliphant, T.E., Haberland, M., Reddy, T., Cournapeau, D., Burovski, E., Peterson, P., Weckesser, W., Bright, J., van der Walt, S.J., Brett, M., Wilson, J., Millman, K.J., Mayorov, N., Nelson, A.R.J., Jones, E., Kern, R., Larson, E., Carey, C.J., Polat, İ., Feng, Y., Moore, E.W., VanderPlas, J., Laxalde, D., Perktold, J., Cimrman, R., Henriksen, I., Quintero, E.A., Harris, C.R., Archibald, A.M., Ribeiro, A.H., Pedregosa, F., van Mulbregt, P., SciPy 1.0 Contributors, 2020. SciPy 1.0: Fundamental algorithms for scientific computing in Python. *Nature Methods* 17, 261–272. <http://dx.doi.org/10.1038/s41592-019-0686-2>.
- Wang, P., Kraus, N.C., 2005. Beach profile equilibrium and patterns of wave decay and energy dissipation across the Surf Zone Elucidated in a large-scale laboratory experiment. *J. Coast. Res.* 2005 (213), 522–534. <http://dx.doi.org/10.2112/03-003.1>.
- Waskom, M.L., 2021. Seaborn: Statistical data visualization. *J. Open Source Softw.* 6 (60), 3021. <http://dx.doi.org/10.21105/joss.03021>.
- Wright, L.D., 1976. Nearshore wave-power dissipation and the coastal energy regime of the Sydney-Jervis Bay region, New South Wales: A comparison. *Mar. Freshwater Res.* 27 (4), 633–640. <http://dx.doi.org/10.1071/mf9760633>.